NANYANG
TECHNOLOGICAL
UNIVERSITY
SINGAPORE

THERMALLY DRAWN POLYMER FIBERS FOR ADVANCED SENSING FABRICS

WANG ZHE

SCHOOL OF ELECTRICAL & ELECTRONIC ENGINEERING

2020

THERMALLY DRAWN POLYMER FIBERS
FOR
ADVANCED SENSING FABRICS

WANG ZHE

School of Electrical & Electronic Engineering

A thesis submitted to the Nanyang Technological University
in partial fulfillment of the requirement for the degree of
Doctor of Philosophy

2020

Statement of Originality

I hereby certify that the work embodied in this thesis is the result of original research, is free of plagiarised materials, and has not been submitted for a higher degree to any other University or Institution.

22-Jul-2020

. . . .

Date

Wang Zhe

. . . .

Wang Zhe

Supervisor Declaration Statement

I have reviewed the content and presentation style of this thesis and declare it is free of plagiarism and of sufficient grammatical clarity to be examined. To the best of my knowledge, the research and writing are those of the candidate except as acknowledged in the Author Attribution Statement. I confirm that the investigations were conducted in accord with the ethics policies and integrity standards of Nanyang Technological University and that the research data are presented honestly and without prejudice.

22-Jul-2020
. . . .
Date

. . . .
Wei Lei

Authorship Attribution Statement

This thesis contains material from three papers published in the following peer-reviewed journals in which I am listed as an author.

Chapter 3 is published as T. Zhang, Z. Wang (equal contributor), B. Srinivasan, Z. Wang, J. Zhang, K. Li, C. Boussard-Pledel, J. Troles, B. Bureau, and L. Wei. Ultraflexible glassy semiconductor fibers for thermal sensing and positioning. *ACS Applied Materials & Interfaces* **11**, 2441-2447 (2019). DOI: 10.1021/acsami.8b20307.

The contributions of the co-authors are as follows:

- Prof. Wei provided the initial project direction and edited the manuscript drafts.
- I prepared the manuscript drafts. The manuscript was revised by Dr. T. Zhang.
- I prepared the preform for thermal drawing, fabricated the thermoelectric fiber, measured the fiber's mechanical and electrical properties, characterized the fiber's morphologies and components distribution, measured the thermal sensing performance, and assembled the thermal sensing fabric.
- Dr. T. Zhang conducted the XRD measurement of the thermoelectric fiber cores and simulated the thermal sensing performance.
- Dr. T. Zhang assisted in building the measurement system, measuring the thermal sensing performance, and analyzing the data.
- B. Srinivasan, C. Boussard-Pledel, J. Troles, and B. Bureau synthesized the bulk sample of chalcogenide glass.
- J. Zhang and K. Li assisted in photo taking and differential scanning calorimetry (DSC) measurement.

Chapter 4 is preparing for publishing as M. Chen, Z. Wang (equal contributor), Q. Zhang, Z. Wang, W. Liu, M. Chen, and L. Wei. Self-powered multifunctional sensing based on super-elastic fibers by soluble-core thermal drawing. *Preparing (2020).*

The contributions of the co-authors are as follows:

- Prof. Wei provided the initial project direction and edited the manuscript drafts.
- I and Dr. M. Chen prepared the manuscript drafts.
- I prepared the preform for thermal drawing, draw the SEBS/PVA fibers, measured the fiber’s electrical performance, built the setup and measured the performance of fiber based TENG and the self-adaptive net fabric, took photos for demonstration, simulated the electric potential distribution.
- Dr. M. Chen conducted the PVA core removal and liquid metal injection process, assembled the fiber-based device, analyzed the mechanical performance of the fibers, and constructed the self-adaptive net fabric.
- Dr. M. Chen assisted in building the measurement system, measuring the electrical performance, and analyzing the data.
- Q. Zhang. and W. Liu. assisted in testing the fibers’ mechanical performance.
- Z. Wang and M. Chen helped in photo taking and data analyzing.

Chapter 5 is published as Z. Wang, T. Wu, Z. Wang, T. Zhang, M. Chen, J. Zhang, L. Liu, M. Qi, Q. Zhang, J. Yang, W. Liu, H. Chen, Y. Luo, and L. Wei. Designer patterned functional fibers via direct imprinting in thermal drawing. *Nature Communications* **11**, 2842 (2020). DOI: 10.1038/s41467-020-17674-8.

The contributions of the co-authors are as follows:

- Prof. Wei provided the initial project direction and edited the manuscript drafts.
- I prepared the manuscript drafts. The manuscript was revised by Dr. T. Wu and Z. Wang.

- I designed the DITD process, prepared the preforms, built the setup for thermal imprinting, fabricated the templates, analyzed the thermal and flow behavior, produced the fibers for plasmonic and TENG, tested the touch sensing fabric, and characterized the morphologies of the fibers.
- Dr. T. Wu, Dr. Y. Luo, and L. Liu performed the dark-field spectroscopy measurement and analyzed the relevant data.
- Z. Wang and J. Yang drew the schematic of DITD process and helped in photo taking.
- T. Zhang and H. Chen assisted in thermal simulation.
- M. Chen and W. Liu helped in TENG performance testing.
- J. Zhang helped in the discussion of flow behavior.
- M. Qi assisted in SEM measurement.
- Q. Zhang. contributed to templates preparation.

22-Jul-2020 Wang Zhe

. . . .

Date Wang Zhe

Acknowledgments

Looking back at my Ph.D. journey, I feel so lucky for having received a lot of help and support from many people. At this moment that I am about to finish this thesis, I would like to express my sincere gratitude to them.

First and foremost, I would like to thank my supervisor, Prof. Wei Lei, who offered me this invaluable opportunity to join the Ph.D. programme at Nanyang Technological University (NTU) and has been provided constant support in both work and life during my Ph.D. study. His open mind, creative insights and patient guidance encourages me to determine my research topic based on my own interests and dig deeper into the topic to accomplish systematic and comprehensive research works. The critical thinking and meticulous attitude I learned from him will be beneficial for my whole life.

I would like to thank Prof. Shum Ping, who often encourages us to explore new things and shares his valuable experience, which greatly broadens our horizons.

I would like to thank my excellent group members, Dr. Li Kaiwei, Dr. Zhang Ting, Dr. Chen Ming, Dr. Chen Mengxiao, Dr. Zhang Qichong, Dr. He Yi, Dr. Jin Yunxia, Dr. Zhang Nan, Dr. Zhang Mengying, Dr. Wu Tingting, Dr. Zhang Jing, Dr. Ma Shaoyang, Wang Zhixun, Qi Miao, Zhang Haozhe, and Wu Junying, for all their help and encouragement in both research work and daily life. I would also like to thank all my colleagues from COFT, FTL, PL2, and CINTRA for their strong support for my projects.

Finally, I would like to thank my beloved family, especially my parents, who always love me and support my every decision, giving me the courage to keep moving forward.

Table of Contents

Summary

Fabrics are one of the earliest forms of human expression. However, they have not evolved much in the long history of being an essential product in our daily life. Enlightened by the rapid development in functional electronic devices over the past few decades, escalating research interests have been focused on achieving functional fabrics for various applications, for example, detecting vital signs, monitoring environmental change, and transmitting data. As the basic building blocks of fabrics are fibers, the functionalization and scalable fabrication of fibers are highly demanded. Fibers with diverse functions such as sensing, actuating, imaging, energy harvesting, and light emitting are crucial for achieving various functional fabrics and supporting their potential applications.

Among all the fiber fabrication methods, a preform-to-fiber thermal drawing technique has been broadly employed for the mass production of longitudinally uniform fibers with an extended length up to tens of kilometers. This technique is applicable to a wide selection of materials, including both structural materials, such as polymers and elastomers, and functional materials such as metals and semiconductors, and even materials in liquid phase, indicating extensive sensing applications. Further, complex inner and outer architectures can be constructed in fibers by the design of the preform or modification of the thermal drawing process. The tremendous possible combinations of materials and architectures in fibers also make them privileged in fabricating wearable triboelectric nanogenerator (TENG), which is frequently used as self-powered touch sensors. In this thesis, thermal and touch sensing fibers and fabrics are developed based on the thermal drawing technique.

First, a thermoelectric fiber is fabricated by thermal co-drawing a macroscopic preform containing a semiconducting glass core and a polymer cladding to deliver thermal sensing function at fiber-optic length scales with excellent flexibility and uniformity. The resulting thermoelectric fiber sensor operates in a wide temperature

range with high sensitivity and accuracy while offering superior flexibility with the bending curvature radius below 2.5 mm. Additionally, a single thermoelectric fiber can either sense the spot temperature variation or locate the heat/cold spot on the fiber. As a proof of concept, a two-dimensional 3 × 3 fiber array is woven into a fabric to simultaneously detect the temperature distribution and the position of heat/cold source with the spatial resolution of millimeters. The results demonstrate the feasibility of the fabrication of large-area, flexible, and wearable temperature sensing fabrics for wearable electronics and advanced artificial intelligence applications.

Second, a two-step soluble-core thermal drawing process is developed. It consists of the traditional thermal drawing and simple post-draw processing to further extend the potential of soft fiber electronics. An ultra-stretchable conductive fiber is achieved, which maintains excellent conductivity even under 1900% strain or freefalling from 1-m height with 1.5 kg load. Moreover, the resulted fiber also acts as a stretchable TENG for self-powered self-adapting multi-dimensional sensing based on the coupling effect of contact electrification and electrostatic induction. A touch sensing net fabric is built from the stretchable fiber and attached to sports gear to monitor sports performance while bearing strong and sudden impacts. This scalable fabrication approach combines with TENG design enables various in-fiber structures, leading to the further promotion of self-powered sensors and large-scale device integration.

Last, to further improve the performance of fiber-based TENG devices and extend the applications of thermally drawn fibers, high-resolution designer micro/nanostructures are achieved on fiber surface by introducing direct imprinting in thermal drawing (DITD) technique. A wide variety of regular and irregular micro/nano-scale surface patterns are successfully created on the entire surfaces of hundreds-meter long fibers with different inner structures and materials. Such a thermal imprinting process is simulated and confirmed by experimental measurements to illustrate the feasibility of the DITD technique. Pattern resolution, repeatability, and pattern depth control are further examined, showing a featured size as small as tens of nanometers. To explore the application prospect of the DITD technique, nanopatterns are fabricated on fibers to form plasmonic metasurfaces. Moreover, double-sided patterned fibers are produced to construct wearable TENGs with enhanced performance compared to fibers with flat surfaces. Further, a self-powered wearable touch sensing fabric with 12 sensing nodes is fabricated using the double-sided patterned fibers. The self-powered wearable touch-sensing fabric can precisely locate single and multiple touchpoints on curved surfaces, revealing a bright future of the DITD technique in wearable multifunctional fiber-based electronics and smart fabrics.

List of Abbreviations

2D	Two-Dimensional
Ag	Silver
Al	Aluminum
As	Arsenic
As_2Se_3	Arsenic Triselenide
Bi_2Te_3	Bismuth Telluride
CNC	Computer numerical control
CNT	Carbon Nanotube
CO_2	Carbon Dioxide
COC	Cyclic Olefin Copolymer
CPC	Carbon-Loaded Polycarbonate
CPE	Carbon-Loaded Polyethylene
Cr	Chrome
CS	Contact–Separation
Cu	Copper
DITD	Direct Imprinting in Thermal Drawing
DMA	Dynamic Mechanical Analyzer
DSC	Differential Scanning Calorimeter
EDX	Energy-Dispersive X-ray
FDTD	Finite-Difference Time-Domain
FESEM	Field Emission Scanning Electron Microscope
FET	Field-Effect-Transistor
FIB	Focused Ion Beam
FT	Freestanding Triboelectric-layer
GAST	$Ge_{15}As_{25}Se_{15}Te_{45}$
Ge	Germanium
HPCVD	High-Pressure Chemical Vapor Deposition
IR	Infrared

LED	Light-Emitting Diode
LS	Lateral-Sliding
NTC	Negative Temperature Coefficient
PA6	Nylon
PBG	Photonic Bandgap
PC	Polycarbonate
PCF	Photonic Crystal Fiber
PEEK	Polyether Ether Ketone
PEI	Polyethylenimine
PES	Polyethersulfone
PET	Polyethylene Terephthalate
PI	Polyimide
PMMA	Poly(Methyl Methacrylate)
PS	Polystyrene
Pt	Platinum
PTFE	Polytetrafluoroethylene
PVA	Polyvinyl Alcohol
PVDF	Polyvinylidene Fluoride
Se	Selenium
SE	Single-Electrode
SEBS	Styrene-Ethylene-Butylene-Styrene
SEM	Scanning Electron Microscope
Si	Silicon
Sn	Tin
Te	Tellurium
TEC	Thermal Expansion Coefficient
TENG	Triboelectric Nanogenerator
WAXS	Wide-Angle X-Ray Scattering
ZnSe	Zinc Selenide
ZT	Figure of Merit

List of Figures

Chapter 1 Introduction

1.1 Background and Motivation

Fabrics have served as an indispensable product in human daily life for thousands of years [1]. Although they were used in tremendous applications with various forms ranging from small pieces, including bandage and towel, to different kinds of apparel, the basic functions of these fabrics haven't evolved much from ancient to modern times. In most cases, they are considered as lacking technological functions and used in cleaning, offering physical protection from the external environment, achieving thermal comfort, or providing aesthetic expression.

In the last few decades, the leaping semiconductor industry enabled the rapid development in electronic devices with numerous functions such as sensing, communicating, computing, and actuating [2-11]. Moreover, these devices are getting smaller in size and lighter in weight, which makes them portable for ease of use and implementation. Inspired by these achievements, escalating research interests have been focused on realizing different functions, such as vital signs monitoring, external environment detecting, and data transmission, on fabrics to construct wearable fabric-based devices towards "smart fabrics" [12-19].

There is no standard definition of smart fabrics. In general, it can be taken as fabrics that can sense and respond to environmental stimuli including mechanical, thermal, electrical, and optical signals [20]. Although only a few products can be found currently, the global market for smart fabrics is forecast to rapid growth [21], considering their huge application perspectives in many fields. For example, sports attire with integrated functions of blood pressure detecting and emergency alerting, clothes with the ability to provide heating or cooling according to the environmental temperature, and artificial skin that can feel touches and actuate accordingly[22-30]. To ensure the smart fabrics act properly when served in these application scenarios, it is essential for the smart fabrics themself to collect the right external information.

From this point of view, sensing plays a fundamental role in smartening fabrics. Therefore, achieving advanced sensing fabrics is crucial for the evolution of smart fabrics.

Fibers, as the building blocks of fabrics, determine the basic properties and the realization of sensing function on fabrics. Thus, the scalable fabrication of flexible fibers compatible with various materials and complex architectures is highly demanded to support the development of sensing fabrics and their wide range of applications. Unfortunately, it is quite challenging to employ fiber as a new platform to develop functional devices. Current processing techniques [31-36] such as lithography [37-42] and molecular beam epitaxy [43-47]are developed for rigid and planar substrates such as wafers, which are not compatible with the soft and highly curved fibers. Besides, the commonly used materials comprising silicon and planar device configurations in conventional devices are difficult to be transferred to fibers. Hence, countless works have been carried out to explore new processing techniques for fiber-based devices. As a result, many fiber processing techniques, such as electrospinning [48-52], dip-coating [53-56], chemical and physical deposition [57-61], electrochemical deposition [62-65], and hydrothermal synthesis [66-69], were developed and some promising applications such as solar cells [70-75], supercapacitors [76-79], nanogenerators [48, 80-83], and light emitting devices [84-86] were demonstrated. However, these approaches always require complex material deposition procedures to form a single fiber and most of the fiber architectures are limited to layered core-shell structure, leading to limited functionalities. Additionally, the weaknesses in durability, axial uniformity, and scalability in production of these fibers also become the bottleneck towards industrial production.

A newly developed preform-to-fiber thermal drawing technique has been broadly employed for the mass production of longitudinally uniform fibers with the extended length up to tens of kilometers [87-92]. The thermal drawing process begins with heating a macroscopic preform containing glassy material such as a thermoplastic polymer above its glass transition temperature till soft. The soft preform with a typical diameter in centimeter range is then pulled under a controlled speed to form viscous flow [93] and thus elongated into a fiber with a uniform diameter ranging from tens of micrometers to several millimeters. During the fiber drawing process, the cross-sectional architecture of the fiber is consistent with the preform except for being scaled down in size after the drawing process. Microscopic fiber with a sophisticated inner structure could be achieved simply by constructing the corresponding inner structure in the macroscopic preform [94]. Furthermore, this thermal drawing technique is applicable to a wide selection of materials including metals [95-98], semiconductors [99-102], and insulators [103-106]. Even materials in liquid phase [107] and commercial components [108] could be incorporated into fibers under good confinement of the glassy materials thanks to their high viscosity (typically 10^4 - 10^8 Pa·s) during the thermal drawing process. Thus, various functional materials and arbitrarily designed inner structure can be highly integrated into a single fiber, enabling this technique a wide application prospect including optoelectronics [109-112], motion sensing [113, 114], thermal sensing [115, 116], energy transducing [103, 117] and bio-fiber interfaces [118-121]. Also, the thermally drawn fibers are particularly durable and even washable as the functional materials and structures are protected inside the glassy material. Finally, it is worth noting to mention that polymer fibers drawn via this technique are compatible with modern textile technology because they are flexible, washable, and high yield, denoting the thermally drawn polymer fibers a promising candidate for advanced sensing fabrics.

Thermal sensor, a device to monitor the temperature, reveals important information about the dynamics of many chemical, physical, and biological phenomena [122-127]. It is one of the most frequently employed sensors for industrial processing, health monitoring, military defense, and so on. In practical, the infrared imaging system has been widely applied in firefighting, disease control, and night surveillance, where the measured objects can be exposed to the camera lens directly without obstacle. However, it is not applicable in the cases where the measured object is covered or shaded, for example, monitoring skin temperature underneath the clothes and measuring temperature distribution on robots or other rugged surfaces. Therefore, developing a thermal sensing fabric with good flexibility to conformably wrap an irregular surface and high spatial resolution to extract the temperature distribution is of great value for these applications. Combing with the thermal drawing technique, the high scalable fabrication and good material compatibility technique, thermally sensitive material including thermistors [122, 128] and thermoelectric material [115, 129] could be conveniently incorporated into the kilometers-long fiber, enabling very large area temperature monitoring network.

Touch sensing fabrics are also expected for many fascinating applications, such as granting the sense of touch to artificial intelligence robot, attaching to sports gears to monitor sports performance, or served as a communication interface between human and smart fabrics [130-134]. Recently, triboelectric nanogenerator (TENG), a device that converts mechanical energy into electricity based on the coupling effect of triboelectrification and electrostatic induction, has been frequently employed as self-powered touch sensor owing to its high output signal, diverse choices of materials, and low cost [135-145]. As surface area is a crucial factor that influencing the performance of TENG [146] while fibers possess very large surface-to-volume ratio because of their unique shape, the durable and ultra-long fiber-based TENG fabricated via fiber drawing technique could be a promising solution for touch sensing fabrics.

Furthermore, previous works [147-149] have confirmed that the microstructure can significantly boost the output performance of TENG due to enlarged surface area and enhanced friction. Additionally, surface patterns will also bring many other unique properties such as hydrophobic surface [150, 151], coloration [152, 153], enhanced gas absorption [154, 155], and antimicrobial [156, 157]. Thus, creating surface patterns on fibers is not only an effective way to improve the performance of touch sensing fibers and fabrics based on TENG but also a decent approach to extend the application variety of fibers and fabrics. However, by far only surface grooves along the fiber’s axial direction were achieved due to structure elongation and surface tension-driven polymer reflow via the traditional drawing process [93, 158-161]. Therefore, an effective yet universal approach to creating high-resolution complex micro/nanostructure beyond axial direction on thermally drawn fibers is vastly demanded for the further development of functional fibers and advanced sensing fabrics.

1.2 Objectives

In this thesis, the thermal drawing technique, a large-scale fabrication approach with good material and architecture compatibility, is applied to develop polymer functional fibers and explore their applications in advanced sensing fabrics, including thermal sensing and touch sensing. Also, the thermal drawing process is modified to fabricate designer surface patterns on fibers, which will enable more unique properties onto function fibers and improve the advanced sensing fabrics. The main objectives of this thesis are:

1. To fabricate a flexible and uniform thermoelectric fiber by thermal drawing technique which contains a semiconducting glass core and a polymer cladding to deliver thermal sensing function, measure the thermoelectric properties of the semiconductor core, simulate and experimentally test the thermal sensing performance of individual fiber, and construct a thermal sensing fabric for simultaneous thermal source detecting and positioning.

2. To develop a strategy for thermally drawing elastic fibers with high stretchability and durability, fabricate conductive elastic fiber-based TENG and measure the performance under different stretch ratios, and build a self-powered touch sensing fabric which can adapt to any surface for monitoring sports performance.

3. To propose a direct imprinting thermal drawing (DITD) technique to achieve arbitrarily designed surface patterns on entire fiber surfaces, simulate and measure the thermal behavior during the drawing process, study the resolution and key parameters of this technique, and explore

different applications of patterned functional fibers including a touch sensing fabric.

1.3 Major Contributions of the Thesis

The novelty of the studies and major contributions of the thesis include:

1. *Realize a thermal sensing fabric for simultaneously realizing thermal sensing and positioning with high spatial resolution*. In this study, a thermoelectric fiber is thermally drawn from a macroscopic preform containing a semiconducting glass core and a polymer cladding. The fiber can be arbitrarily long and shows superior flexibility with the bending curvature radius below 2.5 mm. Also, the thermoelectric fiber exhibit large Seebeck coefficients and high thermal conductivity, working as a thermal sensor in a wide temperature range up to 150 °C. The voltage response is recognizable even the temperature change is smaller than 0.05 °C. Moreover, both the position and the temperature value of the heat or cold source can be detected by the single thermoelectric fiber, which is also confirmed by simulation results. At last, a thermal sensing fabric for simultaneous thermal sensing and positioning is constructed by fiber arrays with a grid size of 24 mm × 24 mm, leading to the realization of large-area thermography, health-monitoring products, and e-skin robotics.

2. *Introduce an ultra-stretchable fiber and demonstrate a self-powered touch sensing net fabric for monitoring sports performance*. First, a two-step soluble-core thermal drawing process is developed for thermally drawing low modulus, low viscosity, and high adhesiveness materials which are hard to be controlled control during the conventional fiber drawing process. Using this process, an ultra-stretchable conductive styrene-ethylene-butylene-styrene (SEBS) fiber is achieved, which maintains excellent conductivity even under 1900% strain or sudden hit

by a 1.5 kg load freefalling from a height of 1 meter. Second, stretchable TENGs are fabricated based on SEBS fibers. Their performance is measured, and the working mechanism is discussed and confirmed via simulation results. Finally, self-powered touch sensing net fabrics are built and demonstrated by attached to sports gear to monitor sports performance. This fabrication process and touch sensing fabrics indicating their future applications in self-powered smart fabric and large-scale device integration.

3. *Propose a direct imprinting thermal drawing (DITD) technique to achieve designer patterned fibers for the further development of functional fibers and advanced sensing fabrics*. a wide variety of regular and irregular surface patterns are created on hundreds-meter long fibers with different materials and inner structures, illustrating the high stability, high yield, and good compatibility of the DITD technique. Key process parameters such as resolution, repeatability, and depth control are examined, exhibiting the feature size as small as tens of nanometers. Nanopatterned fibers are fabricated and their plasmonic behaviors are studied. And double-sided patterned fibers are produced for fiber-based TENGs and further constructed into self-powered wearable touch sensing fabric, revealing a bright future of the DITD technique in wearable multifunctional fiber-based devices and smart fabrics.

1.4 Organization of the Thesis

This thesis consists of 6 chapters:

Chapter 1 gives a brief introduction to the background and motivation to develop thermally drawn polymer fibers for advanced sensing fabrics, especially thermal sensing and touch sensing, set the objectives of this thesis, and clarifies the major contributions of these studies.

Chapter 2 discusses the preparation, implementation, and applications of the thermal drawing technique, followed by the review of recent progress in thermal sensing, fiber-based TENG for touch sensing, and surface patterned fibers.

Chapter 3 describes the fabrication of flexible and uniform thermoelectric fiber by thermal drawing technique. Its thermoelectric properties and thermal sensing performance are tested. And thermal sensing fabric for simultaneous thermal source detecting and positioning is shown.

Chapter 4 develops a two-step soluble-core thermal drawing process for fabricating conductive and ultra-stretchable SEBS fibers. A self-powered touch sensing net fabric based on the SEBS fibers is built and its applications in monitoring sports performance are demonstrated.

Chapter 5 suggests a DITD technique to achieve arbitrarily designed surface patterns on entire fiber surfaces with high resolution in all directions. The thermal behavior, pattern resolution, and other key parameters of this technique are studied. And its application in various fields including metasurface and touch sensing fabric are exhibited.

Chapter 6 draws conclusions of this thesis and recommends future research works towards advanced fabrics based on thermally drawn fibers.

Chapter 2 Literature Review

In this chapter, basic concepts and recent advances in thermal drawing technique and fiber-based TENG are reviewed as background knowledge before introducing the following works towards advanced sensing fabrics. More specifically, Section 2.1 discusses several preform preparation methods, thermal drawing process, and various applications of drawn fibers, especially the applications in thermal sensing; Section 2.2 focuses on TENGs which will be used for self-powered touch sensing in this thesis, including the categories of TENGs, strategies for enhancing the performance of TENGs, and recent progress on fiber-based TENGs; and Section 2.3 presents previous works on drawing surface patterned fibers.

2.1 Thermal Drawing Technique and Its Applications

The preform-to-fiber thermal drawing technique was originally used to fabricate glass fibers for optical communication. Owing to its high production rate and stability, optical fibers become an indispensable item implemented all over the world for long-distance light data transmission today. In addition to telecommunication, thermally drawn glass fibers are also employed for many other applications such as fiber laser [162-164], imaging optics [165, 166], and fiber-optic sensor [167, 168].

Besides glass, thermoplastic polymers are also frequently used in the thermal drawing technique recently. Compared to fragile glass materials that require high processing temperature, polymers can be processed under low temperature and they possess higher flexibility and better machinability, making them compatible with different functional materials and fiber architectures. Over the past few years, numerous thermally drawn polymer fibers have been demonstrated for applications in electronics [169, 170], energy conversion [171, 172], and biomedicine [173, 174], etc.

These various applications based on thermally drawn glass and polymer fibers reveal the bright future of the thermal drawing technique. In this section, this trending technique will be systematically discussed from preform preparation to fiber application.

2.1.1 Preform Preparation

The thermal drawing process begins with heating a macroscopic preform where glassy materials, such as silica and thermoplastic polymer, constitute a great portion as the structural materials. After the glassy material is heated above its glass transition temperature, the preform will be pulled down and elongated into a microscopic fiber under a controlled behavior. The material and architecture of the fiber are consistent with that of the preform. Therefore, a well-constructed preform with desired material located at the prescribed position is requisite to achieve various functional fibers. Till now, many preform preparation approaches have been developed, such as rod-in-tube [175-178], extrusion [179, 180], thin-film rolling [181, 182], deep-hole drilling [183, 184], casting [185, 186], fused deposition modeling [187, 188], double-crucible [189, 190] and additive manufacturing [191]. Each approach possesses its own merits and demerits which make different approaches advance in preparing different preforms. Here, some commonly used approaches will be introduced in detail.

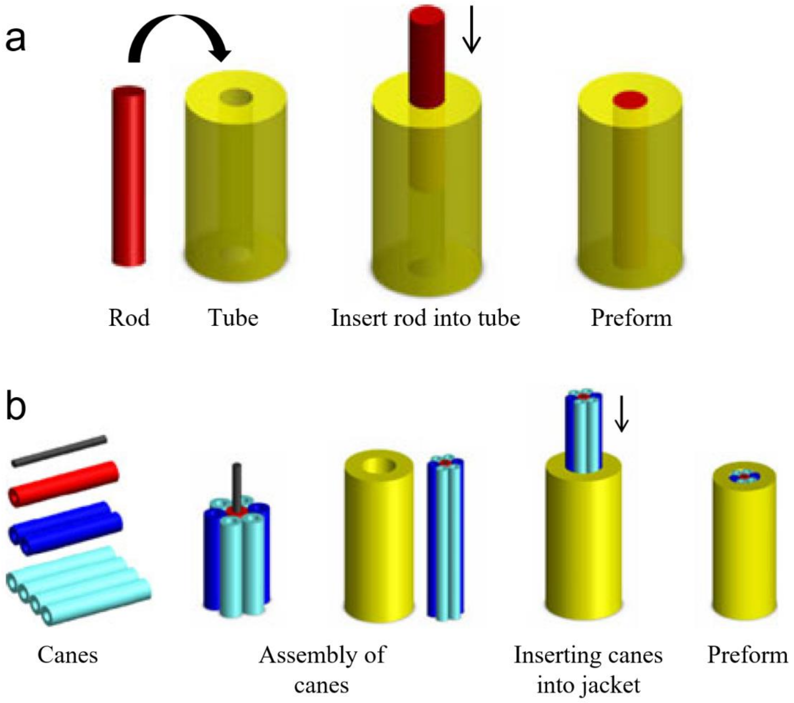

Figure 2-1. Schematic of (a) rod-in-tube approach and (b) stack-and-draw approach [192].

Rod-in-tube

The Rod-in-tube approach is frequently used for constructing a preform with a simple core-shell structure [192]. As sketched in Figure 2-1a, a rod is inserted into a tube with matched size and then sealed under vacuum to form a unity. Generally, the tube is made from glassy materials to support the whole structure during the thermal drawing process, while the rod can be various functional materials. This approach is applicable to both glass and polymer materials. The basic rule is that the rod material should be soft or melt that can flow inside the tube when thermally drawn. Instead of inserting a solid rod, powders and even solution can be filled into the tube in some special cases [107, 115].

Stack-and-draw

Similar to the rod-in-tube approach, the single rod can be replaced with a complex structure by stacking fine tubes or rods (canes) and then inserting them into the outer tube (jacket), as shown in Figure 2-1b. Although the glassy jacket can hold the stacked structures from disassembly, the canes must include glassy materials as well to maintain the complex inner structure during the thermal drawing process. Moreover, as longitudinal air holes are often employed in the stacked structures, the air pressure inside the holes is also a critical factor. Controlling the air pressure during the thermal drawing process could tune the size of the holes and achieve the desired final geometry [193-195]. This approach is extensively used to fabricate optical fibers with sophisticated inner structures including photonic crystal fiber (PCF) [196].

The rod-in-tube approach and stack-and-draw approach can be combined to achieve a fiber with a large number of micro/nanometer functional cores. For example, a three-step size-reduction process was reported by M. Yaman et al. to fabricate various semiconductor nanowires and nanotubes inside fibers [197]. As shown in Figure 2-2, the first step is fabricating a preform with semiconductor core and polymer cladding via the rod-in-tube approach and then drawing the preform into a fiber with core-shell structure. Semiconducting microwires could be obtained at this step. Next, a bundle of the thermally drawn fiber from step 1 was stacked and inserted into a new polymer tube. And the resulted fiber comprised a bundle of semiconductor nanowires. Finally, high-density nanowires array with the diameter of 5-50 nm inside the polymer cladding was achieved via repeating the stack-and-draw approach using the fibers drawn from the second step. This high-throughput nanofabrication process is compatible with a diverse selection of materials including crystalline semiconductors such as selenium (Se), chalcogenide glass such as arsenic triselenide (As_2Se_3), and hollow polymers such as polyvinylidene fluoride (PVDF) nanotube. Thus, a wide range of applications in flexible electronics, nonlinear photonics, nanofluids, and energy conversions can be expected.

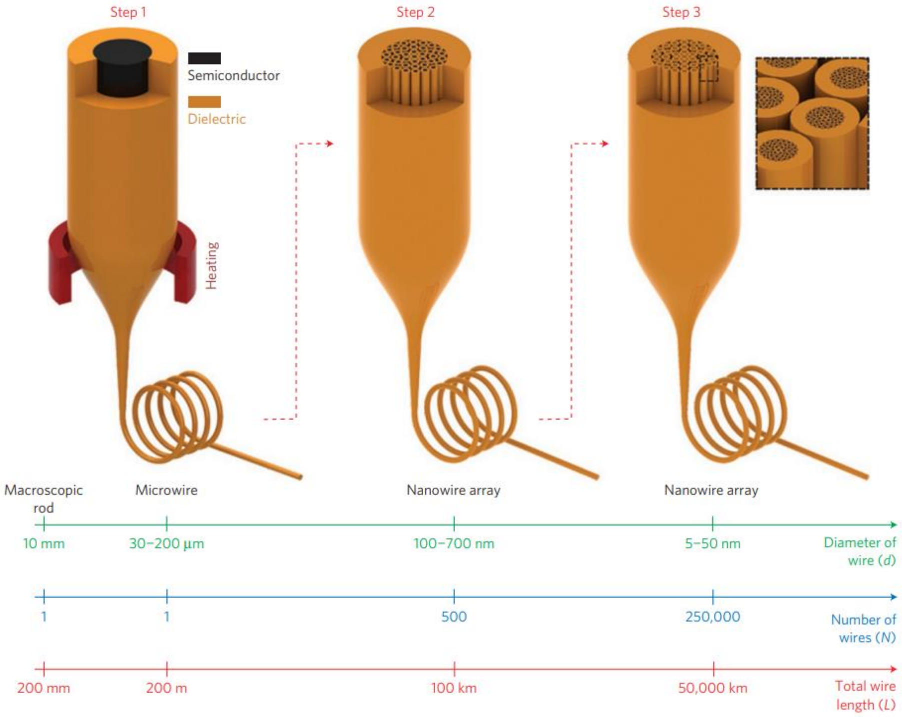

Figure 2-2. A nanofabrication approach based on a three-step size-reduction process [197].

Deep-hole drilling

To fabricate polymer preforms with many air holes along the longitudinal axis, the deep-hole drilling approach is also commonly employed [183, 184, 198]. The drilling process is conducted by a computer numerical control (CNC) machine. According to the desired fiber structure, numerous holes with different sizes could be drilled on a thick polymer rod. Moreover, the drilled holes are uniform throughout the preform and can be precisely distributed with arbitrary patterns. These advantages make it a common approach for fabricating polymer preforms for microstructured optical fibers. However, some limitations should be pointed out. The length to diameter ratio of the drilled holes is usually below 100 [198]. Thus, the length of the preform will be limited if small holes are needed. Furthermore, the drilling bit will not be rigid enough and bent easily during drilling if its diameter is too small. Hence, the size of the drilled holes is usually several millimeters. Additionally, the drilled holes are restricted to circular shapes and may have a rough inner surface,

Casting

Casting is another option to fabricated preforms for microstructured fiber with high yield [185, 186, 199]. A mold that mirrors the needed preform structure should be prepared before casting. It is usually made from high melting point material, such as alloy, and assembled from several elements, such as circular rods and rectangular bars. To facilitate the demolding process, all the surfaces of the elements must be very smooth. The casting approach can be applied to both glass and polymer. For glass preform, a sol-gel technique is used for casting an intermediate preform[199]. The intermediate preform is then released from the mold and sintered into glass followed by drawn into fibers. For polymer preform, chemical precursors are cast into the mold and then transformed into a solid preform after polymerization. Compared with stack-and-draw and deep-hole drilling, the casting approach possesses larger design freedom the hole size, shape, and arrangement could be designed independently on a large scale. Also, casting in a sealed mold can help to limit material contamination. However, the casting process has its own limitations. To release the mold after casting, only elements with uniform size along the longitudinal axis or elements in conical shape could be used. Moreover, the accessible material range is also limited as the preform is formed through a chemical process, which may not be applicable to all the materials for the thermal drawing process.

Thin-film rolling

Polymer preform can also be prepared through rolling a thin polymer film around a rod conformally followed by thermally consolidating the whole structure under vacuum. The thin film can be homogenous material to serve as the cladding of the rod (Figure 2-3a, b) or form a polymer tube by removing the rod. Otherwise, functional materials may be deposited on the thin film beforehand. And alternating layers will be formed inside the preform after rolling, as demonstrated in Figure 2-3c, d. The thickness of the layers can be reduced to sub 100 nanometers [200] after the thermal drawing process (Figure 2-3e). This thin film rolling approach has been widely exploited to fabricate photonic bandgap (PBG) fibers for light guidance, omnidirectional reflection, or other optoelectronic applications [201].

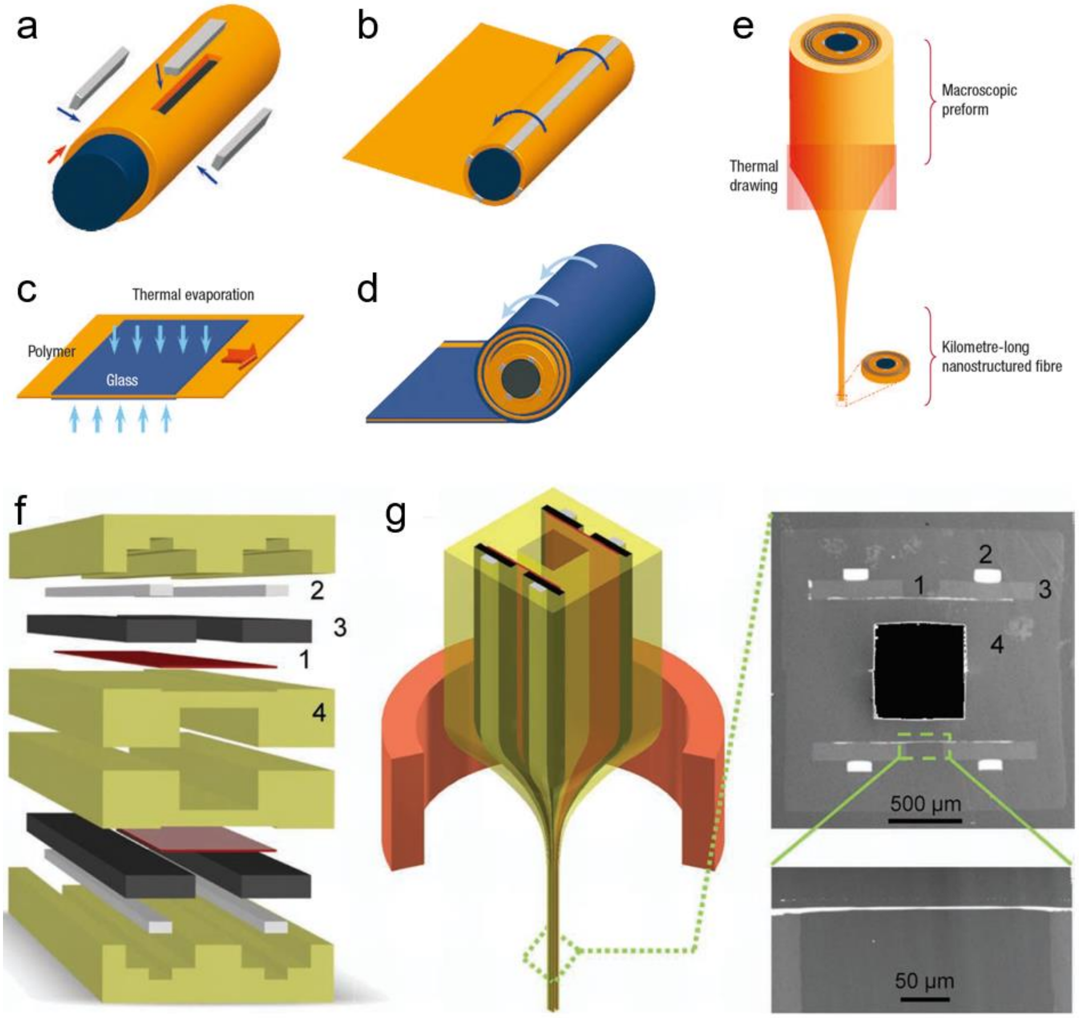

Figure 2-3. Schematic of thin-film rolling approach [200] and direct carving-and-assembly approach [202]. (a) A solid rod is assembled with a glass core, an insulating polymer shell, and four metal electrodes. (b) A polymer film is rolled around the structure to form a protective cladding. (c) A functional material deposited on the thin film. (d) Alternating layers formed by thin-film rolling. (e) The macroscopic preform is thermally drawn into a fiber while maintaining its cross-sectional architecture. (f) Components to be assembled. (1) Thin polymer film, (2) alloy electrode, (3) polymer electrode, and (4) polymer slab. (g) Thermal drawing process and cross-section SEM images of the drawn fiber.

Direct carving-and-assembly

For fabricating triangular, rectangular, or other irregular preforms, direct carving every part and assembling all the parts could be an efficient way to form complex architectures. As shown in Figure 2-3f [202], grooves with different sizes are carved on the four polymer slabs (yellow-green) according to the size of electrodes (grey and black), photosensitive semiconductors (red), as well as the hollow core. After assembling the functional materials and polymer slabs, the whole structure is thermally consolidated in a vacuum oven or hot press machine and then drawn into fiber (Figure 2-3g). As a result, fiber with a complex inner structure is achieved for detecting the incident light from the hollow channel. This direct carving-and-assembly approach has been broadly applied for developing different functional fibers for sensing, actuating, etc. [113, 171]

Fused deposition modeling

Fused deposition modeling is an additive manufacturing technique that can build predesigned structures layer-by-layer by feeding thermoplastic materials into a heated extrusion nozzle. Compared to most other preform preparation approaches that need lots of manual work, a great advantage of this technique is the ability to build preforms with complex structure and short lead time automatically. Additionally, this approach is compatible with most thermoplastic materials including polymer and glass [203, 204]. Therefore, in recent years, increasing amount of works have employed the fused deposition modeling technique to fabricate the preforms for applications such as optical waveguides [187, 205]. Yet, this approach also has some limitations, such as the rough surface (especially the visible layer lines) and limited dimensional accuracy (submillimeter level).

2.1.2 Thermal Drawing Process and Material Selection.

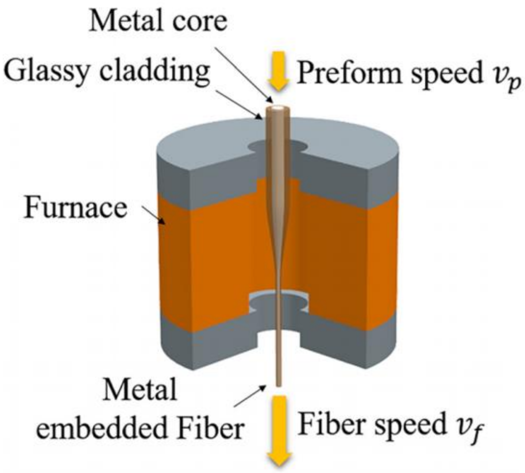

Figure 2-4. Schematic of typical thermal drawing process [206].

Typical thermal drawing process

The setup for the thermal drawing process is called fiber drawing tower. In the beginning, the preform is fixed above a vertical tube furnace and a weight may be attached below the preform. Then the preform is fed down into the furnace and held in the place where the bottom part of the preform is below the heating zone of the furnace. The temperature is set according to the cladding material of the preform, usually 50-100 °C higher than its glass transition temperature. After around half an hour, the temperature of the material at the heating zone is high enough to become soft and necked down under the pulling of the attached weight or the weight of the preform's bottom part. The size of the preform reduces in the neck-down region and finally forms a fiber. To keep drawing the fiber continuously, the preform is then fed into the heating zone at a constant speed (v_p) while the fiber is drawn down and collected by a capstan at a much larger speed (v_f), as sketched in Figure 2-4. Since the total volume of the materials remains unchanged during the thermal drawing process, the diameter of the fiber can be controlled by the preform speed and fiber speed, as the equation described below:

$$D_{fiber} = D_{preform} \times \sqrt{{}^{v_p}/_{v_f}} \tag{1}$$

In this manner, a hundreds-meters-long fiber with a diameter ranging from hundreds of micrometers to several millimeters can be drawn from a hundreds-millimeters-long preform with a diameter of several centimeters, while the inner structure of the fiber may reach as small as tens of nanometers.

Material selection

Typically, all the materials in the prepared preform will be molten or soften and subsequently experience a neck-down process to form a fiber during the thermal drawing process. To achieve this, some criteria should be followed when selecting different materials for codrawing [207].

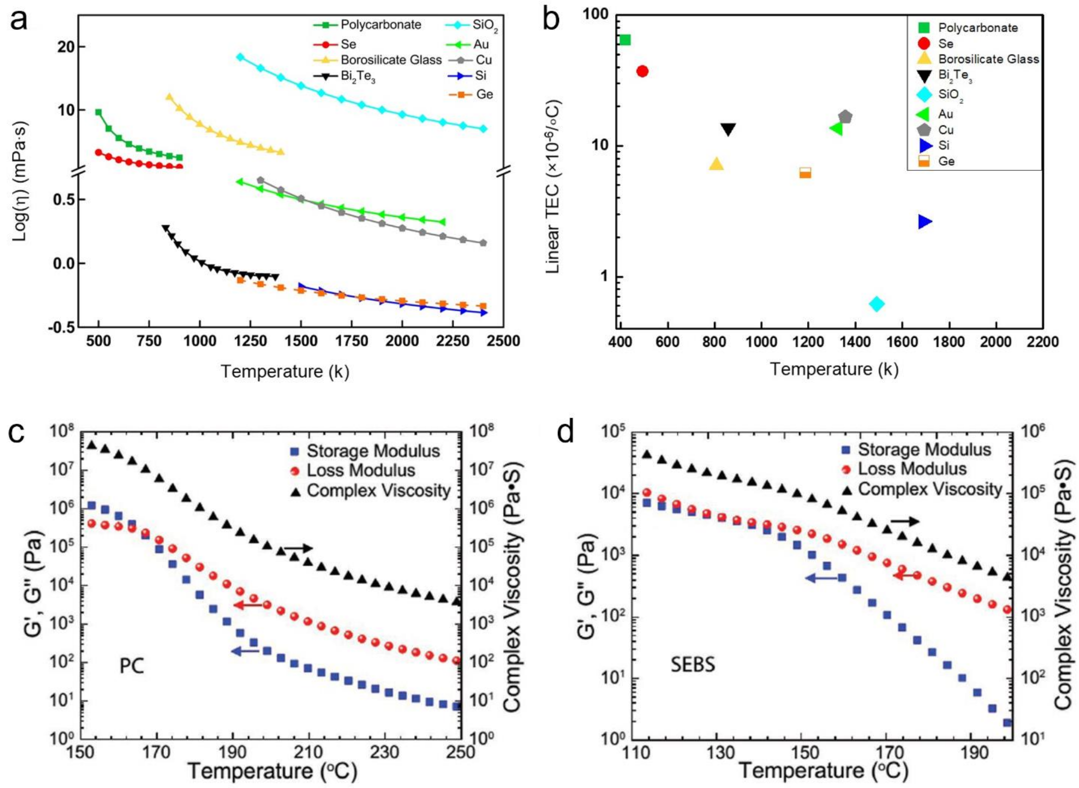

Figure 2-5. Material selection criteria for thermal drawing technique [192, 207, 208]. (a) Dynamic viscosity of different materials as a function of temperature. (b) Linear thermal expansion coefficient at room temperature (Y-axis) and melting temperature (X-axis) of different materials. Rheological properties (storage modulus, loss modulus, and complex viscosity) of (c) PC and (d) SEBS.

First, the preform must consist of at least one thermoplastic material as the frame to support the whole structure of the preform during the thermal drawing process. The drawing temperature is always decided by the thermoplastic material, normally 50-100 °C higher than its glass transition temperature. And it should possess a high viscosity (usually 10^4-10^8 Pa*s) under its drawing temperature to keep the complex structure from deformation. Figure 2-5a shows the viscosity of some common materials as a function of temperature.

Second, all the other materials inside the preform should be softened or molten under the drawing temperature. And the boiling temperature of the crystalline materials should be higher than the drawing temperature.

Third, the materials in the preform should better have similar thermal expansion coefficient (TEC). TEC mismatch may lead to undesired gaps between different materials or large residual stress which may cause mechanical fractures after the thermally drawn fiber cooled down.

Last, all the materials should be chemically stable without decomposition or interpenetration. Also, chemical reactions should be avoided to ensure a steady and continuous drawing process.

These criteria above are general guidelines based on previous experiences. A deeper understanding of rheology dynamics will be helpful to find out the properties that govern the compatibility with the thermal drawing technique. Recently, Y. Qu et al. put forward a rheological criterion to evaluate if a thermal plastic material can be thermally drawn at high viscosity by analyzing the complex shear viscosity, storage moduli (G′), and loss moduli (G″) of the materials [208]. They observed that a material can be drawn at high viscosities in the viscous regime if there is a temperature window where G′ shows a rapid decrease while G″ decrease slowly as the temperature increase. For example, the commonly used thermoplastic material polycarbonate (PC) fits well with this criterion (Figure 2-5c). Following this rheological criterion, they found a high elastic copolymer, SEBS, should be suitable for the thermal drawing process, as the rheology properties shown in Figure 2-5d. And the first thermally drawn elastomer fiber was fabricated, indicating the expansion in the material range of thermal drawing technique. Combining the elastomer material with functional materials and hybrid architectures, various soft and stretchable electronic devices were achieved in their following works.

Modified thermal drawing process

In addition to finding new materials follow the criteria for material selection and exploring diverse applications based on the typical thermal drawing technique, researchers are also trying to modify the thermal drawing process for including more materials beyond the general guidelines to further extend its application range.

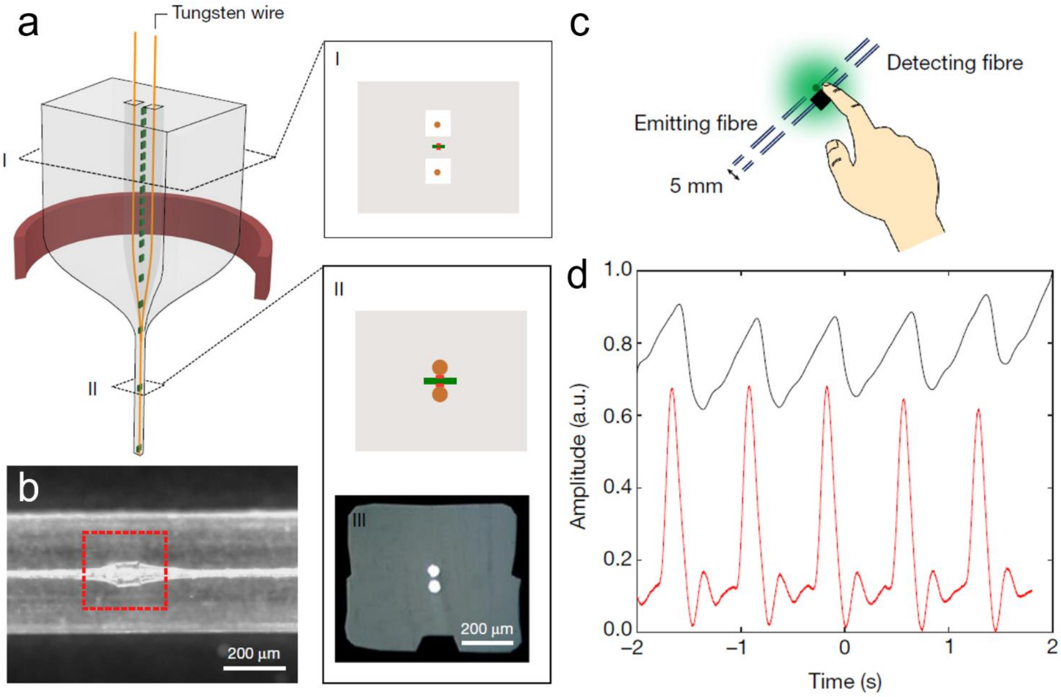

Figure 2-6. Convergence thermal drawing process for incorporating commercial planar devices [108]. (a) Preform structure and thermal drawing process. (b) Side view of the fiber with a LED device. (c) Schematic of the heart-rate measurement setup. (d) Measured signal of the photodetecting fiber (black curve) and a commercial pulse sensor (red curve).

A convergence thermal drawing process was reported in 2018 by Y. Fink et al. to incorporate materials that will not melt or become soft under the thermal drawing temperature [108]. As presented in Figure 2-6a, the rigid commercial semiconducting devices are included in the preform at the prescribed position. And tungsten wires are fed into the channels continuously during the thermal drawing process. As the lateral size reduced during the neck-down process, the wires and commercial devices will be squeezed together and achieve electrical contact, as confirmed by scanning electron microscope (SEM) images in Figure 2-6a$_{III}$ and 2-6b. Therefore, a series of commercial devices can be incorporated into fibers and function well. In their work, light-emitting diode (LED) and photodetector fibers are demonstrated, and a heart-rate measurement setup was assembled, as shown in Figure 2-6c, d. This modified thermal drawing process bridges the thermal drawing technique and the numerous planar semiconductor devices, providing a path to large scale integration of functional devices in fibers.

Some other works [107, 209] also reported modified thermal drawing techniques and showed new applications which will not be discussed in detail here. These efforts in modifying the thermal drawing process and exploring new compatible materials and fiber architectures enable tremendous possible combinations of materials and architectures in fibers for countless applications.

2.1.3 Applications of Thermally Drawn Fibers

Driven by the urgent demand for developing fiber-based devices for wearable electronics and smart fabrics, thermal drawing technique is experiencing a rapid development owing to its unique advantages including good compatibility with a wide range of materials, sophisticated fiber architectures, and high scalability. Over the last few decades, this technique has evolved from mostly producing optical fibers to offering multimaterial and multifunctional fibers for an abundance of applications. In this section, the applications of the thermally drawn fibers in diverse fields will be briefly reviewed.

Photonic bandgap fibers

PBG fibers are a kind of optical fiber that can guide light by photonic bandgap effect, which is different from the conventional optical fibers that guide light by total internal reflection [196]. Bragg fibers are fabricated in the early stage of the development of hollow-core PBG fibers [210]. Such Bragg fibers usually consist of a hollow core and an alternating multilayered structure at the inner surface formed by two materials with a large difference in refractive index, such as polyethersulfone (PES) and As_2Se_3 [182], as demonstrated in Figure 2-7a, b. As a photonic bandgap is formed by the periodic alternating layers, light with specific frequency will be confined inside the hollow core and transmit along the fiber. This specific frequency is tunable by simply changing the thickness of each layer. Figure 2-7c shows fibers with different specific frequencies achieved from the same preform by controlling the outer diameter of the fibers during the thermal drawing process [211]. Besides the scalability of wavelength, another significant advantage of this Bragg fiber is the low loss as the light is transmitted in the air other than solid fiber materials. The reported loss of the PBG fiber with a fundamental bandgap at 10.6 μm is 0.95 dB/m (Figure 2-7d), which is much lower than the state-of-art photonic crystal fiber whose loss is 2.1 dB/m [212].

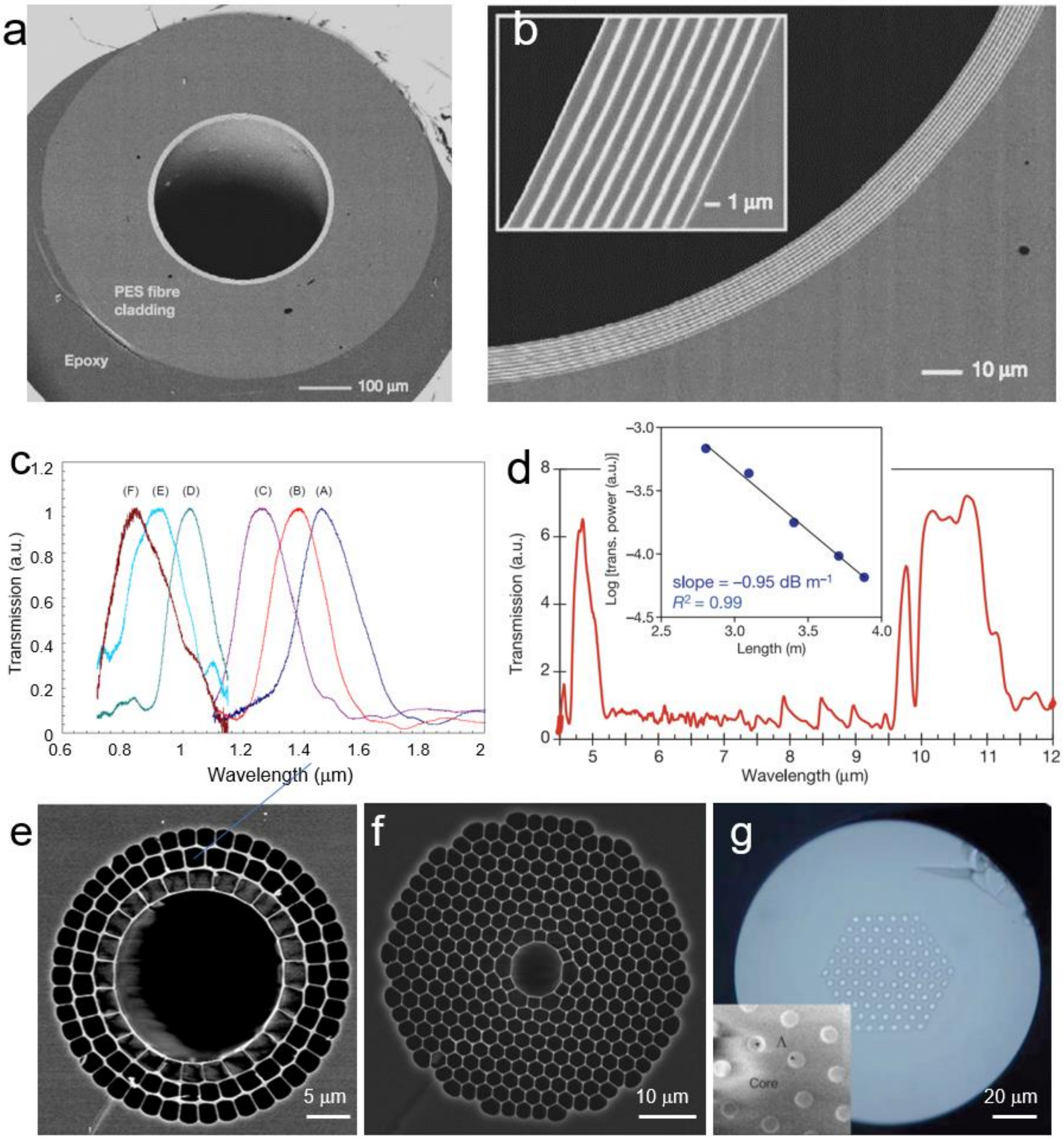

Figure 2-7. PBG fibers [182, 211, 213-215]. (a) Cross-sectional SEM images of hollow core PBG fiber mounted in epoxy. (b) Multilayer structure constructed from PES and As_2Se_3. (c) Different specific frequencies achieved from different layer thicknesses. (d) Transmission spectrum of a hollow PBG fiber. (e) PBG fiber with a hollow core surround by several rings of small air holes. (f) PBG fiber with a hollow core surround by a periodic array of air holes. (g) All-solid PBG fiber.

Besides the hollow-core Bragg fibers constructed from two different materials, there are some other types of PBG fibers [201, 216, 217]. As shown in Figure 2-7e, instead of using materials with different refractive index to form a multilayered structure, the dielectric layers can also be formed by rings of air holes separated by nanoscale support bridges [213, 218]. Such dielectric rings will form the photonic bandgap to guide light in the hollow core, whose refractive index is smaller than the surrounding cladding material. Moreover, the photonic bandgap could also be formed from a 2D periodical array of air holes in a dielectric material (Figure 2-7f), which has been widely studied as another type of PBG fibers since it was first demonstrated in 1998 [196, 214, 219, 220]. Additionally, the PBG fiber with a 2D periodical array can also be formed without air holes but with high-index rods in low-index background, as an all-solid PBG fiber shows in Figure 2-7g [215, 221].

The fundamentally different light guidance mechanism from total internal reflection enables PBG fibers numerous intriguing optical properties, such as ultralow optical nonlinearity, low latency, high damage threshold [201]. These advantages enable the PBG fibers a series of applications such as cylindrical optical resonators [222, 223], high-power laser transmission [182, 224], surface-emitting fiber lasers [163], gas sensing [225, 226], and particle guidance [227, 228].

Optoelectronic fibers

The ability to incorporate conductors and semiconductors enables the interaction between electric field and light in fibers, leading to the development of optoelectronic fibers. Compared to the rigid wafer-based optoelectronic devices, optoelectronic fibers are soft, large area, and not limited to planar configurations. Since the first multimaterial photodetecting fiber is demonstrated in 2004 [110], numerous optoelectronic fibers are developed for photodetecting [229], imaging [230], optical communicating [108], etc.

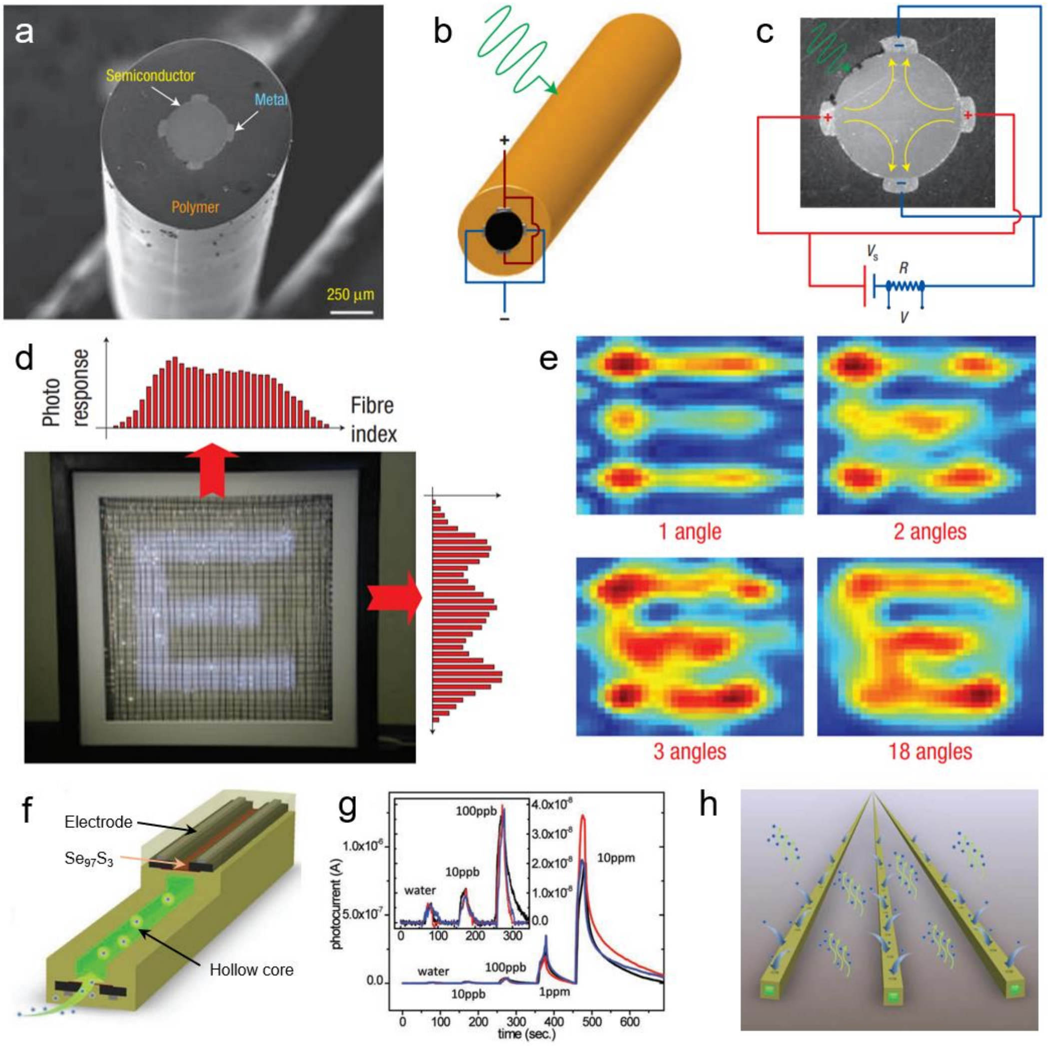

Figure 2-8. Thermally drawn optoelectronic fibers [202, 229]. (a) SEM image, (b) schematic, and (c) testing circuit of a photodetecting fibers. (d) Lensless imaging net constructed from photodetecting fibers. (e) Reconstructed images from the detected signals. (f) Schematic of a chemical sensing fiber for hazard vapors. (g) Sensitivity measurements of the chemical sensing fiber. (h) Concept drawing for remote and distributed sensing using the chemical sensing fibers.

A typical structure of photodetector fibers including semiconductor and paired electrodes is shown in Figure 2-8a [229]. Chalcogenide glass including $Se_{97}S_3$ and $As_{40}Se_{49}Te_{11}Sn_5$ is often employed as the photosensitive semiconductor and the electrode is Tin (Sn) or other low melting point alloys according to the cladding material. The resistance of the semiconductor will decrease when illuminated by external light. And the current will change if a voltage is applied to the electrodes. As shown in Figure 2-8b, c. Also, the direction of light can be distinguished by analyzing the current signal from different electrode pairs. Based on this photodetecting fiber, various sensing and imaging system are demonstrated. Figure 2-8d presents a lensless imaging net constructed from 32 * 32 fibers. After a letter “E” is illuminated on the net, different response signals will be generated on different fibers according to their illuminated areas. Then the image can be reconstructed by coupling the signals from all the fibers in the net, as shown in Figure 2-8e.

Chemical sensing is also realized in optoelectronic fibers [202]. The cross-sectional structure can be found in Figure 2-3g. This chemical sensing fiber comprises 2 photodetecting units and a hollow core. The inner surface of the fiber is coated with a chemiluminescent material. Therefore, when the hazardous vapors enter the hollow core, light will be emitted from the chemiluminescent material and detected by the photodetecting units as sketched in Figure 2-8f. This work achieved a high concentrate resolution of 10 ppb, paving the way for remote and large area sensing (Figure 2-8 g, h).

Electronic fibers

Besides optoelectronic fibers, an abundance of other electronic fibers have been exhibited for extensive applications such as motion sensing [208], thermal sensing [122], actuating [172], field-effect-transistors (FETs) [169], microfluidics [231], energy storage [232, 233], and energy harvesting [115]. Instead of going through all these applications, this sub-section will focus on motion sensing and energy-related applications in this subsection.

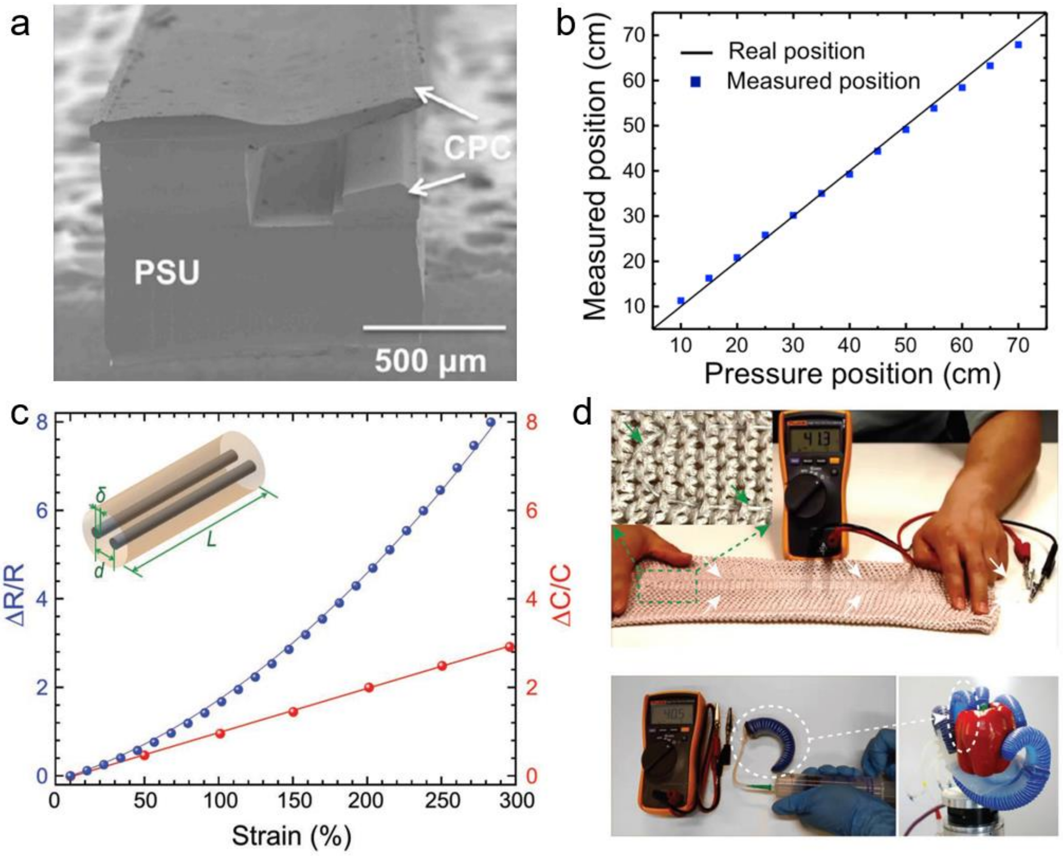

Figure 2-9. Electronic fibers for motion sensing [113, 208]. (a) SEM image of fiber with cantilever-like structure. (b) Measured position versus real position of applied pressure. (c) A stretchable fiber for strain sensing. Its capacitance and resistance change with the strain. (d) The stretchable fiber applied to strain sensing fabrics and a robot finger.

Motion sensing is an essential function for smart fabrics or artificial skin to “feel” the external mechanical stimuli. To effectively couple electronics and mechanics in a single fiber, both the fiber architecture and material should be specially designed according to the application scenario. T. Nguyen-Dang et al. designed a fiber with a cantilever-like structure (Figure 2-9a) for detecting and localizing pressure along the entire fiber length [113]. Carbon-loaded polycarbonate (CPC) is a conductive polymer that served as the cantilever. The CPC cantilever will bend under pressure and contact the other CPC domain below it. In this work, one electrode is connected to the CPC cantilever at the end of the fiber. And the other electrode is connected to the other CPC domain (below the CPC cantilever) at the same end of the fiber. Once the pressure is applied to the CPC cantilever at an unknown point, the CPC cantilever will contact the other CPC domain and forms a close loop between the two electrodes. Hence, the resistance between the two electrodes at the fiber end can be measured. The larger the distance between the fiber end and the pressed point, the larger the resistance between the two electrodes. Thus, after the relationship between the distance and the resistance is calibrated, the location of the pressed point can be identified by the measured resistance. As the resistivity of CPC is much higher than metals, a small position different will result in large resistance difference, leading to high positioning accuracy. The experimental results in Figure 2-9b displaying an excellent agreement between the actual position and measured position. Another example [208] is a strain sensing fiber-based on a superelastic material, SEBS. As the SEBS fiber can be stretch to more than 500% of its original length, a highly deformative liquid metal is used as the electrode. There are 2 parallel channels filled with liquid metal inside the fiber, as shown in Figure 2-9c. When the fiber is stretched, the distance between the channels will decrease while the length of the channels will increase, causing changes in both capacitance and resistance. Thus, the strain can be calculated by the change of capacitance or resistance. This strain sensing fiber is then applied to straining sensing fabrics and robot finger, as demonstrated in Figure 2-9d.

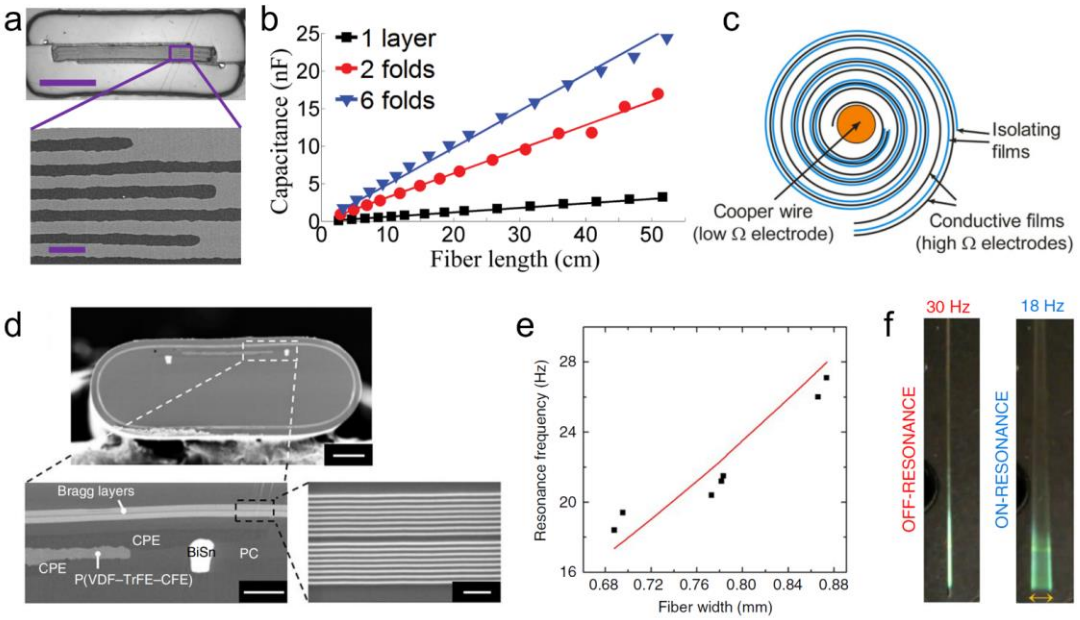

Figure 2-10. Electronic fibers for energy storage and energy conversion [171, 232, 233]. (a) A fiber capacitor with multiple bilayers. (b) The capacitance of the fiber with different folds as a function of fiber length. (c) A cylindrical fiber with increased capacitance. (d) The cross-section SEM images of a fiber actuator. Scale bars on top, bottom left, and bottom right are 100, 20, and 2 μm, respectively. (e) The resonance frequency of the fiber actuator as a function of fiber width. (f) Oscillation amplitudes for on and off-resonance frequency points.

Flexible fiber-based energy storage and energy conversion devices are also of great importance as the portable wearable electronics and smart fabrics are not compatible with the centralized power supply system. A thermally drawn fiber for energy storage was developed by folding multiple bilayers comprising PVDF as the dielectric layer and carbon-loaded polyethylene (CPE) as the electrode layer as shown in Figure 2-10a [232]. This capacitive response reached 20 kHz and the capacitance increased to 47 nF/m when 6 folds of PVDF layer were integrated into a single fiber Figure 2-10b.

The capacitance was further increased to 100 nF/m by a swiss-roll structure cylindrical fiber (Figure 2-10c). And this cylindrical fiber showed the ability to serve as a 1D touch sensor and 2D touchpad sensor when woven into fabrics [233]. As for energy conversion, several multimaterial piezoelectric fibers were fabricated since 2012 [117, 171, 172]. P(VDF-TrFE) and P(VDF–TrFE–CFE) are usually used as piezoelectric thin film sandwiched by CPE, as shown in Figure 2-10d [171]. The piezoelectric fibers can act as actuators under electrical stimulation as the fiber resonance. And the resonance frequency is adjustable by the fiber width, as shown in Figure 2-10e, f. These piezoelectric fibers can also act as an energy harvester by generating voltage signals under vibration such as acoustic waves [117]. Additionally, energy harvesting fibers have been achieved based on other effects such as photoelectric [234], triboelectric [235], and thermoelectric [115].

Fibers for micro/nanofabrication

In the applications introduced above, the as drawn fibers are directly used as functional devices. While in some other applications, thermally drawn fiber can also serve as a platform for postprocessing including new material synthesis [234, 236-238] and micro/nanoparticle fabrication [95, 239-241].

High-pressure chemical vapor deposition (HPCVD) process was firstly reported in 2006 for depositing germanium (Ge) inside capillaries [242]. As sketched in Figure 2-11a, precursors mixed with carrier gases flow through the air channel inside a fiber. The high temperature at the required location induce the decomposition of the precursors and depositing the desired material on the wall of the air channel. As the surfaces of the thermally drawn fiber are extremely smooth [243] and the inner diameter of the air channel is small enough (10^{-8} to 10^{-4} m) to sustain a high pressure in MPa level, the desired material can be deposit at a high speed with a low scattering interface on the channel wall. Layered structure with different materials can be deposited in the same channel by changing the precursor and channels with different materials integrated into a single fiber is achievable from a template fiber with complex architecture such as PCF. As shown in Figure 2-11b-e, many functional materials including platinum (Pt), zinc selenide (ZnSe), and silicon (Si) have been deposited inside fibers via HPCVD process for various applications in photodetection, fiber amplifiers, optical communications, etc. [234, 236, 238]

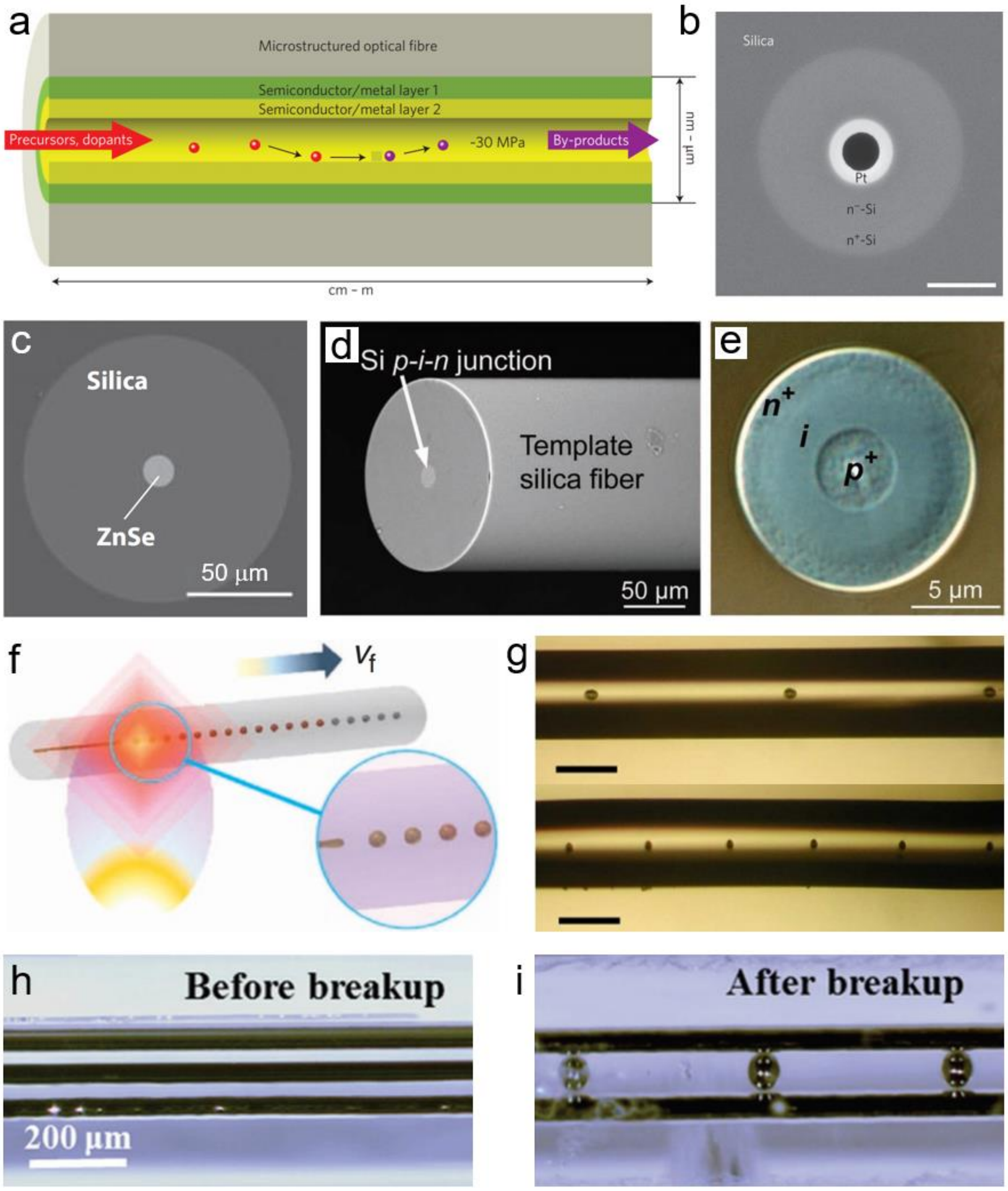

Figure 2-11. In-fiber micro/nanofabrication [234, 236, 238, 240, 244]. (a) Schematic of high-pressure chemical vapor deposition based on optical fiber. (b) Si and Pt, (c) ZnSe, and (d) p-i-n junction based on Si deposited at fiber core. (f) Schematic of micro/nanosphere fabrication via Instability induced breakup. (g) Spheres with different size are fabricated under different feeding speeds. (h, i) Selective breakup for in-fiber device assembly.

Moreover, an interesting approach for the mass production of micro/nanospheres with precise diameter was developed in 2012 [239]. This process starts with fabricating an axially uniform fiber with a core-cladding structure through the thermal drawing process. And then the fiber is heated above the glass transition temperature of the cladding material by fed into furnace, flame, or laser spot at a constant speed [95, 239, 240]. During the heating process, the cladding material will become soft and Plateau-Rayleigh instability-induced breakup will occur in the molten core material driven by the surface tension, forming a series of spheres in the fiber core, as presented in Figure 2-11f. And spheres with different sizes and periods can be precisely controlled by adjusting the feeding speed and core diameter (Figure 2-11g). Many further developments have been demonstrated based on this approach. For example, a p-n junction can be assembled by postprocessing a double-core fiber [240]; the location of the spheres inside the fiber can be further adjusted by laser manipulation [245]; and a selective breakup method (Figure 2-11h, i) is developed for in-fiber device assembly [244]. These works show numerous potential applications such as photodetecting, drug delivery, and tunable optical scattering.

Fibers as multimaterial filaments

Instead of weaving the thermally drawn fibers into fabrics, G. Loke et al. suggested another solution for further integrating the multimaterial function fibers by using the fibers as filaments for 3D printing [246]. Two filaments are demonstrated in their work. One is fiber with 0D light-emitter prepared by thermal drawing process and subsequently laser-induced capillary breakup, as the detailed structure shown in Figure 2-12a. The other one is 1D photodetector fiber consists of PC cladding, CPE electrode, and As_2Se_5 semiconductor (Figure 2-12b). To preserve the functionalities of the filament, a filament surface heating technique is introduced (Figure 2-12c). Only the outermost surface of the filament will be molten to serve as an adhesive promoter while the inner structure will be maintained during the 3D printing process. Thus, disparate 3D light-emitting displays and photodetecting sensors are constructed (Figure 2-12d-f). As the structures are constructed from a single fiber, its electrical connection and functional materials will remain continuous. For the photodetecting globe shown in Figure 2-12g, the 3D coordinate of the point on the globe can be transformed into a 1D distance on a fiber (Figure 2-12h). Therefore, the illuminated position on the structure can be reconstructed from the electrical signal generated in the fiber. Furthermore, a bifunctional light emitting and light detecting airplane wing for structural detecting is demonstrated, illustrating that different filaments can be integrated into one structure through this process. Combining with the diverse thermally drawn fibers reported in previous works, this 3D printing approach will fulfill a wide range of application needs by embedding multifunctional devices into customized 3D structures.

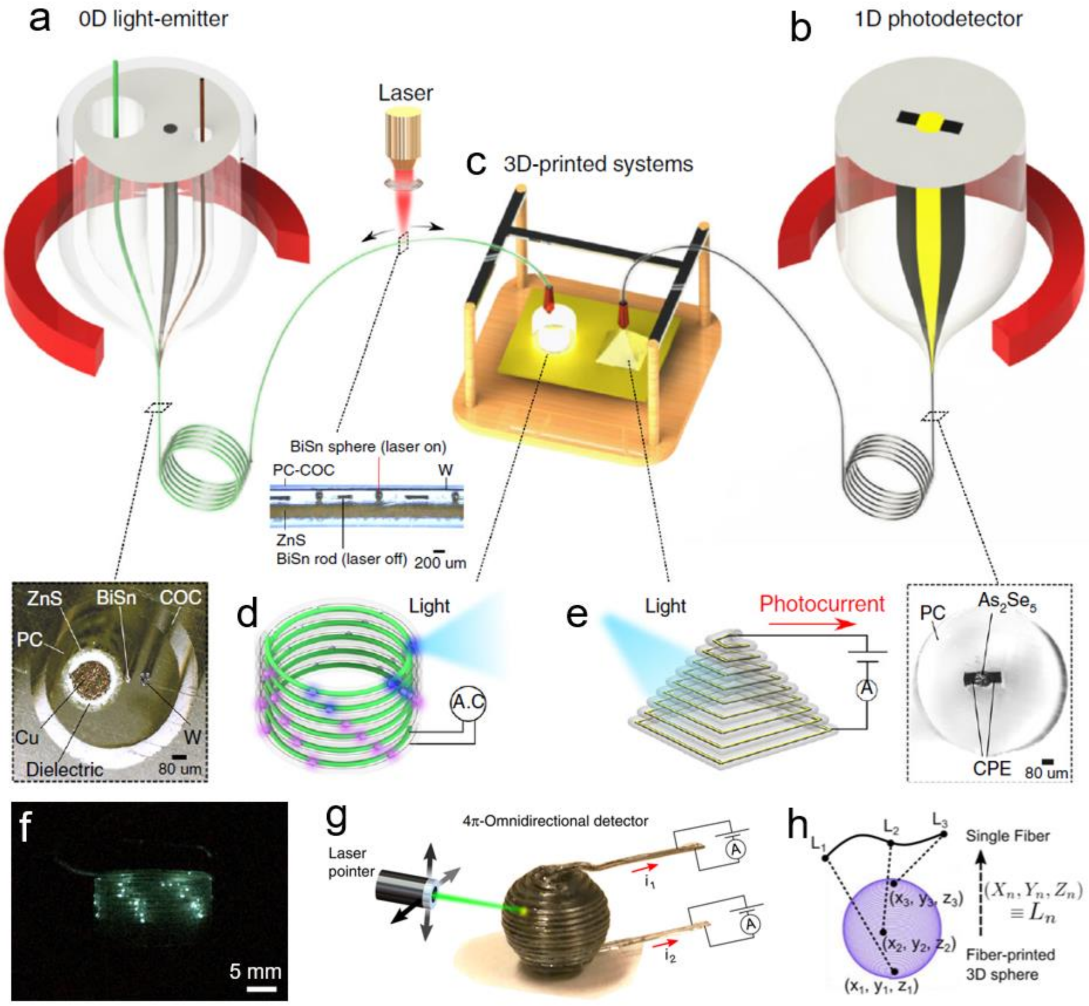

Figure 2-12. Fibers as multimaterial filaments for 3D printing [246]. (a) 0D light emitter and (b) 1D photodetector incorporated in fibers as filaments. The corresponding cross-sectional structures of the two fibers are shown in the enlarged micrographs. (c) The filaments are fed into a 3D printer to construct various structures. (d) Light-emission and (e) photodetection are realized in the entire structure. (f) Photograph of a light-emission cylinder. (g) Photodetecting globe and the schematic of the experimental setup. (h) A 3D coordinate of a point on the globe can be transformed into a 1D distance on a fiber.

Not limited to the applications reviewed above, many other promising functionalities of thermally drawn fibers were also widely studied in disparate fields such as artificial muscle [103], neural interface [118], and radiation detecting [247], which will not be introduced here. In view of this thermal drawing technique's unique advantage in materials and architectures compatibility, it can be envisioned that more and more functionalities will be highly integrated into a single fiber-based device. Also, the underlying science will push many fundamental research areas forward including material processing, rheology, fluid mechanics, and interfacial science.

2.1.4 Thermally Drawn Fibers for Thermal Sensing

As one objective of this thesis is to develop thermal sensing fabrics based on thermally drawn fibers, thermal sensing fibers are picked out from other applications and discuss them in detail here. The functional material in previously reported thermally drawn fiber for thermal sensing can be roughly divided into two categories. One is thermistors and the other one is thermoelectric materials.

Thermal sensing fibers based on thermistors

A thermistor is a type of material whose resistance depends on temperature, which has been widely used in thermal sensing and current regulating. Thermistors with negative temperature coefficient (NTC), whose resistance decreases as temperature increases, is mostly utilized among all the thermistor-based thermal sensors because of their high accuracy and long-term stability.

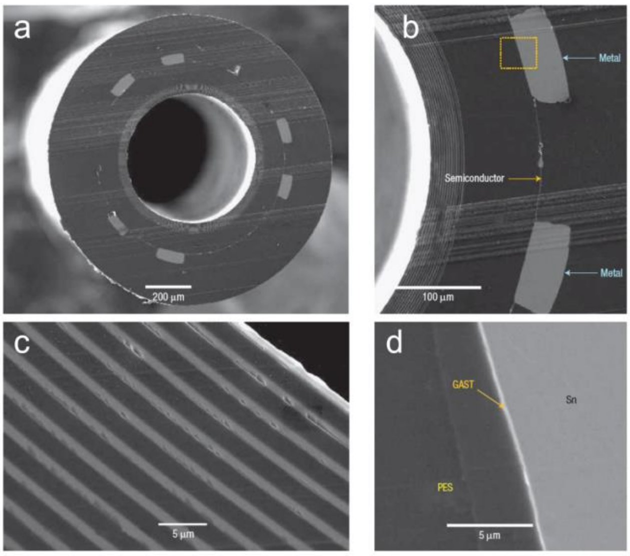

Figure 2-13. SEM images of thermal sensing and light guidance fiber [128]. (a) The cross-section of the entire fiber. (b) Thermal sensing unit consists of metal and semiconductor. (c) Alternating As_2Se_3/PES layers form a PBG structure for light guidance. (d) Enlarged image of the box in (b) showing the insulator-semiconductor-metal interface.

The first thermal sensing fiber was demonstrated by M. Bayindir et al. in 2005 [128]. As the structure shown in Figure 2-13, it comprises both a hollow-core PBG structure for carbon dioxide (CO_2) laser transmission and three thermal sensing units based on Sn as the electrode and $Ge_{15}As_{25}Se_{15}Te_{45}$ (GAST) thin film as the thermistor. The thermal sensing performance is first measured by placing the fiber inside a furnace. The resistance is then measured under a temperature range from room temperature to 120 °C, as presented in Figure 2-14a. And the IV curves in Figure 2-14b illustrate that the ohmic contact between the electrodes and the chalcogenide semiconductor GAST is formed under both high and low temperatures. The PBG diagramed of this fiber (Figure 2-14c) is calculated subsequently. An omnidirectional bandgap near 10.6 μm (emission wavelength of CO_2 laser) is observed. And this result is confirmed by transmission spectrum measurement shown in Figure 2-14d. Hence, a real-time defect monitoring fiber for high-power optical transmission is achieved by combining the two functionalities of this fiber. As shown in the thermal image (Figure 2-14e), a localized defect will lead to the leakage of high-power laser and induced the increase of localized temperature. This temperature change will be detected through real-time current measurement, achieving failure prediction and prevention (Figure 2-14f).

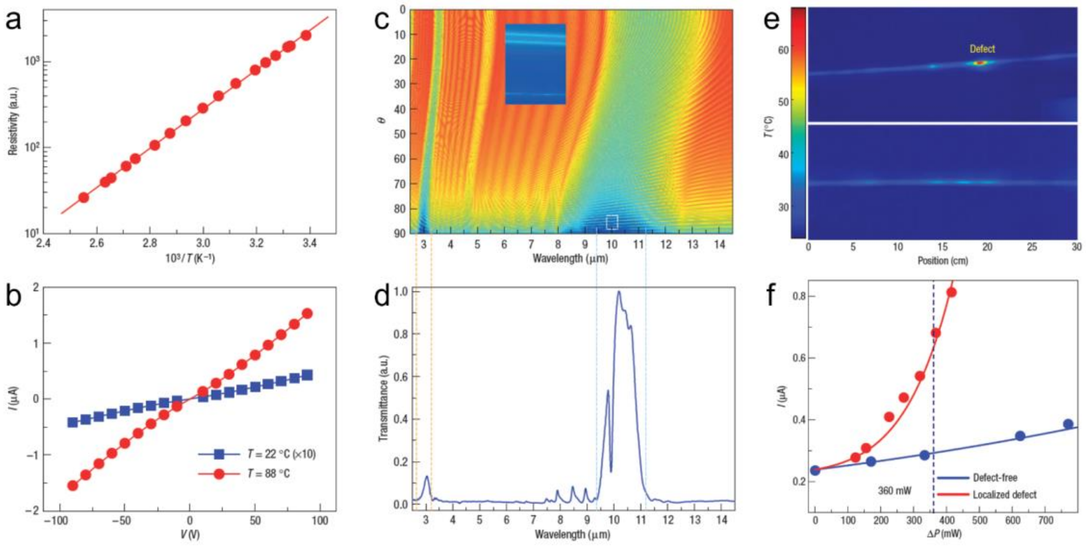

Figure 2-14. thermal sensing performance and optical properties of the fiber [128]. (a) Measured resistivity as a function of temperature. (b) The IV curves of the fiber under high and low temperatures. (c) The calculated band diagram of the hollow PBG fiber. (d) The transmission spectrum of the hollow PBG fiber. (e) Thermal image of a fiber carrying CO_2 laser with a single defect. (f) Measured currents as a function of dissipated laser power for both defect-free fiber and single defect fibers.

Another thermal sensing fiber was developed based on a similar chalcogenide semiconductor but a different inner structure [122]. As the schematic shows in Figure

2-15a, the $Ge_{17}As_{23}Se_{14}Te_{46}$ thermistor rod serves as a solid core surrounded by four $Sn_{96}Ag_4$ alloy electrodes. Compared to the thin film semiconductor introduced above, this configuration includes two pairs of parallel electrodes and a thermistor with a larger cross-section area, which can reduce the resistance between the electrodes. Thus, the applied voltage can be reduced and the current is increased for easier detection. The resistance as a function of temperature measurement is conducted for both bulk GAST sample before thermal drawing and fiber sample after drawing as plotted in Figure 2-15b. The results for both samples show a similar trend under different temperatures except the resistance, proving the stability of GAST. Also, the IV curves of both the hot fiber sample and cold fiber sample present good ohmic behaviors, indicating an intimidating contact between electrodes and the semiconductor. Moreover, the temporal response of the fiber is measured by heated in hot water and cooled by liquid nitrogen (Figure 2-15d). A thermal sensing fabric is further demonstrated by embedding the fibers, where both localized heating and cooling are successfully mapped. This work shows its capability towards large-area and flexible sensing systems at high spatial resolution.

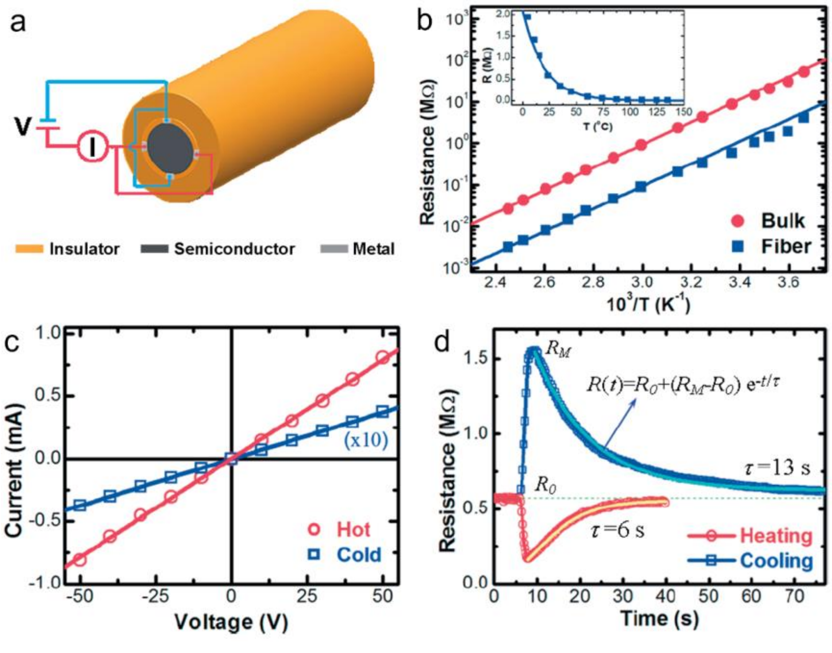

Figure 2-15. Thermal sensing performance of the 4-electrode-fiber [122]. (a) The fiber is connected to a circuit for electrical measurement. (b) The resistance of the bulk and fiber as a function of temperature. (c) IV curves of the fiber under hot (58 °C) and cold (11 °C) conditions. (d) Temporal responses of the fiber under heating and cooling.

Thermal sensing fibers based on thermoelectric materials

Thermoelectric materials are materials showing a strong thermoelectric effect, which can generate electrical potential under temperature difference and vice versa. The basic principle is that the concentration of the charge carriers in the high-temperature side is higher than that in the low-temperature side, causing the diffusion of charge carriers [248]. This effect is usually used in power generation, refrigeration, and thermal sensing. Unlike thermistors, thermoelectric materials can generate voltage themselves without external power supply.

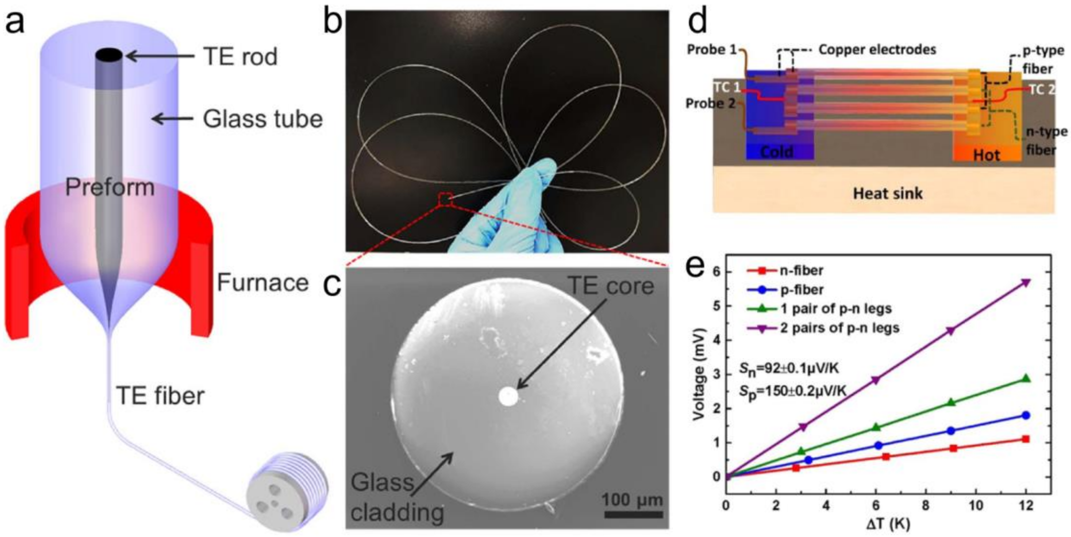

Figure 2-16. Flexible thermoelectric fibers for thermal sensing [115]. (a) Schematic of thermally drawing the thermoelectric fiber. (b) The flexibility of the ultralong fiber. (c) Cross-sectional SEM image of the fiber architecture. (d) Setup for thermal sensing performance measurement. (e) Generated voltage as a function of temperature difference under different fiber configurations.

Thermoelectric fibers based on crystalline semiconductors and chalcogenide glass have been fabricated by T. Zhang et al. in 2017, as shown in Figure 2-16a-c [115]. The resulting fibers are ultra-long and flexible in contrast to the bulk thermoelectric crystal. And p-type $Bi_{0.5}Sb_{1.5}Te_3$ and n-type Bi_2Se_3 are utilized as thermoelectric cores to prepare the glass-cladding fibers, respectively. The generated voltage as a function of temperature difference is measured, showing the Seebeck coefficients of the p-type and n-type thermoelectric fibers are around 150 μV/K and 92 μV/K, respectively (Figure 2-16d, e). And higher output voltage can be achieved by connecting p-type fibers and n-type fibers in series. This fabricating process is also compatible with many other thermoelectric materials ranging from such as SnSe, In_4Se_3, SiGe, etc., providing more possibilities in fiber architecture designing and material selection. Moreover, another work [129] has reported that the performance of the thermoelectric fibers can be further enhanced by annealing after the thermal drawing process.

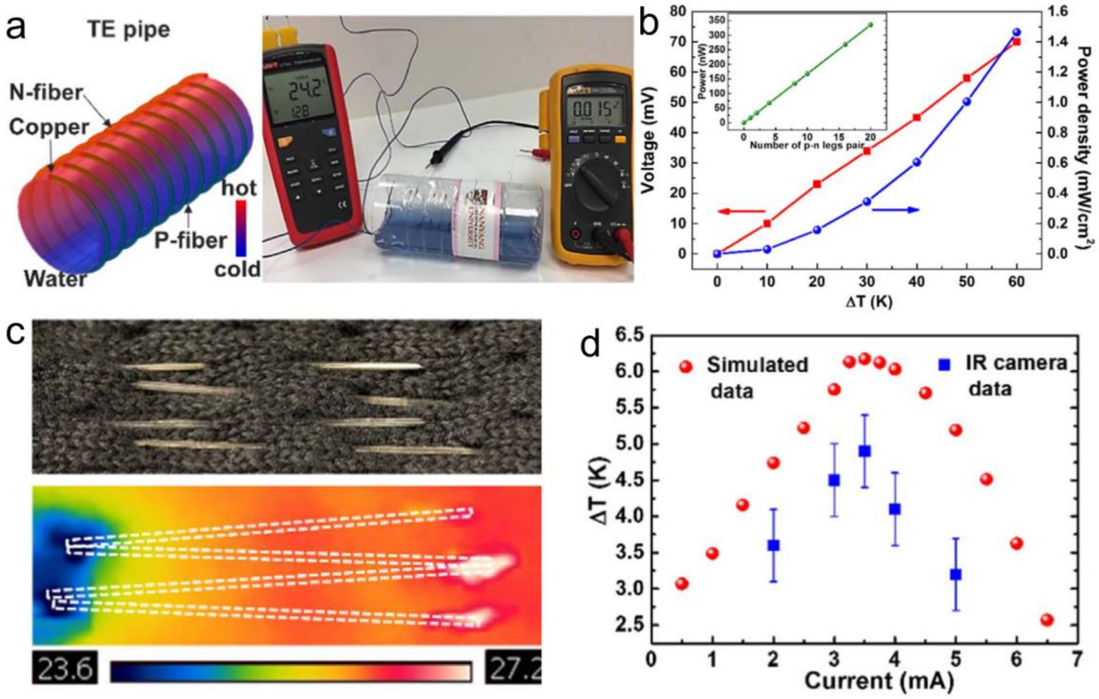

Figure 2-17. Applications of the thermoelectric fiber [115]. (a) A thermoelectric pipe produces electricity when cold water flows through. (b) Measure output voltage and power density as a function of temperature difference for 7 pairs of p-type and n-type fibers. (Inset: Simulated output power with different numbers of pairs of p-type and n-type fibers under a temperature of 40 K). (c) Photograph and thermal image of a cooling fabric. (d) Simulated and measured temperature drop under different input current.

Thermoelectric generators and wearable cooling fabric are constructed based on thermoelectric fibers. The flexible thermoelectric fibers can be wrapped on curved surfaces such as pipes and cups to generate electricity from the temperature difference. As shown in Figure 2-17a, b, 5 pairs of p-type and n-type fibers are connected in series, achieving a power density in mW/cm^2-level under a temperature of 50 K. Likewise, 2 pairs of thermoelectric fibers are woven into a fabric to form a wearable cooling device. As a result, a maximum cooling temperature of 4.9 °C is achieved when a current of 3.5mA is applied. These demonstrated applications reveal the thermoelectric fibers' capability in self-powered large-area thermal sensing, personal thermal management system, electronic skin, and smart fabrics. Considering that the glass fiber is still fragile and needs extra care when operating, further development can be made by seeking high-performance thermoelectric material with low processing temperature for fabricating polymer-based thermoelectric fibers, which will be discussed in Chapter 3.

2.2 Fiber-Based Wearable Triboelectric Nanogenerators

Triboelectric effect is a natural phenomenon that two different materials will be electrically charged after friction with each other. The principle is that different materials possess different abilities to confine its surface electron, causing the electron transfer from a weak confinement surface to a strong confinement surface after contact-and-separation. Many phenomena in our daily life are based on the triboelectric effect. For example, dust can be easily absorbed on charged electrical fans because of the friction between the fan and the air; removing a nylon shirt or sweater may generate sparks; a balloon can be attached to the window after rubbed. As the accumulated triboelectric charge will generate a high voltage on insulating surfaces, a sudden discharge may occur and cause harmful consequences, such as the breakdown of electronic components and the possibility of explosion in flammable areas. Therefore, in most cases, people are trying to avoid triboelectrification historically.

Noticing that the charges generated by triboelectrification possess high localized charge density and high voltage which may be used as an energy source, in 2012, Prof. Zhong Lin Wang’s group developed the first TENG to generate electricity by harvesting mechanical energy from the environment based on the coupling effect of triboelectrification and electrostatic induction [249]. As the mechanical energy from the environment is widespread, continuous, and independent, while the TENGs is lightweight, environment-friendly, low cost, and can be easily driven by a very weak force from disparate forms including vibration [250-252], wind [253-255], sound [256-258], and tide [259-261], TENG is considered as an effective device to harvest the usually wasted mechanical energy from its surroundings and experiencing rapid development since the first TENG reported. So far, diverse TENGs have been developed, which is not only for powering different devices [262-264], but also for self-powered sensing tasks, e.g., motion tracking [265-267], environmental sensing

[268-270], and physiological monitoring [271-273]. In this section, the categories, working mechanism, and performance improvement of the TENGs will be introduced as well as fiber-based wearable TENGs.

2.2.1 Introduction to Triboelectric Nanogenerators

Basically, TENGs consist of insulating dielectric material and conducting electrode material. Triboelectric charges will generate on dielectric materials and induction charges will generate on electrodes after friction. According to the structure and the direction of the driving force, TENGs can be divided by 4 operation modes (Figure 2-18): (a) vertical contact–separation (CS) mode, (b) lateral-sliding (LS) mode, (c) single-electrode (SE) mode, and (d) freestanding triboelectric-layer (FT) mode. Both CS mode [146, 249, 274] and SE mode [275-278] are driven by a force that is perpendicular to the friction layers to make the 2 dielectric material contact and separate repeatedly. The difference between them is that the SE mode TENG only has one electrode and use the ground as the other electrode. The TENGs driven by perpendicular force are often used in harvesting energy from pressing, bending, vibrating, and so on [279-281]. The other two modes, LS mode [282-284] and FT mode [285-287], are driven by a force that is parallel with the friction layers. The difference is that the two electrodes of FT mode TENG are built on the same dielectric material but different segments, while the other dielectric material can move freely. The TENGs driven by parallel force are more suitable in sliding movements, including reciprocating and rotational energy harvesting [283, 288, 289].

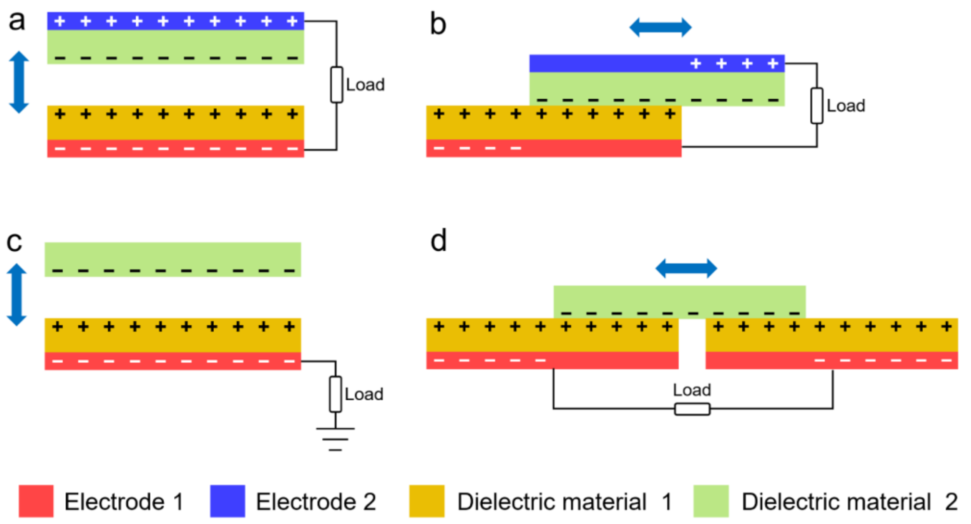

Figure 2-18. Four operation modes of TENGs. (a) Vertical contact–separation (CS) mode, (b) lateral-sliding (LS) mode, (c) single-electrode (SE) mode, and (d) freestanding triboelectric-layer (FT) mode.

The detailed working mechanism of TENGs driven by perpendicular force will be discussed in the following chapters. Here, a TENG driven by parallel force is taken as an example to explain the working principle. As shown in Figure 2-19a, same amount of positive charge and negative charge will generate on the surfaces of dielectric material 1 and 2 respectively after friction. At this stage, the induction charge on the electrodes is negligible because the positive charge and negative charge are so close to each other that they will not influence the electrical potential on electrodes. When a parallel force drives the upper part slide to the right, the negative charge and positive part will not overlap, leading to the electrical potential of electrode 1 increases while the potential of electrode 2 decreases. As the two electrodes are connected through an external circuit, a current will flow from electrode 1 to electrode 2 through the external load (Figure 2-19b). The current will continue flowing as the upper part moving to the right until the two dielectric layers are totally separated. Hence, the negative induction charge will generate on electrode 1 and the positive charge will generate on electrode 2 (Figure 2-19c). Similarly, when the parallel force drives the upper part move back, a reverse current will flow from electrode 2 to electrode 1 through the external circuit (Figure 2-19d) till the TENG finally reach its original state to finish a working cycle. As the parallel force drives the dielectric layers separating and overlapping repeatedly, the current will flow forth and back repeatedly, forming an alternating current in the external circuit. Thus, mechanical energy is harvested and transformed into electricity.

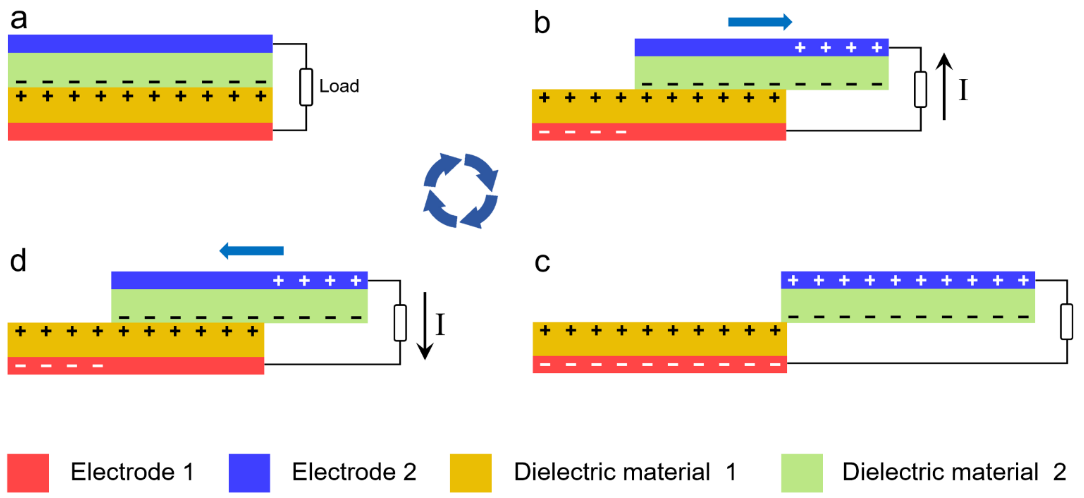

Figure 2-19. The working principle of TENGs driven by a parallel force.

2.2.2 Approaches to Enhance the Output Performance of Triboelectric Nanogenerators

As an energy harvesting device, TENG’s output performance is of vital importance. According to its working mechanism introduced above, increasing the density of the induction charges should be the fundamental solution to enhance the output performance of all kinds of TENGs. To date, many attempts have been reported to enhance the performance of TENG, which can be roughly categorized into 4 approaches.

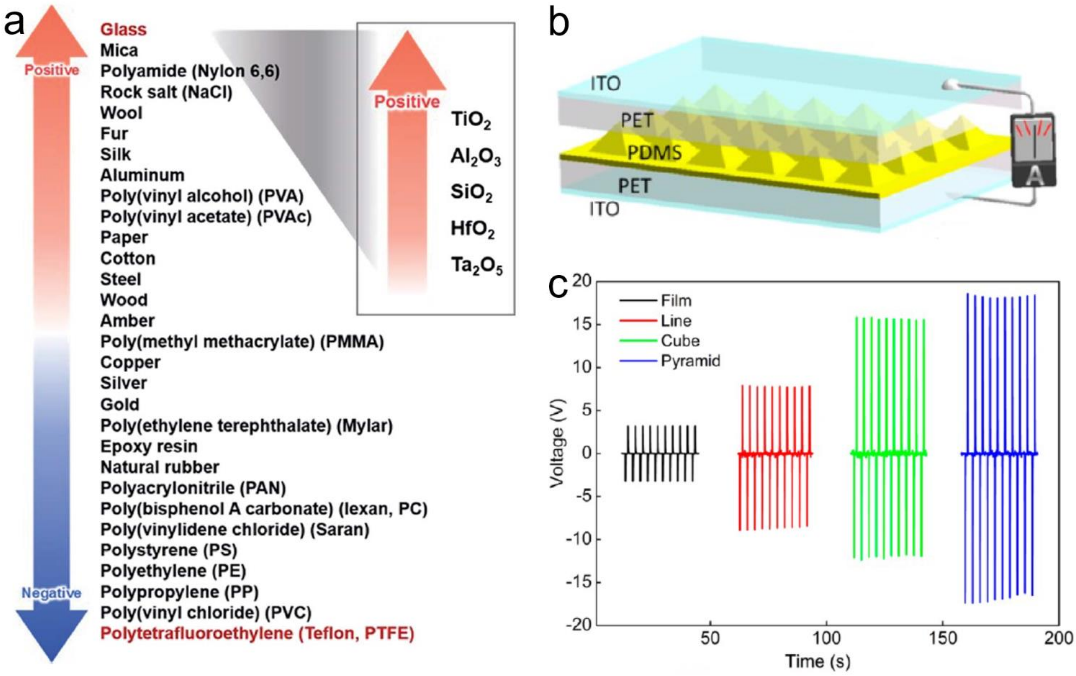

Figure 2-20. (a) triboelectric series of some common materials [290]. (b) Schematic of a TENG with surface structure on the friction layer. (c) The output performance of TENGs with different surface structures [147].

The first approach is to select the right dielectric materials. Different materials will behave different tendencies in losing or trapping surface electrons. For example, metals are easy to lose electrons while fluoropolymers such as PVDF and polytetrafluoroethylene (PTFE) possess a strong ability to trap electrons. Therefore, choosing the proper materials could help the electron transfer and achieve higher charge density during the friction process. The material selection for dielectric materials may refer to the triboelectric series [290], which ranks the materials by the polarity of charge separation after rubbing with other materials, as listed in Figure 2-20a. A general guideline is to select one dielectric material towards the bottom of the series and the other material towards the top. Besides the triboelectric polarity, Y. Kim et al. studied the influence of the material's relative permittivity on TENG's performance [290]. As a result, TENG's performance shows an increasing tendency with the material's relative permittivity increases using PTFE as another dielectric material. This may also be a criterion when choosing positive tribo-materials.

The second approach is to create micro/nanostructures on the surface of dielectric materials. Micro/nanostructures can effectively increase the surface area and friction, leading to a high triboelectric charge density. As shown in Figure 2-20b, c, different surface structures including lines, cubes, and pyramids were fabricated on PDMS as a dielectric layer. And considerable performance improvement is observed when comparing the output voltages of TENGs with different surface structures. So far, numerous methods [291-293] have been employed to fabricate micro/nanostructures and enhance the TENG's performance, such as lithography, self-assembly, and thermal imprint.

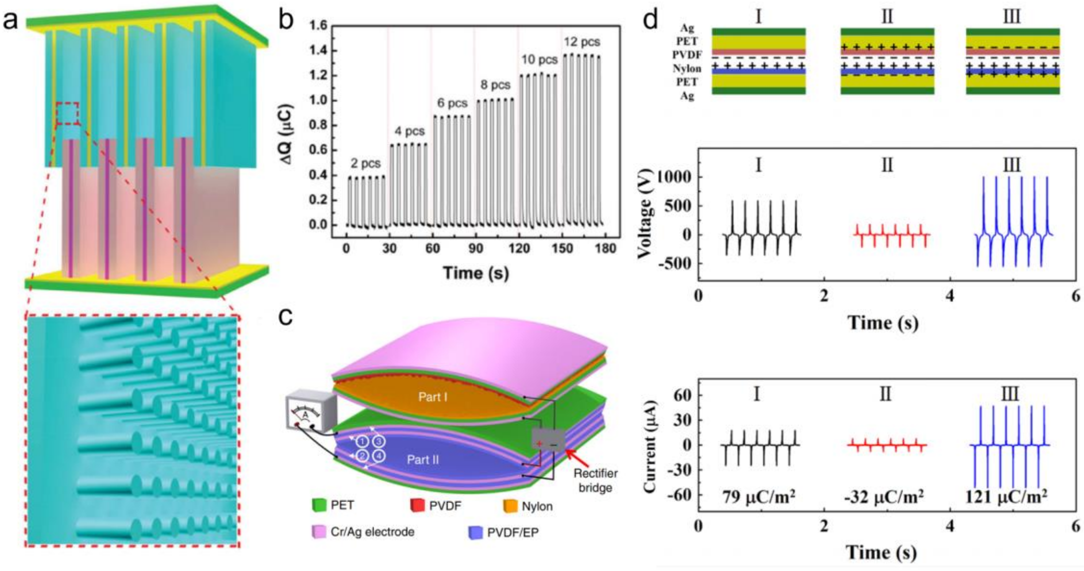

Figure 2-21. Improved device structure and charge injection to enhance the performance of TENGs [149, 294, 295]. (a) TENG with 3D multilayered structure. (b) The output performance of the TENG with different stacking layers. (c) Introducing a simple TENG as a "charge pump" for the TENG with a multilayer structure. (d) Enhancing the performance of the TENG by directly injecting charges into the dielectric materials.

The third approach is to design the device structure, such as the multilayered interdigital structure [296] and 3D integration [295]. For example, a TENG with a 3D multilayered structure is demonstrated in Figure 2-21a, b. As the single layer can be as thin as several hundreds of micrometers, tens of layers can be stacked together within a reasonable device thickness. By connecting the electrodes in parallel, the amount of the induction charge is greatly increased with the number of the friction layers increased. Besides simply stacking layers, a new device configuration including 2 parts of TENG was developed recently [294]. As shown in Figure 2-21c, this configuration employs one TENG as a "charge pump" to pump charge into the other TENG, part II. A much higher induction charge density can be achieved by introducing a well-designed multilayer structure of part II to coordinate the pumped charge and triboelectric charge. A charge density of 1020 μC/m^2 is achieved under this configuration, which is the highest charge density achieved up to now [297].

The last approach is to inject charges directly into the dielectric materials. Instead of focusing on the surface charge of the dielectric materials, several attempts have been reported to inject charges directly into dielectric materials before friction by high voltage, plasma, ion radiation, etc. [149, 298, 299]. The injected charges will work along with the triboelectric charge to further enhance the TENG's performance. As shown in Figure 2-21d, state I is the TENG before charge injection, state II is the TENG in which charges with opposite polarity compared to the dielectric materials are injected, and state III is the TENG in which the same polarity charges are injected. A large enhancement of the output performance is observed comparing state III to state I. Additionally, the output signal in state II is reverse of state I, showing that the amount of the injected charges may higher than that of the triboelectric charges.

After years of effort, the output performance of TENG has been significantly enhanced compared to the first reported TENG. The output voltage has reached more than 2000 V [300] and the current reached the level of mA [301]. So far, the area and volume peak power density have reached 500 W/m^2 and 15 MW/m^3, respectively [302]. And a TENG with an instantaneous energy conversion efficiency of 70.6% has been demonstrated [303]. Such a high output performance strongly supports the further applications of TENG in various fields.

2.2.3 Fiber-Based Wearable Triboelectric Nanogenerators

Benefiting from their merits like wide material selection, flexible structure design, durable, and low driving force, TENGs are regarded as promising devices to work independently for powering dispersed portable devices. Noticing that the human body is also a continuous mechanical energy source and fabrics are indispensable in our daily life, developing fiber-based TENGs and weaving them into fabrics have attracted intensive studies [304-310]. The converted electric energy from human motion energy could conveniently power the daily used portable devices.

Alternatively, the electric signal could also be used for interaction between the external environment and the human body, i.e., using TENG as a self-powered sensing device [311] or inputting device [312].

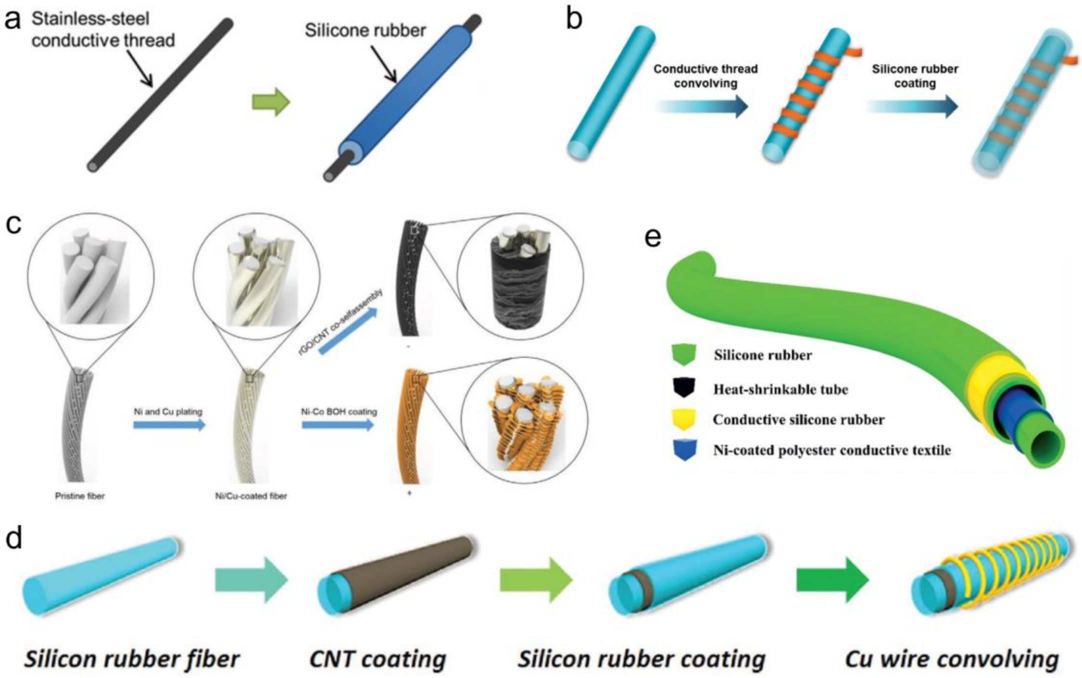

Figure 2-22. Various fabrication processes of fibers for SE mode and CS mode TENGs [313-317]. (a) Fiber with core-shell structure by depositing materials layer by layer. (b) Winding a non-stretchable fiber around a stretchable core to achieve stretchable SE mode TENG. (c) A coaxial structure formed by a twisted fiber bundle with deposited materials. (d) Assemble two electrodes in a single fiber to achieve a fiber-based TENG working under CS mode. (e) Integrating two SE mode fibers to achieve a CS mode fiber.

Fabrication of fibers

The fibers for TENGs are commonly fabricated via depositing materials on fiber cores or combining different fibers by twisting and winding. A simple core-shell structure is shown in sketch 2-22a [313], this fabrication process always employs a solid fiber or hollow tube as the template and subsequently deposits electrode or dielectric materials layer-by-layer through coating, sputtering, electrochemical deposition, etc. However, such core-shell fibers are not stretchable in most cases. A stretchable structure can be achieved by winding a non-stretchable fiber around a stretchable core followed by coating a dielectric layer (Figure 2-22b) [314]. Additionally, coaxial structure was also demonstrated in previous works. As shown in Figure 2-22c, a twisted fiber bundle is used as the template [315]. And different surface morphology and material can be achieved by the following deposition procedure. Such coaxial structure fibers usually possess a larger surface area and higher strength than single-core fibers.

The three fiber structures introduced above only include one conductive core or conductive layer. Hence, these fibers will only work in SE mode before woven into fabrics. The SE mode fibers are easy to fabricate and their diameters can be very small, which is beneficial for further integration. However, the output performance is relatively low when working alone without weaving due to the small surface area. A CS mode fiber could be achieved simply by winding a Cu wire around a stretchable SE mode fiber (Figure 2-22d) [316]. This fiber is driven by stretching force. The inner fiber will become finer under stretching. Thus, the outer surface of the inner fiber will separate from Cu wire. And the inner fiber will recover to the contact state when the stretching force is released. Another kind of CS mode fiber is core-sheath structure [317]. The fabrication process can be considered as preparing two SE mode fibers. One is a hollow core fiber with a large inner diameter while the other fiber should have a smaller diameter to be fitted inside the hollow core and ensure there is a gap between two fibers, as shown in Figure 2-22e. This fiber can be driven by pressing, vibrating, and bending. In general, the fibers in CS mode have better output performance than SE mode fibers. But their diameters are much larger because they have to include a gap between the two friction materials.

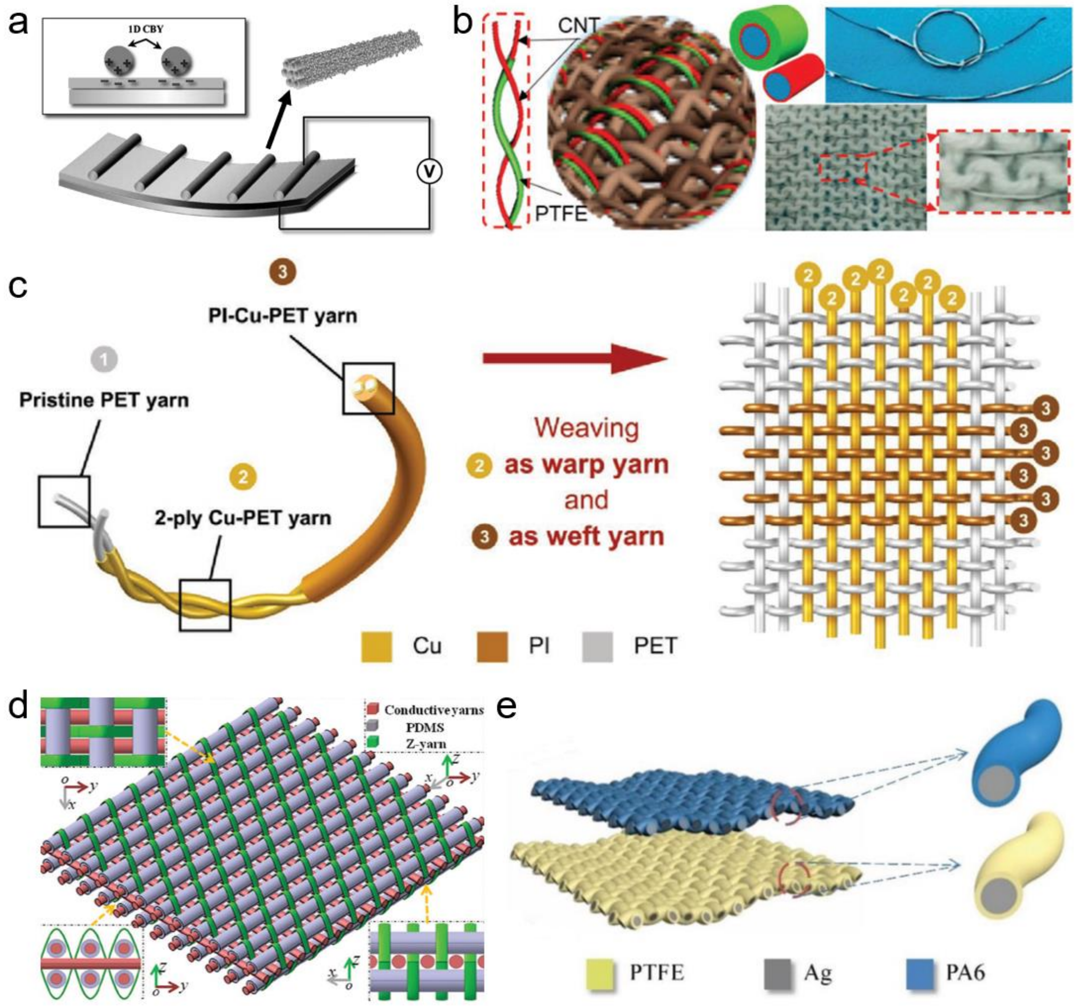

Figure 2-23. Various TENG fabrics fabricated from TENG fibers [311, 318-321]. (a) Directly fixing the TENG fibers on a fabric. (b) Stitching TENG fibers into a commercial fabric. (c) Weaving TENG fibers into fabrics through textile processing technologies. (d) A 3D orthogonal woven structure constructed from TENG fibers and binding yarns. (e) Fabric-based TENG assembled from two independent fabrics woven from different TENG fibers.

Weaving fibers into fabrics

To enhance the performance and wearability, the fibers above can be woven into fabrics through various methods. A wearable TENG fabric could be achieved by combining TENG fibers with commercial fabrics. The most direct method is simply fixing the two ends of the fibers onto fabric, as illustrated in Figure 2-23a. The energy harvesting could be accomplished by the friction between fibers and fabrics [318]. However, this configuration is not durable nor stable. A more integrated structure can be achieved by stitching the fibers into a common fabric. As demonstrated in Figure 2-23b, several pairs of carbon nanotube (CNT) fiber and PTFE coated CNT fiber are sewing into a commercial knitted fabric to form a single layer wearable power shirt

[311]. Alternatively, the fibers themselves could be woven into fabrics through textile processing technologies without commercial fabrics. As the example shown in Figure 2-23c, a plain-pattern fabric is woven from Cu coated polyethylene terephthalate (PET) fibers and polyimide (PI)-Cu-PET fibers [319]. And energy harvesting process could be achieved by the contact and separation between different fibers under pressing or bending. Besides 2D structures, complex 3D structures were also demonstrated to provide more spaces in thickness direction for contacting and separating processes. As shown in Figure 2-23d, a 3D orthogonal woven structure is constructed from conductive fibers, PDMS coated fibers, and non-conductive binding yarn [320]. A relatively high output performance is thus achieved because of the multilayer structure and enlarged space. Additionally, wearable TENGs could also be assembled from multi-fabrics. As shown in Figure 2-23e, PTFE coated silver (Ag) fibers and nylon (PA6) coated fibers are firstly woven into fabrics respectively before the wearable TENG is assembled [321]. It is worth noting to mention that although the TENG fibers used for weaving can only working in SE or CS mode, the TENG fabrics woven from these fibers could work in any of the four operation modes.

Applications of fiber-based wearable TENGs

Countless applications have been demonstrated based on the wearable TENGs. Powering electronic devices could be the most basic application. As shown in Figure 2-24a, a TENG fabric is sewed on a shirt to harvest body motion energy [311]. The generated electricity is used to power the wireless temperature sensor on the wrist. And finally, the temperature data could be sent to the terminal devices (Figure 2-24b, c). Similar applications have been widely developed such as lighting LEDs and charging batteries. Apart from serving as power supply, the wearable TENGs are also broadly employed as self-powered sensors as the generated electrical signals contain some external information. For instance, a stretchable fiber-based TENG fabric is exhibited in Figure 2-24d, e [322]. As the TENG fibers are woven in two orthogonal directions inside the fabric, the stretching direction could be obtained by analyzing the output electrical signals generated from the fibers in both X and Y-axis. Moreover, self-powered motion sensing, pressure sensing, physiological monitoring, etc. are also frequently demonstrated applications [319, 323, 324]. In addition to function as sensors to collect external information, wearable TENGs is also capable of acting as input devices to deliver information from human to machine. Figure 2-24f, g shows a self-powered keyboard including 12 units. The press and releasing motion during typing could be effectively detected and a corresponding electrical signal will be generated and transmitted to receiving devices [312].

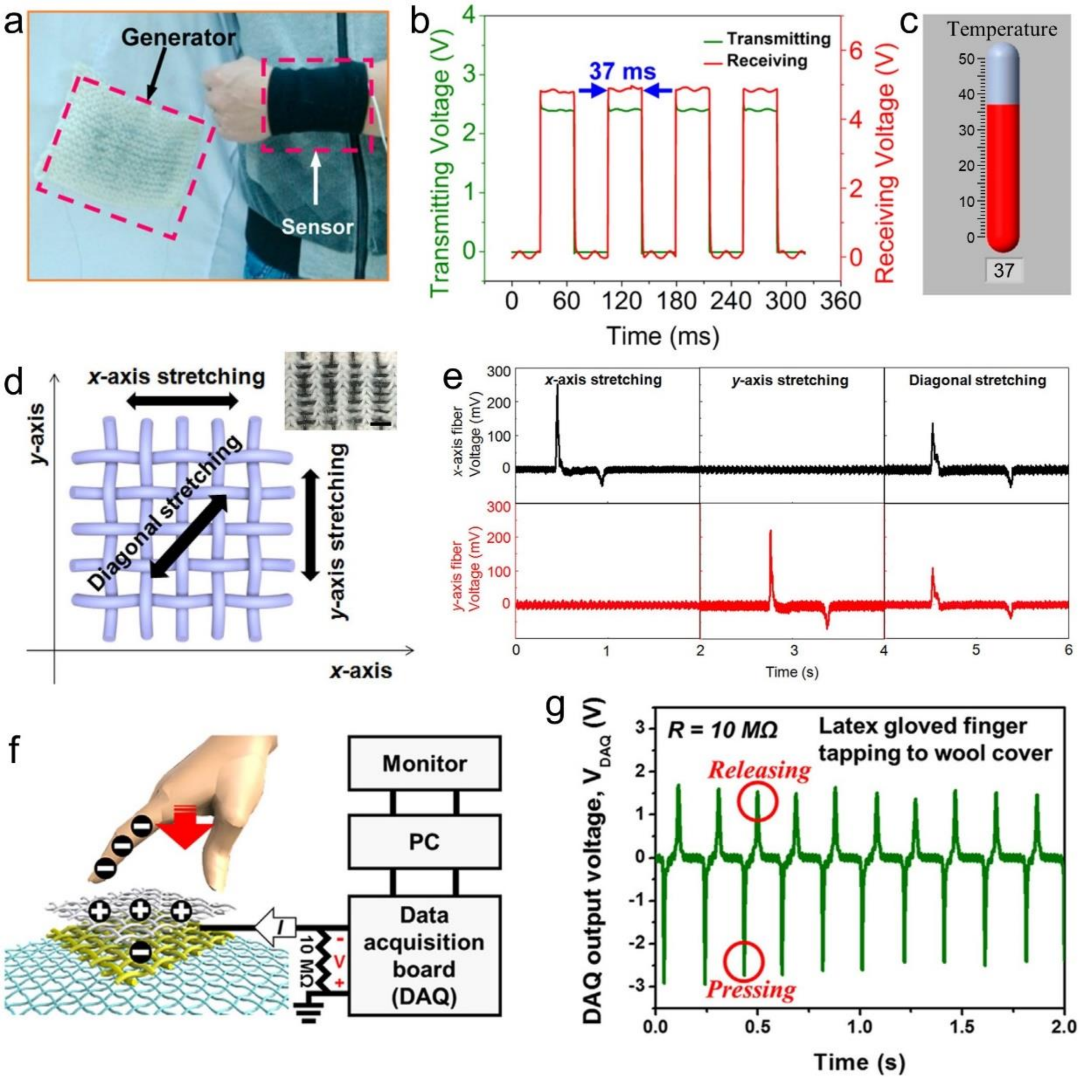

Figure 2-24. Applications of wearable TENGs [311, 312, 322]. (a) Wearable fiber-based TENG powering temperature sensor. The TENG harvests energy from body motion and power the wireless temperature sensor. (b) Signals transmitted from the sensor and received by the terminal device. (c) Visualized temperature information. (d) Stretchable TENG fabric serving as a sensor to detecting force direction. (e) The generated signals under different stretching directions. (f) Wearable TENG serving as a self-powered input device. (g) The pressing and releasing motion can be reflected in the generated signal.

The numerous and ubiquitous applications reveal the huge potential of fiber-based wearable TENGs. Hence, more fascinating applications in diverse fields could be expected, especially in smart fabrics and artificial intelligence. However, more sophisticated functions require wider material range and more accurate and complex device structure, while current fibers are mostly fabricated by depositing materials on existing commercial fibers. These fabrication processes will lead to limited fiber structures (layered structure or coaxial structure), poor material compatibility, complicate coating process, and low wearing resistance of coated materials, which fundamentally hindered the further development of fiber-based wearable TENGs. Based on the introduction in Section 2.1, thermally drawn fiber could be a promising solution to address these limitations, which will be discussed in detail in the following chapters.

2.3 Thermally Drawn Fibers with Patterned Surface

As discussed in Section 2.2.2, creating surface patterns on dielectric materials is universal and effective to enhance the performance of TENG. Therefore, thermally drawing surface patterned fibers is an indispensable path to realize high-performance wearable TENG. Furthermore, creating surface patterns could also endow the fibers with many other unique functionalities, e.g., hydrophobic surface, antimicrobial, coloration. This section will review current progress in creating surface patterns on thermally drawn fibers.

2.3.1 Surface Patterned Fibers Drawn from Patterned Preform

Several attempts have been reported to create surface patterns on thermally drawn fibers by far [93, 158-161]. The fabrication processes of these fibers are quite similar. They usually start from etching grooves on a macroscopic preform through machining, laser etching, or soft lithography. Then the patterned preform is applied to the thermal drawing process. During this process, the macroscopic preform will be elongated to a microscopic fiber and the width of the grooves will be scaled down along with the preform, as sketched in Figure 2-25a [158]. As a result, the patterned cylindrical preform is drawn into a star-shaped fiber with tunable diameter, i.e., one-directional microgrooves along fiber axial direction are achieved on the entire fiber surface (Figure 2-25b, c). And the pattern size can be controlled by alternating the preform pattern or adjusting the drawing parameters including preform feeding speed and fiber drawing speed. Surface patterns on rectangular fibers are also reported. As the SEM images show in Figure 2-25d, e, by thermally drawing a patterned polymer bar, microstructure with the size down to several micrometers is created on fiber surface [159]. Moreover, this process can be used for creating patterns in the inner surface of hollow fiber (Figure 2-25f-h) [160]. Two machined half-preform are prepared followed by consolidating to form a hollow preform with inner surface pattern. And inner surface patterns with different sizes are achieved after the thermal drawing process.

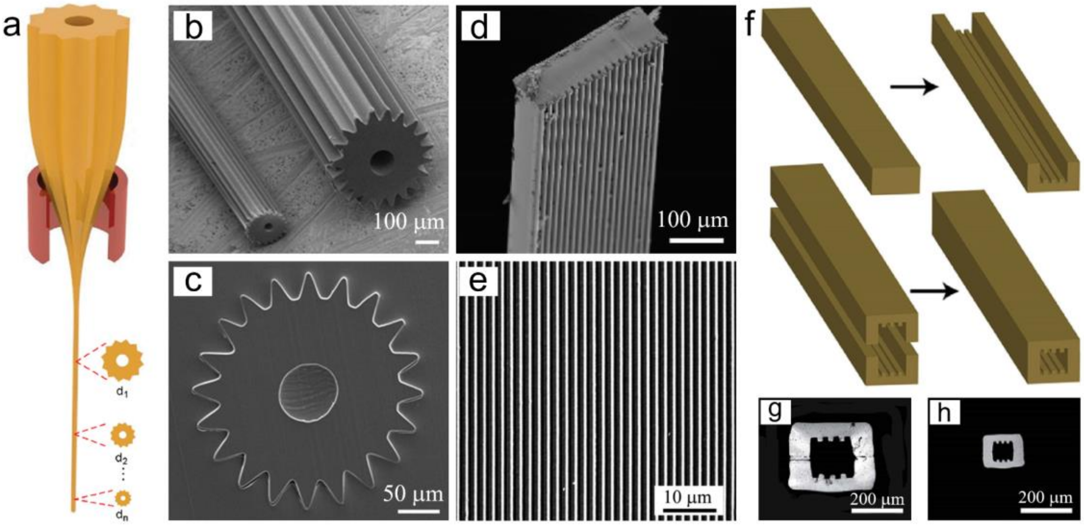

Figure 2-25. Thermally drawn fibers with surface patterns [158-160]. (a) The thermal drawing process of a patterned cylindrical preform. (b, c) SEM images of the surface patterned cylindrical fibers. (d, e) SEM images of a rectangular fiber with surface pattern. (f) The fabrication process of the preform with patterned inner surfaces. (g, h) Inner surface patterned fibers with different sizes.

Applications of the surface patterned fibers mentioned above are also demonstrated in previous works. The periodic microgrooves on the fiber surface could act as a diffraction grating [159]. When a monochromatic light is incident on the grating, the transmitted light will be split and travel in different directions according to the following equation.

$$n\lambda = Dsin\,\alpha \tag{2}$$

where, n is the diffraction order, λ is the wavelength, D is the grating period, and α is the diffraction angle. Thus, fiber with a smaller groove period will lead to larger different angles, which is observed in the experimental results shown in Figure 2-26b-e. Since the diffraction angle could also be influenced by the wavelength of the incident light, the white light will be split after reflected by the grating fiber. Hence, the fiber will exhibit different colors in different observing direction, achieving structural coloration, as demonstrated in Figure 2-26f-h.

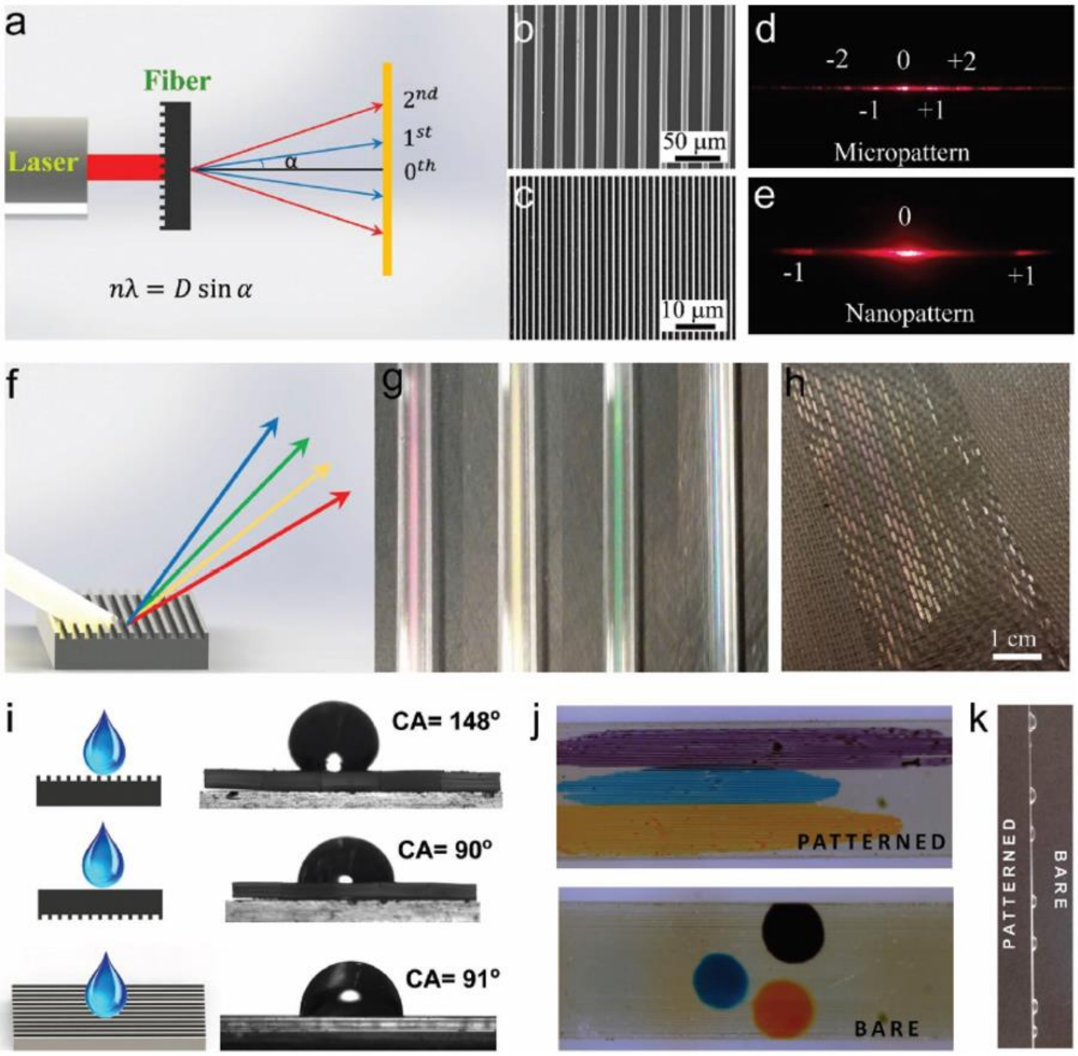

Figure 2-26. Applications of surface patterned fibers [159]. (a) Schematic of a fiber patterned with periodic microgrooves serving as an optical grating. (b-e) Different diffraction patterns observed due to the different surface patterns. (f) Splitting the white light after reflected by the grating fiber. (g) Different colors can be exhibited from different observing directions. (h) Large scale structure coloration achieved by weaving the surface patterned fibers into a fabric. (i) The anisotropic wetting property of the surface patterned fiber. (j) Fluid paths form on the patterned fiber surface along the axial direction. (k) Water repellency of the patterned fiber surface.

Moreover, the one-directional surface grating will lead to anisotropic wetting property as the grooves will trap air when wetted. The wetting properties are tested for both the flat side and the patterned side of the fiber (Figure 2-26i). For the surface patterned side, a contact angle of 148° in the transverse direction is measured while a contact angle of 91° is measured in the longitude direction. And an isotropy contact angle of 90° is observed on the flat side. This anisotropic wetting property could be further exploited in fluid transporting. As demonstrated in Figure 2-26j, several fluid paths along the axial direction are formed on the patterned side without mixing, which is driven by the anisotropic surface energy. As a contrast, the droplets remain still on the flat side. Likewise, when the fiber is placed vertically, the grooves on the fiber surface will lead the water to flow downwards under gravity, while small droplets will stay on the flat side (Figure 2-26k), indicating the potential application of patterned fibers in self-cleaning. Apart from the demonstrations based on rectangular fibers, several microfluid systems based on star-shaped fibers [158] and nerve guidance scaffolds based on fibers with patterned inner surfaces [160] are also realized, exposing a broad perspective of surface patterned fibers.

2.3.2 Improving the Pattern Resolution by Surface Tension Control

Unfortunately, the fabrication process introduced above is only compatible with creating surface grooves with a resolution of several micrometers. To further improve the pattern resolution, an inherent limitation, polymer reflow, has to be addressed. Polymer reflow driven by surface tension occurs when a preform with an uneven surface is heated above its glass transition temperature. As the surface tension always tends to smoothen the uneven surface, the resulting pattern on the fiber surface might be heavily distorted compared to its initial design, especially for a nanoscale pattern. To address this limitation, F. Sorin et al. have studied this reflow process by modeling the underlying flowing mechanism [93]. To simplify the model without losing the generality, they assume that the surface structure on the preform/fiber has the mathematical form of a sinusoidal function (one harmonic): $y^s(x) = d + h\sin\left(\frac{2\pi}{\lambda}x\right)$, where d is the average thickness of the preform, h and λ are the amplitude and the period of the perturbation, respectively, both usually much smaller than the thickness of the preform: h, λ << d. Also, the deformation of the structure during the fiber drawing process is decoupled into two mechanisms: the scaling deformation due to the drawing process (scaling deformation), and the thermal deformation of the microstructure (reflow deformation). In this model, the differential dh representing the change in structure height of the surface pattern at a position z

along the fiber axial direction is divided into two parts, i.e., the scaling deformation dh_{sc} caused by the thermal drawing process, which is the ideal case for thermal drawing process, and the reflow deformation dh_{re} driven by surface tension.

$$dh = dh_{sc} + dh_{re} \tag{3}$$

According to mass conservation and assuming that the polymer is incompressible, the volume flow through the cross-section at position z and $z + dz$ should be the same. Thus, the scaling deformation dh_{sc} can be calculated.

$$dh_{sc} = -\frac{1}{2}\frac{h}{v}dv \tag{4}$$

Where v is the local drawing speed at position z. As the polymer is drawn at a high viscosity (usually 10^4 to 10^8 Pa*s), the Reynolds number of the polymer is estimated to be very small. Thus, the polymer could be considered as a Newtonian fluid. For the ease of calculation, the surface pattern is assumed to be a sinusoidal shape with only one harmonic. And the reflow deformation dh_{re} could then be obtained by solving the Navier-Stokes equation.

$$dh_{re} = -\frac{\pi\gamma h}{\eta\lambda}dt = -\frac{\pi\gamma h}{\eta\lambda}\frac{dz}{v} \tag{5}$$

Where, γ and η is the surface tension and viscosity of the polymer, respectively, and λ is the period of the sinusoidal surface pattern. Noticing that the deformation only occurs at the neck-down region in the furnace with a length of L, the final pattern height $h(L)$ could be obtained by combining equation (3) - (5) followed by integrating from $z = 0$ to $z = L$.

$$h(L) = h_0\left(\frac{v_f}{V_0}\right)^{-\frac{1}{2}} exp\left(\int_0^L -\pi\frac{\gamma}{\eta\lambda}\frac{1}{v}dz\right) \tag{6}$$

In this equation, the first part, $f_{sc} = \left(\frac{v_f}{V_0}\right)^{-\frac{1}{2}}$, is the scale-down ratio of the thermal drawing process. And the second part, $exp\left(\int_0^L -\pi\frac{\gamma}{\eta\lambda}\frac{1}{v}dz\right)$, represents the contribution of surface tension inducted polymer reflow, indicating that the polymer reflow will be enhanced exponentially with the increase of surface tension or decrease of pattern size. The reflow factor could be defined as $f_{re} = 1 - exp\left(\int_0^L -\pi\frac{\gamma}{\eta\lambda}\frac{1}{v}dz\right)$.

It varies from 0 to 1, where tends to 0 means the polymer reflow is negligible and the surface structure has no distortion, while tends to 1 means the polymer reflows heavily and the surface structure is totally collapsed during the thermal drawing process. Therefore, to achieve a smaller pattern size, lower surface tension is required to maintain a small value of the reflow factor.

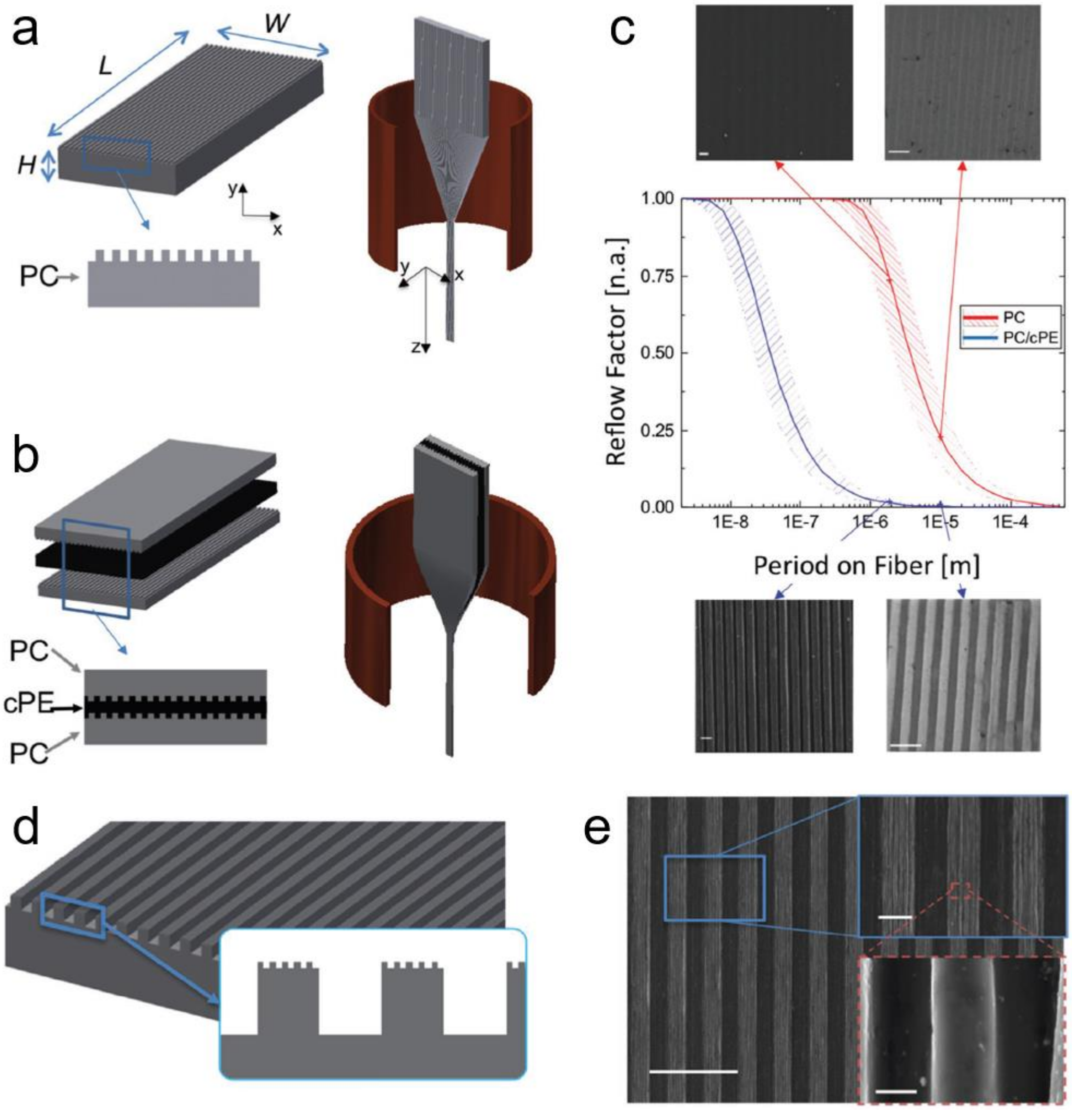

Figure 2-27. Improving the pattern resolution by constructing low surface tension interface [93]. Thermal drawing process of (a) PC preform with patterned surface and (b) a preform with patterned PC/CPE interface. (c) Reflow factor of the patterned surface PC and the patterned PC/CPE interface. The two SEM images on top show the distorted surface pattern on the fiber drawn from PC perform, while the two SEM images at the bottom exhibit a much smaller pattern distortion on the fiber surface drawn from the PC/CPE preform. (d) Hierarchical textures formed on fiber surface by constructing low surface tension interface. (e) SEM images of the hierarchical textures on fiber surface, exhibiting a feature size of around 100 nm.

The experimental verification is then performed. As shown in Figure 2-27 a, b, a patterned PC preform and a preform with patterned PC/CPE interface are prepared for the thermal drawing process. As the surface tension of PC is about 1 order higher than that of PC/CPE interface [93, 325], the reflow factor value of PC is much larger than that of PC/CPE under the same drawing condition, as plotted in Figure 2-27c. For fibers drawing from PC preform, both surface patterns with the periods of 2 μm and 10 μm are heavily distorted (Top of Figure 2-27c). For fibers drawing from PC/CPE preform, the PC layers are peeled off from the CPE layer after the thermal drawing process. Thus, PC fibers with exposed surface patterns are achieved, which show much smaller distortion with similar pattern periods (Bottom of Figure 2-27c). Through the same process, a more complex hierarchical surface pattern on PC fiber is successfully fabricated, reaching a pattern resolution in the sub-micrometer level, as shown in Figure 2-27d, e. Up to now, the smallest feature size of around 100 nm is demonstrated by constructing poly(methyl methacrylate)/polycarbonate (PMMA/PC) interface, which has a very low interfacial tension of 0.39 mN/m [161]. However, all the exhibited surface patterns on fibers are still limited in one-directional structure along the fiber axial direction, which essentially hinders the development of patterned fibers. Hence, creating high-resolution surface patterns in arbitrary directions is highly demanded, which will be discussed in chapter 5.

Chapter 3 Flexible Glassy Semiconductor Fibers for Thermal Sensing and Positioning

3.1 Introduction

Developing flexible thermal sensing fibers via the thermal drawing technique is an intriguing approach to realizing large-area and wearable temperature sensing fabrics for wearable electronics and advanced artificial intelligence applications. As discussed in Section 2.1.4, previous works have reported several thermally drawn fibers achieving thermal sensing based on thermistors or thermoelectric materials. The sensing principle of the thermistors is based on the dependence between the resistance and temperature. Since the drawn fiber should be fine and long for further integration, the resistance of the thermistors inside the fiber will be very large [128]. As a result, a high voltage source as high as 100 V is needed to effectively measure the resistance, which is not convenient nor safe for using on wearable devices. Therefore, the thermoelectric materials which can generate a voltage themselves under a temperature difference could be a better choice. However, all the previously reported thermally drawn thermoelectric fibers employed fragile glass as the cladding material because of the high melting temperature or glass transition temperature of the thermoelectric materials [115, 129]. Thus, a thermoelectric material with low processing temperature and high thermal sensing performance is of profound importance for developing polymer-based flexible thermoelectric fibers.

As for thermoelectric technology, the Seebeck effect states that the charge carriers thermally diffuse in a thermoelectric material under a temperature difference, resulting in an output voltage which equals the temperature difference multiplied by the Seebeck coefficient of the material [248]. Thus, this effect could be utilized to monitor temperature variation according to the corresponding output voltage and has long been adopted in thermocouple applications [326, 327]. The sensitivity of a thermal sensor can be evaluated by how fast and how large such voltage generation occurs from a minimal temperature change. Hence, very large Seebeck coefficients of thermal sensors based on thermoelectric materials are critical in applications that require highly sensitive and accurate measurements of temperature. Recently, the studies on bulk semiconducting glasses of the quaternary Cu−As−Te−Se system demonstrated that these semiconducting glasses possess a large Seebeck coefficient ranging from 400 to 1100 μV/K but a low thermoelectric figure of merit (ZT) [328-330]. Although the low ZT might hinder their further applications such as thermal energy harvesting and thermoelectric cooling, their large Seebeck coefficient enables them a high voltage response when temperature changes, indicating their great potential for thermal sensing applications. Furthermore, the unique feature of the low glass-transition temperature of these semiconducting glasses is well compatible with the thermal drawing process for polymers [331], which makes it possible to fabricate a flexible high-performance thermoelectric fiber for thermal sensing and positioning.

This chapter will present the realization of thermal sensing in arbitrarily long and flexible fiber-based devices by thermally codrawing a semiconducting glass as the core and a thermoplastic polymer as the cladding. The resulting thermoelectric fibers exhibit large Seebeck coefficients, working as a thermal sensor in a wide temperature range up to 150 °C. And the voltage response is recognizable even the temperature change is smaller than 0.05 °C. The sensing performance of a single thermoelectric fiber is characterized via monitoring the temperature change of a thermal source at the fixed point of the fiber or detecting the different points of a thermal source on the fiber with the fixed temperature. To monitor and position a heat/cold source at the same time, a thermal sensing fabric based on a two-dimensional fiber array with a grid size of 24 mm × 24 mm is constructed. Notably, such a thermal sensing fabric requires only a 2N number of fibers to achieve N^2 detection resolution, enabling the applications including large-area and high-resolution thermal sensing and positioning.

3.2 Fabrication of Flexible and Long Thermoelectric Fibers

Preform-to-fiber fabrication by a thermal drawing technique requires the glass-transition temperatures of the supporting materials to be slightly higher than the melting points of the functional materials to support the drawing stress, while continuously and controllably pulling the macroscopic preform down to a microscopic fiber. However, inorganic thermoelectric materials with high thermoelectric performance such as Bi_2Te_3, SnSe, and SiGe alloys normally have high melting points and can only be drawn with a glass cladding [115], resulting in compromised flexibility. To achieve thermoelectric fibers with superior flexibility, an amorphous semiconducting glass $(Te_{85}Se_{15})_{45}As_{30}Cu_{25}$ is synthesized as the thermoelectric core material and a thermoplastic polyetherimide (PEI) polymer with high flexibility as the cladding material.

3.2.1 Preparation of Semiconducting Glass with Low Glass Transition Temperature

The chalcogenide glass rods of quaternary $(Te_{85}Se_{15})_{45}As_{30}Cu_{25}$ with diameters 7 mm and several centimeters in length are firstly prepared from high-purity (5−6N) As, Te, Se, and Cu elements (Sigma Aldrich) using sealed-ampoule melt-quenching techniques. The materials are weighed proportionally and placed into a quartz tube under a nitrogen atmosphere. The tube is cleaned with hydrofluoric acid and then heated to 330 °C for an hour at a rate of 1 °C/min under vacuum to remove surface oxides. The ampoule is formed by sealing the tube under a vacuum of 10^{-5} Torr. It is then heated to 850 °C at a rate of 2 °C/min in a rocking furnace for 8 h. The homogeneous glass liquid is cooled to 600 °C in the rocking furnace and held for 45 min before quenching the glass in cold water. Subsequently, the glass tubes are readily annealed near a Tg of 170 °C for 3 h.

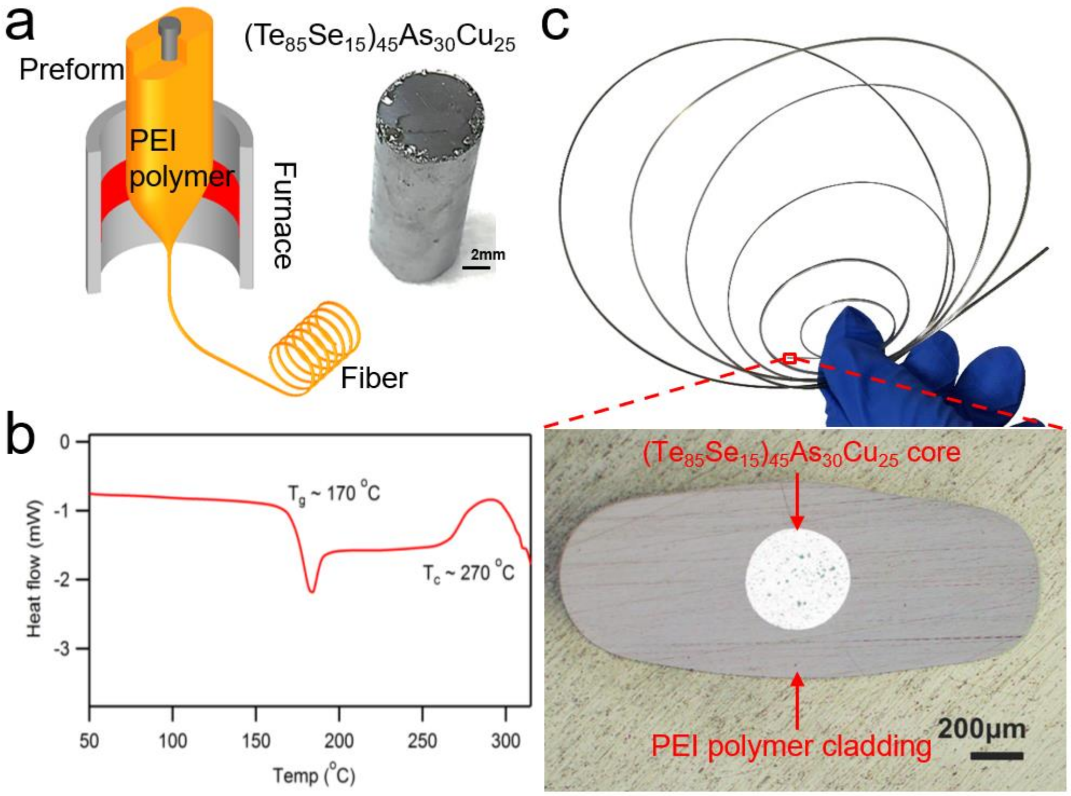

Figure 3-1. Fabrication of flexible and long thermoelectric fiber. (a) Left: schematic of the thermal drawing process of the thermoelectric fiber. Right: thermoelectric chalcogenide glass used in preform preparation. (b) Glass-transition temperature and crystallization temperature of the semiconducting glass measured by DSC. (c) Single thermoelectric fiber with good flexibility and the optical microscope image of fiber cross section.

The resulting chalcogenide glass rod is shown in the right side of Figure 3-1a. This semiconducting glass offers two superior properties in constructing flexible thermal sensors. One is that its Seebeck coefficient is large enough to ensure the sensitivity of thermal sensing. The other is that its glass transition temperature is 170 °C and the crystallization temperature is 270 °C, offering a wide glass stability range of 100 °C, which is measured using a differential scanning calorimeter (DSC Q1000) at a heating rate of 10 °C/min (Figure 3-1b). Such a wide temperature range makes it particularly suitable for the thermal fiber drawing process with the polymer matrix.

3.2.2 Fabrication of Thermoelectric Fibers via Thermal Drawing Technique

PEI polymer with a glass transition temperature of 217 °C is used as a cladding material to support and confine the $(Te_{85}Se_{15})_{45}As_{30}Cu_{25}$ core during the thermal drawing process. To increase the contact area between the heat source and the thermoelectric fiber as well as to reduce the heat loss between the heat source and the semiconducting glass core, a hollow rectangle-shaped PEI block with a cross-section of 20 mm × 8 mm is machined and the diameter of the central hollow channel is 4 mm. The synthesized semiconducting glass is reshaped and filled in the hollow PEI block, and then the entire assembly is thermally consolidated for 60 min at 230 °C in a vacuum oven to remove the trapped gas and form high-quality interfaces. Thus, an all-solid macroscopic preform is prepared for the following thermal drawing process.

The prepared preform is loaded into a two-zone vertical tube furnace on a fiber drawing tower. The top-zone temperature is set at 150 °C and the bottom-zone temperature is set at 250 °C, respectively. After a latency period, the preform is fed down into the furnace at a constant speed of 4 mm/min while the fiber is drawn at a speed of 0.4 m/min. During this process, the viscosity of the PEI cladding is much larger than that of the thermoelectric glass core, thus supporting the whole structure and yielding hundreds of meters of thermoelectric fibers, as sketched in Figure 3-1a.

3.2.3 Morphologies and Components Characterization

Figure 3-1c shows the photograph of the resulting thermoelectric fiber and its optical microscope image of the cross-section. Owing to the presence of polymer cladding, the resulting fiber exhibits high mechanical flexibility to be easily bent, coiled, and woven. The continuous semiconducting glass core is well maintained in a round shape. While the edges of the polymer cladding are smoothened driven by its surface tension, as a relatively high drawing temperature (250 °C) is required by the semiconducting glass core. And the interface between the core and cladding is clearly defined. The diameter of the fiber core is nearly 400 μm and the overall fiber dimension is 1.87 mm × 0.75 mm, which approaches the same dimension ratio of the materials in the original preform, demonstrating that such a thermal drawing is physically proportional size reduction process. The required thermoelectric fiber dimension can be precisely controlled via adjusting the feeding speed of the preform and the drawing speed of the fiber. To further examine the components of the thermoelectric core, the thermoelectric fibers are embedded into an epoxy matrix and polished to expose a smooth cross-section before inserted in a field emission scanning electron microscope (FESEM, JEOL 7600F) equipped with X-ray detector. The energy-dispersive X-ray (EDX) mapping results in Figure 3-2a demonstrate that the functional glass core consists of Cu−As−Te−Se quaternary system and stably confined in the polymer cladding without diffusion or chemical reaction during the drawing process. Moreover, the EDX spectra in Figure 3-2b show that the atomic ratio of Te/Se/As/Cu in the fiber core is about 39:6:30:25, which is close to $(Te_{85}Se_{15})_{45}As_{30}Cu_{25}$ and consistent with the original composition of the semiconducting glass in the preform.

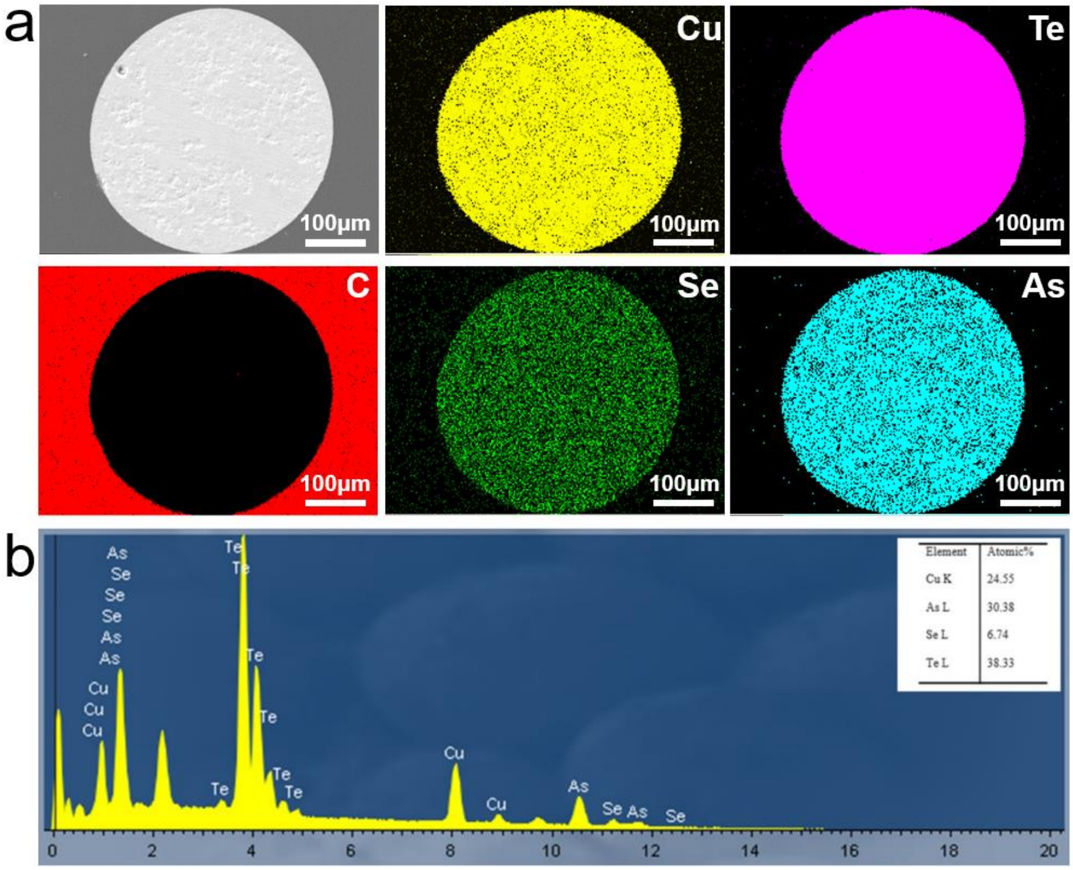

Element	Atomic%
Cu K	24.55
As L	30.38
Se L	6.74
Te L	38.33

Figure 3-2. Components Characterization of the thermoelectric fiber core. (a) EDX mappings of the cross section of the thermoelectric fiber with the core diameter of 400 μm. (b) EDX spectrum of the fiber core and the measured atomic percentage of each element.

3.3 Thermoelectric Properties of Semiconducting Fiber Core

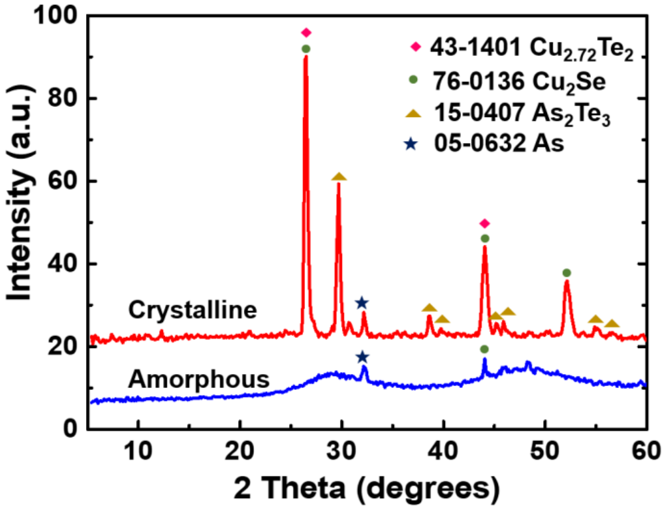

Figure 3-3. XRD spectrums of the semiconducting glass core in amorphous and crystalline states.

The thermoelectric properties of the semiconducting glass depend on its crystal structure. Wide-angle X-ray scattering (WAXS, Xenocs Nano-inXider) is employed to confirm the crystal structures of the fiber core after etching the PEI cladding using dichloromethane solution. The X-ray diffraction spectrum in Figure 3-3 (blue line) and diffraction pattern in Figure 3-4a indicate the amorphous nature of the semiconducting core in the drawn thermoelectric fiber though minor crystallization peaks of As and Cu_2As phases appear. For comparison, the thermoelectric fiber is also crystallized by heating it to 300 °C for 3 h and then cooling to room temperature in a vacuum oven. Figures 3-3 (red line) and Figure 3-4b reveal both its crystal peaks in the X-ray diffraction spectrum and its diffraction ring in the diffraction pattern, which are not observed in the testing results of the original thermoelectric fiber core.

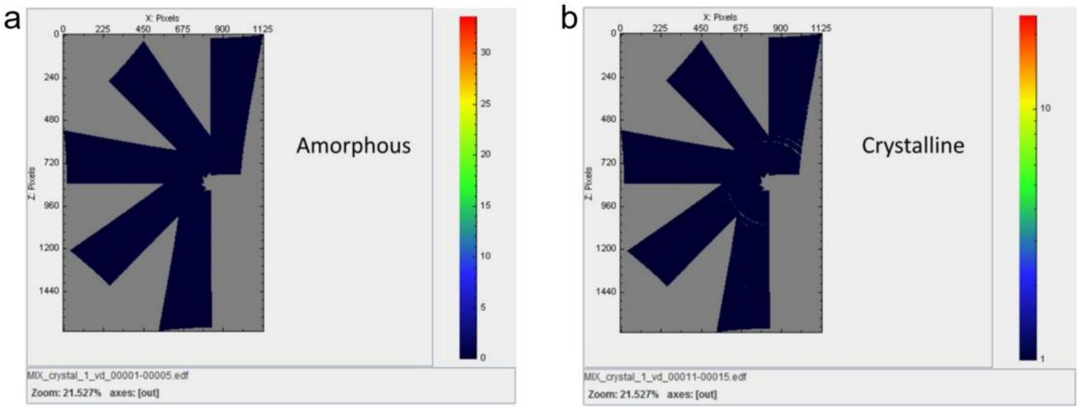

Figure 3-4. X-ray diffraction ring in the WAXS images of the (a) amorphous and (b) crystalline thermoelectric fiber cores.

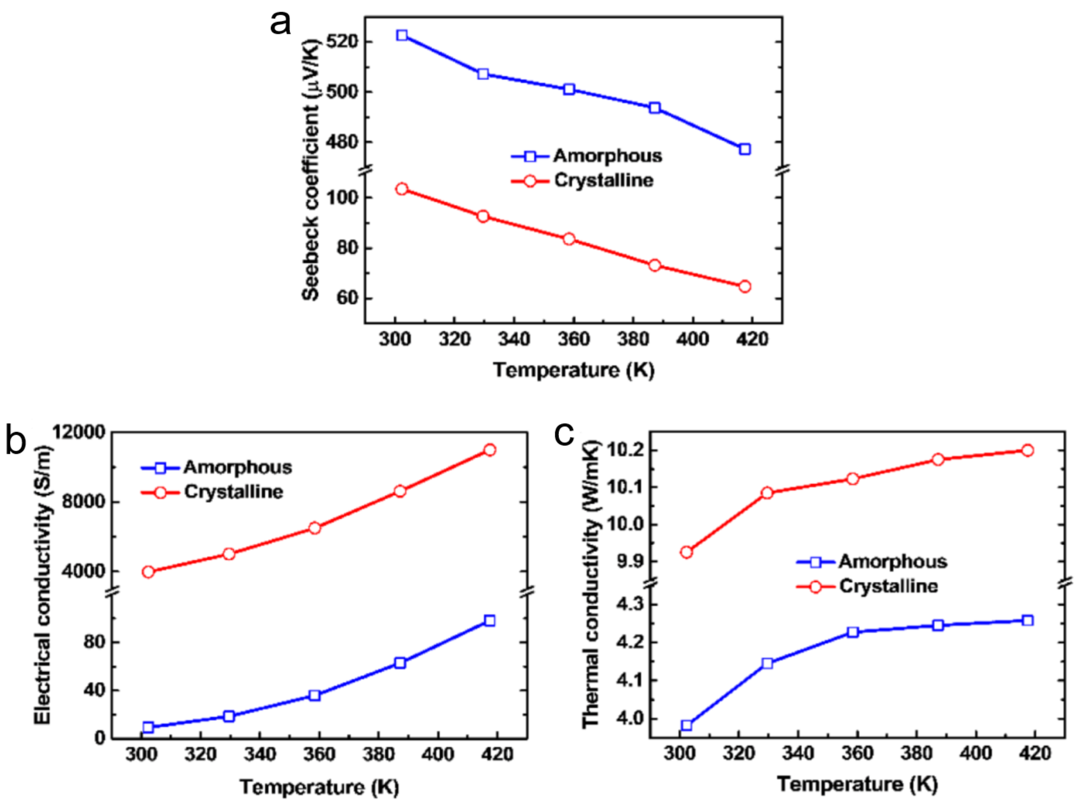

Figure 3-5. The material properties of the semiconducting cores including (a) Seebeck coefficient, (b) electrical conductivity, and (c) thermal conductivity are measured in both amorphous state and crystalline state.

Furthermore, the thermoelectric properties of the semiconducting cores in both amorphous state and crystalline state are measured. Both Seebeck coefficient (S) and electrical resistivity (σ) measurements of the glass cores are carried out by a ULVAC ZEM-3, while the thermal conductivities (κ) are measured under an argon atmosphere using a laser flash (NETZSCH LFA 447). For amorphous state, as shown in Figure 3-5a, b, the thermoelectric glass shows that the Seebeck coefficient decreases from 523 to 477 μV/K with the measured temperature from 300 to 420 K, whereas the electrical conductivity increases from 9.24 to 98.15 S/m. And the thermal conductivity is around 4.0 W/mK in the experimental temperature range (Figure 3-5c), which is higher than the reported thermal conductivities of the amorphous Cu−As−Te−Se glasses [328, 329]. This increment in thermal conductivity can be explained by the emergence of crystalline phases, as the minor crystal peaks in the X-ray diffraction spectrum in Figure 3-3. Compared to the amorphous state, the crystalline fiber core possesses a much smaller Seebeck coefficient and much higher electrical conductivity due to the formed Cu−Te and Cu−Se bonds [330]. And its thermoelectric conductivity is also higher than that in the amorphous state (Figure 3-5a-c). The better conductivity leads to a larger power factor (σS^2) and figure of merits ZT ($\sigma S^2 T/\kappa$) in the temperature ranging from 300 to 400 K, as calculated in Figure 3-6a, b, which may perform better in power generation and cooling applications. However, for thermal sensing properties, large Seebeck coefficient is needed to guarantee high sensitivity and accuracy of the thermal sensor, where a fast and large voltage generation occurs from a minimal temperature change. Therefore, the originally drawn thermoelectric fiber with the amorphous core is more suitable for thermal sensing application.

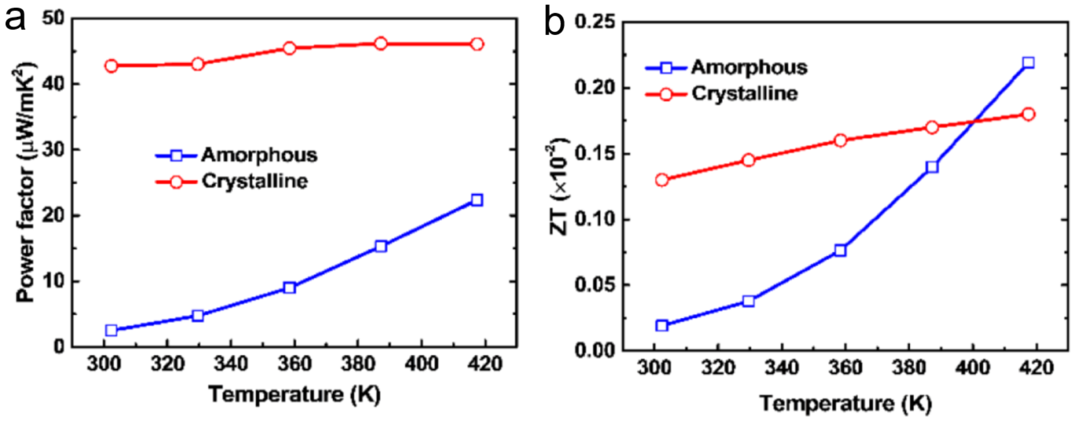

Figure 3-6. The calculated (a) power factors and (b) figure of merits ZT values.

3.4 Thermal Sensing and Positioning Based on a Single Thermoelectric Fiber

The originally drawn amorphous-core fiber is chosen for the thermal sensing applications. Both experimental measurements and finite-element simulations are conducted to study its performance.

3.4.1 Experimental Measurements

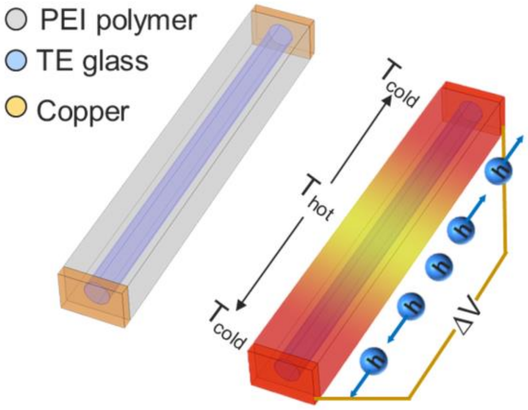

Figure 3-7. Schematic of the measuring principle for the thermal sensing performance of the thermoelectric fiber.

The measuring principle for a single thermoelectric fiber is schematically shown in Figure 3-7. A Keithley 2602B source measure unit is used to power the heat for changing the temperature of the thermal source. Meanwhile, a Keithley 2182A nanovoltmeter is connected to the two copper electrodes at the two ends of the fiber to measure the output thermoelectric voltage and a Keithley 2700 multimeter records the temperature data. According to the Seebeck effect, when a heat source is applied to the thermoelectric fiber, the electrical potential will be built between the heated area and cold area because of the hole carrier diffusion in the semiconductor glass core. If the heated area is not in the middle of the fiber, temperature difference and electrical potential difference between the two ends of the fiber will be established, generating voltage outputs between copper electrodes.

Figure 3-8a records the real-time temperature change of the heat source located on the 20% length of the entire fiber with a total length of 10 cm and plots the output voltage from the temperature difference at two fiber ends. As the temperature of heat source increases from room temperature of 25 °C, the corresponding output voltage increases rapidly with the sampling duration of 500 ms. As shown in Figure 3-8b, the voltage response is still recognizable even the temperature change is smaller than 0.05 °C. This accuracy and sensitivity are comparable with most of the commercial thermal sensors. And the output voltage shows a linear growth in Figure 3-8c as the temperature of the heat source increases. Considering that the location of the heat source also affects the temperature gradient and output voltage between the two ends of the fiber, the relationship between the location of the heat source and the output voltage of a single thermoelectric fiber is further characterized through touching different locations on the fiber with one finger around 35 °C. As plotted in Figure 3-8d, At the central area of the fiber, namely, 50% fiber length, the heat of a finger equally transfers from the central position to both ends. Thus, there is a small temperature and electrical potential difference at the two ends of the fiber, resulting in a weak output voltage. As the finger moves from the central area towards the two fiber ends, the absolute value of the output voltage increases dramatically. Here, the electric potential of the end of the fiber (at 100% fiber length) is taken as the reference potential to measure the potential difference (voltage) of the beginning of the fiber (0% fiber length). The potential of the thermoelectric material in the fiber will decrease as the temperature increases. Therefore, if the figure touches the fiber at the position between the beginning (0% fiber length) and the middle point (50% fiber length), the potential at the beginning of the fiber will be lower than the potential at the end of the fiber. Thus, the measured voltage will be negative. Similarly, the measured voltage will be positive when the figure touches the fiber at the position between 50% fiber length and 100% fiber length. And the positive or negative values are symmetrical with the middle point, indicating that a single thermoelectric fiber is capable of positioning the heat source, rather than simply detecting the temperature [122].

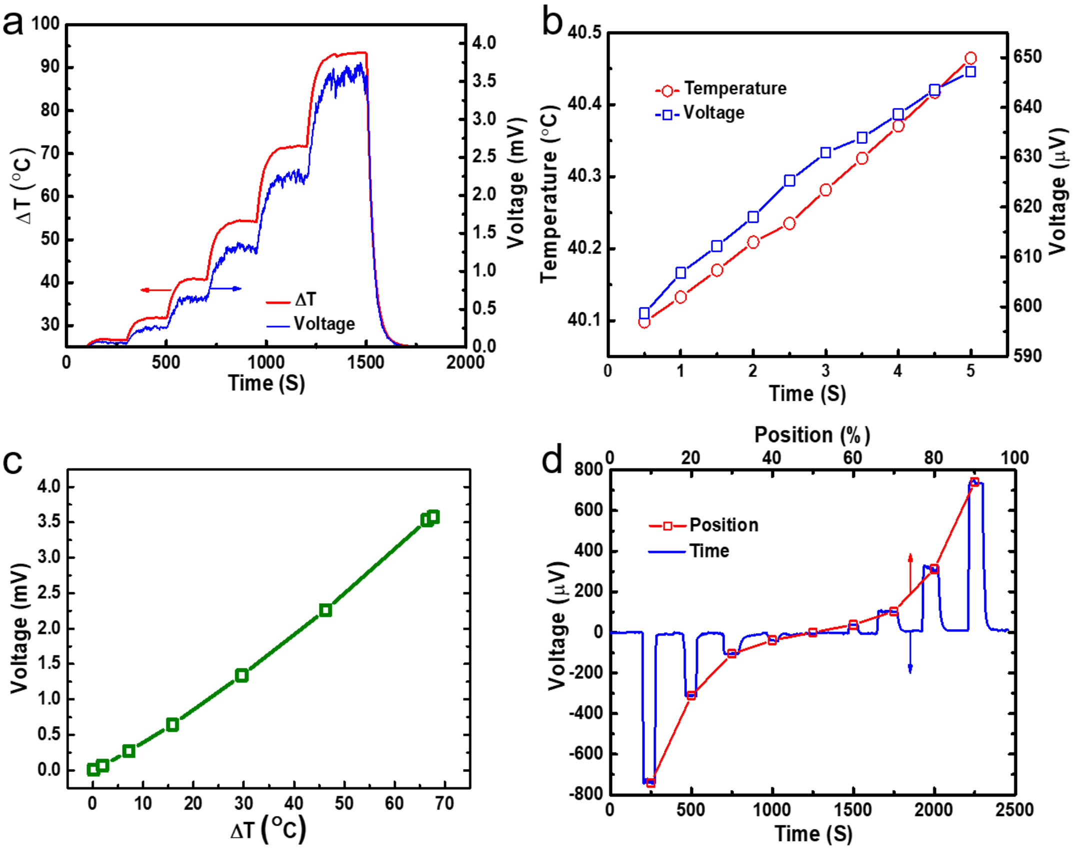

Figure 3-8. Thermal sensing performance of a single thermoelectric fiber. (a) Real-time recording of the temperature of the heat source located at the 20% length of the whole fiber and the corresponding output voltage from the temperature difference at two fiber ends. (b) Temperature resolution of the thermoelectric fiber thermal sensor. (c) The output voltage shows a linear growth as the temperature of the heat source increases. (d) Real-time output voltages from the different positions of the thermal source by finger touching.

Moreover, the temporal response of the fiber is measured to be very fast. It only takes 3 s to reach a steady state after the finger touches as shown in Figure 3-9a. Besides its high thermal sensing performance, its flexibility is also studied, as summarized in Figure 3-9b. The curvature radius decreases largely when the fiber thickness reduces. Even for a thick fiber with a thickness of 0.6 mm, the curvature radius is still less than 2.5 mm, showing much better flexibility in contrast to the thermoelectric fiber with glass cladding [115]. The top-left inset in Figure 3-9b exhibits that the fiber senor is flexible enough to be conformally wrapped on the glass rod surface with a diameter of 3 mm, without any wrinkle or breakage. Thus, it is a promising candidate to fabricate large-area, flexible, and wearable temperature sensing fabrics.

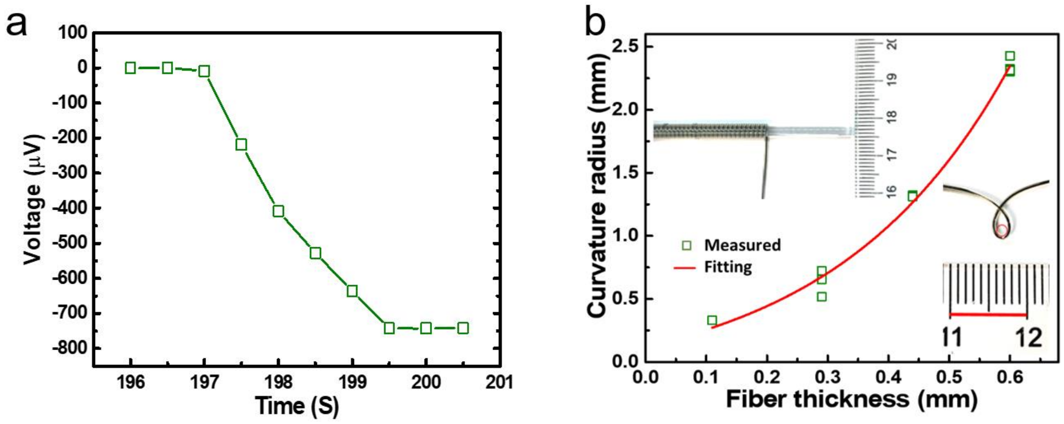

Figure 3-9. (a) Temporal response of the thermoelectric fiber. (b) Minimum curvature radius of thermoelectric fibers with different fiber thicknesses.

3.4.2 Finite-Element Simulations

The thermal sensing performance of thermoelectric fiber mainly depends on the temperature gradient and electrical potential distribution in the semiconducting glass core owing to the Seebeck effect. A multiphysics finite-element solver (COMSOL) is used to simulate the thermal sensing performances of the thermoelectric fiber in a steady state based on the thermoelectric modules, where all the parameters and geometries of the thermoelectric fibers are defined to be close to the actual materials and structures. Specifically, the fiber length is 10 cm. The cross section is a round core with a diameter of 260 μm located at the center of the rectangular cladding. And the mesh is set to “user-controlled mesh”. The element size is calibrated for “general physics”. And the minimum element size is set to “100 μm” while the maximum element size is “1000 μm”. Additionally, the maximum element growth rate is set to “1.45”. The curvature factor is set to “0.5” and the resolution of narrow regions is “0.6”. The temperature gradient and electrical potential distribution in a single thermoelectric fiber are visualized in Figure 3-10a. The relationship between the output voltage and location of the heat source with a fixed temperature is firstly simulated. The environment temperature is set to be 25 °C, while the temperature of the heat source is 36 °C. When the heat source is placed on the fiber surface of 16.5% length, the output voltage between the fiber ends is 504 μV. And the output voltage decreases exponentially and symmetrizes as the thermal source moves from the two ends towards the middle point (Figure 3-10b), which has the same tendency as the experimental results. Area 1 and 2 in Figure 3-10b are enlarged as Figure 3-10c and d, respectively.

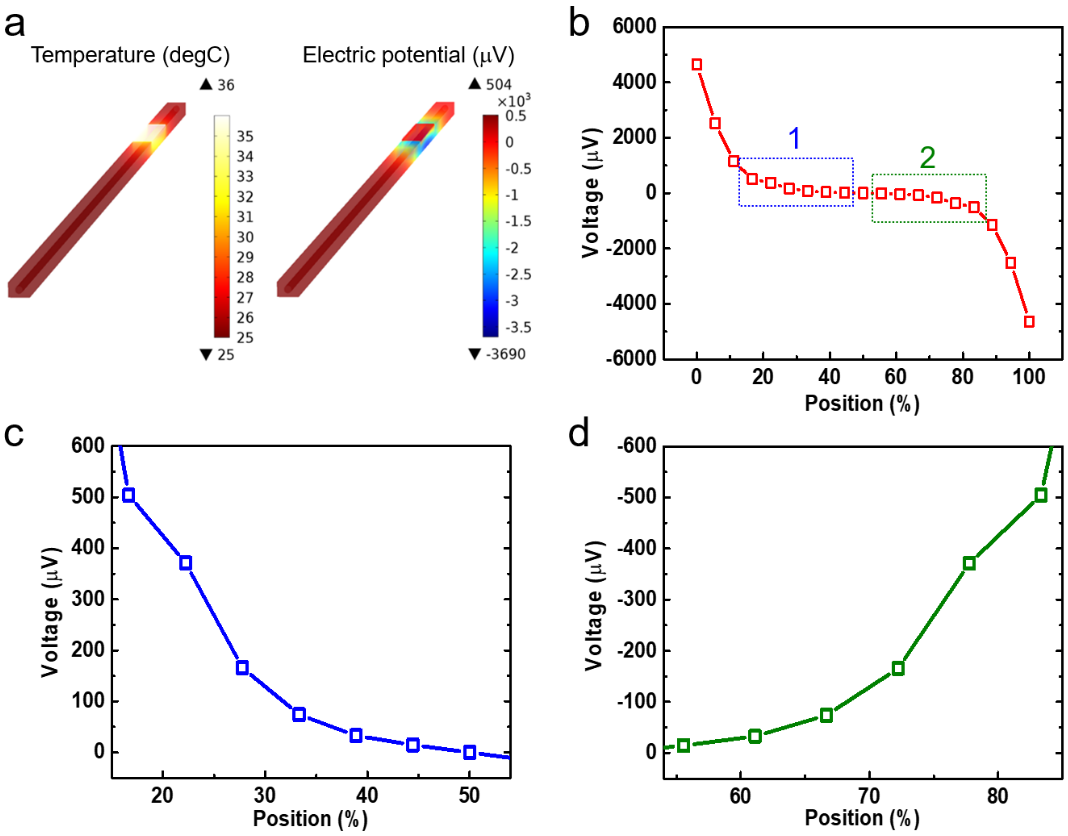

Figure 3-10. Finite-element simulation of the thermal sensing performance. (a) Temperature gradient and electrical potential distribution on a single thermoelectric fiber. (b) Output voltages vary with the heat source of 36 °C moving along the fiber length. (c, d) Enlarged plot corresponding to areas 1 and 2 in (b), respectively.

The relationship between the output voltage of the fiber and the temperature of the heat source at a fixed location is then studied. Figure 3-11a gives the output voltages induced by different temperatures on the middle point, 15%, and 85% fiber length points, respectively. The output voltage of the middle point is almost zero and unchanged with the increased temperature, whereas the absolute values of the output voltage for 15 and 85% fiber length points are identical under the same temperature and increase with the raised temperature because of their symmetry in location. These results further prove that a single thermoelectric fiber can sense the temperature variation of a fixed spot or position the heat source location under a specific temperature applied to the fiber.

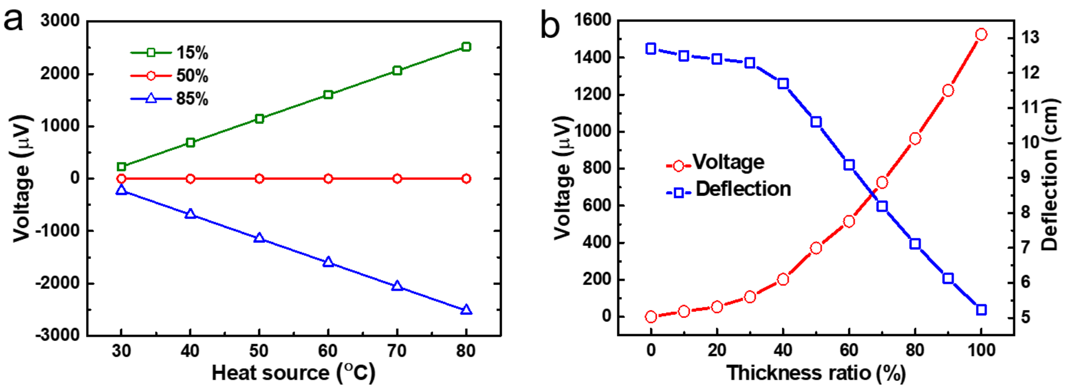

Figure 3-11. (a) Simulated output voltages induced by different temperatures of heat source fixed at different locations. (b) Simulated output voltages and deflections of the fiber thermal sensor for different thickness ratios between the semiconducting glass core and the entire fiber.

The influences of the proportion of the semiconducting glass core in the thermoelectric fiber on the fiber's thermal sensing performance and flexibility are also simulated based on the solid mechanics module. In principle, the higher proportion of semiconducting glass core in the thickness direction of the fiber occupies, the higher thermal sensing performance of the fiber presents because thinner polymer cladding lowers the heat loss and thicker semiconducting glass core enhances electrical conductivity. However, increasing the proportion of the semiconducting glass core will sacrifice the flexibility of the fiber. Figure 3-11b illustrates the simulated output voltages and deflections of the fiber thermal sensor for different thickness ratios between the semiconducting glass core and the entire fiber. The temperature of the heat source is still 36 °C and the location is at 22.2% fiber length. The results indicate that, as the proportion of the semiconducting glass core increases, the sensitivity of the fiber sensor is improved, yet the flexibility is weakened. The optimized proportion is about 50−60%, which approaches the similar dimension of the fabricated thermoelectric fibers.

3.5 Flexible Thermal Sensing Fabric on a 3 × 3 Thermoelectric Fiber Array

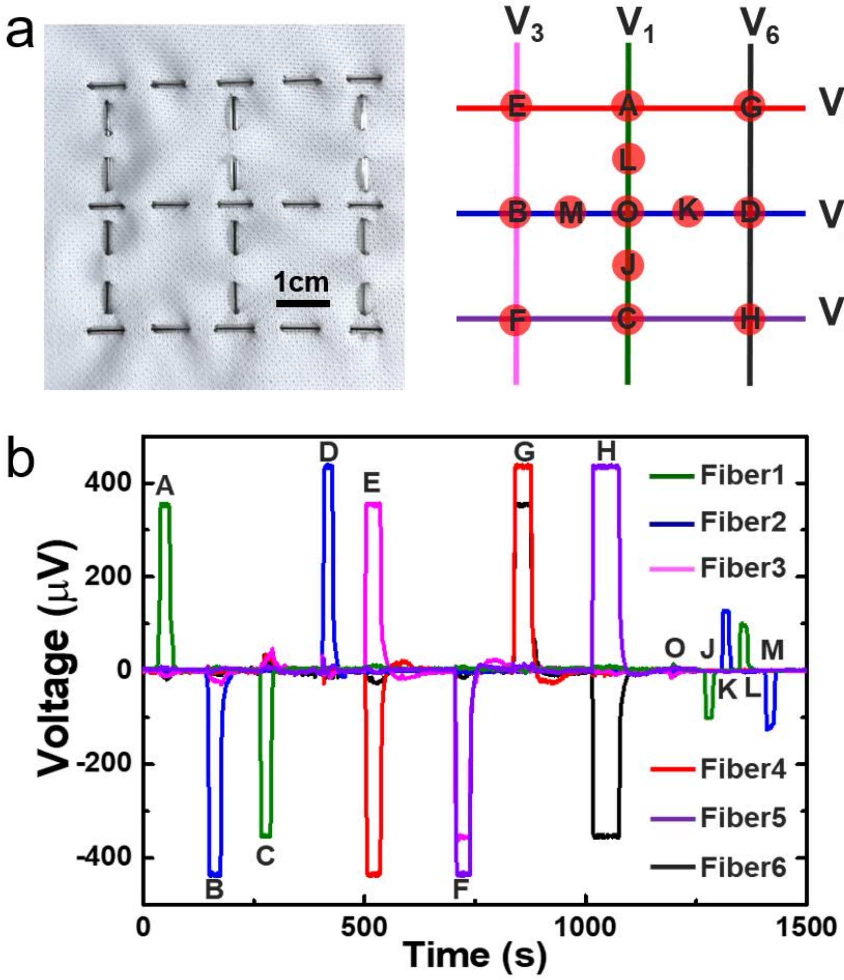

Figure 3-12. Flexible thermal sensing fabric based on a 3 × 3 thermoelectric fiber array for simultaneous thermal source detection and positioning. (a) Left: 3 × 3 TE fiber array woven into a flexible fabric. Right: The finger-touching points schematically marked by capital letters. (b) Output voltages of the thermal sensing fabric for different thermal source positions when the finger touches the marked points.

Although a single thermoelectric fiber is able to sense the temperature with a fixed location or position the thermal source with a fixed temperature by the output voltage, it is hard to obtain both the temperature and the location of the thermal source. For instance, an output voltage of 2.5 mV may be generated either from the heat source with the temperature of 36 °C at the location of 5% fiber length (Figure 3-10b) or the temperature of 80 °C at the location of 15% fiber length (Figure 3-11a). To address this challenge, a flexible thermal sensing fabric is constructed through weaving a 3 × 3 thermoelectric fiber array into a flexible textile. This flexible thermal sensing fabric can serve as a prototype to obtain spatially resolved thermal information including both thermal sensing and positioning. The 3 × 3 thermal sensor array with the grid size of 24 mm × 24 mm is assembled by six thermoelectric fibers with a length of 8 cm, as shown in the left image of Figure 3-12a. While touching the fiber on the thermal sensing fabric with a finger at different points as marked with capital letters in the right image of Figure 3-12a, the output voltages of the six fibers from V1 to V6 are continuously and simultaneously collected by a multichannel data acquisition card of Keithley 7700. The accurate location and temperature of the finger can be subsequently analyzed from the distinguishable voltage signal from each grid axis, as plotted in Figure 3-12b. Moreover, if fiber 1 and fiber 2 are regarded as y-axis and x-axis, respectively, the quadrant of the thermal source can be located by the sign of the distinguishable voltage. For instance, the finger-touching point E shown in Figure 3-12a is resolved in the second quadrant and at the cross point of fiber 3 and fiber 4, owing to a positive voltage form fiber 3 and a negative voltage form fiber 4. Furthermore, the accurate temperature of the finger is determined by the largest output voltage values of the single fiber sensor as discussed above. Interestingly, the absolute value of output voltage from fiber 4 is slightly higher than that from fiber 3 located in thermal point E on the same position of both fiber 3 and fiber 4, which is mainly caused by the heat loss from the upper fiber 4 to the bottom fiber 3. It is worth noting to point out that this difference can be utilized to detect the pointing direction of the thermal source. For example, in this case, the heat point is located at the upper side rather than the bottom side of the thermal sensing fabric.

As a comparison, both thermal infrared (IR) images taken by an IR camera (FLIR C2) and reconstructed thermal maps using the data obtained from the fiber array is presented for two situations. One is the finger heating with a temperature of 33 °C and the other is the ingot cooling with a temperature of 22 °C, as displayed in Figure 3-13a. Both the thermal images and the reconstructed thermal maps are matched well with the actual situations (Figure 3-13b, c), confirming the capability of the thermal sensing fabric for ultraflexible and large-area detecting and positioning the thermal source with high spatial temperature resolution.

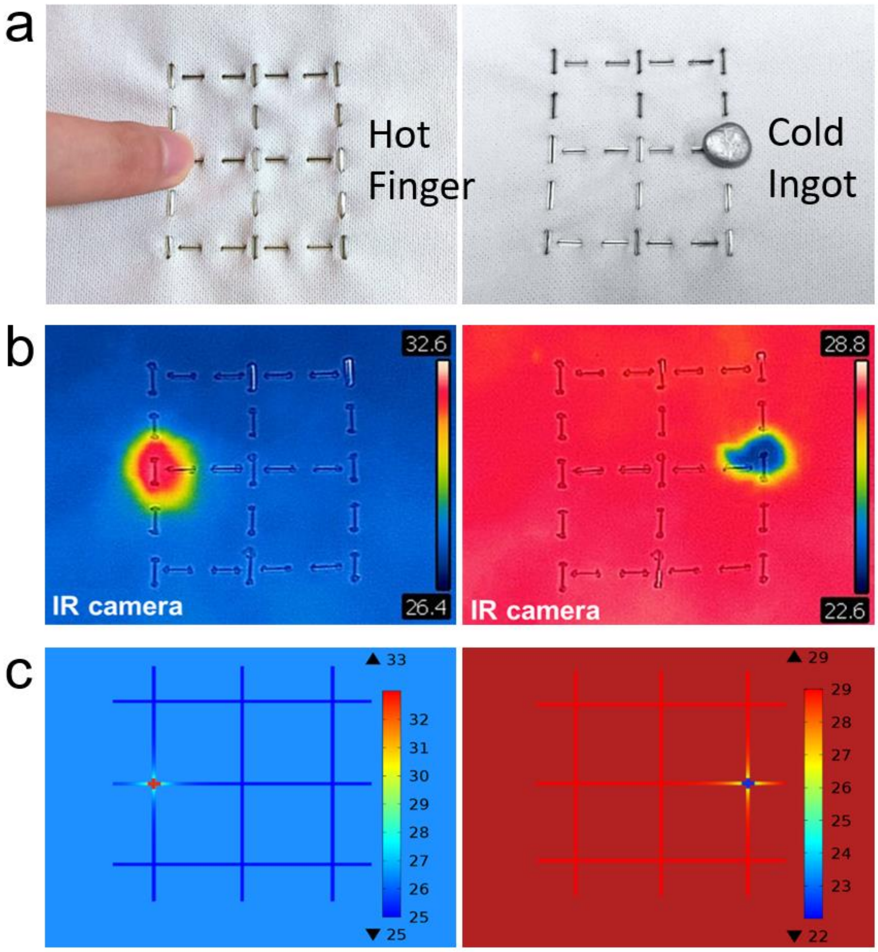

Figure 3-13. Comparison of the measured results between thermal sensing fabric and IR camera. (a) Two working situations: finger heating with a temperature of 33 °C and ingot cooling with a temperature of 22 °C. (b) Thermal images taken by an IR camera. (c) Reconstructed thermal maps using the data obtained from the fiber array.

3.6 Summary

In summary, a polymer-based flexible thermal sensor is fabricated by thermally codrawing a semiconducting glass core and a polymer cladding into a thermoelectric fiber. This fabrication technique delivers thermoelectric fiber functionalities at fiber-optic length scales, flexibility, uniformity, and low cost. The thermoelectric properties of the semiconducting cores in both amorphous and crystalline states are measured. And the performance of a single thermoelectric fiber is experimentally tested and subsequently simulated. The results suggest that the resulting single thermoelectric fiber is capable of efficiently detecting thermal source in a wide temperature range up to 150 °C. The voltage response is still recognizable even the temperature change is smaller than 0.05 °C. And the resolution for positioning thermal source is in millimeter level. Furthermore, a flexible thermal sensing fabric based on a network by 3 × 3 thermoelectric fiber array is experimentally applied for simultaneously realizing thermal sensing and positioning with high spatial resolution. This demonstrated flexible thermal sensing fiber may lead to important applications in thermometry, thermography, smart fabrics, e-skin in robotics, health-monitoring products, and wearable electronics. Nevertheless, because of the relatively low electrical conductivity nature of amorphous materials, realizing long distance thermal sensing and positioning by a single thermoelectric fiber remains a challenge. Further efforts could be made in developing a superior thermoelectric material which possesses both high electrical conductivity and low thermal conductivity.

Chapter 4 Super-Elastic Fibers by Soluble-Core Thermal Drawing for Self-Powered Touch Sensing

4.1 Introduction

Besides thermal sensing, touch sensing is also an indispensable function to be developed for advanced smart fabrics or electronic skins to detect motion of human or external objects. Previous works [113, 233] have demonstrated some thermally drawn electronic fibers for touch sensing applications. The working principles of such fibers are quite similar as introduced in section 2.1.3. The structural deformation of the fiber under external pressure will induce the resistance change of the fiber electrode or the capacitance change between the fiber electrodes. Thus, the motion could be figured out by monitoring the change of the resistance or capacitance. However, it is still a challenge to power this type of electronic fibers as they are supposed to be integrated into fabrics that are not much compatible with a fixed power socket. And for the fibers based on resistance change, their length and small cross-sectional area lead to a large electrode resistance, which may need a higher voltage source than conventional batteries to achieve a recognizable signal [113]. While for the fibers based on capacitance change, more complex powering and measuring circuit may be needed. Moreover, they can only respond to a pressure which is high enough to cause the structural deformation, which may be a restriction in small force applications.

Utilizing fiber-based wearable TENG to harvest the mechanical energy from the touching behavior itself and transform it into electricity should be a promising solution to address the limitations above. On the one hand, this self-powered device will directly generate a recognizable voltage or current signal according to the motion. On the other hand, the output signals of the TENGs are generated from the changes of the external electrical field other than structural deformation, leading to a high sensitivity as the response signal could occur even before the approaching external objects reaches and touches the fiber. In recent years, countless fiber-based TENGs have been developed and numerous intriguing applications in touch sensing have been exhibited [312, 323, 324], as reviewed in 2.2.3. However, most of the fibers used in these works are fabricated by depositing materials on existing commercial fibers [305], resulting in limited fiber structures (layered structure or coaxial structure), poor material compatibility, complicate fabrication process. And the coated materials usually exhibit low wearing resistance, which is especially indecent for touch sensing applications which will suffer frequent contact and friction. Therefore, applying the thermal drawing technique to fabricate highly integrated multimaterial fibers with designable structure and high-yield is highly appreciated for self-powered touch sensing.

Additionally, developing electronic devices based on elastomeric materials is also highly motivated because of the superior flexibility and stretchability [332]. The low-modulus elastomers could be conformally fitted onto any irregular surfaces and endure large deformation without breakup, predicting their promising application in fiber-based touch sensors. However, thermally drawing the thermoplastic elastomers is still a great challenge to date. The fiber architecture will be difficult to maintain during the thermal drawing process due to the low modulus, low viscosity, and high adhesiveness of such thermoplastic elastomers under high temperature, which hinders their further applications in fiber-based soft electronics. Although extrusion seems to be an alternative option to fabricate the elastomer fiber, the geometry of the extruded fiber is highly dependent on the die used for extrusion. For fiber-based electronic devices, fiber with small size and functional inner structures is usually required. If the desired fiber diameter is small (e.g., smaller than 1 mm) and complex in-fiber structure (e.g., multichannel) is required, it is quite difficult to prepare the corresponding die with a precise and complex structure in the micrometer scale. Furthermore, integrating different materials inside one fiber at a customizable position is also a challenge for extruded fiber. Therefore, developing a process for thermally drawing the elastomer materials is of great importance.

This chapter proposes a two-step soluble-core fabrication method to overcome the incompatibility between the low-viscosity thermoplastic elastomers and the thermal drawing process. The first step is the co-drawing of a typical elastomer shell, styrene-ethylene-butylene-styrene (SEBS), and a polyvinyl alcohol (PVA) core into a thin fiber that defines the initial structure. The second step is to dissolve the PVA core to obtain a hollow SEBS tubular fiber. A super-elastic conductive fiber is thus fabricated after injecting liquid metal into the hollow SEBS fiber. This conductive fiber offers outstanding stretchability and flexibility which maintains excellent conductivity even under 1900% strain or sudden hit and stretched by a 1.5 kg load freefalling from a height of 1 meter. The stretchable TENGs are subsequently assembled from the super-elastic conductive fibers. The working mechanism and performance are discussed and matched well with the simulation results. As a proof of concept, a self-adaptive net fabric for self-powered touch sensing is built and attached to a football to perform touch sensing based on a spherical coordinate, revealing its ability in sports performance monitoring while bearing strong and sudden impacts. This fabrication process and touch sensing fabrics indicating their future applications in self-powered smart fabric and large-scale soft device integration.

4.2 Fabrication and Characterization of Super-Elastic Fiber

4.2.1 Soluble-Core Fabrication Process

SEBS pellets (G1643) purchased from Kraton and PVA pellets (G-polymers 8049P) purchased from Nippon Gohsei are used in the soluble-core fabrication process. To prepare the preform for the fiber drawing process, PVA pellets are filled into the heating barrel of the injection molding machine and melted at 200~225 °C for 3~5 mins. Then the melted PVA is injected into the mold under a pressure of 0.7 MPa and kept for 30 seconds to obtain a solid PVA bar after cooled down. The shape of the PVA bar is dependent on the cavity of the mold. Also, SEBS pellets are hot-pressed into thin films under 190 °C for 8 mins. The resulting SEBS films with a thickness of around 200 μm are then cropped to rectangular shape, followed by tightly wrapping the SEBS films around a PVA bar to form a PVA/SEBS core-shell structure (Thin-film rolling approach introduced in section 2.1.1). The whole structure is subsequently wrapped by Teflon thread seal and consolidated in a vacuum oven at 110 °C for 2 hours to remove the moisture and air gap between SEBS layers and SEBS/PVA interface and finally form a preform.

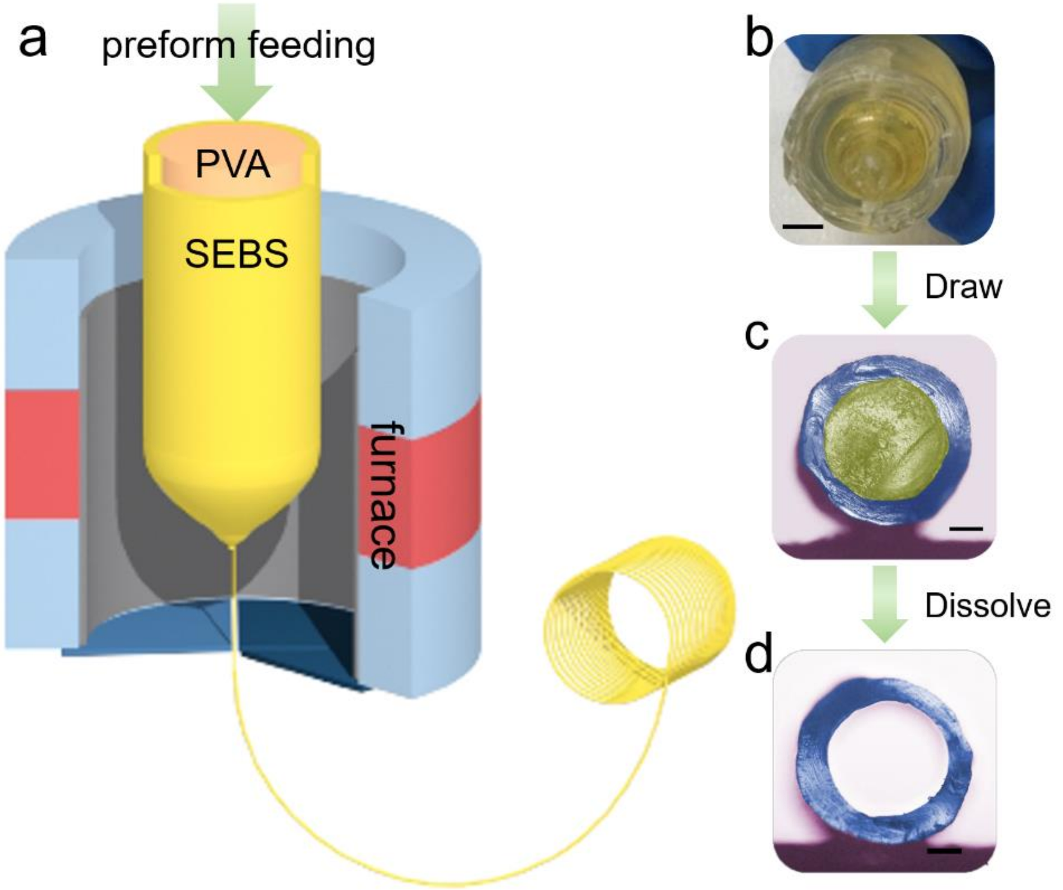

Figure 4-1. Two-step soluble-core fabrication process. (a) Schematic of the thermal drawing process. (b) Photograph of the PVA/SEBS preform before drawing. Scale bar: 3 mm. (c) Photograph of the thermally drawn PVA/SEBS fiber. Scale bar: 200 μm. (d) Photograph of the SEBS hollow fiber after the PVA core is dissolved. Scale bar: 200 μm.

The thermal drawing process is sketched in Figure 4-1a. A cylindrical preform is used for an example as the cross-section image shows in Figure 4-1b (Scale bar: 3 mm). The prepared preform is loaded into a two-zone furnace, where the top and bottom zones are set to 150 °C and 350 °C, respectively. After a latency period around 20 minutes, the preform is drawn down at a constant speed of 1 m/min and a neck-down region from macroscopic preform to microscope fiber will be formed in the furnace. To maintain a uniform fiber diameter, the preform is also fed into the furnace at a constant speed of 3 mm/min. Thus, a uniform fiber with tens of meters long is continuously produced. The scale-down ratio of the preform-to-fiber process could be controlled by the feeding speed and drawing speed. In this work, the outer diameter of the drawn fibers are kept to be around 0.8 mm as the cross-section image shows in Figure 4-1c (Scale bar: 200 μm).

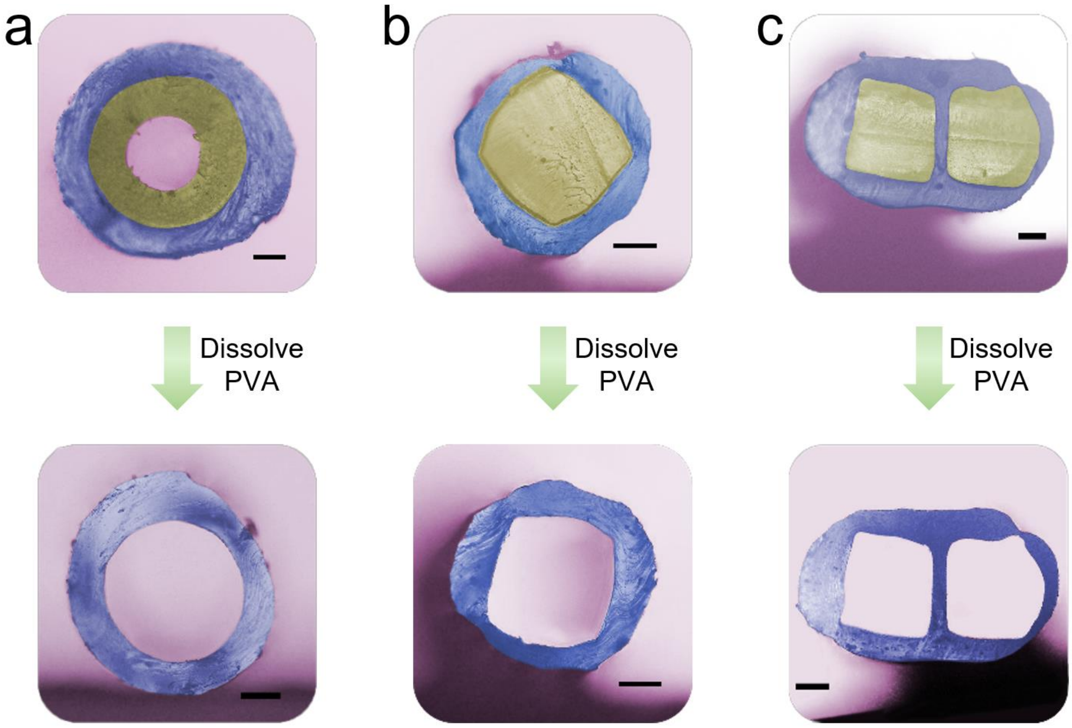

Figure 4-2. SEBS fibers with different fiber architectures before and after dissolving PVA. (a) SEBS/PVA/air channel fiber (before dissolving PVA) and SEBS fiber with a round hollow core (after dissolving PVA). (b) SEBS fiber with a square core. (c) dual-core SEBS fiber. All the scale bars are 200 μm.

After collecting the drawn fiber, it is cut into segments and soaked into 80 °C hot water to dissolve the inner PVA cores, leaving a hollow SEBS fiber as demonstrated in Figure 4-1d (Scale bar: 200 μm). This dissolving process could be very slow when the fiber segment is long. In general, the dissolving process for a 10 cm fiber segment may need more than 10 hours in still water as the solid PVA core is dissolved from the two fiber ends gradually towards the center. To speed up the dissolving process, a fiber with a hollow PVA core is drawn by replacing the PVA rod with a PVA tube inside the preform. As shown in Figure 4-2a, the water can be filled into the hollow core during the dissolving process, which significantly reduces the dissolving time. Similarly, by changing the mold of the injection molding machine and wrapping process, the PVA core and structure of the preform could be customized to disparate configurations. And corresponding fiber structure could be achieved after thermal drawing and dissolving process, as the square hollow core SEBS fiber and dual-core SEBS fiber which are shown in Figure 4-2b, c, respectively.

It is worth mentioning that, in principle, this soluble-core fabrication process could be applied to all the thermoelectric materials whose viscosity is too low to be drawn independently. And various fiber structures could be obtained owing to the presence of the soluble PVA or other soluble materials. A potential limitation of current process is that it is not easy to get a fiber with sharp edge on the outer surface because the outer SEBS is easy to reflow [93] due to its low viscosity, as exhibited in Figure 4-2c. This limitation could be possibly addressed by add another layer of PVA outside the PVA/SEBS core-shell preform to confine the whole structure from distortion during the thermal drawing process. And all the PVA could be dissolved subsequently to get a SEBS fiber with sharp edge.

4.2.2 Mechanical Properties

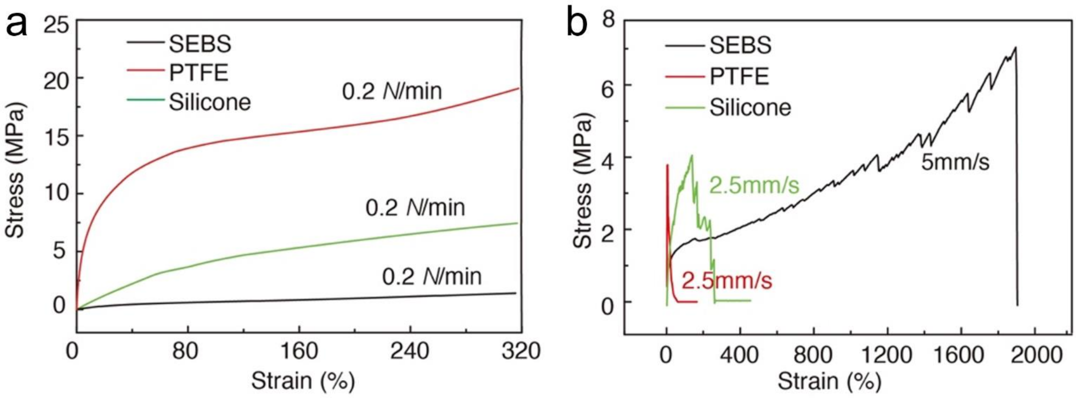

Figure 4-3. Mechanical properties of the hollow SEBS fiber, hollow PTFE fiber, and hollow silicone fiber. (a) Stress-strain curves measured by DMA. (b) Measurements of the highest stretch ratio.

The stretchability is measured for hollow SEBS fiber, as well as hollow PTFE fiber and hollow silicone fiber for comparison. The hollow SEBS fiber used in this test has an inner diameter of 500 μm and an outer diameter of 900 μm. The hollow PTFE fiber used in this test has an inner diameter of 600 μm and an outer diameter of 950 μm. And the hollow silicone fiber used in this test has an inner diameter of 600 μm and an outer diameter of 1000 μm. Before each test, these diameters are input into the measurement instruments for calculating the corresponding cross-sectional area. Thus, the stress-strain curves instead of force-strain curves could be acquired from the instruments after each test. As plotted in Figure 4-3a, the stress-strain curves for the three fibers are measured under a quasi-static force by a dynamic mechanical analyzer (DMA, TA Q800), where the applied force increases in a very slow rate of 0.2 N/min. The curve of PTFE fiber shows a linear elastic region where the stress is proportional to the strain and a strain hardening region where the strain increases much faster than stress as the plastic deformation occurs. A similar trend is observed in the curve of silicone fiber while the curve of SEBS fiber shows an approximately linear growth. And the Youngs' moduli of 1.5 MPa, 5.8MPa, and 204.1 MPa are calculated from the linear elastic regions of the SEBS, silicone, and PTFE fibers, respectively. The working distance of the DMA is too short for the breakup of the SEBS fiber because of its superior stretchability. Hence, an MTS Criterion Model 42 is used for testing the highest stretch ratio of the fibers. As presented in Figure 4-3b, the SEBS fiber can endure a strain as high as more than 1900%, which is much higher than that of silicone and PTFE fibers.

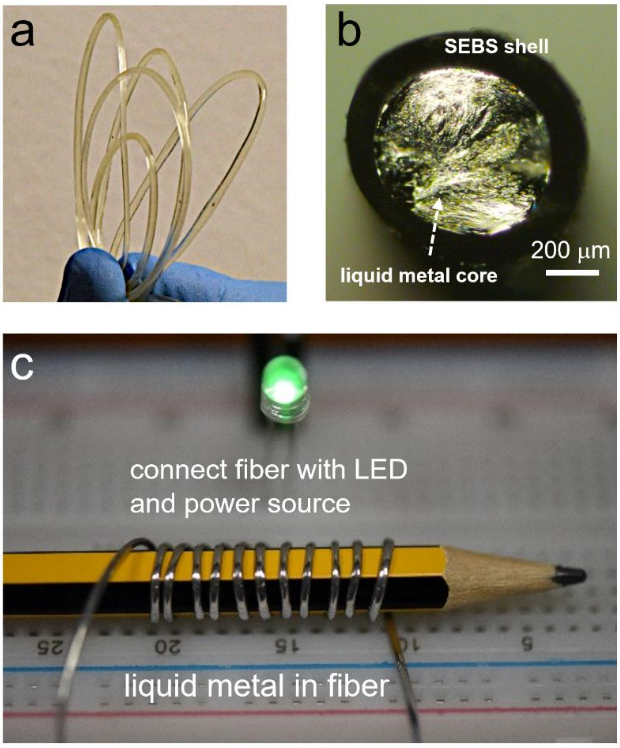

Figure 4-4. Flexible and conductive SEBS fiber. (a) Uniform and flexible hollow SEBS fiber. (b) Liquid metal is injected into the hollow core of the SEBS fiber. (c) The conductivity is maintained when conformally coiled on a pencil.

Figure 4-4a displays the flexibility of the drawn SEBS fiber with a continuous hollow channel running within the entire fiber length. To match with its superior stretchability, a liquid metal, GaIn eutectic alloy, is chosen as the conductive filler of the hollow SEBS fiber, as shown in Figure 4-4b. The GaIn eutectic alloy is composed of Ga and In with a mass fraction of 75.5% and 24.5, respectively. According to the datasheet from the supplier (Alfa Aesar), its melting point and density are 15.7 °C and 6250 kg/m^3, respectively. Therefore, it is in liquid state which can be easily injected into the hollow channel in SEBS fiber under room temperature. Also, this liquid metal possesses good conductivity, which is reported to be $3.4*10^6$ S/m [333, 334]. Thus, a super-elastic conductive fiber is formed after two copper wires are inserted and sealed at its two ends. This fiber exhibits outstanding flexibility which could be conformally coiled on a pencil while maintaining the electrical connection to serve as a conductive wire and light up a green LED, as shown in Figure 4-4c. Besides liquid metal, ionic liquid and other functional solutions are also compatible with this technique to develop other electronic devices according to specific application scenarios. Moreover, increasing the number of channels within a single fiber will potentially lead to highly integrated multifunctional electronic devices.

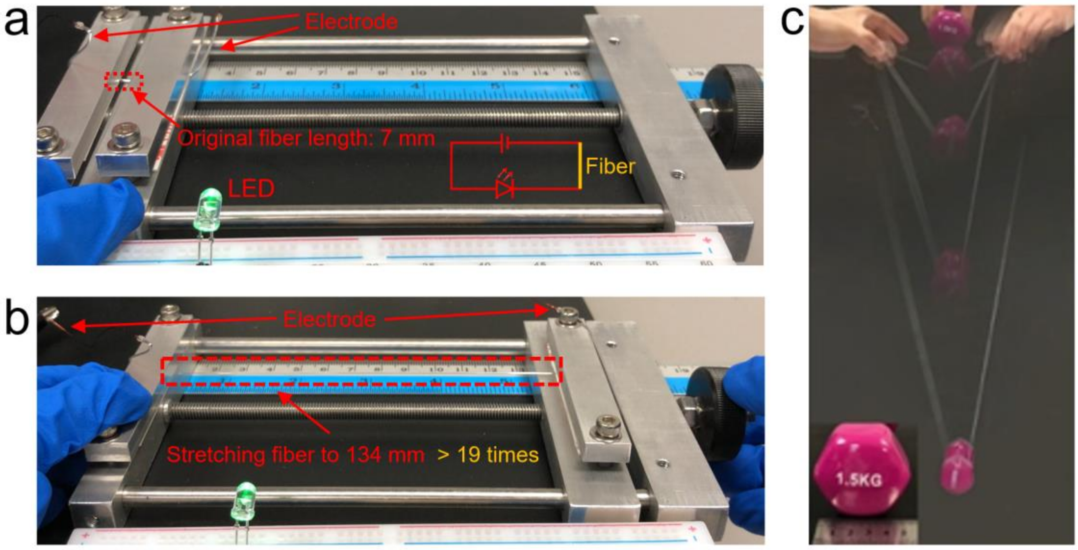

Figure 4-5. Stretchability of the conductive SEBS fiber. (a) The conductive SEBS fiber is clamped on a displacement stage and connected to a circuit with a battery and a LED. (b) The conductive SEBS fiber works normally when stretched to around 19 times of its original length. (c) The conductive SEBS fiber works normally after hit and stretched rapidly by a free-falling dumbbell.

The electrical connection inside the conductive fiber is further examined under stretching. As demonstrated in Figure 4-5a, both ends of the fiber are clamped on a displacement stage, leaving a fiber length of 7 mm between the two clamps. The two ends are connected into a circuit with a battery and a LED to light up the LED. Then the fiber is gradually stretched to 134 mm, around 19 times of its original length (Figure 4-5b). And the LED is still lighted, indicating that filling liquid metal inside the hollow channel does not affect the stretchability of the SEBS fiber. In addition to stretching the fiber gently, the fiber is also tested under a sudden deformation. As illustrated in Figure 4-5c, the fiber is held at 1-meter-high from the ground and a 1.5 kg dumbbell is subsequently released above the fiber. The fiber remains unbroken after hit and stretched rapidly by the free-falling dumbbell, revealing its capability to bear a sudden impact, which is beneficial for applications in a harsh environment.

4.3 Triboelectric Nanogenerators Based on Super-Elastic Conductive Fibers

4.3.1 Experimental Setup

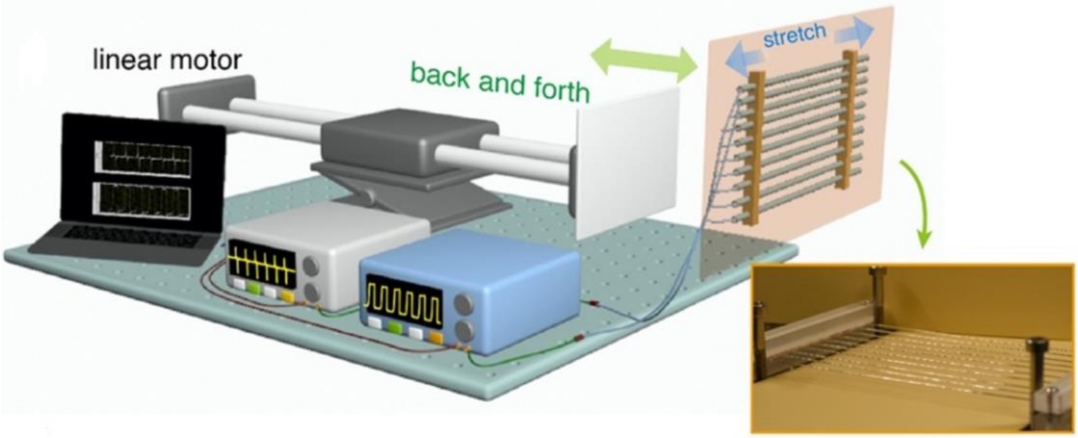

Figure 4-6. Setup for measuring the output performance of the fiber-based TENG.

To quantitively study the electrical output performance of the TENGs based on ultra-stretchable conductive fibers, a test platform is built as shown in Figure 4-6. One end of the fiber is sealed with copper wire as electrode while the other end is sealed directly. And the sealed fibers are fixed in parallel between two clamps with an original distance of 25 mm for the ease of adjusting their strain simultaneously, as demonstrated in the inset of Figure 4-6. A grounded aluminum (Al) plate serving as another electrode is driven by a linear motor (LinMot E1100) to realize periodical contact-and-separate movement with the fibers. The driving speed of the motor is set at 0.1m/s, while the open-circuit voltage and close-circuit current between the Al plate and fibers are measured by a Keithley 6517B electrometer, and a Stanford 570 current preamplifier, respectively. The measured signals are collected by an analog input module (NI-9125) inserted in NI CompactDAQ Chassis (cDAQ-9171) which is connected to a computer.

4.3.2 Working Mechanism

The working mechanism of the TENG based on single ultra-stretchable conductive fiber under this test mode is shown in Figure 4-7a, b, corresponding to the cross-sectional views in perpendicular and parallel with fiber axial direction, respectively. The charge distribution is sketched on the Al plate and the upper part of the conductive SEBS fiber only to simplify the discussion. During the working process, the Al plate and the fiber contact and separate repeatedly. Thus, the electrons in the

Al plate will be transferred to the surface of SEBS and accumulated on its surface because of triboelectrification [335]. Because of the presence of the negative charge on the fiber surface, the positive charge will be induced in the fiber electrode (liquid metal core in the SEBS fiber) when the Al plate is separated from the fiber. As the Al plate moving towards the fiber till contact, its electrical potential will decrease and drive the positive charge in the fiber electrode flow to Al plate, forming a current from fiber to Al plate through the external circuit (the lower part of Figure 4-7a, b). Similarly, when the Al plate and fiber are separated again, a reverse current from Al plate to fiber will be generated through the external circuit, as shown in the upper part of Figure 4-7a, b. Hence, an alternating current will be generated during the repeated contact-and-separate process, i.e., the mechanical energy is transformed into electricity.

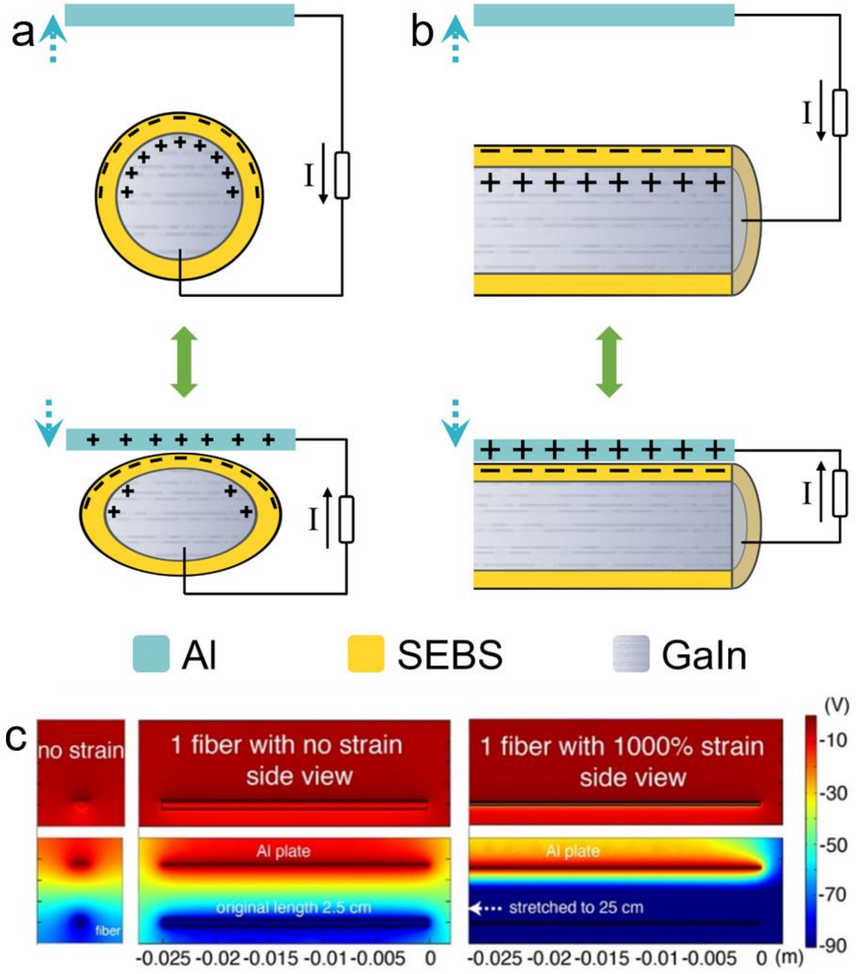

Figure 4-7. working mechanism of a stretchable TENG based on conductive fiber. (a) Working principle is shown from the cross-sectional view in perpendicular to fiber axial direction. (b) Working principle is shown from the cross-sectional view in parallel with fiber axial direction. (c) Simulations

of the electrical potential distribution when the fiber and Al plate contact and separate under normal and stretched conditions.

Further simulations are conducted using COMSOL to verify the working mechanism. All the parameters and geometries of the Al plate and conductive SEBS fibers are defined to be close to the actual materials and structures. The Al plate is grounded and kept at a potential of 0 V while the charge density on the fiber surface is set according to the subsequent charge amount measurement. As shown in Figure 4-7c, the electrical potential distribution inside and around the Al plate and the fiber are simulated under different states. Both contact (upper row) and separate (bottom row) states are visualized in cross-sectional views. And the cut planes of these cross-sections are in perpendicular (left column) and parallel (middle column) to fiber axial, respectively, in the case that the fiber is not stretched. These simulated results exhibit that the potential of the fiber electrode is much lower when separated from Al plate. This potential difference will be the driving force of the positive charge flow from Al plate to fiber electrode if they are connected electrically, which matches the above discussion of the working mechanism very well. Moreover, the potential of the fiber under 1000% strain is much lower than that under the original length (right column of Figure 4-7c), which can be attributed to the larger charge amount brought by the increased surface area of the stretched fiber.

4.3.3 Output Performance

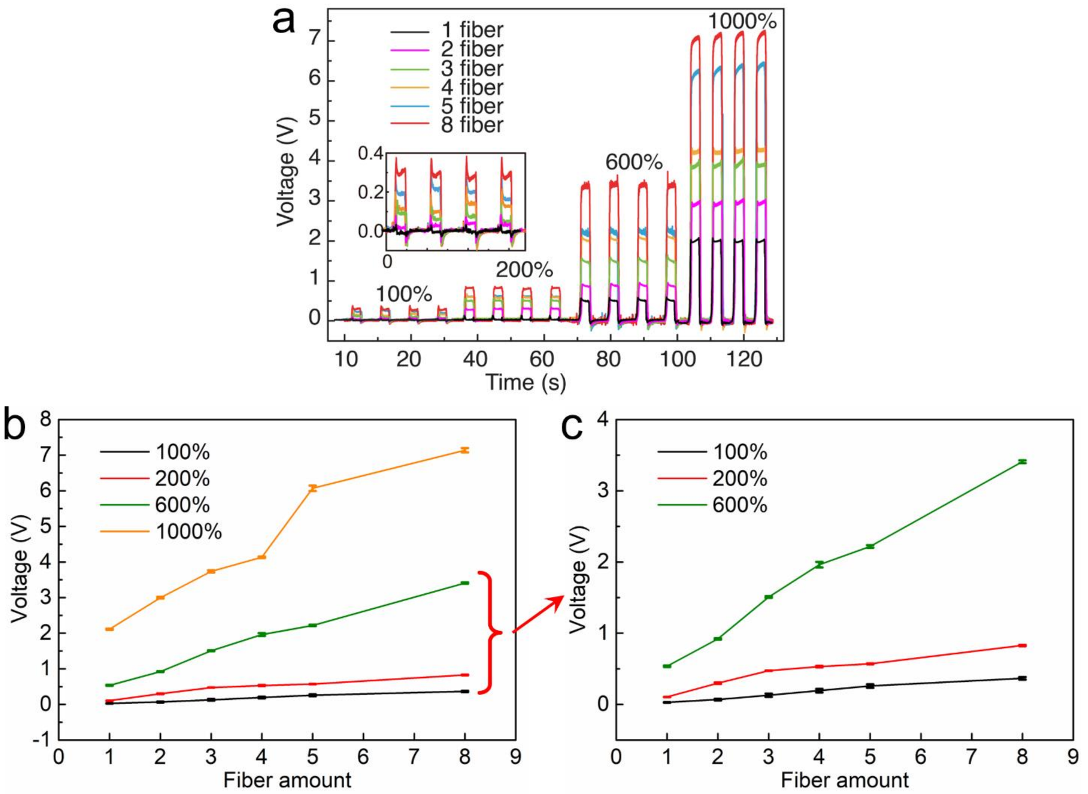

Figure 4-8. The output open-circuit voltage of the fiber-based TENGs with different fiber amounts and strains. (a) Measured voltage curves of the fiber-based TENGs. (b) Extracted peak values with error bars of the measured voltage curves. (c) Enlarged graph of the 100%, 200%, and 600% curves in (b).

Based on the setup shown in Figure 4-6, the output performance of the fiber-based TENGs with different fiber amounts (1,2,3,4,5, and 8 fibers) under different strains (100%, 200%, 600%, and 1000%) is measured. The original length of the TENG fiber is 25 mm. The open-circuit voltage is plotted in Figure 4-8a. And the mean values and their standard deviations (error bars) of the peak voltages under different testing conditions (fiber amount and strain) are extracted and plotted in Figure 4-8b, c. A slight change in the positions of the fibers and Al plate might occur during the sample loading process at each test condition, which could result in a small deviation in the output performance. However, the output voltage signal is rather stable once the positions of the fibers and Al plate are fixed during the measurements, leading to a small error of the peak voltages. As shown in Figure 4-8b, c, a clear trend is revealed that the output voltage increases as the fiber amount increases or the strain increases. And the highest voltage of about 7.5 V is reached from 8 fibers connected in parallel under the strain of 1000%.

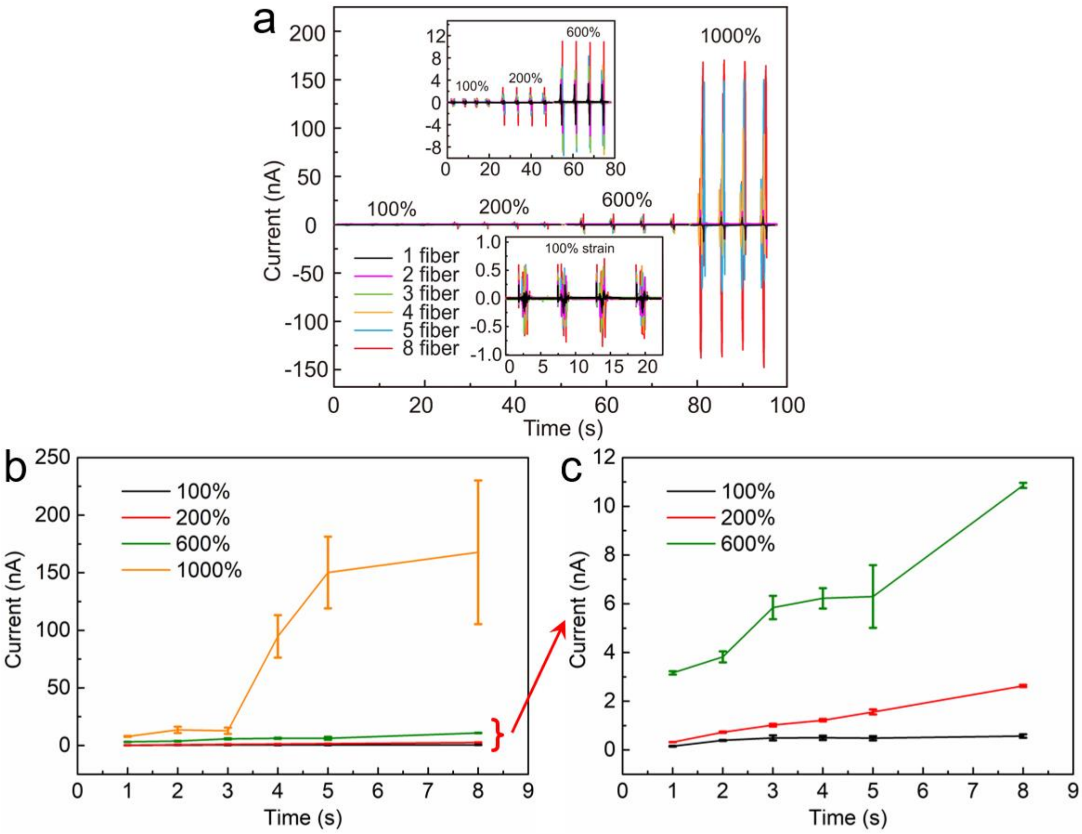

Figure 4-9. The output short-circuit current of the fiber-based TENGs with different fiber amounts and strains. (a) Measured current curves of the fiber-based TENGs. (b) Extracted peak values with error bars of the measured current curves. (c) Enlarged graph of the 100%, 200%, and 600% curves in (b).

Similarly, the short-circuit currents of the fiber-based TENGs are measured with different fiber amounts under different strains, as the measured current curves shown in Figure 4-9a. Also, the peak values of currents under different test conditions are extracted and their mean values and standard deviations are plotted in Figure 4-9b, c. Although the trend of the output signal of short-circuit current is also exhibited growing as the fiber amount or strain increases, it grows not as smoothly as the voltage signal and possesses large errors, especially under 1000% strain and larger fiber amount. The large fluctuation and errors are due to that the current signal reflects the current flow speed through the external circuit, which could be heavily influenced by the relative velocity between the fiber electrode and the Al plate. As only the two ends of the fiber are fixed, there will be an obvious vibration in the middle part of the fibers when the fiber is stretched to a high strain. The vibration will contribute to the relative velocity between the fiber electrode and the Al plate. Thus, the current signal is more sensitive to instantaneous slight variations in the working process. Under the

1000% strain condition, especially with multiple fibers, the instantaneous signal could be larger, leading to a large fluctuation compared to the TENGs under lower strains and with fewer fibers.

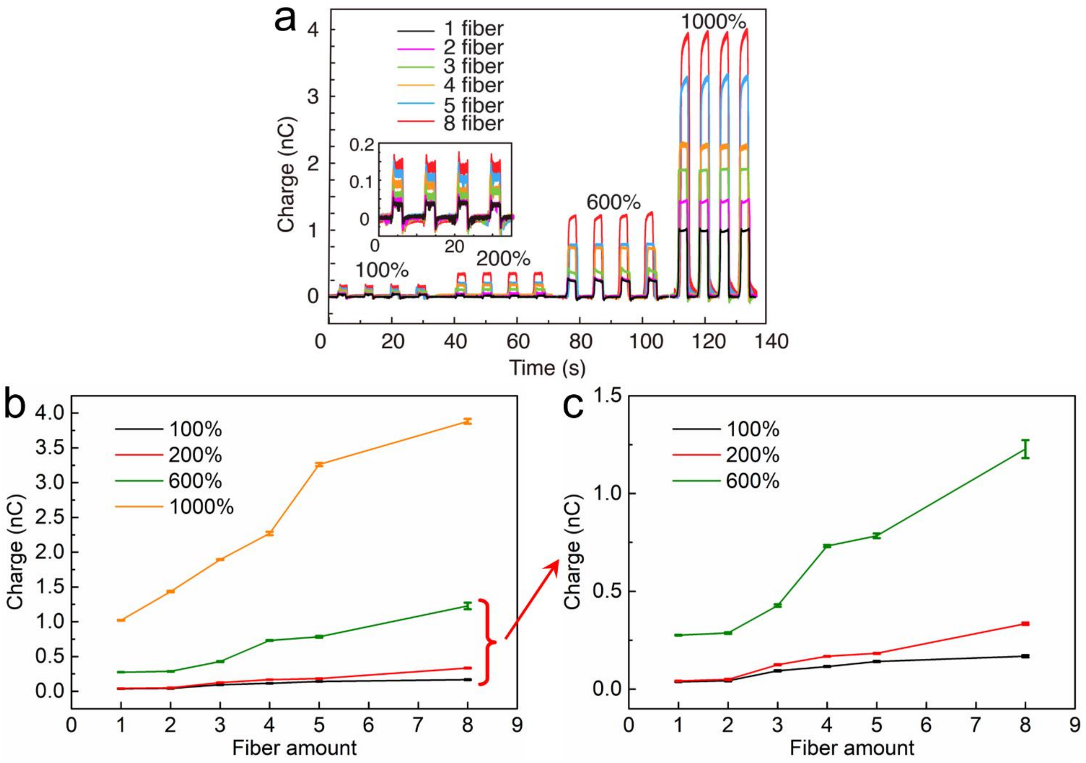

Figure 4-10. The measured charge amount of the fiber-based TENGs with different fiber amounts and strains. (a) Measured charge amount curves of the fiber-based TENGs. (b) The measured charge amount (with error bars) flows between the two electrodes. (c) Enlarged graph of the 100%, 200%, and 600% curves in (b).

Fortunately, the current over the time of a single working cycle can always be integrated to obtain the charge amount flows between the fiber electrode and Al plate, which is more stable as it will not be influenced by the relative velocity between the fiber electrode and the Al plate. The charge amount can also be simply measured by an electrometer, as shown in Figure 4-10. As the fiber amount and strain increase, a growing trend similar to the trend of open-circuit voltage is observed. According to the measured charge amount, the electrical potential distribution is further simulated for the TENGs with 4 fiber and 8 fibers under original length (25 mm) and 1000% strain at contact and separate states, which is consistent with the experimental results, as shown in Figure 4-11.

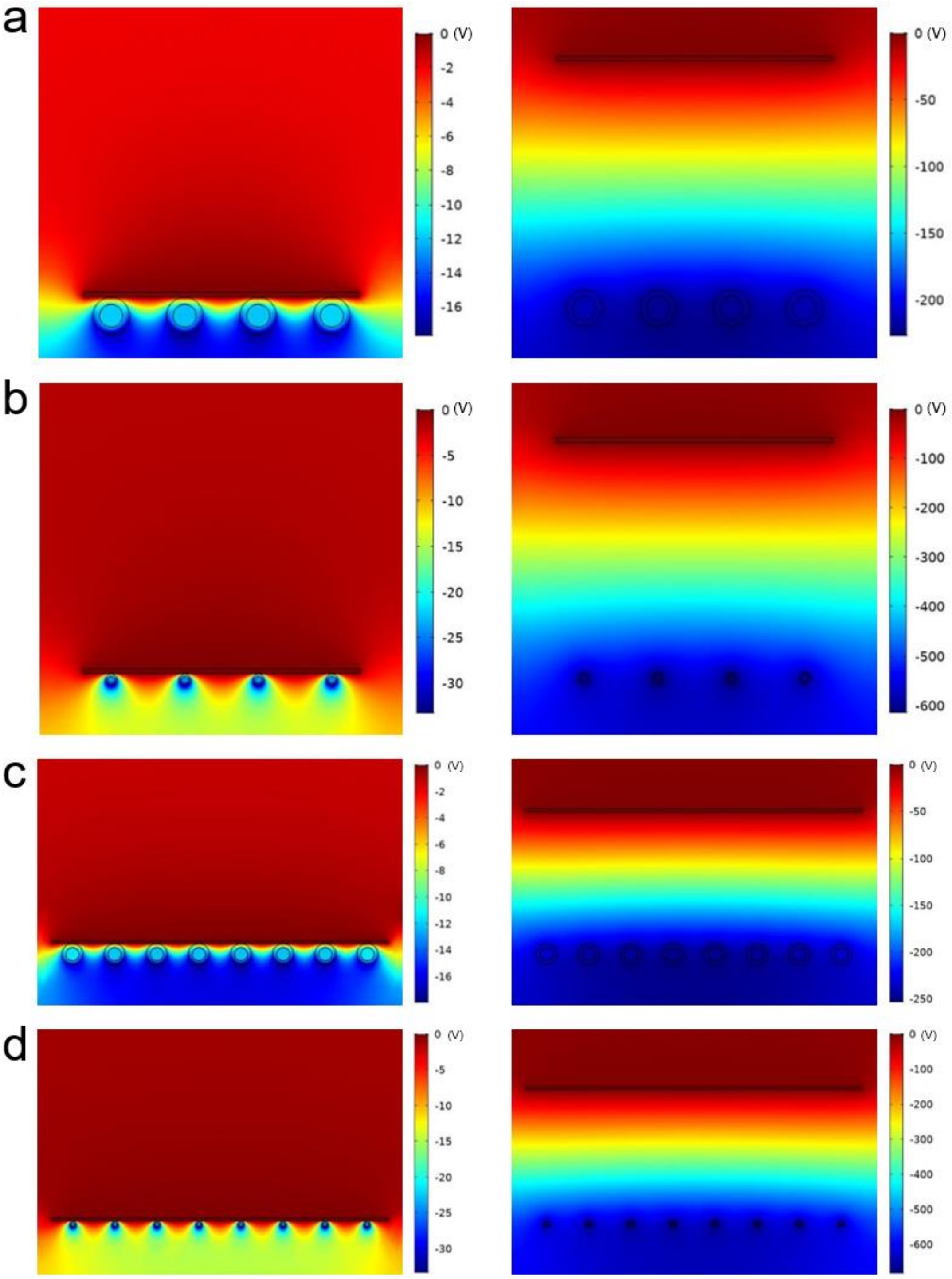

Figure 4-11. The simulated electrical potential distribution of the TENGs with 4 fiber and 8 fibers under original length and 1000% strain at contact and separate states. (a) Simulated results for the TENG based on 4 fibers under the original length. (b) Simulated results for the TENG based on 4 fibers under 1000% strain. (c) Simulated results for the TENG based on 8 fibers under the original length. (d) Simulated results for the TENG based on 8 fibers under 1000% strain.

The durability of the TENG based on 6 10-cm conductive fibers is further tested. The output current is measured continuously for around 5 h and the output signal before and after 1000, 2000, and 3000 working cycles is demonstrated in Figure 4-12a. The periodic fluctuation of the peak current at 2000 and 3000 cycles is caused by the reduced sampling rate to prevent the data logging software from crashing over a long-term measurement. Overall, the peak current is maintained at around 7 nA and -10 nA, indicating its capability in long-term and stable operation. Moreover, the output power densities of the TENG with different external loads is studied. The peak values of both voltage and current signals are recorded in Figure 4-12b. The output voltage increases while the current decreases as the external load increases from 1 kΩ to 1000 MΩ. Also, the corresponding peak power density is calculated and plotted in Figure 4-12c. The maximum peak power density of 10.2 μW/m^2 is observed at the external load of about 200 MΩ, indicating that this device could serve as a current source with a large internal resistance, which is beneficial for a high-impedance external circuit.

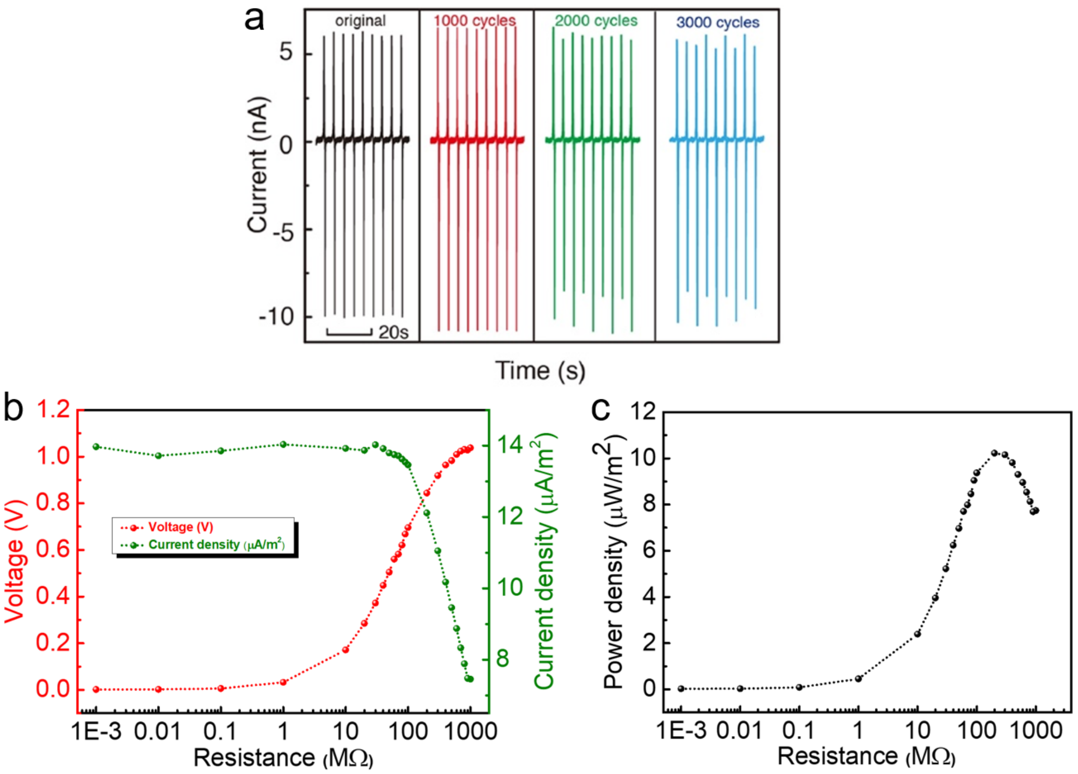

Figure 4-12. Measurements of the long-term performance and output power densities with different external loads. (a) Output signals before and after 1000, 2000, and 3000 working cycles. (b) Output voltage and current of the fiber-based TENG with different external loads. (c) The relationship between the output power density and external resistance.

4.4 Self-Adaptive Net Fabric for Self-Powered Touch Sensing

Owing to its superior flexibility and stretchability, the conductive SEBS fiber could be conformally adapted to regular or irregular surfaces, which is promising for constructing self-adaptive fabric for touch sensing applications on arbitrary surfaces to detect various activities. A preliminary test is carried out to examine the capability of conductive SEBS fiber-based TENG in maintaining mechanical energy harvesting and sensing performance under sudden strong impact and large deformation. As shown in Figure 4-13a, two ends of the fiber are fixed, and the fiber is straightened by a slight stretch. A sudden impact is applied to the fiber by a rapid foot stepping and the subsequent deformation occurs as the foot stepped down. The output signal during the stepping is recorded in Figure 4-13b. The first peak indicates the motion that the shoe contacts the fiber (step on), while the last peak indicates the step-off motion.

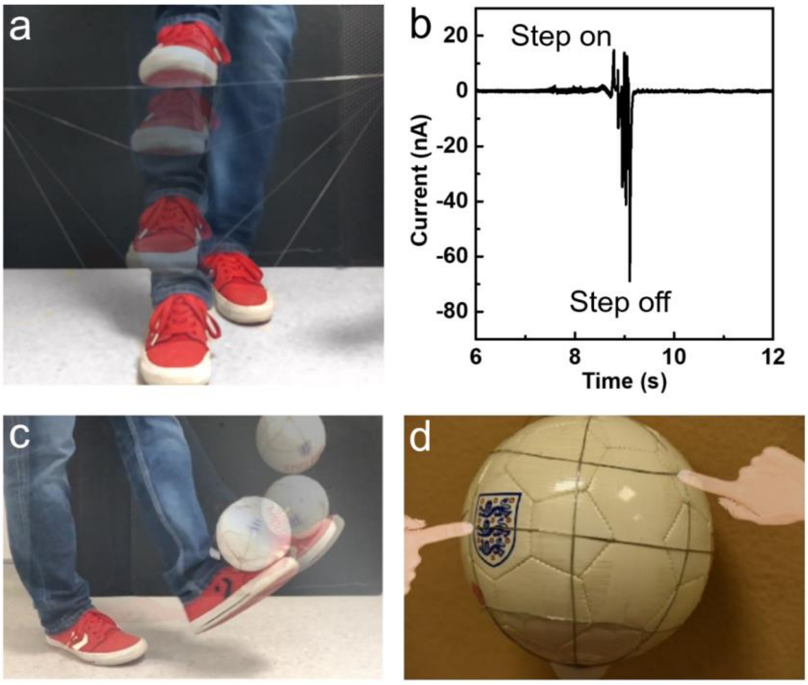

Figure 4-13. Applications of the stretchable SEBS fiber-based TENG. (a) The fiber-based TENG is tested under a sudden impact applied by foot. (b) The measured output signal when stepping on the fiber-based TENG. (c) Demonstration of the self-adaptive net fabric for self-powered sports performance monitoring. (d) Testing the self-adaptive net fabric by figure touches.

The test above reveals the TENG's feasibility in performing touch sensing while bearing high impact or deformation. For example, this flexible and stretchable TENG is quite suitable for self-powered sports performance monitoring by adapted to the surfaces of sports gears conformally and detecting the real-time motion. As displayed in Figure 4-13c, these conductive fibers could be applied to the curved surface of a football to build a net fabric and perform the contact point detection based on a spherical coordinate [229]. 6 fibers with a length of 26 cm are attached horizontally on the football surface to form longitude lines of 0° (360°), 60°, 120°, 180°, 240°, and 300°, while another 3 fibers form the latitude lines of 45°, 90° and 135°. Thus, each cross point of the fibers can be addressed as a coordinate point in the spherical coordinate system. As a proof of concept, the test is performed by finger touch instead of foot kick for a stable testing condition here, as shown in Figure 4-13d. Current signals are measured to detect and identify the touch point. As the conductive SEBS fibers are very sensitive to slight vibration, a special data processing method is adopted to improve the signal-to-noise ratio and avoid possible noise jamming. When a finger touches a point, current signals from all the longitude and latitude lines will be received. For each line, the maximum peak value of the measured signal and average peak value of the baseline when untouched are extracted. And then take the ratio of maximum peak value/baseline peak value as the line value (R_L). Thus, for each touch behavior, 9 R_L from the 9 fibers can be obtained. As the target is to detect which cross point is touched, the value of a cross point (R_p) is defined as the product of the two R_L from the two crossing lines. For instance, the detected value for point (60°, 90°) is the product of the values of the 60° longitude line and the 90° latitude lines, i.e., $R_p(\mathrm{lon}60°, \mathrm{lat}90°) = R_L(\mathrm{lon}60°) * R_L(\mathrm{lat}90°)$. Hence, for each touch, 18 detected values (R_p) could be obtained for the 18 cross points, respectively. To make the sensing results more intuitively, a spherical coordinate system framework including all the 18 cross points is constructed to visualize the entire sensing net fabric, as demonstrated in Figure 4-14. The 18 R_p values are assigned to the corresponding positions on the spherical coordinate, and the minimum detected value is assigned to the rest coordinate points on the sphere. Then the coordinate sphere is colored depending on the coordinate point value. If both coordinate line values (R_L) of a point are high enough, i.e. R_p is much higher than other points, the upright area of the coordinate point will be highlighted, indicating that this cross point is pressed. The reason that the supporting lines on the constructed spherical coordinate framework are more than the tested fibers is that the sphere surface will be tangled when the supporting longitude and latitude lines are removed. Hence, they are just kept here and assigned a minimum value. As a result, three points, (0°, 45°), (60°, 90°), and (120°, 135°), are touched successively and the measured signals are visualized in Figure 4-14a-c, respectively, which matches well with the touch behaviors. This application exhibits the wide potential of this self-powered touch sensing fabric in contact point positioning and large area motion tracking.

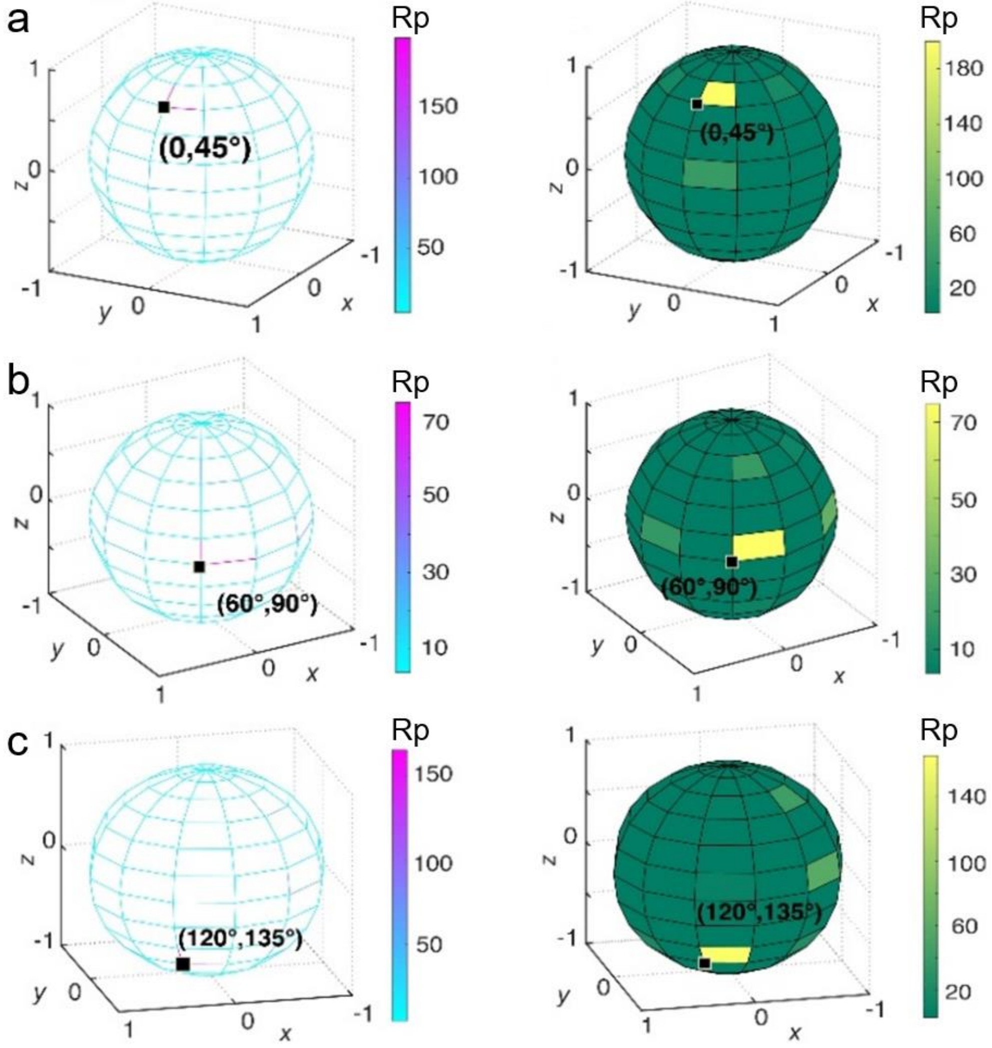

Figure 4-14. Contact point detection based on a spherical coordinate. The spherical framework is reconstructed according to the 18 cross points and the measured signals from the touch sensing net fabric. When a cross point is pressed, the corresponding signal is visualized on the spherical coordinates. (a) Point (0°, 45°) is pressed. (b) Point (60°, 90°) is pressed. (c) Point (120°, 135°) is pressed. Color bars: Calculated cross point value (Rp), which is the product of the two crossing line values. For example: $R_p(lon60°, lat90°) = R_L(lon60°) * R_L(lat90°)$.

4.5 Summary

In summary, a two-step soluble-core thermal drawing process is developed for thermally drawing low modulus and low viscosity thermoplastic materials. Super-elastic fibers with different architectures are thus obtained and ultra-stretchable conductive SEBS fibers are further achieved by injecting liquid metal into hollow SEBS fibers. The conductive SEBS fiber offers outstanding stretchability and flexibility which maintains excellent conductivity even under 1900% strain or sudden hit and stretched by a 1.5 kg load freefalling from a height of 1 meter. Based on the triboelectrification effect and electrostatic induction, stretchable and flexible fiber-based TENGs are fabricated. The working mechanism is clarified and verified by both simulation and experimental measurements. Owing to the superior mechanical properties of the conductive SEBS fiber, this TENG could work normally under a sudden impact and high deformation. Finally, a self-powered touch sensing net fabric is built and adapted to the football surface to realize sports performance monitoring. The compatibility of is fabrication process with thermoplastic elastomers and the demonstration of the touch sensing fabric revealing their broad prospects for self-powered smart fabric and large-scale soft device integration. Nevertheless, there are still some limitations of the conductive SEBS fiber based TENG. The output current signal is relatively small, which may result in a limited signal to noise ratio in some application scenarios. Creating surface structures on the fiber surface could be an effective method to improve its performance, which will be discussed in the next chapter. Moreover, although the ends of the SEBS fiber have been carefully sealed and the fiber has been tested under high impact, the leakage of the liquid metal is always a risk for practical use. Further improvement could be made by developing a highly stretchable and conductive electrode instead of using the liquid electrode.

Chapter 5 Functional Fibers with Designable Surface Pattern via Direct Imprinting in Thermal Drawing

5.1 Introduction

In Chapter 4, a conductive SEBS fiber is developed via the thermal drawing process. And fiber-based TENGs are further fabricated and applied in constructing self-powered touch sensing fabric, showing a broad prospect in motion tracking and electronic skin. For such a self-powered touch sensor based on TENGs, a higher output signal could always lead to a higher sensitivity and signal-to-noise ratio. Thus, further efforts should be made for enhancing the performance of TENG. As discussed in Section 2.2.2, creating surface patterns on dielectric materials is universal and effective to enhance the performance of TENG. Besides, creating micro/nanostructures on fiber surface could enable many other unique properties onto the current functional fibers to extend their application fields, such as hydrophobic surface, coloration, tunable plasmonic behavior, and antimicrobial. Therefore, thermally drawing surface patterned fibers is indispensable for both realizing high-performance wearable TENG and extending the application fields of functional fibers.

However, by far only surface grooves along the fiber's axial direction were achieved [158-161]. To create high-resolution complex surface patterns in arbitrary directions, two fundamental challenges must be addressed. The first challenge is the structure elongation when a preform is drawn into a fiber. Typically, the resulting fiber is 2 to 6 orders of magnitude longer than the original preform. Although a well-controlled elongation ensures the uniformity along the entire fiber, it in turn stretches all the pre-defined structures on the preform by the same orders of magnitude along the axial direction. This is the main reason that all the reported surface patterns to date are aligned along the axial direction. The other challenge is the reflow of heated thermoplastic materials driven by surface tension [93], which leads to the distortion of the desired structures, thus resulting in low pattern resolution. F. Sorin, et al, have studied the reflow behavior and improved the pattern resolution to sub-micrometer by introducing a polymer interface with low surface tension [161]. However, choosing two different polymers to construct low surface tension interface not only largely restricts the selection of applicable materials, but also reduces the compatibility with other inner functional structures, which essentially obstructs the further development and applications of surface patterned fibers. Therefore, an effective yet universal approach to creating high-resolution complex micro/nanostructure beyond axial direction on thermally drawn fibers is vastly demanded.

This chapter will propose and demonstrate direct imprinting in thermal drawing (DITD) technique to address the above-mentioned challenges and achieve high-resolution designer micro/nanostructures on fiber surface with good compatibility on both materials and inner structures. This technique is based on the fact that the thermoplastic materials can be re-shaped during the thermal drawing process by directly imprinting high-resolution patterns in arbitrary directions on the soft fiber surface after the elongation [336-339], while the imprinted fiber can be cooled down rapidly to significantly restrain reflow. Using this technique, a wide variety of regular and irregular surface patterns are created on hundreds-meter long fibers with different materials and inner structures, illustrating the high stability, high yield, and good compatibility of the DITD technique. To understand this process, temperature distribution during the DITD process is studied by simulation and verified by experimental results. Moreover, key process parameters such as resolution, repeatability, and depth control are examined, exhibiting the feature size as small as tens of nanometers. Plasmonic behavior of nanopatterned fibers is investigated to demonstrate their potential in optical applications. Finally, to reveal this technique’s extensive application prospect and good compatibility with functional fibers, TENGs are fabricated based on fibers with both flat and patterned surfaces. The output signals show that the surface pattern can significantly enhance TENG’s performance. Furthermore, a self-powered wearable multipoint touch sensing fabric is successfully built based on the patterned TENG fibers, indicating the DITD technique's promising future in wearable multifunctional fiber-based devices and smart fabrics.

5.2 Fabrication of Various Surface Patterns on Fibers with Different Materials via DITD Process

5.2.1 Introduction of the DITD Process

The DITD process is performed on a fiber drawing tower built by SG Controls Ltd. Compared to the traditional thermal drawing process, the DITD process introduces a pair of rollers with desired surface structures as templates to thermally imprint surface patterns onto the drawn fiber. The fabrication process of a PVDF fiber patterned with two-dimensional (2D) microdot array will be introduced here as a general example of DITD technique.

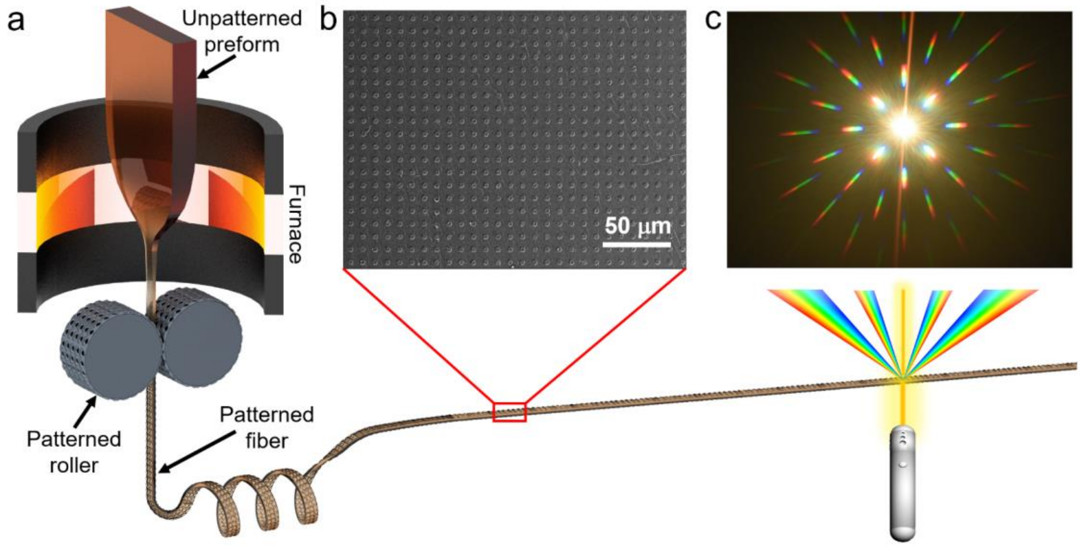

Figure 5-1. DITD process for producing 2D microdot array on fiber surface. (a) Schematic of the DITD process. (b) SEM image of 2D microdot array on fiber surface. (c) Interference pattern when the fiber is illuminated by a white supercontinuum laser.

As sketched in Figure 5-1a, an unpatterned PVDF preform with the width, length, and thickness of 30 mm, 200 mm, and 12 mm, respectively, is fixed on top of the tower and slowly fed into a furnace with two heating zones at a speed of 1 mm/min. The upper heating zone is set at 200 °C for preheating, while the lower zone is set at

380 °C to soften the perform. The softened preform in the lower zone is continuously drawn down at a speed of 1 m/min. Then a neck-down region is formed in the lower heating zone as the softened preform is scaled down cross-sectionally and elongated into fiber because of fast drawing and slow feeding. A pair of surface patterned rollers are fixed on a pair of 3-axis stages (Thorlabs) and located at both sides of the fiber right below the neck-down region. The positions of the two rollers can be adjusted by the two stages to make sure the fiber pressed between the two rollers under a pressure around 6 MPa. Since the temperature of the neck-down region is still high enough to reshape the fiber, an exactly inverted surface pattern can be created on both sides of the drawn fiber after being directly pressed by the patterned rollers acting as templates. Meanwhile, the patterned fiber cools down rapidly because of the physical contact with the rollers, which greatly restricts subsequent distortion caused by reflow [93]. While the fiber is being drawn down continuously, the rollers keep rotating to imprint patterns onto fiber surfaces smoothly and repeatedly, creating a continuous surface pattern on the entire length of the drawn fiber. The drawn fiber is finally collected on a capstan.

In the process above, a polyethylene terephthalate (PET)-based 2D micro-hole array is attached to both rollers. As a result, PVDF fiber with the inverted surface pattern, 2D microdot array, on both sides is successfully fabricated via the DITD technique, which is verified by SEM in Figure 5-1b. This surface pattern is further tested under illumination by white supercontinuum laser as the 2D microdot array served as a 2D optical grating. After the white supercontinuum laser propagated through the patterned PVDF fiber, the laser is split into several beams in the spatial domain and laser with different wavelengths is also separated in different angles in the presence of the 2D optical grating. Thus, a sharp 2D interference pattern with “rainbow” colors is formed and captured in Figure 5-1c, proving the high quality of the periodic surface pattern on PVDF fiber.

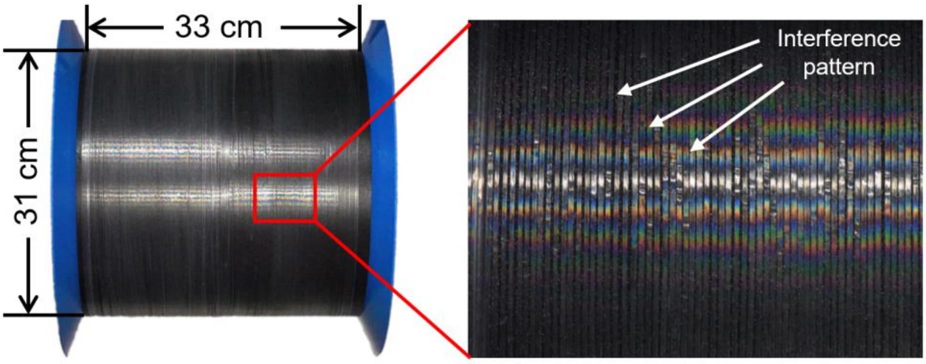

Figure 5-2. 300-meter long fully patterned fiber collected on a cylindrical bobbin. The enlarged photograph shows the interference pattern on the fiber-wrapped bobbin.

It is worth mentioning that the DITD technique is a high throughput process with excellent reliability to produce a single continuous patterned fiber. As exhibited in Figure 5-2, a 300-meter long fiber with 2D dot array fully covered on both sides is fabricated and collected on a bobbin. The interference pattern can be observed on the whole capstan, indicating that the surface pattern is created continuously on the entire surface of the 300-meter long fiber.

5.2.2 Creating Various Surface Patterns on Fibers

The surface pattern of the resulting fiber is determined by the patterned rollers in the DITD process. The surface patterned rollers can be prepared either by directly modifying the roller surface or simply attaching a patterned flexible substrate on the roller surface. Therefore, almost all of the processes for fabricating micro/nanostructure such as self-assembly [340], lithography [341, 342], focused ion beam (FIB) etching [343], and laser machining [344, 345] could be used for preparing the patterned rollers, which enables the DITD technique to fabricate fibers with a wide variety of surface patterns.

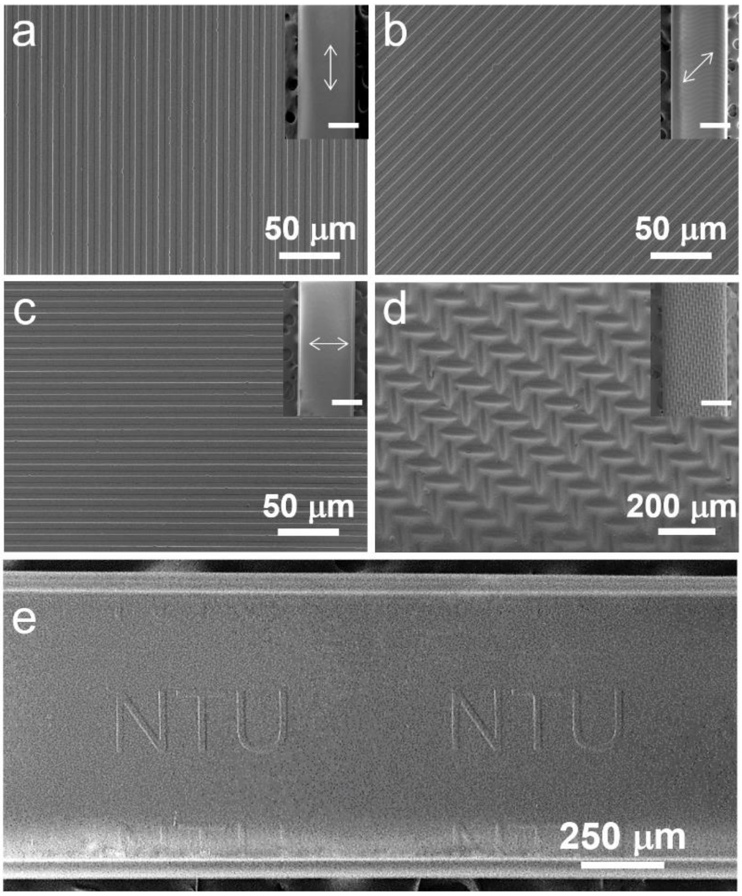

Figure 5-3. Various Surface Patterns created on Fibers. (a-c) Parallel lines with both linewidth and spacing of 5 µm created in different directions (parallel, perpendicular, and 45-degree angle to the fiber's axial direction). Insets: overviews of the patterned fibers. The double arrows represent the groove directions (scale bar, 500 µm). (d) Surface pattern with nonuniform depth. Inset scale bar, 500 µm. (e) Fiber patterned with customized letters "NTU".

As a preliminary demonstration, a Chrome (Cr) mask which frequently used in lithography is firstly manufactured with various micro patterns, Then the mask is covered by a piece of PEI film and heated to 240 °C under vacuum for 30 mins. The inverted patterns are thus transferred to PEI film after cooling down and peeled off. Finally, the patterned PEI film is cut and attached on the surfaces of the rollers to serve as the templates. Based on these templates with different surface patterns, a series of fibers with various surface patterns are fabricated under the same conditions via the DITD process. Firstly, parallel lines with both width and spacing of 5 µm in three directions (parallel, perpendicular, and 45-degree angle to the fiber's axial direction) are created on the surface of PVDF fibers, as shown in Figure 5-3a-c. The strict periodicity and sharp edges confirmed the high resolution of the surface patterns. Secondly, a more complex pattern (Figure 5-3d) with nonuniform depth is fabricated by changing the template to a 1000-mesh stainless steel screen. Insets of Figure 5-3a-d present the overview of the respective micropatterned fiber (all the scale bars in the insets are 500 μm). Further, the ability of imprinting in all directions and high resolution enables the DITD technique to produce fibers with arbitrarily designed surface pattern. As displayed in Figure 5-3e, customized letters "NTU" is successfully imprinted on the fiber surface.

5.2.3 Creating Surface Patterns on Fibers with Different Materials

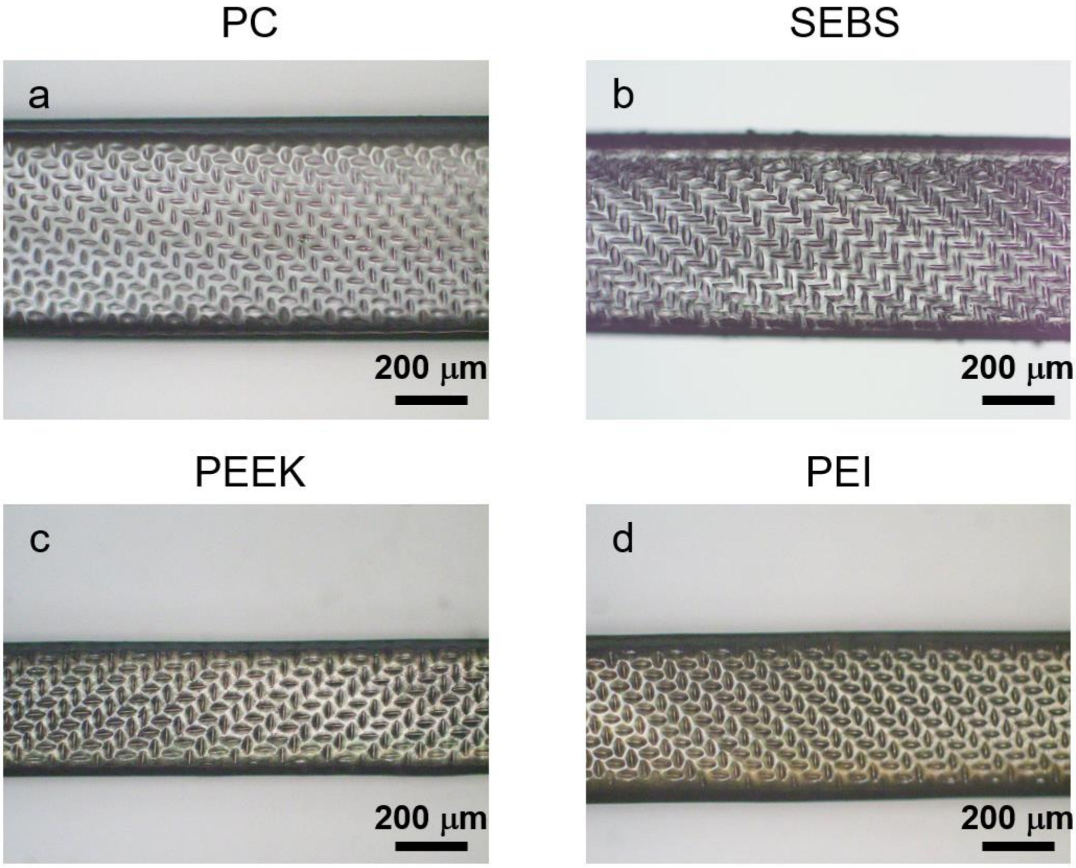

Figure 5-4. Surface patterns created on fibers with different materials.

Knowing that almost all the thermoplastic materials are applicable to the imprinting process, the DITD process is in principle compatible with all the thermoplastic materials employed in the thermal fiber drawing process, including amorphous polymers such as PC, PEI, cyclic olefin copolymer (COC), and polystyrene (PS), semicrystalline polymers such as polyether ether ketone (PEEK) and PVDF, and elastomers such as Santoprene and SEBS. As a verification, fibers drawn from PC, PEI, PEEK, and SEBS with the identical surface pattern are fabricated through the DITD process as shown in Figure 5-4.

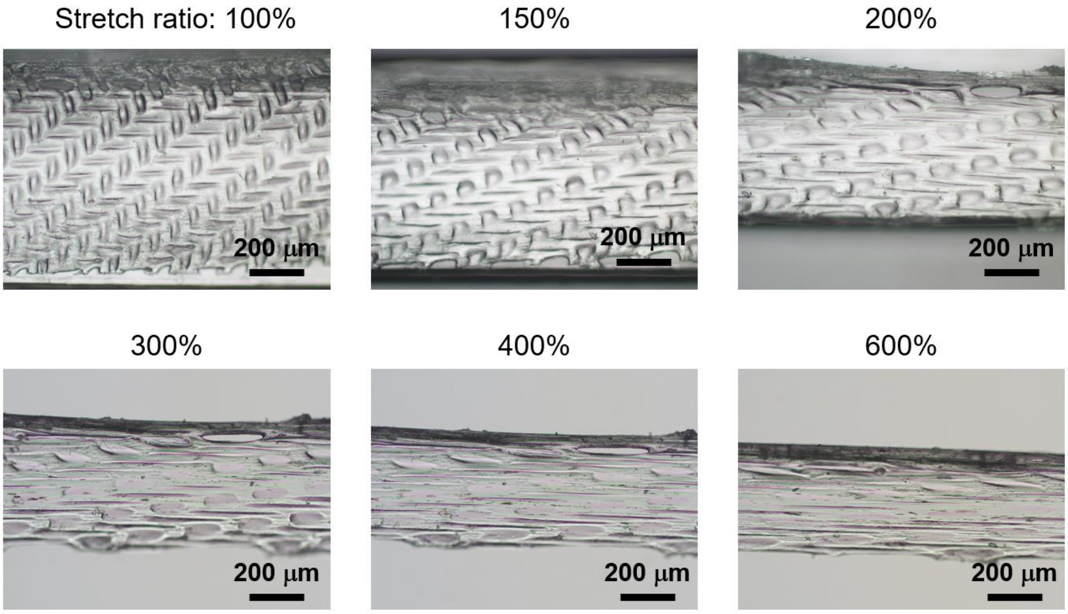

Figure 5-5. Surface patterned SEBS fiber under different stretch ratios.

Furthermore, the surface pattern does not influence the instinct properties of the materials. As shown in Figure 5-5, SEBS fiber with surface pattern fabricated above can preserve its superior flexibility as it is stretched to 600% of its original length without breaking. The high compatibility on materials selection offers the DITD technique great potentials in a wide range of applications.

5.3 Study of the Thermal Behavior and Flow Behavior during the DITD Process

Studying the thermal behavior and flow behavior of the fiber is crucial to gain a better understanding of the DITD process. According to the process introduction in Section 5.2.1, the DITD process can be treated as two consecutive processes: traditional thermal drawing process followed by surface pattern imprinting process. Since a number of previous works [346-348] have carried out in-depth studies of the thermal behavior and flow behavior during the thermal drawing process, this section will focus on the surface pattern imprinting process after the fiber is drawn out of the neck-down region.

5.3.1 Thermal Behavior during the Imprinting Process

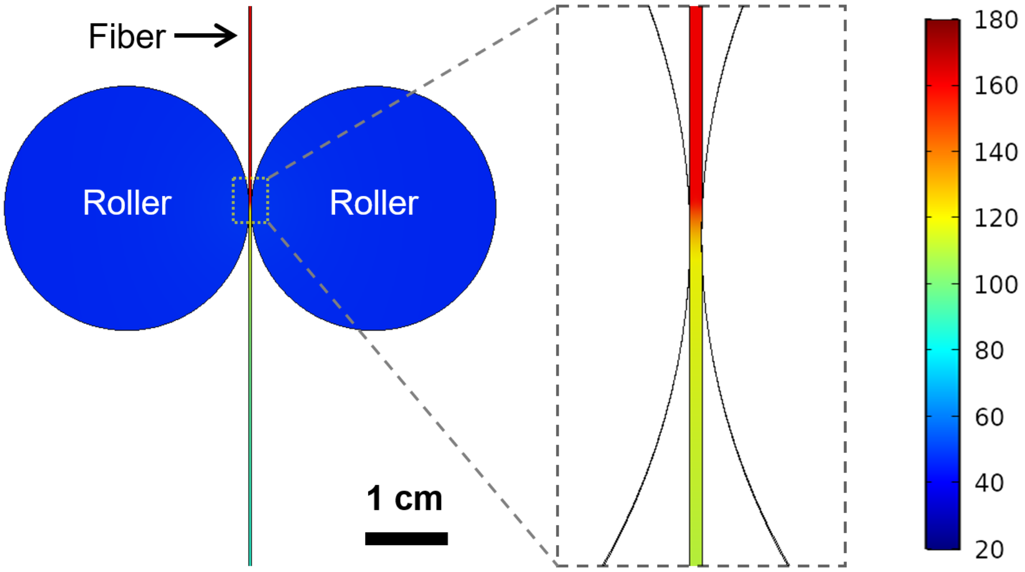

Figure 5-6. Simulated temperature distribution by setting fiber temperature to 160 °C before contacting rollers.

Finite element analysis is conducted by COMSOL to simulate heat transfer among fiber, rollers, and ambient air as well as thermal radiation of all surfaces. All the geometry and parameters are defined according to the actual sizes and materials used in the DITD process. Specifically, the width, length, and thickness of the fiber are 1 mm, 100 mm, and 0.3 mm, respectively. And the width and radius of the roller are 10 mm and 15 mm, respectively. The materials of the rollers and fiber are defined as "steel" and "PVDF", respectively, which are directly chosen from the build-in material database in COMSOL. Figure 5-6 shows the simulated temperature distribution by setting fiber temperature to 160 °C before contacting with the rollers.

And the temperature of the fiber drops rapidly to around 118 °C after being pressed by rollers, as shown in the enlarged area of Figure 5-6. The rapid temperature drop of the fiber during the contact is mainly caused by two factors. One factor is the thermal conductivity contrast between the roller and air. The roller used here is made of steel, whose thermal conductivity coefficient is around 30 W/m·K, which is about 3 orders of magnitude higher than that of air. Thus, the heat transfer between roller and fiber is much faster than that between roller and air under the same temperature difference. The other factor is the total heat capacity contrast between roller and fiber. During the contact, the fast heat transfer leads to a rapid temperature drop of the fiber because of its low heat capacity, while the temperature of the roller only increases a little because of the high heat capacity, which helps maintain a high temperature difference. Additionally, the large roller size could also help in dissipating heat form roller to air. Thus, the temperature of the roller could be maintained at a relatively low value by absorbing heat from the fiber and dissipating heat to air simultaneously.

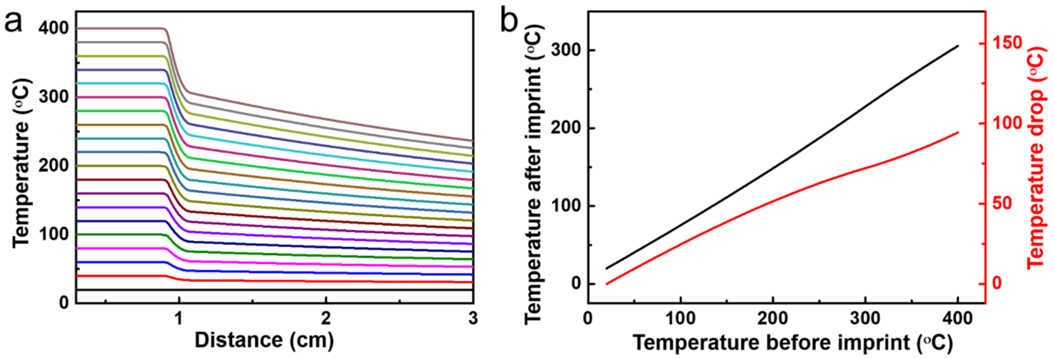

Figure 5-7. (a) Simulated temperature distribution along fibers under different drawing temperatures. Rollers are placed at 1 cm. (b) Simulated fiber temperature after the imprinting process under different drawing temperatures (black line) and simulated temperature drop under different drawing temperatures (red line).

Considering that the drawing temperature varied with different materials, a parameter sweep is further conducted to obtain the temperature distribution along the fiber under different drawing temperatures. To simplify the simulation, the temperature of fiber is assumed to be constant before contacting rollers. The temperature as a function of the distance from the neck-down region is plotted in Figure 5-7a. A rapid temperature drop under all drawing temperatures is observed at the distance of 1 cm, which is the position of the rollers in the geometry model. At a larger distance, the temperature keeps decreasing as the fiber leaves rollers and is drawn downward. The smaller curve slops after the fiber left the rollers indicate that the thermal contact between fiber and rollers dominates the heat transfer in the imprinting process. Additionally, the higher the drawing temperature used, the more the temperature drops when being pressed by rollers. To show the trend more clearly, the temperature drop of the fiber being cooled down by the rollers under different drawing temperature is plotted in Figure 5-7b.

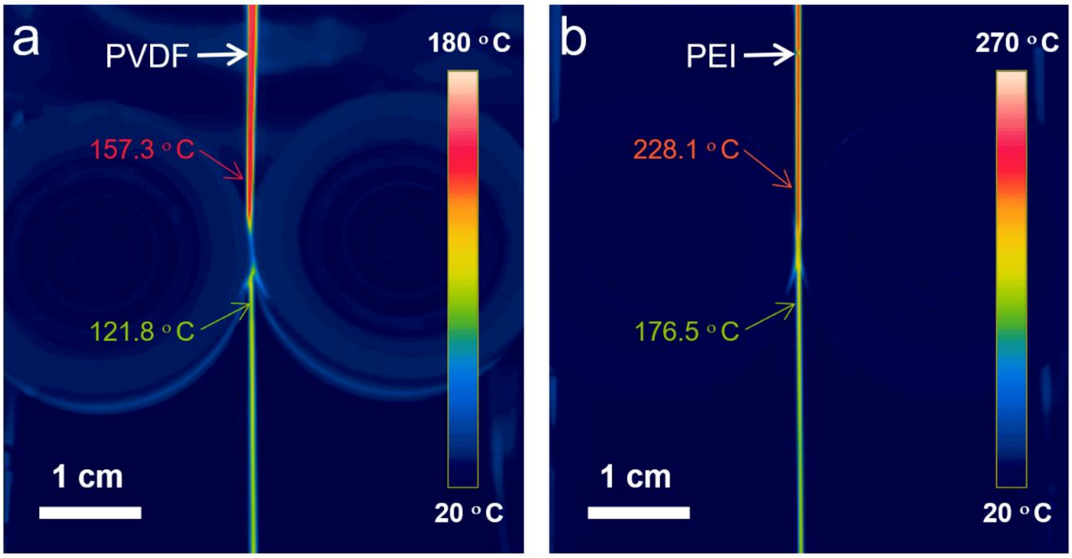

Figure 5-8. Thermal images of (a) PVDF fiber and (b) PEI fiber during the DITD process.

To verify the simulation results, thermal images of PVDF and PEI are captured by a thermal camera (FLIR T540) during the DITD process, as shown in Figure 5-8. The observed temperature distribution in Figure 5-8a matches with the simulated results in Figure 5-6 very well. And the temperature distribution of PEI fiber in Figure 5-8b follows a similar trend with the simulated temperature distribution shown in Figure 5-7a. Also, a temperature drop of 35.5 °C and 51.6 °C is observed after PVDF and PEI fiber is pressed by rollers, respectively.

5.3.2 Flow Behavior during the Imprinting Process

The imprinting process could be considered as a pattern transferred from the template to the fiber surface. Hence, the ultimate resolution of the imprinted pattern is mainly decided by the template. A high-fidelity pattern transfer process ensures the surface pattern on the fiber reaches a resolution as high as the template. To achieve this, understanding the flow behavior during the imprinting process is crucial. Based on the thermal simulation and experimental results above, the thermal imprinting process can be divided into two phases for a more detailed discussion about the flow behavior.

Phase 1: cavity-fill process

Phase 1 is the surface pattern creating by pressing the template to high-temperature fiber, i.e., the polymer on fiber surface fills into the cavities on the template to form an inverted pattern under pressure. This cavity-fill process determines if high-fidelity surface patterns could be created on fibers under high temperature.

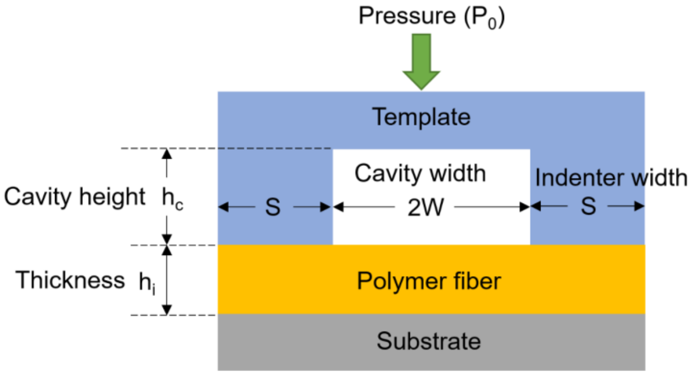

Figure 5-9. A simplified model for the flow behavior discussion of the imprint process.

As sketched in Figure 5-9, the discussion on the flow behavior will base on a simplified model, where a template with a rectangular cavity is pressed to a polymer fiber on a planar hard substrate. This rectangular cavity is the unit template structure of both the striped pattern in this work and many other works in film-based nanoimprint lithography [336, 338, 349].

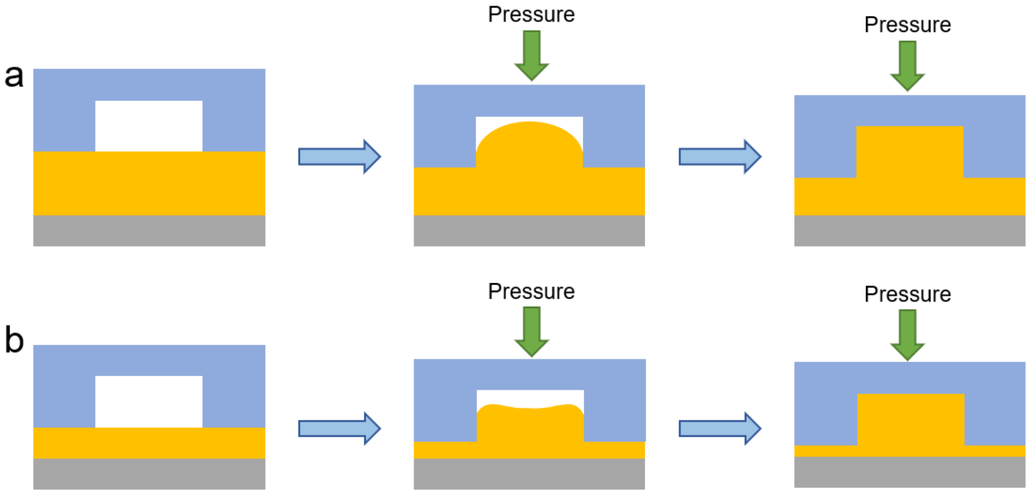

Figure 5-10. Two flow modes when the polymer fills into the cavity. (a) Single peak formed. (b) Double peaks formed.

There are two possible flow modes as the indenter is pressed downward and the polymer flows into the cavity [336, 338]. One is a single polymer peak formed in the middle of the cavity (Figure 5-10a). In the case that the polymer fiber is thick, the polymer near the sidewall will flow downward driven by the downward shearing force from the sidewall, which has less influence on the polymer in the middle of the cavity. Thus, a peak in the middle is formed. The other flow mode is double polymer peaks formed near the cavity sidewalls corresponding to Figure 5-10b. This mode occurs when the polymer fiber is not thick enough. The polymer between the indenter and substrate will form a recognizable lateral flow towards the cavity because of the limited space. This lateral flow will slow down after entering the cavity as it is driven by the shear near the indenter. Hence, a larger amount of polymer will stay near the two sidewalls, forming the double polymer peaks.

H. Rowland et al. put forward a criterion to predict which flow mode will occur during imprinting based on their simulation results [336]. They found that a single polymer peak would occur when the ratio of cavity half-width (W) to initial film thickness (h_i) is smaller than 1.2. Otherwise, the double polymer peak will be formed. This criterion agrees well with other reported works except for small variations around the ratio value of 1.2.

Here in the DITD process, the thickness of the drawn fibers is mostly around 360 μm. The cavity widths (2W) used in the template are ranging from 300 nm to 20 μm (in the next section). Considering that the fiber may be patterned on both sides, h_i is taken as 180 μm. Thus, the ratios of W/hi in this work are ranging from 8.3E-4 to 0.06, which is much smaller than 1.2. Thus, it could be predicted that a single polymer peak will occur in the imprint process (Figure 5-10a). In fact, the thickness of the fiber produced via the thermal drawing process is generally larger than 100 μm. Therefore, the flow mode will always be single peak mode in the DITD process except for producing micro/nanopatterned fibers with the pattern size larger than the fiber thickness, which is hundreds of micrometers.

Further experiments are conducted to verify that this model and criterion is applicable to the imprint process. A template with a square cavity as the unit structure is used. And both the cavity width (2W) and cavity height (h_c) are 20 μm. Two kinds of fibers are drawn under the same condition and imprinted by the same template except for different applied pressure as shown in Figure 5-11. As the lower pressure will lead to a longer time for the polymer to fully fill the cavity, the middle state of polymer flow in the imprint process could thus be observed as the contact time between roller and fiber is shorter than the needed time to fully fill the polymer. A single peak mode is exhibited in Figure 5-11a, which agrees well with the analysis above.

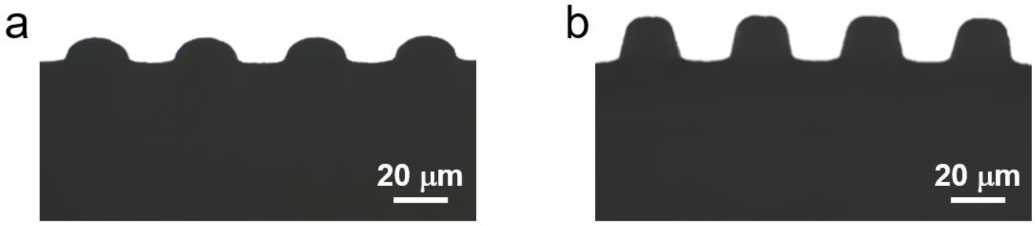

Figure 5-11. Experimental verification of the single peak flow mode during cavity-fill process. (a) Patterned fiber drawn under low imprint pressure (~6 MPa), showing the middle state of the polymer filling into the cavity. (b) Patterned fiber drawn under high imprint pressure (~12 MPa).

Additionally, Reynolds number ($Re = \rho uD/\eta$) should be examined to decide the flow pattern (laminar flow or turbulence flow). In the expression, ρ is the density of the polymer, u is the flow speed, D is the width of the cavity (2W) in this case, and η is the viscosity of the polymer. In the DITD process, the employed polymer is always compatible with the thermal drawing process. Thus, the viscosity range is 10^4 Pa·s to 10^8 Pa·s. For micro/nanopatterns, 2W is ranging from 10^{-8} m to 10^{-4} m. And polymer density could be estimated at the level of 10^3 kg/m^3. Thus, the value of $\rho D/\eta$ should be ranging from 10^{-5} s/m to 10^{-14} s/m, indicating a very small Reynolds number (much smaller than 1). Typically, the laminar flow occurs when Re is below 2000 [350]. Thus, the flow pattern in the imprint process can be decided as laminar flow.

Based on the discussion above, the polymer flow behavior can be inferred: the polymer will flow into the cavity in a laminar pattern and form a single peak in the middle of the cavity and no obvious literal could be observed. It is worth nothing to mention that for an independent nanoimprinting process, regardless of the flow mode and flow pattern, the cavity-filling under pressure could always be completed as long as the given fill time is long enough, leading to a high-fidelity pattern transfer. However, in the DITD process, the imprint process is combined with the thermal drawing process. As the fiber is drawing down continuously during the DITD process, each point on the fiber surface only contacts with the template for a limited time. If the contact time is not long enough for the polymer filling into the cavity of the template, the polymer will not be able to fully fill the cavity in the template, resulting in a heavily distorted pattern, like the case shown in Figure 5-11a. Therefore, to achieve a high-fidelity pattern transfer, the fill time should be smaller than the contact time.

The flow speed as well as the fill time could be estimated according to the flow behavior during the cavity-fill process. Assumptions are made that the polymer is incompressible, and the laminar flow is steady and in parallel with the sidewalls of the cavity. Thus, it follows the continuity equation $\partial u/\partial x = 0$ (x is the direction is perpendicular to the sidewalls.). Applying the boundary conditions as assumed above to the Navier–Stokes equations in fluid mechanics [351], the character flow velocity (V) can be obtained as follows.

$$V = D^2 P/3\eta L \tag{7}$$

where D is the half cavity width (W), L is the character distance, and P is the pressure difference between the character distance. In this model, L is taken as cavity height (h_c), and P as the pressure imposed on the polymer through the indenter ($P = P_0\frac{W+S}{S}$). Thus, the character flow velocity can be expressed as follows.

$$V = P_0(2W)^2(S+W)/12\eta h_c S \tag{8}$$

Also, the character fill time for polymer filling can be estimated by taking hc as the character distance.

$$t = h_c/V = 12\eta S h_c^2/P_0(2W)^2(S+W) \tag{9}$$

Where η is the viscosity, S is the indenter with, h_c is the depth of the cavity, and P_0 is imprinting pressure. Here, the template used in Figure 5-3a is taken as an example, where S, W, and h_c are $2.5*10^{-6}$ m, $2.5*10^{-6}$ m, and $1*10^{-7}$ m, respectively. P_0 is estimated to be 5.7 MPa while a typical viscosity of 10^6 Pa·s is used. And thus, the character flows velocity and fill time can be estimated to be $2.38*10^{-4}$ m/s and 0.42 ms, respectively. This fill time is much shorter than the estimated contact time of 50 ms, which largely depends on the drawing speed. Therefore, the cavity-fill process can be completed in this DITD process.

Phase 2: cooling down process

Phase 2 is the cooling down of the patterned fiber when contacting rollers. This cooling down process will help to hinder the reflow deformation and maintain the pattern created in Phase 1 after the patterned surface is separated from the templates. According to Figure 5-7b, it can be found that during the contact, the rollers will decrease the fiber's temperature by more than 35 °C in general as the commonly used materials in fiber drawing are always drawn above 150 °C. For semicrystalline polymers such as PVDF and PEEK, such a significant temperature drop will solidify them immediately as the relatively strong intermolecular forces will prevent them from softening below the melting temperature [352]. Hence, the reflow should be negligible after being cooled down by the rollers. While for most amorphous materials such as PC and PEI, the temperature will directly drop below their glass transition temperature (T_g) after passing through the rollers, thus reflow is also restricted. Only for materials with a relatively low T_g such as PS, the temperature may stay higher than their Tg after being separated from rollers. Then, the characteristic reflow time can be estimated for a periodic surface pattern which is defined as $\tau = \lambda\eta/\pi\gamma$ [161], where λ is the period and γ is surface tension. The viscosity will significantly increase when temperature decreases, e.g., the viscosity of PS will increase by 3 orders of magnitude when the temperature drops from 170 °C to 130 °C [353]. Here PS's viscosity and surface tension are taken as 10^8 Pa·s and 40 mN/m [354] at 130 °C. In the case of imprinting a pattern with a period of 10^{-6} m, the reflow time can be calculated to be 800 s. Noticing that fiber's temperature will keep decreasing under ambient air after being separated with rollers (Figure 5-7a), PS's temperature will drop below T_g in few seconds, which is much shorter than the reflow time of 800 s. Thus, the reflow during phase 2 is negligible and the surface pattern created on fibers during phase 1 could be well maintained.

Combining phase 1 and phase 2, conclusion can be made that this imprinting process during fiber drawing is in principle compatible with a wide range of materials and patterns. Additionally, the DITD process can always be adapted to a specific material or pattern by adjusting the drawing or imprinting parameters including temperature, pressure, and drawing speed.

5.4 Pattern Resolution, Repeatability Test, and Depth Control of the DITD Process

A resolution test pattern is designed to find the feature size of the DITD technique. The high-resolution template (Figure 5-12a) is fabricated by directly writing the pattern on PEI film under FIB (Zeiss Crossbeam 540) and an inverted pattern is created on the PVDF fiber surface, as shown in Figure 5-12b. A series of raised rectangular blocks with different sizes and orientations are created. As demonstrated in the enlarged SEM image in Figure 5-12b, the rectangular blocks with a length of 1.5 μm and a width of 500 nm basically maintained their shapes in all directions except for some distortions on edges, confirming a feature size in tens of nanometers. In view of the slight distortion in the template itself (Figure 5-12a), the actual resolution of the patterns should be better than it appears.

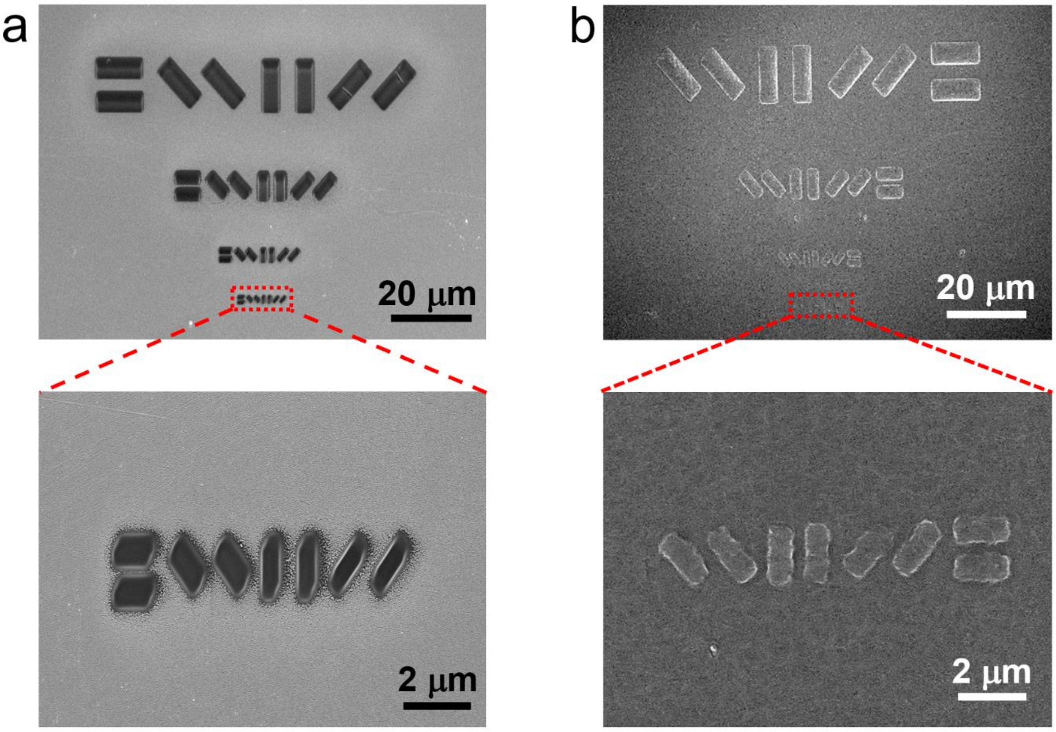

Figure 5-12. Resolution test pattern including rectangular blocks with different sizes and orientations. (a) The high-resolution template fabricated by FIB. (b) Transferred pattern on fiber surface.

Moreover, various nanopattern arrays are created on fibers to examine the stability and repeatability of the DITD technique, as presented in Figure 5-13a-c. Each array included a large amount of circular or rectangular nanoelements with a predesigned period. The round elements have the same radius of 150 nm but different pattern period (400 nm in Figure 5-13a and 800 nm in Figure 5-13b), while the rectangle element is 2.1 µm in length and 700 nm in width. All these nanoelements remains a regular shape, exhibiting a stable and repeatable high-fidelity pattern transfer process. Additionally, as the fibers' cross-section images show in Figure 5-13d, a set of similarly patterned fibers are fabricated with the pattern depths of 2 µm, 8 µm, and 20 µm, indicating that the pattern depth is also controllable. The high resolution, high stability, and controllable depth of the DITD technique will offer the surface patterned fibers extensive application areas.

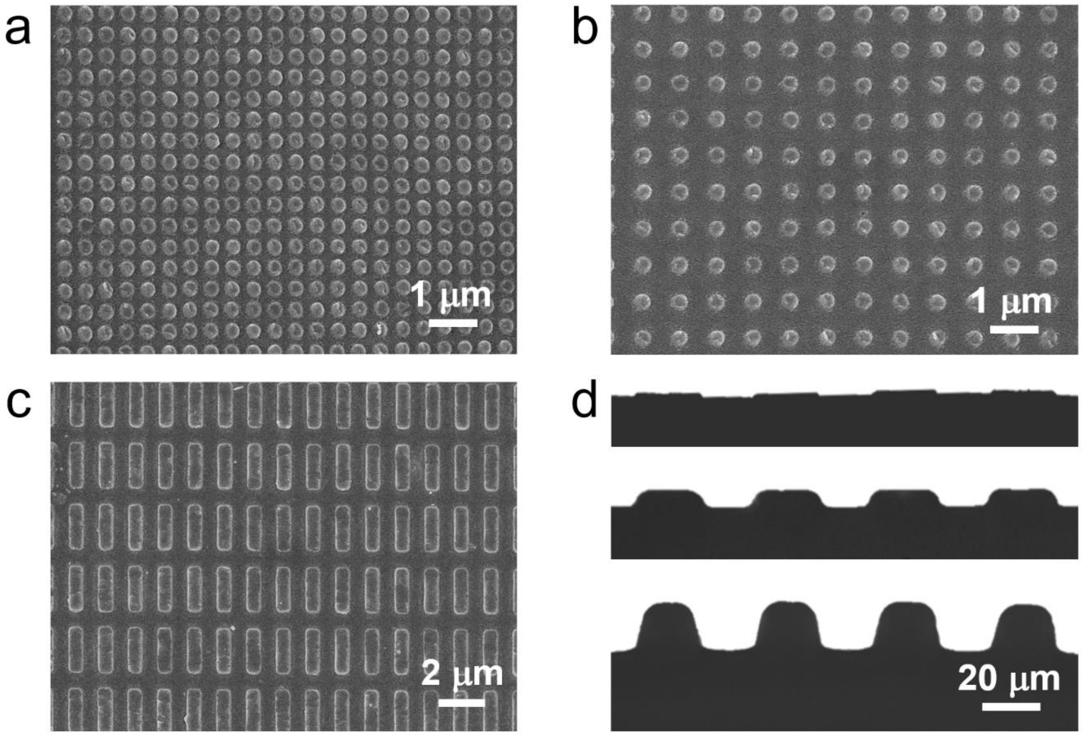

Figure 5-13. Repeatability Test, and Depth Control of the DITD Process. (a) Circular element array on fiber surface with radius and period of 150 nm and 400 nm. (b) Circular element array on fiber surface with radius and period of 150 nm and 800 nm. (c) Rectangular element array on fiber surface. The width and length of the rectangular rods are 700 nm and 2.1 μm. (d) Cross-sectional images of the patterned fibers, demonstrating the pattern depths of 2 μm, 8 μm, and 20 μm.

5.5 Applications of the Surface Patterned Fibers

5.5.1 Plasmonic Behavior of Nanopatterned Fibers

The ability to combine patterned fiber with plasmonics provides opportunities for a variety of applications of fibers, such as biosensing [355], bioimaging [356], and mode converters [357]. Here, the plasmonic behavior of the nanopatterned fibers (with a 30-nm-thick gold film deposited on top) is investigated using dark-field spectroscopy.

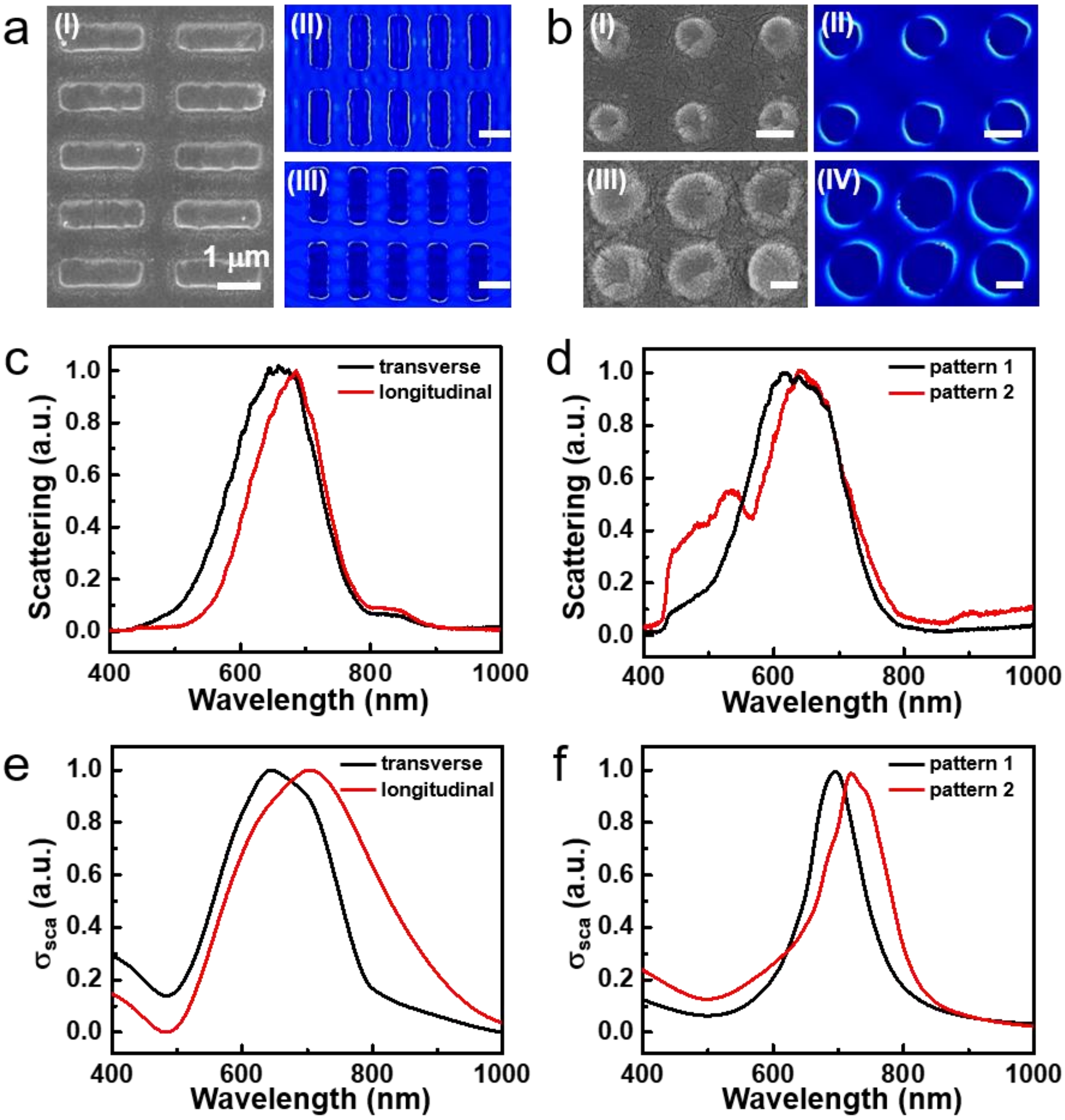

Figure 5-14. Plasmonic behavior of nanopatterned fibers. (a) (I) SEM image of the gold nanorods with an aspect ratio of 3 and the corresponding local electric field spatial distributions with (II) transverse and (III) longitudinal laser polarizations. Scale bars of (II) and (III): 1 µm. (b) SEM image and the corresponding local electric field spatial distributions of the gold cylinders with an array period of (I)(II) ≈ 800 nm and (III)(IV) ≈ 400 nm. Scale bars: (I)(II) 300 nm and (III)(IV) 150 nm. Dark-field scattering spectra of the gold nanorods (c) and gold cylinders (d). Simulated scattering cross-section of the gold nanorods (e) and gold cylinders (f).

To fabricate the nanopatterned fibers, a solid PVDF preform with the width, length, and thickness of 30 mm, 200 mm, and 12 mm, respectively, is prepared. The templates used in the DITD process are the same as those in the repeatability tests above. The resultant fiber has a width and thickness of around 1 mm and 400 µm, respectively. Then the drawn fibers are cut into segments with a length of 3 cm followed by a 30-nm-thick gold film deposition process on fiber surface under electron beam evaporation system (Edwards Auto 306) at a rate of 0.2 Å/s.

Finite-difference time-domain (FDTD) simulations are performed and the local electric field spatial distributions of the fiber plasmonic systems are shown in Figure 5-14a, b, which suggest that hot spots are stimulated. The gold pattern models in FDTD are generated from the SEM images as shown in Figure 5-14a$_{(I)}$, 5-14b$_{(I)}$, and 5-14b$_{(III)}$. For the nanorod structures indicated in Figure 5-14a$_{(I)}$, the measured dark-field scattering spectra of the plasmonic fiber with transverse (black line) and longitudinal (red line) laser polarizations are presented in Figure 5-14c. Two different resonances correspond to the transverse and longitudinal modes of the nanorods. For the nanocylinder arrays indicated in Figure 5-14b$_{(I)}$ and 5-14b$_{(III)}$, the dark-field scattering spectra with an incidence of non-polarized light are presented in Figure 5-14d. Pattern 1 and pattern 2 refer to Figure 5-14b$_{(I)}$ and 5-14b$_{(III)}$, respectively. Arrays with a smaller period (see Figure 5-14b$_{(IV)}$) possess longer plasmonic resonance which is induced by the near-field coupling. An additional peak near 520 nm is introduced by the edge roughness. The resulting scattering spectra are reproduced by the simulated scattering cross-sections, as presented in Figure 5-14e, f. The slight shift of the resonance peaks for both etched patterns when compared with the experimental characterizations can be attributed to the gold layer surface roughness and the minor edge defects, but a good agreement between the shapes of the measured scatterings and the simulated scattering cross-sections is obtained for different patterns.

5.5.2 TENGs Based on Micropatterned Multimaterial Fibers

Another feature of the DITD process is that it only modifies fiber's surface structure without influencing its inner structure. This makes it compatible with fibers owning different complex inner structures, predicting a bright future of multifunctional fibers [207]. TENG is an energy harvesting device that converts mechanical energy including sound, vibration, tide, and wind from surroundings to electricity. It has been widely studied for powering portable devices and self-powered sensing [358, 359].

Previous works [147, 148] have confirmed that introducing surface pattern can effectively enhance the output performance of TENG. Here, TENGs are assembled using surface patterned multimaterial fibers fabricated by the DITD technique.

The fabrication process begins with preparing a multimaterial PVDF-cladding/CPE-core preform. A rectangular hole is engraved in the center of a solid PVDF bar's surface. The width, length, and thickness of the PVDF bar is 30 mm, 200 mm, and 6 mm, respectively, while it is 16 mm, 120 mm, and 2 mm, respectively for the rectangular hole. CPE film is then cut and filled into the rectangular hole layer by layer. Subsequently, another solid PVDF bar with the width, length, and thickness of 30 mm, 200 mm, and 4 mm is put on the CPE filled PVDF bar and the whole structure is wrapped by thread seal tape. The preform preparation finishes after consolidating the wrapped preform in vacuum over under 175 °C for 2 hours.

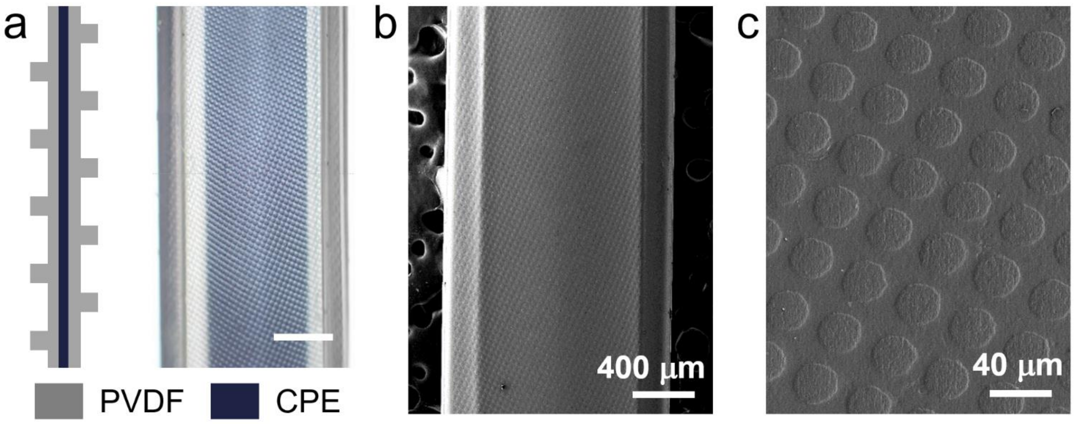

Figure 5-15. Patterned multimaterial fiber for TENG. (a) Sketch of the patterned fiber's cross-sectional structure (left) and optical image of fiber's top view (right, scale bar, 400 μm).). (b) SEM image of the patterned fiber. (c) Enlarged image of the surface pattern.

Patterned multimaterial fiber is thus fabricated from the preform prepared above via the DITD process. Figure 5-15a schematics the fiber's cross-sectional structure in fiber's axial direction (left) and displays the optical image of fiber's top view (right, scale bar, 400 μm). PVDF is selected as cladding material because of its high electronegativity [360], while carbon-loaded polyethylene (CPE) serves as the electrode. Both sides of the fiber are patterned with microcylinder array as the SEM images show in Figure 5-15b, c.

For comparison, the flat-surface fiber with the same dimension is also fabricated from the same preform via the traditional fiber drawing process. Both patterned fiber and flat fiber followed the same procedure to be assembled into fiber-based TENG. Both flat and patterned fibers are cut into short fibers with a length of 10 cm. One end of copper wire with a diameter of 50 μm is wrapped around one end of short fiber. Silver paste is then applied to connect copper wire and CPE exposed at the cross-section followed by drying under room temperature. The assembly of single-electrode fiber-based TENG is completed after a thin layer of PDMS is painted onto the surface of dried silver paste to encapsulate the connection area for a stable electrical contact.

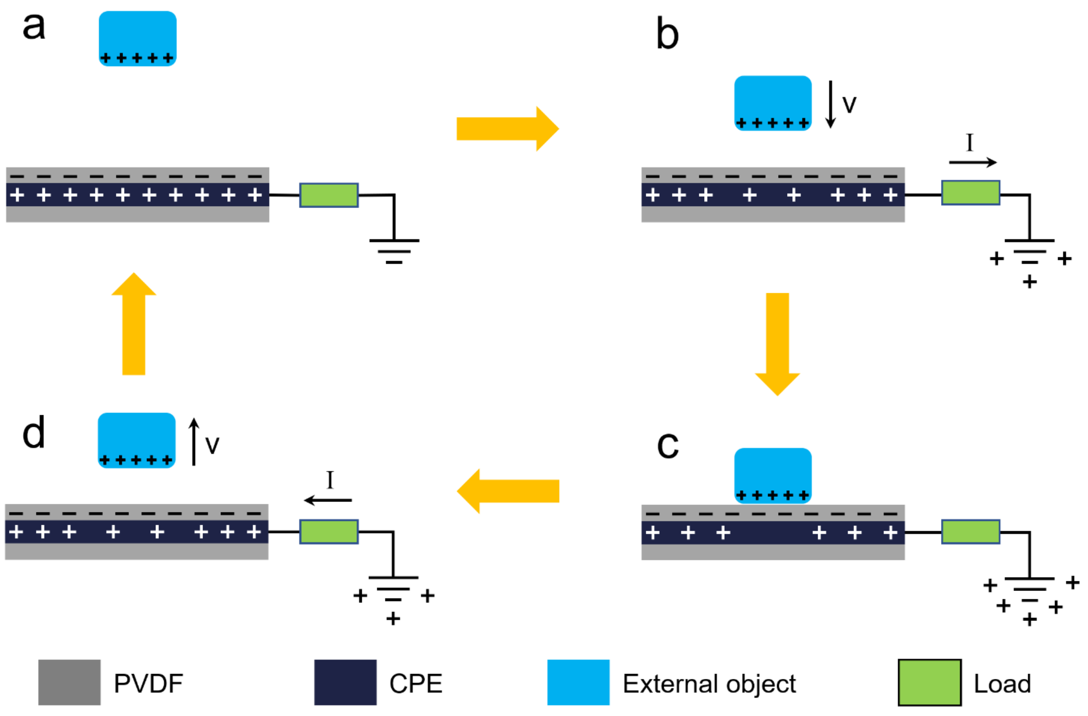

Figure 5-16. Working mechanism of the single-electrode TENG based on patterned multimaterial fiber.

The working mechanism of the single-electrode TENG is illustrated in Figure 5-16. When external object friction with PVDF, the electron on the surface of the external object will be transferred to the surface of PVDF because of its strong electronegativity. Thus, the surface of PVDF will bear negative charge while the external object bears positive charge. Positive charge will be generated on the CPE electrode inside PVDF fiber because of electrostatic induction, as shown in Supplementary Figure 5-16a. As the positively charged object is moving close to the PVDF fiber, the electrostatic potential of the electrode will increase, resulting in the positive charge in the electrode flow towards the ground through the load (Figure 5-

16b). When the object contacts the PVDF fiber, a large amount of positive charge will move to the ground as sketched in Figure 5-16c. Similarly, when the object moves away from the PVDF fiber, the positive charge will flow back to the electrode as the potential of electrode decreases, generating current from ground to the electrode (Figure 5-16d). Finally, the charge distribution will go back to the original state after the object moves far away from the PVDF fiber. As the external moves close to and away from the PVDF fiber repeatedly, an alternating current will flow through the load, converting mechanical energy into electricity.

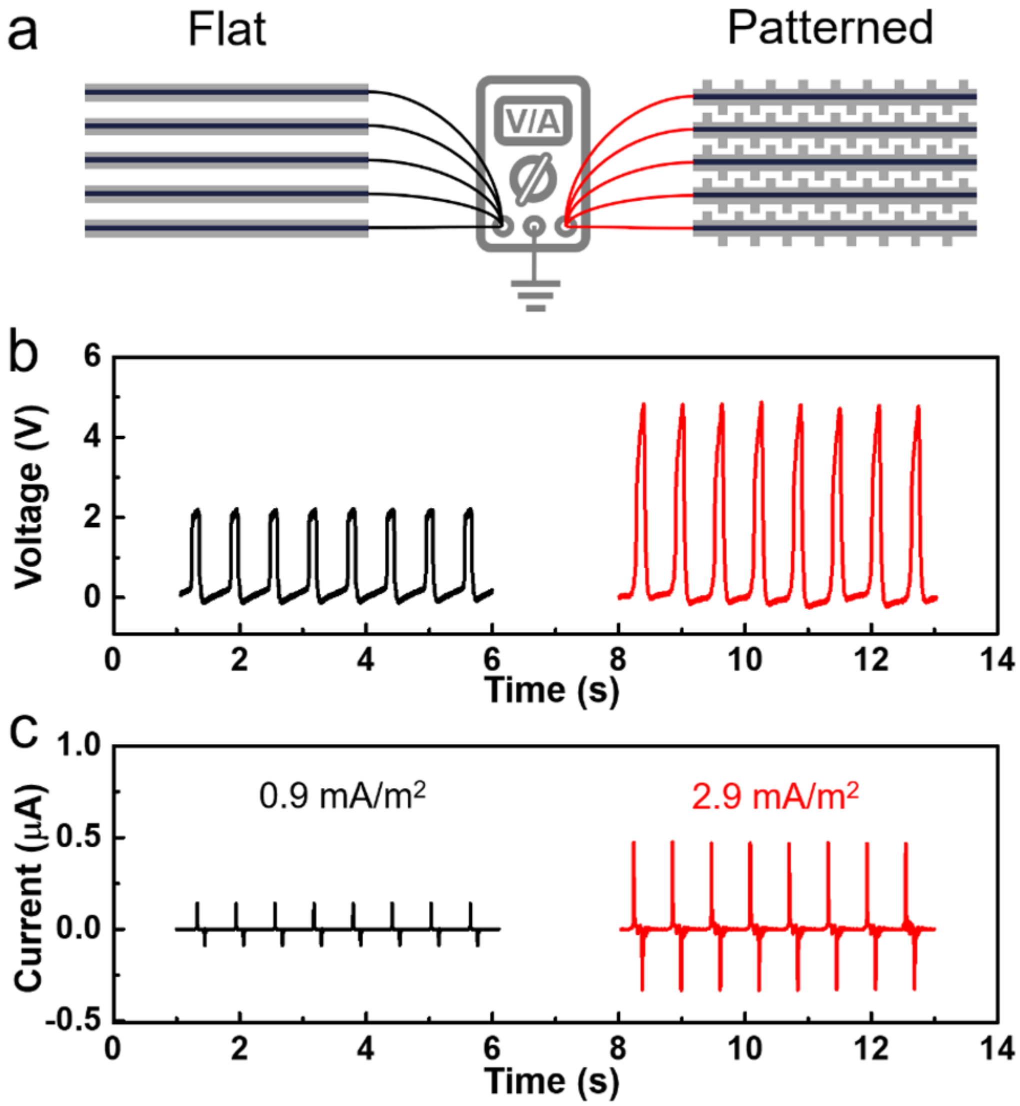

Figure 5-17. Output performance of both flat and patterned fiber-based TENGs. (a) Schematic of TENG's performance measurement. (b) Open-circuit voltage of both flat and patterned fiber-based TENGs. (c) Short-circuit current of both flat and patterned fiber-based TENGs.

The working mechanism discussed above indicates that the charge amount on the fiber surface is crucial to the performance of TENG. Creating a surface pattern has been proved to be an effective approach to increase the surface charge amount as the surface pattern could increase the surface charge density and enhance the friction [148, 149]. Therefore, the TENG based on surface patterned fibers is expected to offer better performance than that based on flat fibers. As sketched in Figure 5-17a, the output performance of the TENGs based on both flat and patterned fibers is measured by connecting 5 copper wires from 5 short fibers together. As plotted in Figure 5-17b, c, the open circuit peak voltage of TENG increases from 2.1 V to 4.8 V due to the presence of surface pattern, while the short circuit peak current of TENG increases from 160 nA to 500 nA, corresponding to the current density of 0.9 mA/m^2 and 2.9 mA/m^2, respectively.

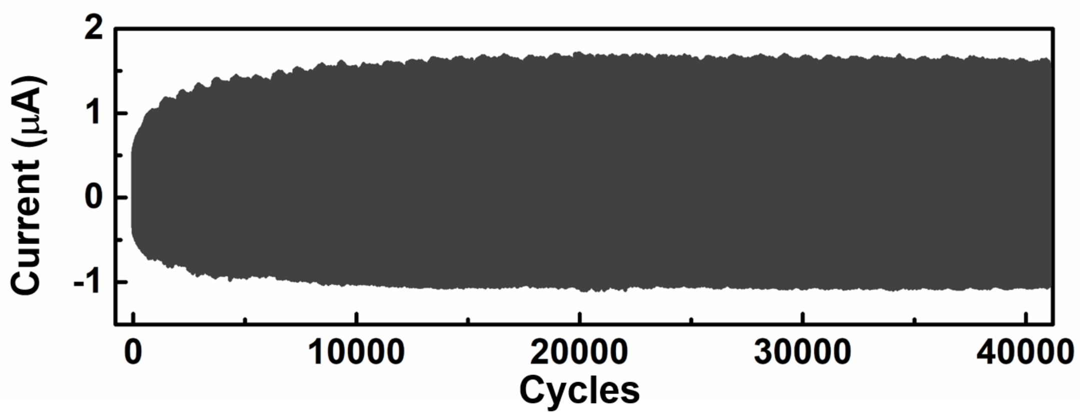

Figure 5-18. Durability test for patterned fiber-based TENG.

Moreover, a long-term stability test of TENG based on patterned fibers is conducted as shown in Figure 5-18. The TENG experiences a charge accumulation period at first and then works stably for more than 40k working cycles. These experimental results indicate that the patterned fiber fabricated by DITD is durable enough for wearable applications.

5.5.3 Self-Powered Wearable Multipoint Touch Sensing Fabric

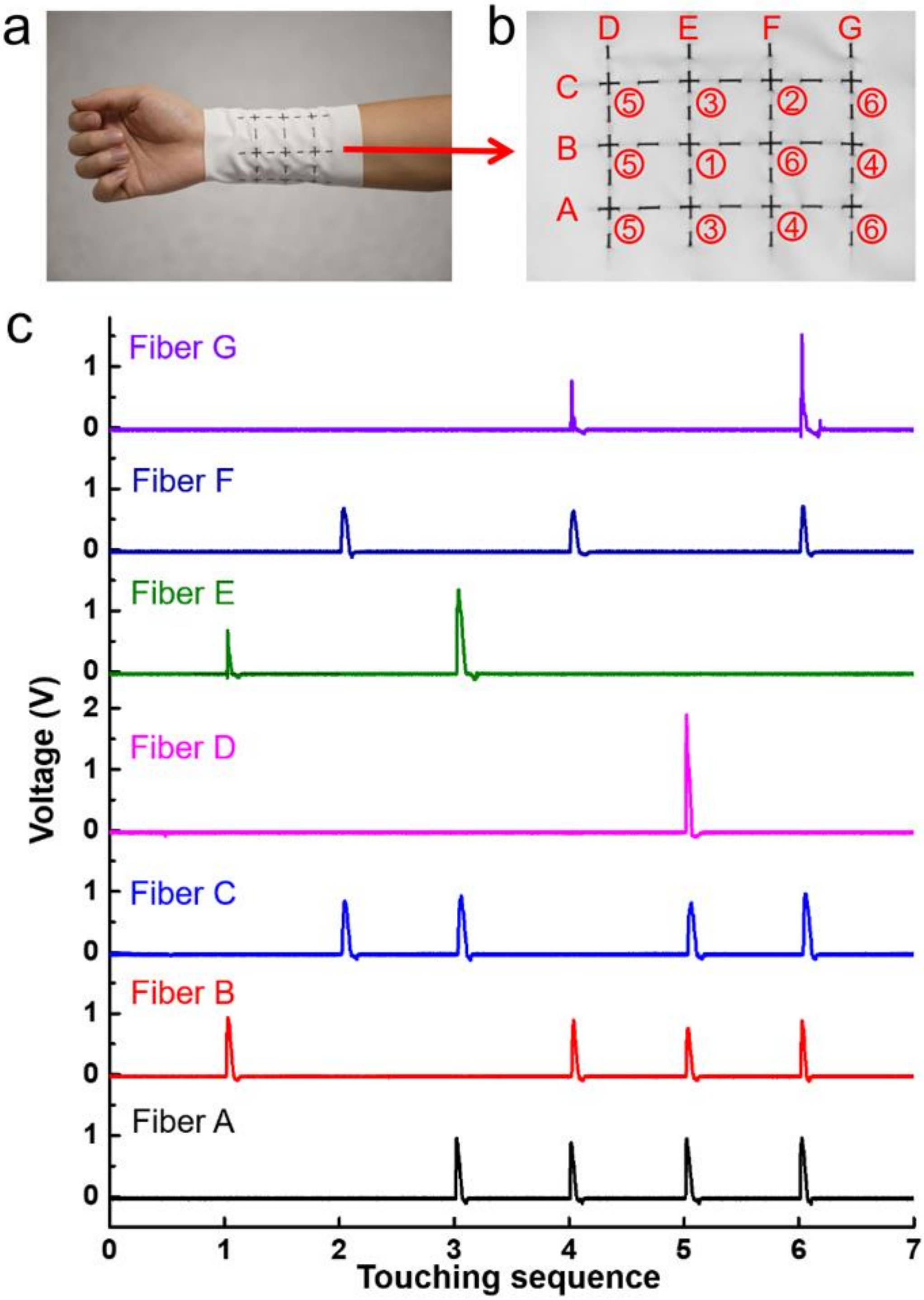

Figure 5-19. Self-powered wearable multipoint touch sensing fabric. (a) Self-powered wearable multipoint touch sensing fabric wrapped on a wrist. (b) The developed view of the touch sensing fabric. Letter "A" to "G" denoting the 7 fibers respectively, while the number representing the touching sequence labeled in (c). (c) Measured output signals from all the 7 fibers in the touch sensing fabric.

A TENG with higher performance will lead to higher sensitivity and higher signal-to-noise ratio when applied to self-powered sensing applications. Therefore, based on the patterned fibers fabricated above, a wearable self-powered multipoint touch sensing fabric is further developed. As demonstrated in Figure 5-19a, three 10-cm-long patterned fibers and four 8-cm-long patterned fibers are weaved into a piece of cloth and intersected at 12 sensing nodes wrapped around the wrist. When an external object such as fingers, gloves, and metal blocks approaches a certain sensing node, the charge distribution on the electrodes of the two crossed fibers connecting to this node changes because of the electrostatic induction, resulting in voltage output. Hence, the touched point can be electrically illustrated by monitoring the output signals of the 7 fibers. Both single-point and multipoint tests are performed by slight finger touches. And the output signals are recorded in Figure 5-19c. The numbers labeled on the nodes in the developed view of the wearable sensor (Figure 5-19b) represent the touching sequence under test. For instance, the first touch occurs on the node intersected by fiber B and E, matching with the result that output voltage is only detected on fiber B and E. Similarly, in the 5th touching test, output voltages are detected on fiber A, B, C, and D simultaneously, indicating a multipoint touching on the leftmost 3 nodes. All the nodes are tested during the 6 touches and the results agree with touch behaviors very well. Additionally, all the generated voltage from the touch sensing fabric is several volts, which is convenient to be detected.

5.6 Summary

In this chapter, a DITD technique is successfully developed for one-step and large-scale fabrication of micro/nano-patterned fibers. The surface patterns can be implemented in all directions and possess a feature size of tens of nanometers. This technique is compatible with almost all the materials and inner structures used in the thermal fiber drawing process. The thermal behavior and flow behavior of the fiber during the DITD process are comprehensively studied. The pattern resolution, repeatability, and depth control are also examined to demonstrate the great potential of the DITD technique in a variety of applications. As a proof of concept, three applications are further demonstrated. The plasmonic behavior of nanopatterned fibers is investigated. And a patterned multimaterial fiber-based TENG is assembled which is proved to have a higher performance than the TENG assembled from the flat-surface fiber. Moreover, a wearable self-powered multipoint touch sensing fabric is constructed and tested. These applications represent the bright future of the DITD technology in multifunctional fiber-based devices, wearable electronics, and smart fabrics.

Chapter 6 Conclusions and Recommendations

6.1 Conclusions

In this thesis, novel functional polymer fibers for thermal sensing and touch sensing applications are developed based on the thermal drawing technique which possesses unique advantages such as high throughput and good compatibility. And sensing fabrics based on these fibers are further demonstrated to reveal their promising prospects. Additionally, various surface patterns are created on the fiber surface by modifying traditional thermal drawing technique, which could both improve the sensing fabrics and realize more unique functionalities for future applications in fiber-based devices and smart fabrics. More specific results are summarized as follows.

First, a thermoelectric fiber is developed for thermal sensing and positioning fabric. The thermally drawn thermoelectric fiber compromises a polymer cladding and an amorphous semiconductor core, leading to high flexibility and uniformity. Owing to the large Seebeck coefficient of the thermoelectric core, the voltage response is recognizable even the temperature change is smaller than 0.05 °C. And the spatial resolution for positioning thermal source is in millimeter level. These results are also verified by simulations. Furthermore, a flexible thermal sensing fabric based on a network by 3 × 3 thermoelectric fiber array is constructed for simultaneously realizing thermal sensing and positioning, suggesting applications in health-monitoring products, large-area thermography, and electronic skins.

Second, an ultra-stretchable conducive SEBS fiber is achieved and a self-powered touch sensing net fabric is built for monitoring sports performance. A two-step soluble-core thermal drawing process designed for low modulus and low viscosity materials is introduced for fabricating SEBS fibers with customized architectures. The ultra-stretchable conducive SEBS fiber is thus achieved by injecting liquid metal into the hollow core of SEBS fiber. The conductivity is well maintained under 1900% strain or sudden hit by a 1.5 kg load freefalling from a height of 1 meter. Subsequently, TENGs based on the conducive SEBS fiber are studied and their performance under high impact and long-term working are tested. Finally, a self-powered touch sensing net fabric is built and adapted to the football surface to realize sports performance monitoring. This two-step soluble-core thermal drawing process and the touch sensing fabric indicate their broad prospects for self-powered smart fabric and large-scale soft device integration.

Last, a DITD technique is proposed for fabricating micro/nano-patterned fibers for further improving the performance of fiber-based TENG devices and extend the applications of thermally drawn fibers. The surface patterns can be implemented in all directions and possess a feature size of tens of nanometers. And the DITD technique is compatible with almost all the materials and inner structures used in the thermal fiber drawing process. Both thermal behavior and flow behavior of the fiber during the DITD process are comprehensively discussed to illustrate the feasibility of the DITD technique. Moreover, Pattern resolution, repeatability, and pattern depth control are further examined, showing a featured size as small as tens of nanometers. Al last, three applications are further demonstrated. The plasmonic behavior of nanopatterned fibers is investigated to reveal its potential in mode converter and biosensing. A patterned multimaterial fiber-based TENG is assembled, which shows a higher performance than the TENG assembled from the flat-surface fiber. And a wearable self-powered multipoint touch sensing fabric is constructed and tested. These applications represent the bright future of the DITD technology in multifunctional fiber-based electronics and smart fabrics.

6.2 Recommendations for Future Works

Based on the works in this thesis, several future directions can be recommended as below.

Developing thermoelectric fibers with higher thermoelectric performance and new functionalities such as power generation and refrigeration. This thesis exhibits the possibility of incorporating thermoelectric material into polymer fiber to realize thermal sensing with a simple core-shell structure. As the thermal drawing technique possesses the ability to incorporate multimaterial and complex architectures in a single fiber, further development of the thermoelectric fibers could be achieved by integrating several thermoelectric cores or construct different electrode configurations. For example, incorporating several pairs of n-type and p-type thermoelectric cores and connecting them in series will effectively increase the output voltage, which is beneficial in thermal sensing applications. Also, integrating electrodes inside the fiber along the entire fiber length, that is, electrically connecting the thermoelectric cores at two sides instead of connecting at two fiber ends, will lead to lower internal resistance for higher performance in power generation and cooling applications. Furthermore, a convergence fiber drawing approach is recently developed for including materials with a high melting temperature into the low-temperature polymer fibers [108, 361]. Hence, thermoelectric materials with higher performance such as SnSe and Bi_2Te_3 may be incorporated into polymer fibers through this approach. Achieving this and combining with well-designed fiber architecture and electrode configuration could lead to a great advance towards personal thermal management fabrics that achieving both thermal sensing and human body thermal comfort.

Applying modern textile technology to thermally drawn fibers for producing highly integrated functional fabrics at industrial scales. Although the demonstrated fabrics in this thesis are hand made with a simple structure as a proof of concept, the thermally drawn fibers introduced are all fabricated at hundreds of meters scale, which is potentially compatible with the modern textile technology. Previous works in TENGs [362-364] have demonstrated various fabric structures such as 2D weaving, 2D knitting, and 3D penetrated and shown better output performance than single fibers. Also, fabrics with different structures possess different advantages in mechanical properties such as high flexibility, strength, and stretchability. Thus, it can be inferred that combining the high yield and good compatibility thermal drawing technique with modern textile technology will enable the fabrics with a wide range of advanced functions not limited to TENG-based touch sensing. Furthermore, the ability to incorporate different fibers into fabric will lead to multifunctional fabrics towards smart fabrics.

Integrating disparate functions in a single fiber by combining surface patterns, functional materials, and fiber architectures. Chapter 5 proposes a DITD technique to create surface patterns on fibers and demonstrate its application in enhancing the performance of fiber-based TENG. Noticing that different surface patterns could realize different functions and the created surface pattern only alter the surface of the fibers without affecting inner material and architecture, various functionalities can be brought to current functional fibers as additional values. Therefore, the tremendous combinations of surface patterns, functional materials, and fiber architectures represent the countless possibilities of multifunctional fibers. For example, according to the thermal sensing fiber and touch sensing fibers introduced in this thesis, a fiber can be further developed by designing an architecture to incorporate both thermoelectric material and in-fiber electrode followed by creating a superhydrophobic surface. This developed fiber will integrate three functionalities: thermal sensing, touch sensing, and self-cleaning, which will be of great potential in self-cleaning sensing fabrics.

Publications

1. **Z. Wang**, T. Wu, Z. Wang, T. Zhang, M. Chen, J. Zhang, L. Liu, M. Qi, Q. Zhang, J. Yang, W. Liu, H. Chen, Y. Luo, and L. Wei. Designer patterned functional fibers via direct imprinting in thermal drawing. *Nature Communications **11**, 2842* (2020).
2. M. Chen, **Z. Wang (equal contributor)**, Q. Zhang, Z. Wang, W. Liu, and L. Wei. Self-powered multifunctional sensing based on super-elastic fibers by soluble-core thermal drawing. submitted, (2020).
3. T. Zhang, **Z. Wang (equal contributor)**, B. Srinivasan, Z. Wang, J. Zhang, K. Li, C. Boussard-Pledel, J. Troles, B. Bureau, and L. Wei. Ultraflexible glassy semiconductor fibers for thermal sensing and positioning. *ACS Applied Materials & Interfaces* **11,** 2441-2447 (2019).
4. J. Yang, **Z. Wang**, Z. Wang, J. Zhang, Q. Zhang, P. P. Shum, and L. Wei. All-metal phosphide electrodes for high-performance quasi-solid-state fiber-shaped aqueous rechargeable Ni–Fe batteries. *ACS Applied Materials & Interfaces* **12,** 12801-12808 (2020).
5. J. Zhang, **Z. Wang**, Z. Wang, T. Zhang, and L. Wei. In-fibre particle manipulation and device assembly via laser induced thermocapillary convection. *Nature Communications* **10,** 5206 (2019).
6. J. Zhang, **Z. Wang**, Z. Wang, T. Zhang, and L. Wei. In-fiber production of laser-structured stress-mediated semiconductor particles. *ACS Applied Materials & Interfaces* **11,** 45330-45337 (2019).
7. Y. He, **Z. Wang**, J. Zhang, and L. Wei. A stable and long-lasting concentration cell based on a reduced graphene oxide membrane and natural resource electrolyte. *Journal of Materials Chemistry A* **5,** 21130-21133 (2017).
8. Y. He, Y. Sun, **Z. Wang**, S. Ma, N. Zhang, J. Zhang, S. Soh, and L. Wei. Pristine graphene oxide film-based contactless actuators driven by electrostatic forces. *Journal of Materials Chemistry C* **5,** 9534-9539 (2017).
9. M. Chen, Z. Wang, X. Ge, **Z. Wang**, K. Fujisawa, J. Xia, Q. Zeng, K. Li, T. Zhang, Q. Zhang, M. Chen, N. Zhang, T. Wu, S. Ma, G. Gu, Z. Shen, L. Liu, Z. Liu, M. Terrones, and L. Wei. Controlled fragmentation of single-atom-thick polycrystalline graphene. *Matter* **2,** 666-679 (2020).
10. J. Yang, Q. Zhang, Z. Wang, **Z. Wang**, L. Kang, M. Qi, M. Chen, W. Liu, W. Gong, W. Lu, P. P. Shum, and L. Wei. Rational construction of self-standing sulfur-doped Fe_2O_3 anodes with promoted energy storage capability for wearable aqueous rechargeable NiCo-Fe batteries. *Advanced Energy Materials*, 2001064 (2020).
11. S. Ma, T. Ye, T. Wu, **Z. Wang**, Z. Wang, S. Ramakrishna, C. Vijila, and L. Wei. Hollow rice grain-shaped TiO_2 nanostructures for high-efficiency and large-area perovskite solar cells. *Solar Energy Materials and Solar Cells* **191,** 389-398 (2019).

12. N. M. Y. Zhang, M. Qi, Z. Wang, **Z. Wang**, M. Chen, K. Li, P. Shum, and L. Wei. One-step synthesis of cyclodextrin-capped gold nanoparticles for ultra-sensitive and highly-integrated plasmonic biosensors. *Sensors and Actuators B: Chemical* **286,** 429-436 (2019).

13. K. Li, N. Zhang, T. Zhang, **Z. Wang**, M. Chen, T. Wu, S. Ma, M. Zhang, J. Zhang, D. U. S, P. P. Shum, M. Olivo, and L. Wei. Formation of ultra-flexible, conformal, and nano-patterned photonic surfaces via polymer cold-drawing. *Journal of Materials Chemistry C* **6,** 4649-4657 (2018).

14. S. Ma, T. Ye, T. Zhang, **Z. Wang**, K. Li, M. Chen, J. Zhang, Z. Wang, S. Ramakrishna, and L. Wei. Highly oriented electrospun P(VDF-TrFE) fibers via mechanical stretching for wearable motion sensing. *Advanced Materials Technologies* **3,** 1800033 (2018).

15. N. M. Y. Zhang, K. Li, T. Zhang, P. Shum, **Z. Wang**, Z. Wang, N. Zhang, J. Zhang, T. Wu, and L. Wei. Electron-rich two-dimensional molybdenum trioxides for highly integrated plasmonic biosensing. *ACS Photonics* **5,** 347-352 (2018).

16. T. Zhang, K. Li, J. Zhang, M. Chen, **Z. Wang**, S. Ma, N. Zhang, and L. Wei. High-performance, flexible, and ultralong crystalline thermoelectric fibers. *Nano Energy* **41,** 35-42 (2017).

17. P. Man, Q. Zhang, Z. Zhou, M. Chen, J. Yang, **Z. Wang**, Z. Wang, B. He, Q. Li, W. Gong, W. Lu, Y. Yao, and L. Wei. Engineering MoS_2 nanosheets on spindle-like α-Fe_2O_3 as high-performance core–shell pseudocapacitive anodes for fiber-shaped aqueous lithium-ion capacitors. *Advanced Functional Materials,* 2003967 (2020).

18. J. Zhang, T. Zhang, H. Zhang, Z. Wang, C. Li, **Z. Wang**, K. Li, X. Huang, M. Chen, Z. Chen, Z. Tian, H. Chen, L. Zhao, and L. Wei. Single-crystal SnSe thermoelectric fibers via laser-induced directional crystallization: from one-dimensional fibers to multi-dimensional fabrics. *Advanced Materials,* in press, (2020).

19. J. Zhang, K. Li, T. Zhang, P. J. S. Buenconsejo, M. Chen, **Z. Wang**, M. Zhang, Z. Wang, and L. Wei. Laser-induced in-fiber fluid dynamical instabilities for precise and scalable fabrication of spherical particles. *Advanced Functional Materials* **27,** 1703245 (2017).

20. Q. Zhang, P. Man, B. He, C. Li, Q. Li, Z. Pan, Z. Wang, J. Yang, **Z. Wang**, Z. Zhou, X. Lu, Z. Niu, Y. Yao, and L. Wei. Binder-free $NaTi_2(PO_4)_3$ anodes for high-performance coaxial-fiber aqueous rechargeable sodium-ion batteries. *Nano Energy* **67,** 104212 (2020).

21. M. Chen, J. Xia, J. Zhou, Q. Zeng, K. Li, K. Fujisawa, W. Fu, T. Zhang, J. Zhang, **Z. Wang**, Z. Wang, X. Jia, M. Terrones, Z. X. Shen, Z. Liu, and L. Wei. Ordered and atomically perfect fragmentation of layered transition metal dichalcogenides via mechanical instabilities. *ACS Nano* **11,** 9191-9199 (2017).

Bibliography

1. J. C. Splitstoser, T. D. Dillehay, J. Wouters, and A. Claro. Early pre-hispanic use of indigo blue in Peru. *Science Advances* **2,** e1501623 (2016).
2. L. Bruchhaus, P. Mazarov, L. Bischoff, J. Gierak, A. D. Wieck, and H. Hövel. Comparison of technologies for nano device prototyping with a special focus on ion beams: A review. *Applied Physics Reviews* **4,** 011302 (2017).
3. S. Canovas-Carrasco, A.-J. Garcia-Sanchez, and J. Garcia-Haro. On the nature of energy-feasible wireless nanosensor networks. *Sensors (Basel, Switzerland)* **18,** 1356 (2018).
4. S. Canovas-Carrasco, A.-J. Garcia-Sanchez, F. Garcia-Sanchez, and J. Garcia-Haro. Conceptual design of a nano-networking device. *Sensors (Basel, Switzerland)* **16,** 2104 (2016).
5. S. Feng, F. Farha, Q. Li, Y. Wan, Y. Xu, T. Zhang, and H. Ning. Review on smart gas sensing technology. *Sensors* **19,** 3760 (2019).
6. I. Jeerapan, and S. Poorahong. Review—flexible and stretchable electrochemical sensing systems: Materials, energy sources, and integrations. *Journal of The Electrochemical Society* **167,** 037573 (2020).
7. U. Lee, K. Han, H. Cho, K.-M. Chung, H. Hong, S.-J. Lee, Y. Noh, S. Park, and J. M. Carroll. Intelligent positive computing with mobile, wearable, and iot devices: Literature review and research directions. *Ad Hoc Networks* **83,** 8-24 (2019).
8. A. Lendlein, and O. E. C. Gould. Reprogrammable recovery and actuation behaviour of shape-memory polymers. *Nature Reviews Materials* **4,** 116-133 (2019).
9. L. Ricotti, B. Trimmer, A. W. Feinberg, R. Raman, K. K. Parker, R. Bashir, M. Sitti, S. Martel, P. Dario, and A. Menciassi. Biohybrid actuators for robotics: A review of devices actuated by living cells. *Science Robotics* **2,** eaaq0495 (2017).
10. M. I. Tiwana, S. J. Redmond, and N. H. Lovell. A review of tactile sensing technologies with applications in biomedical engineering. *Sensors and Actuators A: Physical* **179,** 17-31 (2012).
11. Y. Yang, Y. Wu, C. Li, X. Yang, and W. Chen. Flexible actuators for soft robotics. *Advanced Intelligent Systems* **2,** 1900077 (2020).
12. M. Ghahremani Honarvar, and M. Latifi. Overview of wearable electronics and smart textiles. *The Journal of The Textile Institute* **108,** 631-652 (2017).
13. Y. Peng, and Y. Cui. Advanced textiles for personal thermal management and energy. *Joule* **4,** 724-742 (2020).
14. K. Singha, J. Kumar, and P. Pandit. Recent advancements in wearable & smart textiles: An overview. *Materials Today: Proceedings* **16,** 1518-1523 (2019).
15. L. M. Castano, and A. B. Flatau. Smart fabric sensors and e-textile technologies: A review. *Smart Materials and Structures* **23,** 053001 (2014).
16. K. Cherenack, and L. v. Pieterson. Smart textiles: Challenges and opportunities. *Journal of Applied Physics* **112,** 091301 (2012).
17. M. Stoppa, and A. Chiolerio. Wearable electronics and smart textiles: A critical review. *Sensors (Basel, Switzerland)* **14,** 11957-11992 (2014).
18. F. Mokhtari, Z. Cheng, R. Raad, J. Xi, and J. Foroughi. Piezofibers to smart textiles: A review on recent advances and future outlook for wearable technology. *Journal of Materials Chemistry A* **8,** 9496-9522 (2020).
19. Z. Gong, Z. Xiang, X. OuYang, J. Zhang, N. Lau, J. Zhou, and C. C. Chan. Wearable fiber optic technology based on smart textile: A review. *Materials* **12,** 3311 (2019).
20. A. Lymberis, and R. Paradiso. Smart fabrics and interactive textile enabling wearable personal applications: R&d state of the art and future challenges. *30th Annual*

International Conference of the IEEE Engineering in Medicine and Biology Society 5270-5273 (2008).

21. V. Koncar. *Smart textiles and their applications. Ch. 1.* (Woodhead Publishing, Oxford, 2016).
22. A. K. Yetisen, H. Qu, A. Manbachi, H. Butt, M. R. Dokmeci, J. P. Hinestroza, M. Skorobogatiy, A. Khademhosseini, and S. H. Yun. Nanotechnology in textiles. *ACS Nano* **10,** 3042-3068 (2016).
23. R. Stewart. Cords and chords: Exploring the role of e-textiles in computational audio. *Frontiers in ICT* **6,** (2019).
24. T. Hughes-Riley, T. Dias, and C. Cork. A historical review of the development of electronic textiles. *Fibers* **6,** 34 (2018).
25. E. Ismar, S. Kurşun Bahadir, F. Kalaoglu, and V. Koncar. Futuristic clothes: Electronic textiles and wearable technologies. *Global Challenges* **4,** 1900092 (2020).
26. R. McLaren, F. Joseph, C. Baguley, and D. Taylor. A review of e-textiles in neurological rehabilitation: How close are we? *Journal of NeuroEngineering and Rehabilitation* **13,** 59 (2016).
27. S. Patel, H. Park, P. Bonato, L. Chan, and M. Rodgers. A review of wearable sensors and systems with application in rehabilitation. *Journal of NeuroEngineering and Rehabilitation* **9,** 21 (2012).
28. Q. Huang, D. Wang, and Z. Zheng. Textile-based electrochemical energy storage devices. *Advanced Energy Materials* **6,** 1600783 (2016).
29. Z. Liu, F. Mo, H. Li, M. Zhu, Z. Wang, G. Liang, and C. Zhi. Advances in flexible and wearable energy-storage textiles. *Small Methods* **2,** 1800124 (2018).
30. S. Zhai, H. E. Karahan, L. Wei, Q. Qian, A. T. Harris, A. I. Minett, S. Ramakrishna, A. K. Ng, and Y. Chen. Textile energy storage: Structural design concepts, material selection and future perspectives. *Energy Storage Materials* **3,** 123-139 (2016).
31. M. Datta, and D. Landolt. Fundamental aspects and applications of electrochemical microfabrication. *Electrochimica Acta* **45,** 2535-2558 (2000).
32. M. F. El-Kady, and R. B. Kaner. Scalable fabrication of high-power graphene micro-supercapacitors for flexible and on-chip energy storage. *Nature Communications* **4,** (2013).
33. Z. P. Huang, N. Geyer, P. Werner, J. de Boor, and U. Gosele. Metal-assisted chemical etching of silicon: A review. *Advanced Materials* **23,** 285-308 (2011).
34. W. Lu, and C. M. Lieber. Nanoelectronics from the bottom up. *Nature Materials* **6,** 841-850 (2007).
35. L. X. Yang, I. Akhatov, M. Mahinfalah, and B. Z. Jang. Nano-fabrication: A review. *Journal of the Chinese Institute of Engineers* **30,** 441-446 (2007).
36. C. D. Dimitrakopoulos, and P. R. L. Malenfant. Organic thin film transistors for large area electronics. *Advanced Materials* **14,** 99-+ (2002).
37. R. M. M. Hasan, and X. Luo. Promising lithography techniques for next-generation logic devices. *Nanomanufacturing and Metrology* **1,** 67-81 (2018).
38. S. T. Howell, A. Grushina, F. Holzner, and J. Brugger. Thermal scanning probe lithography—a review. *Microsystems & Nanoengineering* **6,** 21 (2020).
39. H. Lorenz, M. Despont, N. Fahrni, N. LaBianca, P. Renaud, and P. Vettiger. Su-8: A low-cost negative resist for mems. *Journal of Micromechanics and Microengineering* **7,** 121-124 (1997).
40. A. Pimpin, and W. Srituravanich. Review on micro- and nanolithography techniques and their applications. *Engineering Journal-Thailand* **16,** 37-55 (2012).
41. K. T. M. Tran, and T. D. Nguyen. Lithography-based methods to manufacture biomaterials at small scales. *Journal of Science: Advanced Materials and Devices* **2,** 1-14 (2017).

42. B. Wu, and A. Kumar. Extreme ultraviolet lithography: A review. *Journal of Vacuum Science & Technology B: Microelectronics and Nanometer Structures Processing, Measurement, and Phenomena* **25,** 1743-1761 (2007).
43. A. G. Bhuiyan, A. Hashimoto, and A. Yamamoto. Indium nitride (inn): A review on growth, characterization, and properties. *Journal of Applied Physics* **94,** 2779-2808 (2003).
44. S. A. Chambers. Epitaxial growth and properties of thin film oxides. *Surface Science Reports* **39,** 105-180 (2000).
45. B. A. Joyce. Molecular beam epitaxy. *Reports on Progress in Physics* **48,** 1637-1697 (1985).
46. L. Liu, and J. H. Edgar. Substrates for gallium nitride epitaxy. *Materials Science & Engineering R-Reports* **37,** 61-127 (2002).
47. M. R. Melloch. Review of the application of molecular beam epitaxy for high efficiency solar cell research. *Solar Cells* **30,** 313-321 (1991).
48. Y. Guo, X.-S. Zhang, Y. Wang, W. Gong, Q. Zhang, H. Wang, and J. Brugger. All-fiber hybrid piezoelectric-enhanced triboelectric nanogenerator for wearable gesture monitoring. *Nano Energy* **48,** 152-160 (2018).
49. T. Subbiah, G. S. Bhat, R. W. Tock, S. Pararneswaran, and S. S. Ramkumar. Electrospinning of nanofibers. *Journal of Applied Polymer Science* **96,** 557-569 (2005).
50. N. Bhardwaj, and S. C. Kundu. Electrospinning: A fascinating fiber fabrication technique. *Biotechnology Advances* **28,** 325-347 (2010).
51. W. E. Teo, and S. Ramakrishna. A review on electrospinning design and nanofibre assemblies. *Nanotechnology* **17,** R89-R106 (2006).
52. Z. M. Huang, Y. Z. Zhang, M. Kotaki, and S. Ramakrishna. A review on polymer nanofibers by electrospinning and their applications in nanocomposites. *Composites Science and Technology* **63,** 2223-2253 (2003).
53. L. Lao, L. Fu, G. Qi, E. P. Giannelis, and J. Fan. Superhydrophilic wrinkle-free cotton fabrics via plasma and nanofluid treatment. *ACS Applied Materials & Interfaces* **9,** 38109-38116 (2017).
54. E. Mohseni, E. Zalnezhad, and A. R. Bushroa. Comparative investigation on the adhesion of hydroxyapatite coating on ti-6al-4v implant: A review paper. *International Journal of Adhesion and Adhesives* **48,** 238-257 (2014).
55. T. Todorov, and D. B. Mitzi. Direct liquid coating of chalcopyrite light-absorbing layers for photovoltaic devices. *European Journal of Inorganic Chemistry* 17-28 (2010).
56. T. Yuranova, R. Mosteo, J. Bandara, D. Laub, and J. Kiwi. Self-cleaning cotton textiles surfaces modified by photoactive sio2/tio2 coating. *Journal of Molecular Catalysis a-Chemical* **244,** 160-167 (2006).
57. Z. Liu, D. Qi, G. Hu, H. Wang, Y. Jiang, G. Chen, Y. Luo, X. J. Loh, B. Liedberg, and X. Chen. Surface strain redistribution on structured microfibers to enhance sensitivity of fiber-shaped stretchable strain sensors. *Advanced Materials* **30,** 1704229 (2018).
58. T. L. Andrew, L. Zhang, N. Cheng, M. Baima, J. J. Kim, L. Allison, and S. Hoxie. Melding vapor-phase organic chemistry and textile manufacturing to produce wearable electronics. *Accounts of Chemical Research* **51,** 850-859 (2018).
59. S. Hu, C.-Y. Lee, and H.-T. Chiu. Chemical vapor deposition of carbon nanocoils three-dimensionally in carbon fiber cloth for all-carbon supercapacitors. *ACS Omega* **4,** 195-202 (2019).
60. J. Kong, A. M. Cassell, and H. J. Dai. Chemical vapor deposition of methane for single-walled carbon nanotubes. *Chemical Physics Letters* **292,** 567-574 (1998).
61. Y. L. Li, I. A. Kinloch, and A. H. Windle. Direct spinning of carbon nanotube fibers from chemical vapor deposition synthesis. *Science* **304,** 276-278 (2004).

62. Z. Wen, M.-H. Yeh, H. Guo, J. Wang, Y. Zi, W. Xu, J. Deng, L. Zhu, X. Wang, C. Hu, L. Zhu, X. Sun, and Z. L. Wang. Self-powered textile for wearable electronics by hybridizing fiber-shaped nanogenerators, solar cells, and supercapacitors. *Science Advances* **2,** e1600097 (2016).
63. Q. Hong, and H. Lu. In-situ electrodeposition of highly active silver catalyst on carbon fiber papers as binder free cathodes for aluminum-air battery. *Scientific Reports* **7,** 3378 (2017).
64. S.-L. Lim, J. Kim, J. Park, S. Kim, and J.-J. Lee. Electrochemical deposition of copper on polymer fibers. *J. Electrochem. Sci. Technol* **7,** 132-138 (2016).
65. C. F. Wang, M. Zhao, J. Li, J. L. Yu, S. F. Sun, S. S. Ge, X. K. Guo, F. Xie, B. Jiang, E. K. Wujcik, Y. D. Huang, N. Wang, and Z. H. Guo. Silver nanoparticles/graphene oxide decorated carbon fiber synergistic reinforcement in epoxy-based composites. *Polymer* **131,** 263-271 (2017).
66. Y. Qin, X. Wang, and Z. L. Wang. Microfibre–nanowire hybrid structure for energy scavenging. *Nature* **451,** 809-813 (2008).
67. M. Shandilya, R. Rai, and J. Singh. Review: Hydrothermal technology for smart materials. *Advances in Applied Ceramics* **115,** 354-376 (2016).
68. X. D. Wu, C. H. Lu, Z. H. Zhou, G. P. Yuan, R. Xiong, and X. X. Zhang. Green synthesis and formation mechanism of cellulose nanocrystal-supported gold nanoparticles with enhanced catalytic performance. *Environmental Science-Nano* **1,** 71-79 (2014).
69. D. S. Yu, K. Goh, H. Wang, L. Wei, W. C. Jiang, Q. Zhang, L. M. Dai, and Y. Chen. Scalable synthesis of hierarchically structured carbon nanotube-graphene fibres for capacitive energy storage. *Nature Nanotechnology* **9,** 555-562 (2014).
70. T. Chen, S. Wang, Z. Yang, Q. Feng, X. Sun, L. Li, Z.-S. Wang, and H. Peng. Flexible, light-weight, ultrastrong, and semiconductive carbon nanotube fibers for a highly efficient solar cell. *Angewandte Chemie International Edition* **50,** 1815-1819 (2011).
71. Z. Lv, J. Yu, H. Wu, J. Shang, D. Wang, S. Hou, Y. Fu, K. Wu, and D. Zou. Highly efficient and completely flexible fiber-shaped dye-sensitized solar cell based on tio2 nanotube array. *Nanoscale* **4,** 1248-1253 (2012).
72. A. Bedeloglu, A. Demir, Y. Bozkurt, and N. S. Sariciftci. A photovoltaic fiber design for smart textiles. *Textile Research Journal* **80,** 1065-1074 (2010).
73. A. Ehrmann, and T. Blachowicz. Recent coating materials for textile-based solar cells. *Aims Materials Science* **6,** 234-251 (2019).
74. Z. B. Lv, J. F. Yu, H. W. Wu, J. Shang, D. Wang, S. C. Hou, Y. P. Fu, K. Wu, and D. C. Zou. Highly efficient and completely flexible fiber-shaped dye-sensitized solar cell based on tio2 nanotube array. *Nanoscale* **4,** 1248-1253 (2012).
75. L. B. Qiu, J. Deng, X. Lu, Z. B. Yang, and H. S. Peng. Integrating perovskite solar cells into a flexible fiber. *Angewandte Chemie-International Edition* **53,** 10425-10428 (2014).
76. Z. Zhang, X. Chen, P. Chen, G. Guan, L. Qiu, H. Lin, Z. Yang, W. Bai, Y. Luo, and H. Peng. Integrated polymer solar cell and electrochemical supercapacitor in a flexible and stable fiber format. *Advanced Materials* **26,** 466-470 (2014).
77. M. Y. Li, M. Zu, J. S. Yu, H. F. Cheng, and Q. W. Li. Stretchable fiber supercapacitors with high volumetric performance based on buckled mno2/oxidized carbon nanotube fiber electrodes. *Small* **13,** (2017).
78. G. X. Qu, J. L. Cheng, X. D. Li, D. M. Yuan, P. N. Chen, X. L. Chen, B. Wang, and H. S. Peng. A fiber supercapacitor with high energy density based on hollow graphene/conducting polymer fiber electrode. *Advanced Materials* **28,** 3646-3652 (2016).
79. X. Xiao, T. Q. Li, P. H. Yang, Y. Gao, H. Y. Jin, W. J. Ni, W. H. Zhan, X. H. Zhang, Y. Z. Cao, J. W. Zhong, L. Gong, W. C. Yen, W. J. Mai, J. Chen, K. F. Huo, Y. L.

Chueh, Z. L. Wang, and J. Zhou. Fiber-based all-solid-state flexible supercapacitors for self-powered systems. *ACS Nano* **6,** 9200-9206 (2012).

80. W. Zeng, X.-M. Tao, S. Chen, S. Shang, H. L. W. Chan, and S. H. Choy. Highly durable all-fiber nanogenerator for mechanical energy harvesting. *Energy & Environmental Science* **6,** 2631-2638 (2013).
81. T. Huang, C. Wang, H. Yu, H. Z. Wang, Q. H. Zhang, and M. F. Zhu. Human walking-driven wearable all-fiber triboelectric nanogenerator containing electrospun polyvinylidene fluoride piezoelectric nanofibers. *Nano Energy* **14,** 226-235 (2015).
82. L. Persano, C. Dagdeviren, Y. W. Su, Y. H. Zhang, S. Girardo, D. Pisignano, Y. G. Huang, and J. A. Rogers. High performance piezoelectric devices based on aligned arrays of nanofibers of poly(vinylidenefluoride-co-trifluoroethylene). *Nature Communications* **4,** (2013).
83. W. Zeng, L. Shu, Q. Li, S. Chen, F. Wang, and X. M. Tao. Fiber-based wearable electronics: A review of materials, fabrication, devices, and applications. *Advanced Materials* **26,** 5310-5336 (2014).
84. B. O'Connor, K. H. An, Y. Zhao, K. P. Pipe, and M. Shtein. Fiber shaped light emitting device. *Advanced Materials* **19,** 3897-3900 (2007).
85. S. M. Jeong, S. Song, H. J. Seo, W. M. Choi, S. H. Hwang, S. G. Lee, and S. K. Lim. Battery-free, human-motion-powered light-emitting fabric: Mechanoluminescent textile. *Advanced Sustainable Systems* **1,** (2017).
86. K.-J. Ko, H. B. Lee, and J.-W. Kang. Flexible, wearable organic light-emitting fibers based on pedot:Pss/ag-fiber embedded hybrid electrodes for large-area textile lighting. *Advanced Materials Technologies* **5,** 2000168 (2020).
87. X. Cheng, and Y. Jaluria. Effect of furnace thermal configuration on optical fiber heating and drawing. *Numerical Heat Transfer Part a-Applications* **48,** 507-528 (2005).
88. M. G. Forest, and H. Zhou. Unsteady analyses of thermal glass fibre drawing processes. *European Journal of Applied Mathematics* **12,** 479-496 (2001).
89. F. Just, R. Spittel, J. Bierlich, S. Grimm, M. Jager, and H. Bartelt. The influence of the fiber drawing process on intrinsic stress and the resulting birefringence optimization of pm fibers. *Optical Materials* **42,** 345-350 (2015).
90. Y. Liao, D. C. Shan, Z. F. Liu, and M. Wang. Thermal analysis of the necking phenomenon in fiber drawing. *Journal of Thermal Analysis and Calorimetry* **122,** 323-327 (2015).
91. J. Yang, and Y. Jaluria. Feasibility and optimization of the hollow optical fiber drawing process. *International Journal of Heat and Mass Transfer* **52,** 4108-4116 (2009).
92. H. Zhou, and M. G. Forest. A numerical study of unsteady, thermal, glass fiber drawing processes. *Communications in Mathematical Sciences* **3,** 27-45 (2005).
93. T. Nguyen-Dang, A. C. de Luca, W. Yan, Y. Qu, A. G. Page, M. Volpi, T. Das Gupta, S. P. Lacour, and F. Sorin. Controlled sub-micrometer hierarchical textures engineered in polymeric fibers and microchannels via thermal drawing. *Advanced Functional Materials* **27,** 1605935 (2017).
94. G. Loke, W. Yan, T. Khudiyev, G. Noel, and Y. Fink. Recent progress and perspectives of thermally drawn multimaterial fiber electronics. *Advanced Materials* **32,** 1904911 (2020).
95. J. Zhang, K. Li, T. Zhang, P. J. S. Buenconsejo, M. Chen, Z. Wang, M. Zhang, Z. Wang, and L. Wei. Laser-induced in-fiber fluid dynamical instabilities for precise and scalable fabrication of spherical particles. *Advanced Functional Materials* **27,** 1703245 (2017).
96. T. C. Lin, J. Zhao, A. Javadi, and X. Li. Feasibility study on thermal drawing of polymer fibers containing micro/nano metal wires. *2016 International Symposium on Flexible Automation (ISFA)* 378-381 (2016).

97. J. Zhao, and X. Li. A long wavelength model for manufacturing of continuous metal microwires by thermal fiber drawing from a preform. *Journal of Micro and Nano-Manufacturing* **6,** (2017).
98. Z. Feng, S. Yang, S. Jia, Y. Zhang, S. Jiang, L. Yu, R. Li, G. Song, A. Wang, T. Martin, L. Zuo, and X. Jia. Scalable, washable and lightweight triboelectric-energy-generating fibers by the thermal drawing process for industrial loom weaving. *Nano Energy* **74,** 104805 (2020).
99. W. Yan, Y. Qu, T. D. Gupta, A. Darga, D. T. Nguyên, A. G. Page, M. Rossi, M. Ceriotti, and F. Sorin. Semiconducting nanowire-based optoelectronic fibers. *Advanced Materials* **29,** 1700681 (2017).
100. J. J. Kaufman, G. M. Tao, S. Shabahang, D. S. S. Deng, Y. Fink, and A. F. Abouraddy. Thermal drawing of high-density macroscopic arrays of well-ordered sub-5-nm-diameter nanowires. *Nano Letters* **11,** 4768-4773 (2011).
101. N. D. Orf, O. Shapira, F. Sorin, S. Danto, M. A. Baldo, J. D. Joannopoulos, and Y. Fink. Fiber draw synthesis. *Proceedings of the National Academy of Sciences* **108,** 4743-4747 (2011).
102. C. Strutynski, C. Labrugere, A. Poulon-Quintin, M. Dussauze, F. Adamietz, T. Cardinal, and S. Danto. In-situ fiber drawing induced synthesis of silver-tellurium semiconductor compounds. *Journal of Non-Crystalline Solids* **543,** (2020).
103. M. Kanik, S. Orguc, G. Varnavides, J. Kim, T. Benavides, D. Gonzalez, T. Akintilo, C. C. Tasan, A. P. Chandrakasan, Y. Fink, and P. Anikeeva. Strain-programmable fiber-based artificial muscle. *Science* **365,** 145-150 (2019).
104. G. Brambilla, F. Xu, P. Horak, Y. M. Jung, F. Koizumi, N. P. Sessions, E. Koukharenko, X. Feng, G. S. Murugan, J. S. Wilkinson, and D. J. Richardson. Optical fiber nanowires and microwires: Fabrication and applications. *Advances in Optics and Photonics* **1,** 107-161 (2009).
105. L. M. Tong, R. R. Gattass, J. B. Ashcom, S. L. He, J. Y. Lou, M. Y. Shen, I. Maxwell, and E. Mazur. Subwavelength-diameter silica wires for low-loss optical wave guiding. *Nature* **426,** 816-819 (2003).
106. G. Coviello, V. Finazzi, J. Villatoro, and V. Pruneri. Thermally stabilized pcf-based sensor for temperature measurements up to 1000 degrees c. *Optics Express* **17,** 21551-21559 (2009).
107. B. Grena, J.-B. Alayrac, E. Levy, A. M. Stolyarov, J. D. Joannopoulos, and Y. Fink. Thermally-drawn fibers with spatially-selective porous domains. *Nature Communications* **8,** 364 (2017).
108. M. Rein, V. D. Favrod, C. Hou, T. Khudiyev, A. Stolyarov, J. Cox, C.-C. Chung, C. Chhav, M. Ellis, J. Joannopoulos, and Y. Fink. Diode fibres for fabric-based optical communications. *Nature* **560,** 214-218 (2018).
109. A. M. Stolyarov, L. Wei, O. Shapira, F. Sorin, S. L. Chua, J. D. Joannopoulos, and Y. Fink. Microfluidic directional emission control of an azimuthally polarized radial fibre laser. *Nature Photonics* **6,** 229-233 (2012).
110. M. Bayindir, F. Sorin, A. F. Abouraddy, J. Viens, S. D. Hart, J. D. Joannopoulos, and Y. Fink. Metal–insulator–semiconductor optoelectronic fibres. *Nature* **431,** 826-829 (2004).
111. S. Park, G. Loke, Y. Fink, and P. Anikeeva. Flexible fiber-based optoelectronics for neural interfaces. *Chemical Society Reviews* **48,** 1826-1852 (2019).
112. W. Yan, T. Das Gupta, I. Richard, F. Sorin, and Ieee. *2018 conference on lasers and electro-optics.* (2018).
113. T. Nguyen-Dang, A. G. Page, Y. Qu, M. Volpi, W. Yan, and F. Sorin. Multi-material micro-electromechanical fibers with bendable functional domains. *Journal of Physics D: Applied Physics* **50,** 144001 (2017).

114. A. Leber, A. G. Page, D. Yan, Y. Qu, S. Shadman, P. Reis, and F. Sorin. Compressible and electrically conducting fibers for large-area sensing of pressures. *Advanced Functional Materials* **30,** 1904274 (2020).
115. T. Zhang, K. Li, J. Zhang, M. Chen, Z. Wang, S. Ma, N. Zhang, and L. Wei. High-performance, flexible, and ultralong crystalline thermoelectric fibers. *Nano Energy* **41,** 35-42 (2017).
116. T. Zhang, Z. Wang, B. Srinivasan, Z. Wang, J. Zhang, K. Li, C. Boussard-Pledel, J. Troles, B. Bureau, and L. Wei. Ultraflexible glassy semiconductor fibers for thermal sensing and positioning. *ACS Applied Materials & Interfaces* **11,** 2441-2447 (2019).
117. S. Wang, T. Zhang, K. Li, S. Ma, M. Chen, P. Lu, and L. Wei. Flexible piezoelectric fibers for acoustic sensing and positioning. *Advanced Electronic Materials* **3,** 1600449 (2017).
118. S. Park, Y. Guo, X. Jia, H. K. Choe, B. Grena, J. Kang, J. Park, C. Lu, A. Canales, R. Chen, Y. S. Yim, G. B. Choi, Y. Fink, and P. Anikeeva. One-step optogenetics with multifunctional flexible polymer fibers. *Nature Neuroscience* **20,** 612-619 (2017).
119. Y. Guo, S. Jiang, B. J. B. Grena, I. F. Kimbrough, E. G. Thompson, Y. Fink, H. Sontheimer, T. Yoshinobu, and X. Jia. Polymer composite with carbon nanofibers aligned during thermal drawing as a microelectrode for chronic neural interfaces. *ACS Nano* **11,** 6574-6585 (2017).
120. L. Ren, Q. Jiang, K. Chen, Z. Chen, C. Pan, and L. Jiang. Fabrication of a micro-needle array electrode by thermal drawing for bio-signals monitoring. *Sensors* **16,** 908 (2016).
121. A. Canales, S. Park, A. Kilias, and P. Anikeeva. Multifunctional fibers as tools for neuroscience and neuroengineering. *Accounts of Chemical Research* **51,** 829-838 (2018).
122. M. Bayindir, A. F. Abouraddy, J. Arnold, J. D. Joannopoulos, and Y. Fink. Thermal-sensing fiber devices by multimaterial codrawing. *Advanced Materials* **18,** 845-849 (2006).
123. P. R. N. Childs, J. R. Greenwood, and C. A. Long. Review of temperature measurement. *Review of Scientific Instruments* **71,** 2959-2978 (2000).
124. J. D. Kalma, T. R. McVicar, and M. F. McCabe. Estimating land surface evaporation: A review of methods using remotely sensed surface temperature data. *Surveys in Geophysics* **29,** 421-469 (2008).
125. W. Talataisong, R. Ismaeel, and G. Brambilla. A review of microfiber-based temperature sensors. *Sensors (Basel, Switzerland)* **18,** 461 (2018).
126. J. A. Voogt, and T. R. Oke. Thermal remote sensing of urban climates. *Remote Sensing of Environment* **86,** 370-384 (2003).
127. D. Xu, Y. Wang, B. Xiong, and T. Li. Mems-based thermoelectric infrared sensors: A review. *Frontiers of Mechanical Engineering* **12,** 557-566 (2017).
128. M. Bayindir, O. Shapira, D. Saygin-Hinczewski, J. Viens, A. F. Abouraddy, J. D. Joannopoulos, and Y. Fink. Integrated fibres for self-monitored optical transport. *Nature Materials* **4,** 820-825 (2005).
129. M. Sun, G. Tang, G. Qian, W. Liu, Z. Shi, D. Chen, Q. Qian, and Z. Yang. In4se3 alloy core thermoelectric fibers. *Materials Letters* **217,** 13-15 (2018).
130. X. Lee, T. Yang, X. Li, R. Zhang, M. Zhu, H. Zhang, D. Xie, J. Wei, M. Zhong, K. Wang, D. Wu, Z. Li, and H. Zhu. Flexible graphene woven fabrics for touch sensing. *Applied Physics Letters* **102,** 163117 (2013).
131. M. Park, B. G. Bok, J. H. Ahn, and M. S. Kim. Recent advances in tactile sensing technology. *Micromachines* **9,** (2018).
132. J.-S. Roh. Textile touch sensors for wearable and ubiquitous interfaces. *Textile Research Journal* **84,** 739-750 (2014).

133. S. Seyedin, P. Zhang, M. Naebe, S. Qin, J. Chen, X. Wang, and J. M. Razal. Textile strain sensors: A review of the fabrication technologies, performance evaluation and applications. *Materials Horizons* **6,** 219-249 (2019).
134. D. Silvera-Tawil, D. Rye, and M. Velonaki. Artificial skin and tactile sensing for socially interactive robots: A review. *Robotics and Autonomous Systems* **63,** 230-243 (2015).
135. F.-R. Fan, Z.-Q. Tian, and Z. Lin Wang. Flexible triboelectric generator. *Nano Energy* **1,** 328-334 (2012).
136. G. Zhu, B. Peng, J. Chen, Q. Jing, and Z. Lin Wang. Triboelectric nanogenerators as a new energy technology: From fundamentals, devices, to applications. *Nano Energy* **14,** 126-138 (2015).
137. X. J. Pu, H. Y. Guo, J. Chen, X. Wang, Y. Xi, C. G. Hu, and Z. L. Wang. Eye motion triggered self-powered mechnosensational communication system using triboelectric nanogenerator. *Science Advances* **3,** (2017).
138. X. S. Zhang, M. D. Han, R. X. Wang, F. Y. Zhu, Z. H. Li, W. Wang, and H. X. Zhang. Frequency-multiplication high-output triboelectric nanogenerator for sustainably powering biomedical microsystems. *Nano Letters* **13,** 1168-1172 (2013).
139. K. N. Kim, J. Chun, J. W. Kim, K. Y. Lee, J. U. Park, S. W. Kim, Z. L. Wang, and J. M. Baik. Highly stretchable 2d fabrics for wearable triboelectric nanogenerator under harsh environments. *ACS Nano* **9,** 6394-6400 (2015).
140. G. Zhu, J. Chen, T. J. Zhang, Q. S. Jing, and Z. L. Wang. Radial-arrayed rotary electrification for high performance triboelectric generator. *Nature Communications* **5,** (2014).
141. Y. Yang, H. L. Zhang, J. Chen, Q. S. Jing, Y. S. Zhou, X. N. Wen, and Z. L. Wang. Single-electrode-based sliding triboelectric nanogenerator for self-powered displacement vector sensor system. *ACS Nano* **7,** 7342-7351 (2013).
142. F. R. Fan, L. Lin, G. Zhu, W. Z. Wu, R. Zhang, and Z. L. Wang. Transparent triboelectric nanogenerators and self-powered pressure sensors based on micropatterned plastic films. *Nano Letters* **12,** 3109-3114 (2012).
143. Z. L. Wang. Triboelectric nanogenerators as new energy technology for self-powered systems and as active mechanical and chemical sensors. *ACS Nano* **7,** 9533-9557 (2013).
144. Z. H. Lin, G. Cheng, L. Lin, S. Lee, and Z. L. Wang. Water-solid surface contact electrification and its use for harvesting liquid-wave energy. *Angewandte Chemie-International Edition* **52,** 12545-12549 (2013).
145. X. Pu, L. X. Li, M. M. Liu, C. Y. Jiang, C. H. Du, Z. F. Zhao, W. G. Hu, and Z. L. Wang. Wearable self-charging power textile based on flexible yarn supercapacitors and fabric nanogenerators. *Advanced Materials* **28,** 98-+ (2016).
146. G. Zhu, Z.-H. Lin, Q. Jing, P. Bai, C. Pan, Y. Yang, Y. Zhou, and Z. L. Wang. Toward large-scale energy harvesting by a nanoparticle-enhanced triboelectric nanogenerator. *Nano Letters* **13,** 847-853 (2013).
147. F.-R. Fan, L. Lin, G. Zhu, W. Wu, R. Zhang, and Z. L. Wang. Transparent triboelectric nanogenerators and self-powered pressure sensors based on micropatterned plastic films. *Nano Letters* **12,** 3109-3114 (2012).
148. S. Lv, B. Yu, T. Huang, H. Yu, H. Wang, Q. Zhang, and M. Zhu. Gas-enhanced triboelectric nanogenerator based on fully-enclosed structure for energy harvesting and sensing. *Nano Energy* **55,** 463-469 (2019).
149. Z. Wang, L. Cheng, Y. Zheng, Y. Qin, and Z. L. Wang. Enhancing the performance of triboelectric nanogenerator through prior-charge injection and its application on self-powered anticorrosion. *Nano Energy* **10,** 37-43 (2014).
150. L. Feng, S. Li, H. Li, J. Zhai, Y. Song, L. Jiang, and D. Zhu. Super-hydrophobic surface of aligned polyacrylonitrile nanofibers. *Angewandte Chemie International Edition* **41,** 1221-1223 (2002).

151. L. Gao, and T. J. McCarthy. A perfectly hydrophobic surface (θa/θr = 180°/180°). *Journal of the American Chemical Society* **128,** 9052-9053 (2006).
152. J. Sun, B. Bhushan, and J. Tong. Structural coloration in nature. *RSC Advances* **3,** 14862-14889 (2013).
153. Y. Yang, Y. Pan, and P. Guo. Structural coloration of metallic surfaces with micro/nano-structures induced by elliptical vibration texturing. *Applied Surface Science* **402,** 400-409 (2017).
154. S. Lu, Y. Ma, C. Zhu, S. Shen, and Q. He. The effect of hydrophobic modification of zeolites on CO_2 absorption enhancement. *Chinese Journal of Chemical Engineering* **17,** 36-41 (2009).
155. A. Z. Sadek, W. Wlodarski, K. Shin, R. B. Kaner, and K. Kalantar-zadeh. A layered surface acoustic wave gas sensor based on a polyaniline/in2o3nanofibre composite. *Nanotechnology* **17,** 4488-4492 (2006).
156. D. Roe, B. Karandikar, N. Bonn-Savage, B. Gibbins, and J.-B. Roullet. Antimicrobial surface functionalization of plastic catheters by silver nanoparticles. *Journal of Antimicrobial Chemotherapy* **61,** 869-876 (2008).
157. M. Ben-Sasson, K. R. Zodrow, Q. Genggeng, Y. Kang, E. P. Giannelis, and M. Elimelech. Surface functionalization of thin-film composite membranes with copper nanoparticles for antimicrobial surface properties. *Environmental Science & Technology* **48,** 384-393 (2014).
158. A. Yildirim, M. Yunusa, F. E. Ozturk, M. Kanik, and M. Bayindir. Surface textured polymer fibers for microfluidics. *Advanced Functional Materials* **24,** 4569-4576 (2014).
159. T. Khudiyev, C. Hou, A. M. Stolyarov, and Y. Fink. Sub-micrometer surface-patterned ribbon fibers and textiles. *Adv Mater* **29,** 1605868 (2017).
160. R. A. Koppes, S. Park, T. Hood, X. Jia, N. Abdolrahim Poorheravi, A. H. Achyuta, Y. Fink, and P. Anikeeva. Thermally drawn fibers as nerve guidance scaffolds. *Biomaterials* **81,** 27-35 (2016).
161. T. Nguyen Dang, I. Richard, E. Goy, F. Sordo, and F. Sorin. Insights into the fabrication of sub-100 nm textured thermally drawn fibers. *Journal of Applied Physics* **125,** 175301 (2019).
162. N. Zhang, H. Liu, A. M. Stolyarov, T. Zhang, K. Li, P. P. Shum, Y. Fink, X. W. Sun, and L. Wei. Azimuthally polarized radial emission from a quantum dot fiber laser. *ACS Photonics* **3,** 2275-2279 (2016).
163. O. Shapira, K. Kuriki, N. D. Orf, A. F. Abouraddy, G. Benoit, J. F. Viens, A. Rodriguez, M. Ibanescu, J. D. Joannopoulos, Y. Fink, and M. M. Brewster. Surface-emitting fiber lasers. *Optics Express* **14,** 3929-3935 (2006).
164. V. G. Truong, L. Bigot, A. Lerouge, M. Douay, and I. Razdobreev. Study of thermal stability and luminescence quenching properties of bismuth-doped silicate glasses for fiber laser applications. *Applied Physics Letters* **92,** 041908 (2008).
165. B. A. Flusberg, E. D. Cocker, W. Piyawattanametha, J. C. Jung, E. L. M. Cheung, and M. J. Schnitzer. Fiber-optic fluorescence imaging. *Nature Methods* **2,** 941-950 (2005).
166. J. W. Nicholson, A. D. Yablon, S. Ramachandran, and S. Ghalmi. Spatially and spectrally resolved imaging of modal content in large-mode-area fibers. *Optics Express* **16,** 7233-7243 (2008).
167. R. Slavík, J. Homola, J. Čtyroký, and E. Brynda. Novel spectral fiber optic sensor based on surface plasmon resonance. *Sensors and Actuators B: Chemical* **74,** 106-111 (2001).
168. N. M. Y. Zhang, M. Qi, Z. Wang, Z. Wang, M. Chen, K. Li, P. Shum, and L. Wei. One-step synthesis of cyclodextrin-capped gold nanoparticles for ultra-sensitive and highly-integrated plasmonic biosensors. *Sensors and Actuators B: Chemical* **286,** 429-436 (2019).

169. S. Danto, F. Sorin, N. D. Orf, Z. Wang, S. A. Speakman, J. D. Joannopoulos, and Y. Fink. Fiber field-effect device via in situ channel crystallization. *Advanced Materials* **22,** 4162-4166 (2010).

170. S. Danto, Z. Ruff, Z. Wang, J. D. Joannopoulos, and Y. Fink. Ovonic memory switching in multimaterial fibers. *Advanced Functional Materials* **21,** 1095-1101 (2011).

171. T. Khudiyev, J. Clayton, E. Levy, N. Chocat, A. Gumennik, A. M. Stolyarov, J. Joannopoulos, and Y. Fink. Electrostrictive microelectromechanical fibres and textiles. *Nature Communications* **8,** 1435 (2017).

172. S. Egusa, Z. Wang, N. Chocat, Z. M. Ruff, A. M. Stolyarov, D. Shemuly, F. Sorin, P. T. Rakich, J. D. Joannopoulos, and Y. Fink. Multimaterial piezoelectric fibres. *Nature Materials* **9,** 643-648 (2010).

173. C. Lu, S. Park, T. J. Richner, A. Derry, I. Brown, C. Hou, S. Rao, J. Kang, C. T. Moritz, Y. Fink, and P. Anikeeva. Flexible and stretchable nanowire-coated fibers for optoelectronic probing of spinal cord circuits. *Science Advances* **3,** e1600955 (2017).

174. A. Canales, X. Jia, U. P. Froriep, R. A. Koppes, C. M. Tringides, J. Selvidge, C. Lu, C. Hou, L. Wei, Y. Fink, and P. Anikeeva. Multifunctional fibers for simultaneous optical, electrical and chemical interrogation of neural circuits in vivo. *Nature Biotechnology* **33,** 277-284 (2015).

175. E. Snitzer, and R. Tumminelli. Sio2-clad fibers with selectively volatilized soft-glass cores. *Optics Letters* **14,** 757-759 (1989).

176. J. Ballato, and A. C. Peacock. Perspective: Molten core optical fiber fabrication—a route to new materials and applications. *APL Photonics* **3,** 120903 (2018).

177. J. Ballato, and E. Snitzer. Fabrication of fibers with high rare-earth concentrations for faraday isolator applications. *Applied Optics* **34,** 6848-6854 (1995).

178. Y. C. Huang, Y. K. Lu, J. C. Chen, Y. C. Hsu, Y. M. Huang, S. L. Huang, and W. H. Cheng. Broadband emission from cr-doped fibers fabricated by drawing tower. *Optics Express* **14,** 8492-8497 (2006).

179. G. Tao, S. Shabahang, E.-H. Banaei, J. J. Kaufman, and A. F. Abouraddy. Multimaterial preform coextrusion for robust chalcogenide optical fibers and tapers. *Optics Letters* **37,** 2751-2753 (2012).

180. M. Zhu, X. Wang, Z. Pan, C. Cheng, Q. Zhu, C. Jiang, Q. Nie, P. Zhang, Y. Wu, S. Dai, T. Xu, G. Tao, and X. Zhang. Fabrication of an IR hollow-core Bragg fiber based on chalcogenide glass extrusion. *Applied Physics A* **119,** 455-460 (2015).

181. S. D. Hart, G. R. Maskaly, B. Temelkuran, P. H. Prideaux, J. D. Joannopoulos, and Y. Fink. External reflection from omnidirectional dielectric mirror fibers. *Science* **296,** 510-513 (2002).

182. B. Temelkuran, S. D. Hart, G. Benoit, J. D. Joannopoulos, and Y. Fink. Wavelength-scalable hollow optical fibres with large photonic bandgaps for CO_2 laser transmission. *Nature* **420,** 650-653 (2002).

183. T. P. White, R. C. McPhedran, C. M. de Sterke, L. C. Botten, and M. J. Steel. Confinement losses in microstructured optical fibers. *Opt Lett* **26,** 1660-1662 (2001).

184. L. Xavier, and D. Elangovan. Effective parameters for improving deep hole drilling process by conventional method - a review. *International journal of engineering research and technology* **2,** (2013).

185. G. Woyessa, A. Fasano, C. Markos, H. K. Rasmussen, and O. Bang. Low loss polycarbonate polymer optical fiber for high temperature fbg humidity sensing. *Ieee Photonics Technology Letters* **29,** 575-578 (2017).

186. Y. N. Zhang, K. Li, L. L. Wang, L. Y. Ren, W. Zhao, R. C. Miao, M. C. J. Large, and M. A. van Eijkelenborg. Casting preforms for microstructured polymer optical fibre fabrication. *Optics Express* **14,** 5541-5547 (2006).

187. K. Cook, J. Canning, S. Leon-Saval, Z. Reid, M. A. Hossain, J. E. Comatti, Y. H. Luo, and G. D. Peng. Air-structured optical fiber drawn from a 3d-printed preform. *Optics Letters* **40,** 3966-3969 (2015).
188. P. M. Toal, L. J. Holmes, R. X. Rodriguez, and E. D. Wetzel. Microstructured monofilament via thermal drawing of additively manufactured preforms. *Additive Manufacturing* **16,** 12-23 (2017).
189. R. Mossadegh, J. S. Sanghera, D. Schaafsma, B. J. Cole, V. Q. Nguyen, R. E. Miklos, and I. D. Aggarwal. Fabrication of single-mode chalcogenide optical fiber. *Journal of Lightwave Technology* **16,** 214-217 (1998).
190. S. Shabahang, F. A. Tan, J. D. Perlstein, G. Tao, O. Alvarez, F. Chenard, A. Sincore, L. Shah, M. C. Richardson, K. L. Schepler, and A. F. Abouraddy. Robust multimaterial chalcogenide fibers produced by a hybrid fiber-fabrication process. *Optical Materials Express* **7,** 2336-2345 (2017).
191. K. Cook, G. Balle, J. Canning, L. Chartier, T. Athanaze, M. A. Hossain, C. Han, J.-E. Comatti, Y. Luo, and G.-D. Peng. Step-index optical fiber drawn from 3d printed preforms. *Optics Letters* **41,** 4554-4557 (2016).
192. G. Tao, A. M. Stolyarov, and A. F. Abouraddy. Multimaterial fibers. *International Journal of Applied Glass Science* **3,** 349-368 (2012).
193. G. T. Jasion, E. N. Fokoua, J. S. Shrimpton, D. J. Richardson, and F. Poletti. Studying the limits of production rate and yield for the volume manufacturing of hollow core photonic band gap fibers. *Optics Express* **23,** 32179-32190 (2015).
194. R. Kostecki, H. Ebendorff-Heidepriem, S. C. Warren-Smith, and T. M. Monro. Predicting the drawing conditions for microstructured optical fiber fabrication. *Optical Materials Express* **4,** 29-40 (2014).
195. G. Luzi, P. Epple, M. Scharrer, K. Fujimoto, C. Rauh, and A. Delgado. Influence of surface tension and inner pressure on the process of fibre drawing. *Journal of Lightwave Technology* **28,** 1882-1888 (2010).
196. R. F. Cregan, B. J. Mangan, J. C. Knight, T. A. Birks, P. S. J. Russell, P. J. Roberts, and D. C. Allan. Single-mode photonic band gap guidance of light in air. *Science* **285,** 1537-1539 (1999).
197. M. Yaman, T. Khudiyev, E. Ozgur, M. Kanik, O. Aktas, E. O. Ozgur, H. Deniz, E. Korkut, and M. Bayindir. Arrays of indefinitely long uniform nanowires and nanotubes. *Nature Materials* **10,** 494-501 (2011).
198. E. Arrospide, I. Bikandi, I. Larrañaga, X. Cearsolo, J. Zubia, and G. Durana. Harnessing deep-hole drilling to fabricate air-structured polymer optical fibres. *Polymers* **11,** 1739 (2019).
199. R. T. Bise, and D. J. Trevor. Sol-gel derived microstructured fiber: Fabrication and characterization. *OFC/NFOEC Technical Digest. Optical Fiber Communication Conference, 2005.* **3,** 3 pp. Vol. 3 (2005).
200. A. F. Abouraddy, M. Bayindir, G. Benoit, S. D. Hart, K. Kuriki, N. Orf, O. Shapira, F. Sorin, B. Temelkuran, and Y. Fink. Towards multimaterial multifunctional fibres that see, hear, sense and communicate. *Nature Materials* **6,** 336-347 (2007).
201. F. Poletti, M. N. Petrovich, and D. J. Richardson. Hollow-core photonic bandgap fibers: Technology and applications. *Nanophotonics* **2,** 315 (2013).
202. A. Gumennik, A. M. Stolyarov, B. R. Schell, C. Hou, G. Lestoquoy, F. Sorin, W. McDaniel, A. Rose, J. D. Joannopoulos, and Y. Fink. All-in-fiber chemical sensing. *Advanced Materials* **24,** 6005-6009 (2012).
203. Q. Zhao, F. Tian, X. Yang, S. Li, J. Zhang, X. Zhu, J. Yang, Z. Liu, Y. Zhang, T. Yuan, and L. Yuan. Optical fibers with special shaped cores drawn from 3d printed preforms. *Optik* **133,** 60-65 (2017).
204. R. M. Zaki, C. Strutynski, S. Kaser, D. Bernard, G. Hauss, M. Faessel, J. Sabatier, L. Canioni, Y. Messaddeq, S. Danto, and T. Cardinal. Direct 3d-printing of phosphate glass by fused deposition modeling. *Materials & Design* **194,** 108957 (2020).

205. W. Talataisong, R. Ismaeel, T. H. R. Marques, S. Abokhamis Mousavi, M. Beresna, M. A. Gouveia, S. R. Sandoghchi, T. Lee, C. M. B. Cordeiro, and G. Brambilla. Mid-ir hollow-core microstructured fiber drawn from a 3d printed petg preform. *Scientific Reports* **8,** 8113 (2018).

206. J. Zhao, A. Javadi, T.-C. Lin, I. Hwang, Y. Yang, Z. Guan, and X. Li. Scalable manufacturing of metal nanoparticles by thermal fiber drawing. *Journal of Micro and Nano-Manufacturing* **4,** (2016).

207. W. Yan, A. Page, T. Nguyen-Dang, Y. Qu, F. Sordo, L. Wei, and F. Sorin. Advanced multimaterial electronic and optoelectronic fibers and textiles. *Adv Mater* **31,** e1802348 (2019).

208. Y. Qu, T. Nguyen-Dang, A. G. Page, W. Yan, T. Das Gupta, G. M. Rotaru, R. M. Rossi, V. D. Favrod, N. Bartolomei, and F. Sorin. Superelastic multimaterial electronic and photonic fibers and devices via thermal drawing. *Advanced Materials* **30,** 1707251 (2018).

209. C. Hou, X. Jia, L. Wei, S.-C. Tan, X. Zhao, J. D. Joannopoulos, and Y. Fink. Crystalline silicon core fibres from aluminium core preforms. *Nature Communications* **6,** 6248 (2015).

210. P. Yeh, A. Yariv, and E. Marom. Theory of Bragg fiber. *Journal of the Optical Society of America* **68,** 1196-1201 (1978).

211. K. Kuriki, O. Shapira, S. D. Hart, G. Benoit, Y. Kuriki, J. F. Viens, M. Bayindir, J. D. Joannopoulos, and Y. Fink. Hollow multilayer photonic bandgap fibers for nir applications. *Optics Express* **12,** 1510-1517 (2004).

212. R. R. Gattass, D. Rhonehouse, D. Gibson, C. C. McClain, R. Thapa, V. Q. Nguyen, S. S. Bayya, R. J. Weiblen, C. R. Menyuk, L. B. Shaw, and J. S. Sanghera. Infrared glass-based negative-curvature anti-resonant fibers fabricated through extrusion. *Optics Express* **24,** 25697-25703 (2016).

213. G. Vienne, Y. Xu, C. Jakobsen, H. J. Deyerl, J. B. Jensen, T. Sorensen, T. P. Hansen, Y. Y. Huang, M. Terrel, R. K. Lee, N. A. Mortensen, J. Broeng, H. Simonsen, A. Bjarklev, and A. Yariv. Ultra-large bandwidth hollow-core guiding in all-silica Bragg fibers with nano-supports. *Optics Express* **12,** 3500-3508 (2004).

214. J. T. Kristensen, A. Houmann, X. M. Liu, and D. Turchinovich. Low-loss polarization-maintaining fusion splicing of single-mode fibers and hollow-core photonic crystal fibers, relevant for monolithic fiber laser pulse compression. *Optics Express* **16,** 9986-9995 (2008).

215. G. B. Ren, P. Shum, L. R. Zhang, X. Yu, W. J. Tong, and J. Luo. Low-loss all-solid photonic bandgap fiber. *Optics Letters* **32,** 1023-1025 (2007).

216. M. Skorobogatiy. Microstructured and photonic bandgap fibers for applications in the resonant bio- and chemical sensors. *Journal of Sensors* **2009,** 524237 (2009).

217. G. K. L. Wong, A. Y. H. Chen, S. W. Ha, R. J. Kruhlak, S. G. Murdoch, R. Leonhardt, and J. D. Harvey. Characterization of chromatic dispersion in photonic crystal fibers using scalar modulation instability. *Optics Express* **13,** 8662-8670 (2005).

218. A. Argyros, M. A. van Eijkelenborg, M. C. J. Large, and I. M. Bassett. Hollow-core microstructured polymer optical fiber. *Optics Letters* **31,** 172-174 (2006).

219. J. C. Knight, J. Broeng, T. A. Birks, and P. S. J. Russell. Photonic band gap guidance in optical fibers. *Science* **282,** 1476-1478 (1998).

220. J. C. Knight. Photonic crystal fibres. *Nature* **424,** 847-851 (2003).

221. M. Y. Chen. All-solid silica-based photonic crystal fibers. *Optics Communications* **266,** 151-158 (2006).

222. G. Benoit, S. D. Hart, B. Temelkuran, J. D. Joannopoulos, and Y. Fink. Static and dynamic properties of optical microcavities in photonic bandgap yarns. *Advanced Materials* **15,** 2053-2056 (2003).

223. G. Benoit, K. Kuriki, J. F. Viens, J. D. Joannopoulos, and Y. Fink. Dynamic all-optical tuning of transverse resonant cavity modes in photonic bandgap fibers. *Optics Letters* **30,** 1620-1622 (2005).

224. Z. Ruff, D. Shemuly, X. A. Peng, O. Shapira, Z. Wang, and Y. Fink. Polymer-composite fibers for transmitting high peak power pulses at 1.55 microns. *Optics Express* **18,** 15697-15703 (2010).

225. A. M. Cubillas, M. Silva-Lopez, J. M. Lazaro, O. M. Conde, M. N. Petrovich, and J. M. Lopez-Higuera. Methane detection at 1670-nm band using a hollow-core photonic bandgap fiber and a multiline algorithm. *Optics Express* **15,** 17570-17576 (2007).

226. T. Ritari, J. Tuominen, H. Ludvigsen, J. C. Petersen, T. Sorensen, T. P. Hansen, and H. R. Simonsen. Gas sensing using air-guiding photonic bandgap fibers. *Optics Express* **12,** 4080-4087 (2004).

227. F. Benabid. Hollow-core photonic bandgap fibre: New light guidance for new science and technology. *Philosophical Transactions of the Royal Society a-Mathematical Physical and Engineering Sciences* **364,** 3439-3462 (2006).

228. F. Benabid, and P. J. Roberts. Linear and nonlinear optical properties of hollow core photonic crystal fiber. *Journal of Modern Optics* **58,** 87-124 (2011).

229. A. F. Abouraddy, O. Shapira, M. Bayindir, J. Arnold, F. Sorin, D. S. Hinczewski, J. D. Joannopoulos, and Y. Fink. Large-scale optical-field measurements with geometric fibre constructs. *Nature Materials* **5,** 532-536 (2006).

230. F. Sorin, O. Shapira, A. F. Abouraddy, M. Spencer, N. D. Orf, J. D. Joannopoulos, and Y. Fink. Exploiting collective effects of multiple optoelectronic devices integrated in a single fiber. *Nano Letters* **9,** 2630-2635 (2009).

231. R. Yuan, J. Lee, H.-W. Su, E. Levy, T. Khudiyev, J. Voldman, and Y. Fink. Microfluidics in structured multimaterial fibers. *Proceedings of the National Academy of Sciences* **115,** E10830-E10838 (2018).

232. G. Lestoquoy, N. Chocat, Z. Wang, J. D. Joannopoulos, and Y. Fink. Fabrication and characterization of thermally drawn fiber capacitors. *Applied Physics Letters* **102,** 152908 (2013).

233. S. Gorgutsa, J. F. Gu, and M. Skorobogatiy. A woven 2d touchpad sensor and a 1d slide sensor using soft capacitor fibers. *Smart Materials and Structures* **21,** 015010 (2011).

234. R. He, T. D. Day, M. Krishnamurthi, J. R. Sparks, P. J. A. Sazio, V. Gopalan, and J. V. Badding. Silicon p-i-n junction fibers. *Advanced Materials* **25,** 1461-1467 (2013).

235. M. Kanik, M. Marcali, M. Yunusa, C. Elbuken, and M. Bayindir. Continuous triboelectric power harvesting and biochemical sensing inside poly(vinylidene fluoride) hollow fibers using microfluidic droplet generation. *Advanced Materials Technologies* **1,** 1600190 (2016).

236. R. He, P. J. A. Sazio, A. C. Peacock, N. Healy, J. R. Sparks, M. Krishnamurthi, V. Gopalan, and J. V. Badding. Integration of gigahertz-bandwidth semiconductor devices inside microstructured optical fibres. *Nature Photonics* **6,** 174-179 (2012).

237. A. C. Peacock, and N. Healy. Semiconductor optical fibres for infrared applications: A review. *Semiconductor Science and Technology* **31,** 103004 (2016).

238. J. R. Sparks, R. He, N. Healy, M. Krishnamurthi, A. C. Peacock, P. J. A. Sazio, V. Gopalan, and J. V. Badding. Zinc selenide optical fibers. *Advanced Materials* **23,** 1647-1651 (2011).

239. J. J. Kaufman, G. Tao, S. Shabahang, E.-H. Banaei, D. S. Deng, X. Liang, S. G. Johnson, Y. Fink, and A. F. Abouraddy. Structured spheres generated by an in-fibre fluid instability. *Nature* **487,** 463-467 (2012).

240. A. Gumennik, L. Wei, G. Lestoquoy, A. M. Stolyarov, X. Jia, P. H. Rekemeyer, M. J. Smith, X. Liang, B. J. B. Grena, S. G. Johnson, S. Gradečak, A. F. Abouraddy, J.

D. Joannopoulos, and Y. Fink. Silicon-in-silica spheres via axial thermal gradient in-fibre capillary instabilities. *Nature Communications* **4,** 2216 (2013).

241. A. Gumennik, E. C. Levy, B. Grena, C. Hou, M. Rein, A. F. Abouraddy, J. D. Joannopoulos, and Y. Fink. Confined in-fiber solidification and structural control of silicon and silicon−germanium microparticles. *Proceedings of the National Academy of Sciences* **114,** 7240-7245 (2017).
242. P. J. A. Sazio, A. Amezcua-Correa, C. E. Finlayson, J. R. Hayes, T. J. Scheidemantel, N. F. Baril, B. R. Jackson, D.-J. Won, F. Zhang, E. R. Margine, V. Gopalan, V. H. Crespi, and J. V. Badding. Microstructured optical fibers as high-pressure microfluidic reactors. *Science* **311,** 1583-1586 (2006).
243. P. J. Roberts, F. Couny, H. Sabert, B. J. Mangan, D. P. Williams, L. Farr, M. W. Mason, A. Tomlinson, T. A. Birks, J. C. Knight, and P. S. J. Russell. Ultimate low loss of hollow-core photonic crystal fibres. *Optics Express* **13,** 236-244 (2005).
244. L. Wei, C. Hou, E. Levy, G. Lestoquoy, A. Gumennik, A. F. Abouraddy, J. D. Joannopoulos, and Y. Fink. Optoelectronic fibers via selective amplification of in-fiber capillary instabilities. *Advanced Materials* **29,** 1603033 (2017).
245. J. Zhang, Z. Wang, Z. Wang, T. Zhang, and L. Wei. In-fibre particle manipulation and device assembly via laser induced thermocapillary convection. *Nature Communications* **10,** 5206 (2019).
246. G. Loke, R. Yuan, M. Rein, T. Khudiyev, Y. Jain, J. Joannopoulos, and Y. Fink. Structured multimaterial filaments for 3d printing of optoelectronics. *Nature Communications* **10,** 4010 (2019).
247. X. Xu, S. Wen, Q. Mao, and Y. Feng. N-anchoring in rare earth-doped amorphous tio2 as a route to broadband down-conversion phosphor. *ACS Applied Materials & Interfaces* **10,** 39238-39244 (2018).
248. A. Shakouri. Recent developments in semiconductor thermoelectric physics and materials. *Annual Review of Materials Research* **41,** 399-431 (2011).
249. G. Zhu, C. Pan, W. Guo, C.-Y. Chen, Y. Zhou, R. Yu, and Z. L. Wang. Triboelectric-generator-driven pulse electrodeposition for micropatterning. *Nano Letters* **12,** 4960-4965 (2012).
250. W. Yang, J. Chen, G. Zhu, X. Wen, P. Bai, Y. Su, Y. Lin, and Z. Wang. Harvesting vibration energy by a triple-cantilever based triboelectric nanogenerator. *Nano Research* **6,** 880-886 (2013).
251. W. Yang, J. Chen, Q. Jing, J. Yang, X. Wen, Y. Su, G. Zhu, P. Bai, and Z. L. Wang. 3d stack integrated triboelectric nanogenerator for harvesting vibration energy. *Advanced Functional Materials* **24,** 4090-4096 (2014).
252. J. Chen, G. Zhu, W. Yang, Q. Jing, P. Bai, Y. Yang, T.-C. Hou, and Z. L. Wang. Harmonic-resonator-based triboelectric nanogenerator as a sustainable power source and a self-powered active vibration sensor. *Advanced Materials* **25,** 6094-6099 (2013).
253. Z. Zhao, X. Pu, C. Du, L. Li, C. Jiang, W. Hu, and Z. L. Wang. Freestanding flag-type triboelectric nanogenerator for harvesting high-altitude wind energy from arbitrary directions. *ACS Nano* **10,** 1780-1787 (2016).
254. S. Chen, C. Gao, W. Tang, H. Zhu, Y. Han, Q. Jiang, T. Li, X. Cao, and Z. Wang. Self-powered cleaning of air pollution by wind driven triboelectric nanogenerator. *Nano Energy* **14,** 217-225 (2015).
255. Y. Xie, S. Wang, L. Lin, Q. Jing, Z.-H. Lin, S. Niu, Z. Wu, and Z. L. Wang. Rotary triboelectric nanogenerator based on a hybridized mechanism for harvesting wind energy. *ACS Nano* **7,** 7119-7125 (2013).
256. X. Fan, J. Chen, J. Yang, P. Bai, Z. Li, and Z. L. Wang. Ultrathin, rollable, paper-based triboelectric nanogenerator for acoustic energy harvesting and self-powered sound recording. *ACS Nano* **9,** 4236-4243 (2015).

257. N. Cui, L. Gu, J. Liu, S. Bai, J. Qiu, J. Fu, X. Kou, H. Liu, Y. Qin, and Z. L. Wang. High performance sound driven triboelectric nanogenerator for harvesting noise energy. *Nano Energy* **15,** 321-328 (2015).
258. F. Chen, Y. Wu, Z. Ding, X. Xia, S. Li, H. Zheng, C. Diao, G. Yue, and Y. Zi. A novel triboelectric nanogenerator based on electrospun polyvinylidene fluoride nanofibers for effective acoustic energy harvesting and self-powered multifunctional sensing. *Nano Energy* **56,** 241-251 (2019).
259. Z. L. Wang, T. Jiang, and L. Xu. Toward the blue energy dream by triboelectric nanogenerator networks. *Nano Energy* **39,** 9-23 (2017).
260. X. Wang, Z. Wen, H. Guo, C. Wu, X. He, L. Lin, X. Cao, and Z. L. Wang. Fully packaged blue energy harvester by hybridizing a rolling triboelectric nanogenerator and an electromagnetic generator. *ACS Nano* **10,** 11369-11376 (2016).
261. L. Pan, J. Wang, P. Wang, R. Gao, Y.-C. Wang, X. Zhang, J.-J. Zou, and Z. L. Wang. Liquid-FEP-based u-tube triboelectric nanogenerator for harvesting water-wave energy. *Nano Research* **11,** 4062-4073 (2018).
262. Q. Jiang, C. Wu, Z. Wang, A. C. Wang, J.-H. He, Z. L. Wang, and H. N. Alshareef. Mxene electrochemical microsupercapacitor integrated with triboelectric nanogenerator as a wearable self-charging power unit. *Nano Energy* **45,** 266-272 (2018).
263. F. Xi, Y. Pang, W. Li, T. Jiang, L. Zhang, T. Guo, G. Liu, C. Zhang, and Z. L. Wang. Universal power management strategy for triboelectric nanogenerator. *Nano Energy* **37,** 168-176 (2017).
264. X. Zhong, Y. Yang, X. Wang, and Z. L. Wang. Rotating-disk-based hybridized electromagnetic-triboelectric nanogenerator for scavenging biomechanical energy as a mobile power source. *Nano Energy* **13,** 771-780 (2015).
265. L. Dhakar, P. Pitchappa, F. E. H. Tay, and C. Lee. An intelligent skin based self-powered finger motion sensor integrated with triboelectric nanogenerator. *Nano Energy* **19,** 532-540 (2016).
266. X. Pu, H. Guo, J. Chen, X. Wang, Y. Xi, C. Hu, and Z. L. Wang. Eye motion triggered self-powered mechnosensational communication system using triboelectric nanogenerator. *Science Advances* **3,** e1700694 (2017).
267. F. Yi, L. Lin, S. Niu, P. K. Yang, Z. Wang, J. Chen, Y. Zhou, Y. Zi, J. Wang, Q. Liao, Y. Zhang, and Z. L. Wang. Stretchable-rubber-based triboelectric nanogenerator and its application as self-powered body motion sensors. *Advanced Functional Materials* **25,** 3688-3696 (2015).
268. M.-L. Seol, J.-W. Han, D.-I. Moon, and M. Meyyappan. Triboelectric nanogenerator for mars environment. *Nano Energy* **39,** 238-244 (2017).
269. M. Xu, Y.-C. Wang, S. L. Zhang, W. Ding, J. Cheng, X. He, P. Zhang, Z. Wang, X. Pan, and Z. L. Wang. An aeroelastic flutter based triboelectric nanogenerator as a self-powered active wind speed sensor in harsh environment. *Extreme Mechanics Letters* **15,** 122-129 (2017).
270. Z. Zhou, X. Li, Y. Wu, H. Zhang, Z. Lin, K. Meng, Z. Lin, Q. He, C. Sun, J. Yang, and Z. L. Wang. Wireless self-powered sensor networks driven by triboelectric nanogenerator for in-situ real time survey of environmental monitoring. *Nano Energy* **53,** 501-507 (2018).
271. X. Chen, K. Parida, J. Wang, J. Xiong, M.-F. Lin, J. Shao, and P. S. Lee. A stretchable and transparent nanocomposite nanogenerator for self-powered physiological monitoring. *ACS Applied Materials & Interfaces* **9,** 42200-42209 (2017).
272. X. Chen, Y. Song, Z. Su, H. Chen, X. Cheng, J. Zhang, M. Han, and H. Zhang. Flexible fiber-based hybrid nanogenerator for biomechanical energy harvesting and physiological monitoring. *Nano Energy* **38,** 43-50 (2017).

273. Q. Zheng, Y. Zou, Y. Zhang, Z. Liu, B. Shi, X. Wang, Y. Jin, H. Ouyang, Z. Li, and Z. L. Wang. Biodegradable triboelectric nanogenerator as a life-time designed implantable power source. *Science Advances* **2,** e1501478 (2016).
274. B. Yang, W. Zeng, Z.-H. Peng, S.-R. Liu, K. Chen, and X.-M. Tao. A fully verified theoretical analysis of contact-mode triboelectric nanogenerators as a wearable power source. *Advanced Energy Materials* **6,** 1600505 (2016).
275. Y. Yang, Y. S. Zhou, H. Zhang, Y. Liu, S. Lee, and Z. L. Wang. A single-electrode based triboelectric nanogenerator as self-powered tracking system. *Advanced Materials* **25,** 6594-6601 (2013).
276. B. Meng, W. Tang, Z.-h. Too, X. Zhang, M. Han, W. Liu, and H. Zhang. A transparent single-friction-surface triboelectric generator and self-powered touch sensor. *Energy & Environmental Science* **6,** 3235-3240 (2013).
277. N. Kaur, J. Bahadur, V. Panwar, P. Singh, K. Rathi, and K. Pal. Effective energy harvesting from a single electrode based triboelectric nanogenerator. *Scientific Reports* **6,** 38835 (2016).
278. M. Wang, N. Zhang, Y. Tang, H. Zhang, C. Ning, L. Tian, W. Li, J. Zhang, Y. Mao, and E. Liang. Single-electrode triboelectric nanogenerators based on sponge-like porous PTFE thin films for mechanical energy harvesting and self-powered electronics. *Journal of Materials Chemistry A* **5,** 12252-12257 (2017).
279. L. Jin, J. Chen, B. Zhang, W. Deng, L. Zhang, H. Zhang, X. Huang, M. Zhu, W. Yang, and Z. L. Wang. Self-powered safety helmet based on hybridized nanogenerator for emergency. *ACS Nano* **10,** 7874-7881 (2016).
280. L. Jin, J. Tao, R. Bao, L. Sun, and C. Pan. Self-powered real-time movement monitoring sensor using triboelectric nanogenerator technology. *Scientific Reports* **7,** 10521 (2017).
281. T. Li, J. Zou, F. Xing, M. Zhang, X. Cao, N. Wang, and Z. L. Wang. From dual-mode triboelectric nanogenerator to smart tactile sensor: A multiplexing design. *ACS Nano* **11,** 3950-3956 (2017).
282. Q. Jing, G. Zhu, P. Bai, Y. Xie, J. Chen, R. P. S. Han, and Z. L. Wang. Case-encapsulated triboelectric nanogenerator for harvesting energy from reciprocating sliding motion. *ACS Nano* **8,** 3836-3842 (2014).
283. L. Lin, S. Wang, Y. Xie, Q. Jing, S. Niu, Y. Hu, and Z. L. Wang. Segmentally structured disk triboelectric nanogenerator for harvesting rotational mechanical energy. *Nano Letters* **13,** 2916-2923 (2013).
284. W. Zhang, D. Diao, K. Sun, X. Fan, and P. Wang. Study on friction-electrification coupling in sliding-mode triboelectric nanogenerator. *Nano Energy* **48,** 456-463 (2018).
285. Y. Zi, J. Wang, S. Wang, S. Li, Z. Wen, H. Guo, and Z. L. Wang. Effective energy storage from a triboelectric nanogenerator. *Nature Communications* **7,** 10987 (2016).
286. C. Zhang, W. Tang, Y. Pang, C. Han, and Z. L. Wang. Active micro-actuators for optical modulation based on a planar sliding triboelectric nanogenerator. *Advanced Materials* **27,** 719-726 (2015).
287. S. Niu, Y. Liu, X. Chen, S. Wang, Y. S. Zhou, L. Lin, Y. Xie, and Z. L. Wang. Theory of freestanding triboelectric-layer-based nanogenerators. *Nano Energy* **12,** 760-774 (2015).
288. Y. Xie, S. Wang, S. Niu, L. Lin, Q. Jing, J. Yang, Z. Wu, and Z. L. Wang. Grating-structured freestanding triboelectric-layer nanogenerator for harvesting mechanical energy at 85% total conversion efficiency. *Advanced Materials* **26,** 6599-6607 (2014).
289. W. Shang, G. Q. Gu, F. Yang, L. Zhao, G. Cheng, Z.-l. Du, and Z. L. Wang. A sliding-mode triboelectric nanogenerator with chemical group grated structure by shadow mask reactive ion etching. *ACS Nano* **11,** 8796-8803 (2017).

290. Y. J. Kim, J. Lee, S. Park, C. Park, C. Park, and H.-J. Choi. Effect of the relative permittivity of oxides on the performance of triboelectric nanogenerators. *RSC Advances* **7,** 49368-49373 (2017).

291. X.-S. Zhang, M.-D. Han, R.-X. Wang, F.-Y. Zhu, Z.-H. Li, W. Wang, and H.-X. Zhang. Frequency-multiplication high-output triboelectric nanogenerator for sustainably powering biomedical microsystems. *Nano Letters* **13,** 1168-1172 (2013).

292. C. K. Jeong, K. M. Baek, S. Niu, T. W. Nam, Y. H. Hur, D. Y. Park, G.-T. Hwang, M. Byun, Z. L. Wang, Y. S. Jung, and K. J. Lee. Topographically-designed triboelectric nanogenerator via block copolymer self-assembly. *Nano Letters* **14,** 7031-7038 (2014).

293. B. Dudem, D. H. Kim, A. R. Mule, and J. S. Yu. Enhanced performance of microarchitectured PTFE-based triboelectric nanogenerator via simple thermal imprinting lithography for self-powered electronics. *ACS Applied Materials & Interfaces* **10,** 24181-24192 (2018).

294. L. Cheng, Q. Xu, Y. Zheng, X. Jia, and Y. Qin. A self-improving triboelectric nanogenerator with improved charge density and increased charge accumulation speed. *Nature Communications* **9,** 3773 (2018).

295. W. Du, X. Han, L. Lin, M. Chen, X. Li, C. Pan, and Z. L. Wang. A three dimensional multi-layered sliding triboelectric nanogenerator. *Advanced Energy Materials* **4,** 1301592 (2014).

296. P. Bai, G. Zhu, Z.-H. Lin, Q. Jing, J. Chen, G. Zhang, J. Ma, and Z. L. Wang. Integrated multilayered triboelectric nanogenerator for harvesting biomechanical energy from human motions. *ACS Nano* **7,** 3713-3719 (2013).

297. L. Xu, T. Z. Bu, X. D. Yang, C. Zhang, and Z. L. Wang. Ultrahigh charge density realized by charge pumping at ambient conditions for triboelectric nanogenerators. *Nano Energy* **49,** 625-633 (2018).

298. S. Wang, Y. Xie, S. Niu, L. Lin, C. Liu, Y. S. Zhou, and Z. L. Wang. Maximum surface charge density for triboelectric nanogenerators achieved by ionized-air injection: Methodology and theoretical understanding. *Advanced Materials* **26,** 6720-6728 (2014).

299. J. J. Shao, W. Tang, T. Jiang, X. Y. Chen, L. Xu, B. D. Chen, T. Zhou, C. R. Deng, and Z. L. Wang. A multi-dielectric-layered triboelectric nanogenerator as energized by corona discharge. *Nanoscale* **9,** 9668-9675 (2017).

300. T. Zhou, L. Zhang, F. Xue, W. Tang, C. Zhang, and Z. L. Wang. Multilayered electret films based triboelectric nanogenerator. *Nano Research* **9,** 1442-1451 (2016).

301. G. Zhu, J. Chen, T. Zhang, Q. Jing, and Z. L. Wang. Radial-arrayed rotary electrification for high performance triboelectric generator. *Nature Communications* **5,** 3426 (2014).

302. G. Zhu, Y. S. Zhou, P. Bai, X. S. Meng, Q. Jing, J. Chen, and Z. L. Wang. A shape-adaptive thin-film-based approach for 50% high-efficiency energy generation through micro-grating sliding electrification. *Advanced Materials* **26,** 3788-3796 (2014).

303. W. Tang, T. Jiang, F. R. Fan, A. F. Yu, C. Zhang, X. Cao, and Z. L. Wang. Liquid-metal electrode for high-performance triboelectric nanogenerator at an instantaneous energy conversion efficiency of 70.6%. *Advanced Functional Materials* **25,** 3718-3725 (2015).

304. J. Liu, L. Gu, N. Cui, Q. Xu, Y. Qin, and R. Yang. Fabric-based triboelectric nanogenerators. *Research* **2019,** 13 (2019).

305. K. Dong, X. Peng, and Z. L. Wang. Fiber/fabric-based piezoelectric and triboelectric nanogenerators for flexible/stretchable and wearable electronics and artificial intelligence. *Advanced Materials* **32,** 1902549 (2020).

306. Y. Hu, and Z. Zheng. Progress in textile-based triboelectric nanogenerators for smart fabrics. *Nano Energy* **56,** 16-24 (2019).

307. S. S. Kwak, H. Kim, W. Seung, J. Kim, R. Hinchet, and S. W. Kim. Fully stretchable textile triboelectric nanogenerator with knitted fabric structures. *ACS Nano* **11,** 10733-10741 (2017).

308. F. Peng, D. Liu, W. Zhao, G. Zheng, Y. Ji, K. Dai, L. Mi, D. Zhang, C. Liu, and C. Shen. Facile fabrication of triboelectric nanogenerator based on low-cost thermoplastic polymeric fabrics for large-area energy harvesting and self-powered sensing. *Nano Energy* **65,** 104068 (2019).

309. X. Pu, W. Song, M. Liu, C. Sun, C. Du, C. Jiang, X. Huang, D. Zou, W. Hu, and Z. L. Wang. Wearable power-textiles by integrating fabric triboelectric nanogenerators and fiber-shaped dye-sensitized solar cells. *Advanced Energy Materials* **6,** 1601048 (2016).

310. Z. Wang, Z. Ruan, W. S. Ng, H. Li, Z. Tang, Z. Liu, Y. Wang, H. Hu, and C. Zhi. Integrating a triboelectric nanogenerator and a zinc-ion battery on a designed flexible 3d spacer fabric. *Small Methods* **2,** 1800150 (2018).

311. J. Zhong, Y. Zhang, Q. Zhong, Q. Hu, B. Hu, Z. L. Wang, and J. Zhou. Fiber-based generator for wearable electronics and mobile medication. *ACS Nano* **8,** 6273-6280 (2014).

312. S.-B. Jeon, S.-J. Park, W.-G. Kim, I.-W. Tcho, I.-K. Jin, J.-K. Han, D. Kim, and Y.-K. Choi. Self-powered wearable keyboard with fabric based triboelectric nanogenerator. *Nano Energy* **53,** 596-603 (2018).

313. Y.-C. Lai, J. Deng, S. L. Zhang, S. Niu, H. Guo, and Z. L. Wang. Single-thread-based wearable and highly stretchable triboelectric nanogenerators and their applications in cloth-based self-powered human-interactive and biomedical sensing. *Advanced Functional Materials* **27,** 1604462 (2017).

314. J. Park, A. Y. Choi, C. J. Lee, D. Kim, and Y. T. Kim. Highly stretchable fiber-based single-electrode triboelectric nanogenerator for wearable devices. *RSC Advances* **7,** 54829-54834 (2017).

315. M. Liu, Z. Cong, X. Pu, W. Guo, T. Liu, M. Li, Y. Zhang, W. Hu, and Z. L. Wang. High-energy asymmetric supercapacitor yarns for self-charging power textiles. *Advanced Functional Materials* **29,** 1806298 (2019).

316. X. He, Y. Zi, H. Guo, H. Zheng, Y. Xi, C. Wu, J. Wang, W. Zhang, C. Lu, and Z. L. Wang. A highly stretchable fiber-based triboelectric nanogenerator for self-powered wearable electronics. *Advanced Functional Materials* **27,** 1604378 (2017).

317. Z. Tian, J. He, X. Chen, T. Wen, C. Zhai, Z. Zhang, J. Cho, X. Chou, and C. Xue. Core–shell coaxially structured triboelectric nanogenerator for energy harvesting and motion sensing. *RSC Advances* **8,** 2950-2957 (2018).

318. W. B. Ko, D. S. Choi, C. H. Lee, J. Y. Yang, G. S. Yoon, and J. P. Hong. Hierarchically nanostructured 1d conductive bundle yarn-based triboelectric nanogenerators. *Advanced Materials* **29,** 1704434 (2017).

319. Z. Zhao, C. Yan, Z. Liu, X. Fu, L.-M. Peng, Y. Hu, and Z. Zheng. Machine-washable textile triboelectric nanogenerators for effective human respiratory monitoring through loom weaving of metallic yarns. *Advanced Materials* **28,** 10267-10274 (2016).

320. K. Dong, J. Deng, Y. Zi, Y.-C. Wang, C. Xu, H. Zou, W. Ding, Y. Dai, B. Gu, B. Sun, and Z. L. Wang. 3d orthogonal woven triboelectric nanogenerator for effective biomechanical energy harvesting and as self-powered active motion sensors. *Advanced Materials* **29,** 1702648 (2017).

321. H. Li, S. Zhao, X. Du, J. Wang, R. Cao, Y. Xing, and C. Li. A compound yarn based wearable triboelectric nanogenerator for self-powered wearable electronics. *Advanced Materials Technologies* **3,** 1800065 (2018).

322. H. J. Sim, C. Choi, S. H. Kim, K. M. Kim, C. J. Lee, Y. T. Kim, X. Lepró, R. H. Baughman, and S. J. Kim. Stretchable triboelectric fiber for self-powered kinematic sensing textile. *Scientific Reports* **6,** 35153 (2016).

323. K. N. Kim, J. Chun, J. W. Kim, K. Y. Lee, J.-U. Park, S.-W. Kim, Z. L. Wang, and J. M. Baik. Highly stretchable 2d fabrics for wearable triboelectric nanogenerator under harsh environments. *ACS Nano* **9,** 6394-6400 (2015).

324. M. Zhu, Y. Huang, W. S. Ng, J. Liu, Z. Wang, Z. Wang, H. Hu, and C. Zhi. 3d spacer fabric based multifunctional triboelectric nanogenerator with great feasibility for mechanized large-scale production. *Nano Energy* **27,** 439-446 (2016).

325. H. T. Pham, and C. J. Carriere. The effect of temperature on the interfacial tension of polycarbonate/polyethylene blends. *Polymer Engineering & Science* **37,** 636-639 (1997).

326. A. W. Van Herwaarden, and P. M. Sarro. Thermal sensors based on the seebeck effect. *Sensors and Actuators* **10,** 321-346 (1986).

327. A. Mzerd, F. Tcheliebou, A. Sackda, and A. Boyer. Improvement of thermal sensors based on Bi_2Te_3, Sb_2Te_3 and $Bi_{0.1}Sb_{1.9}Te_3$. *Sensors and Actuators A: Physical* **47,** 387-390 (1995).

328. S. Cui, C. Boussard-plédel, L. Calvez, F. Rojas, K. Chen, H. Ning, M. J. Reece, T. Guizouarn, and B. Bureau. Comprehensive study of tellurium based glass ceramics for thermoelectric application. *Advances in Applied Ceramics* **114,** S42-S47 (2015).

329. P. Lucas, C. Conseil, Z. Yang, Q. Hao, S. Cui, C. Boussard-Pledel, B. Bureau, F. Gascoin, C. Caillaud, O. Gulbiten, T. Guizouarn, P. Baruah, Q. Li, and J. Lucas. Thermoelectric bulk glasses based on the Cu–As–Te–Se system. *Journal of Materials Chemistry A* **1,** 8917-8925 (2013).

330. B. Srinivasan, S. Cui, C. Prestipino, A. Gellé, C. Boussard-Pledel, S. Ababou-Girard, A. Trapananti, B. Bureau, and S. Di Matteo. Possible mechanism for hole conductivity in Cu–As–Te thermoelectric glasses: A xanes and exafs study. *The Journal of Physical Chemistry C* **121,** 14045-14050 (2017).

331. W. Yan, C. Dong, Y. Xiang, S. Jiang, A. Leber, G. Loke, W. Xu, C. Hou, S. Zhou, M. Chen, R. Hu, P. P. Shum, L. Wei, X. Jia, F. Sorin, X. Tao, and G. Tao. Thermally drawn advanced functional fibers: New frontier of flexible electronics. *Materials Today* **35,** 168-194 (2020).

332. R. I. Haque, P.-A. Farine, and D. Briand. Soft triboelectric generators by use of cost-effective elastomers and simple casting process. *Sensors and Actuators A: Physical* **271,** 88-95 (2018).

333. M. D. Dickey, R. C. Chiechi, R. J. Larsen, E. A. Weiss, D. A. Weitz, and G. M. Whitesides. Eutectic gallium-indium (egain): A liquid metal alloy for the formation of stable structures in microchannels at room temperature. *Advanced Functional Materials* **18,** 1097-1104 (2008).

334. D. Zrnic, and D. S. Swatik. On the resistivity and surface tension of the eutectic alloy of gallium and indium. *Journal of The Less Common Metals* **18,** 67-68 (1969).

335. Z. L. Wang. On maxwell's displacement current for energy and sensors: The origin of nanogenerators. *Materials Today* **20,** 74-82 (2017).

336. H. D. Rowland, A. C. Sun, P. R. Schunk, and W. P. King. Impact of polymer film thickness and cavity size on polymer flow during embossing: Toward process design rules for nanoimprint lithography. *Journal of Micromechanics and Microengineering* **15,** 2414-2425 (2005).

337. L. J. Guo. Nanoimprint lithography: Methods and material requirements. *Advanced Materials* **19,** 495-513 (2007).

338. J. J. Dumond, and H. Y. Low. Recent developments and design challenges in continuous roller micro- and nanoimprinting. *Journal of Vacuum Science & Technology B* **30,** 010801 (2012).

339. N. Kooy, K. Mohamed, L. T. Pin, and O. S. Guan. A review of roll-to-roll nanoimprint lithography. *Nanoscale Research Letters* **9,** 320 (2014).

340. J. Zhang, Y. Li, X. Zhang, and B. Yang. Colloidal self-assembly meets nanofabrication: From two-dimensional colloidal crystals to nanostructure arrays. *Advanced Materials* **22,** 4249-4269 (2010).
341. C. Vieu, F. Carcenac, A. Pépin, Y. Chen, M. Mejias, A. Lebib, L. Manin-Ferlazzo, L. Couraud, and H. Launois. Electron beam lithography: Resolution limits and applications. *Applied Surface Science* **164,** 111-117 (2000).
342. D. Qin, Y. Xia, and G. M. Whitesides. Soft lithography for micro- and nanoscale patterning. *Nature Protocols* **5,** 491-502 (2010).
343. J. Melngailis. Focused ion beam technology and applications. *Journal of Vacuum Science & Technology B: Microelectronics Processing and Phenomena* **5,** 469-495 (1987).
344. J. H. Brannon, and J. R. Lankard. Pulsed CO_2 laser etching of polyimide. *Applied Physics Letters* **48,** 1226-1228 (1986).
345. M. S. Amer, M. A. El-Ashry, L. R. Dosser, K. E. Hix, J. F. Maguire, and B. Irwin. Femtosecond versus nanosecond laser machining: Comparison of induced stresses and structural changes in silicon wafers. *Applied Surface Science* **242,** 162-167 (2005).
346. S. Xue, G. Barton, S. Fleming, and A. Argyros. Heat transfer modeling of the capillary fiber drawing process. *Journal of Heat Transfer* **139,** (2017).
347. A. G. Page, M. Bechert, F. Gallaire, and F. Sorin. Unraveling radial dependency effects in fiber thermal drawing. *Applied Physics Letters* **115,** 044102 (2019).
348. H. Papamichael, and I. N. Miaoulis. Thermal behavior of optical fibers during the cooling stage of the drawing process. *Journal of Materials Research* **6,** 159-167 (1991).
349. G. L. W. Cross, R. M. Langford, B. S. O'Connell, and J. B. Pethica. The mechanics of nanoimprint forming. *MRS Proceedings* **841,** R1.6 (2004).
350. K. Avila, D. Moxey, A. de Lozar, M. Avila, D. Barkley, and B. Hof. The onset of turbulence in pipe flow. *Science* **333,** 192-196 (2011).
351. B. R. Munson, D. F. Young, and T. H. Okiishi. *Fundamentals of fluid mechanics. pp. 322-323.* (Wiley, New York, 2013).
352. A. Shrivastava. *Introduction to plastics engineering. Ch. 1.* (William Andrew Publishing, Norwich, NY, 2018).
353. H.-C. Scheer, N. Bogdanski, and M. Wissen. Issues in nanoimprint processes: The imprint pressure. *Japanese Journal of Applied Physics* **44,** 5609-5616 (2005).
354. J. C. Moreira, and N. R. Demarquette. Influence of temperature, molecular weight, and molecular weight dispersity on the surface tension of ps, pp, and pe. I. Experimental. *Journal of Applied Polymer Science* **82,** 1907-1920 (2001).
355. A. V. Kabashin, P. Evans, S. Pastkovsky, W. Hendren, G. A. Wurtz, R. Atkinson, R. Pollard, V. A. Podolskiy, and A. V. Zayats. Plasmonic nanorod metamaterials for biosensing. *Nature Materials* **8,** 867-871 (2009).
356. D. Débarre, W. Supatto, A.-M. Pena, A. Fabre, T. Tordjmann, L. Combettes, M.-C. Schanne-Klein, and E. Beaurepaire. Imaging lipid bodies in cells and tissues using third-harmonic generation microscopy. *Nature Methods* **3,** 47-53 (2006).
357. Z. Li, M.-H. Kim, C. Wang, Z. Han, S. Shrestha, A. C. Overvig, M. Lu, A. Stein, A. M. Agarwal, M. Lončar, and N. Yu. Controlling propagation and coupling of waveguide modes using phase-gradient metasurfaces. *Nature Nanotechnology* **12,** 675-683 (2017).
358. C. Wu, A. C. Wang, W. Ding, H. Guo, and Z. L. Wang. Triboelectric nanogenerator: A foundation of the energy for the new era. *Advanced Energy Materials* **9,** 1802906 (2019).
359. M. Chen, X. Li, L. Lin, W. Du, X. Han, J. Zhu, C. Pan, and Z. L. Wang. Triboelectric nanogenerators as a self-powered motion tracking system. *Advanced Functional Materials* **24,** 5059-5066 (2014).

360. S. Ebnesajjad. *Melt processible fluoroplastics. Ch. 2.* (William Andrew Publishing, Norwich, NY, 2003).

361. M. M. Tousi, Y. J. Zhang, S. W. Wan, L. Yu, C. Hou, N. Yan, Y. Fink, A. B. Wang, and X. T. Jia. Scalable fabrication of highly flexible porous polymer-based capacitive humidity sensor using convergence fiber drawing. *Polymers* **11,** (2019).

362. K. Dong, Y.-C. Wang, J. Deng, Y. Dai, S. L. Zhang, H. Zou, B. Gu, B. Sun, and Z. L. Wang. A highly stretchable and washable all-yarn-based self-charging knitting power textile composed of fiber triboelectric nanogenerators and supercapacitors. *ACS Nano* **11,** 9490-9499 (2017).

363. C. Ning, L. Tian, X. Zhao, S. Xiang, Y. Tang, E. Liang, and Y. Mao. Washable textile-structured single-electrode triboelectric nanogenerator for self-powered wearable electronics. *Journal of Materials Chemistry A* **6,** 19143-19150 (2018).

364. L. Liu, J. Pan, P. Chen, J. Zhang, X. Yu, X. Ding, B. Wang, X. Sun, and H. Peng. A triboelectric textile templated by a three-dimensionally penetrated fabric. *Journal of Materials Chemistry A* **4,** 6077-6083 (2016).